Ultrashort-pulse laser ablation of silicon toward device applications

ULTRASHORT-PULSE LASER ABLATION OF SILICON TOWARD DEVICE APPLICATIONS

BY

EUGENE HSU, B. Eng., M.A.Sc.

A THESIS

SUBMITTED TO THE DEPARTMENT OF ENGINEERING PHYSICS

AND THE SCHOOL OF GRADUATE STUDIES

OF MCMASTER UNIVERSITY

IN PARTIAL FULFILMENT OF THE REQUIREMENTS

FOR THE DEGREE OF

DOCTOR OF PHILOSOPHY

Doctor of Philosophy (2012)   McMaster University

(Engineering Physics)   Hamilton, Ontario, Canada

TITLE: Ultrashort-pulse laser ablation of silicon toward device
                    applications

AUTHOR: Eugene Hsu

                    M.A.Sc. (McMaster University)

                    B.Eng. (Carleton University)

SUPERVISOR: Dr. Harold Haugen

NUMBER OF PAGES: xxiii, 202

Abstract

This thesis presents investigations on ultrafast laser irradiation of silicon towards the goal of hybridizing ultrafast laser processing and conventional semiconductor fabrication techniques to improve device applications. The fundamental sub-threshold damage accumulation mechanisms for potential defect engineering applications were studied through the use of positron annihilation spectroscopy, *in situ* sample heating during laser irradiation, varying the laser repetition rate, and samples implanted with various ion species at different conditions. Positron annihilation spectroscopy results suggest an increase in the divacancy density at the surface region of silicon following near- and slightly sub-threshold ultrafast laser irradiations. Laser irradiations at increasing sample temperature up to 600°C show a general decreasing trend of single-shot thresholds, and an increase in the suppression of sub-threshold damage accumulation. There is also a temperature dependence on the surface morphology resulting from ultrafast laser irradiation. Ion implantation modified the ablation threshold fluence, and a dependence on the ion implantation conditions was observed. Surface microstructuring of silicon was shown to improve absorption of light with a sub-bandgap wavelength of 1550 nm. An initial attempt with sulfur implantation did not exhibit further improvement in the optical absorption, and first attempts in device fabrication did not provide photoresponsivity at sub-bandgap wavelengths. Ultrafast

laser irradiation of SiO_2-on-Si structures yielded different modification thresholds for different thicknesses of the oxide layer. Surface morphologies obtained in the irradiation of these structures can affect potential applications. Selected studies of ultrafast laser irradiation of GaP, metal-SiO_2-Si structures, quartz, diamond, and porcine bone demonstrated similarities in ablation behavior and morphologies, and the potential for a broad range of applications. The results in combination with the proposed future work in this thesis can contribute to potential device applications while providing valuable insights into the ultrafast laser ablation mechanisms.

Acknowledgements

First off I would like to thank my supervisor Professor Harold Haugen for providing the opportunity for me to conduct research work in the Photonics Research Laboratory at McMaster University. Learning from Professor Haugen's great patience, ethics and attention to details allowed me to improve tremendously both in laboratory work and in general. Both of Dr. Haugen's supervisory and interpersonal styles have been a great match for me, and have made my graduate school experience enjoyable.

I would also like to thank my supervisory committee members, Dr. John Preston and Dr. Gianluigi Botton, for their support and guidance all along my graduate studies. Also Dr. Chang-Qing Xu who was a former supervisory committee member before the focus of my Ph.D. changed course (from THz-based research) also had provided guidance, support and encouragement. Dr. Paul Jessop, and Dr. Andrew Knights in particular, have provided a tremendous collaborative opportunities for me. It is one thing to have access to expert knowledge in silicon photonics in the department, but Dr. Knight's enthusiasms in the project had been very encouraging and motivating.

Aside from Dr. Haugen's guidance, of course, our very own former research scientist engineer Dr. Henry Tiedje, now Drs. Travis Crawford and Andrew Budz have taught me practically everything I know and can do in the lab. Then there

my interest in research and helped launching me down the path I took.

There are great many people whose friendship have made my stay in Hamilton a pleasant time and kept me grounded during hectic times that it will not be possible to include everyone here, but special mentions would go out to Andrew and Hanna Budz, Jasper Brawley-Hayes, Paul Okrutny, Kevin Liu, Ran An, Tara Power, Vickram Lakhian, Laura Beaudin, and many others. A big thank you to you all.

Lastly, the family. My parents Joseph and Anita Hsu, and my loving wife Emily Wong have been nothing short of being phenomenal in terms of being supportive and encouraging, not just throughout my stay in Hamilton for graduate school but in life up to this point in general.

Contents

ix

List of Tables

List of Figures

Symbols and abbreviations

α_{eff} Effective absorption coefficient in laser-material interactions

α_{linear} Linear absorption coefficient

β Two photon absorption coefficient

λ Incident laser irradiation wavelength (in air)

ω_o Incident laser spot size ($1/\text{e}^2$ radius)

ϕ_{th} Threshold peak laser fluence

$\phi_{\text{th}}(1)$ Single-shot threshold fluence

$\phi_{\text{th}}(\infty)$ Threshold fluence for infinite numbers of shots (used in exponential model)

$\phi_{\text{th}}(N)$ Threshold fluence for N shots of laser pulses

ϕ_o Peak laser fluence used

ξ Incubation coefficient (used in the power law incubation model)

D Measured diameter of laser-ablation feature

E_{ref} Energy level used as a reference for a specific experimental condition or geometry

E_{th} Threshold laser energy (for a given spot size)

E_o Laser pulse energy used

f Laser repetition rate (Hz)

I_o Laser intensity employed

k Incubation coefficient (used in exponential model [1])

L Ablation depth per pulse

N Number of laser pulses

n Refractive index of material

N_{eff} Effective number of shots (seen by a given position in translational irradiation)

R Small signal reflectivity

v Translation speed of laser beam across sample surface

AFM   Atomic force microscopy

DIC   Differential interference contrast

EDX/EDS   Energy dispersive x-ray spectroscopy

FIB   Focused ion beam

FWHM   Full-width at half-maximum

HSFL   High spatial frequency LIPSS

LIPSS   Laser induced period surface structures

LSFL   Low spatial frequency LIPSS

O.D.   Optical density

OM   Optical microscopy

PL   Photoluminescence

SEM   Scanning electron microscopy

TEM   Transmission electron microscopy

ULSFL   Ultra-low spatial frequency LIPSS

Academic achievement

For the experiments presented in this thesis, unless otherwise stated as collaborative efforts, I have been the main coordinator of projects and carried out the experiments with the guidance of my supervisor Professor Harold Haugen. Included in this section is a list of journal articles published during my Ph.D. program, either as the primary or collaborative research student, and a rough description of my role in each project. As the initial focus of my Ph.D. program was on THz-based research, my role in the collaborative laser ablation projects was prompted by my experience with the laser ablation work available to the laboratory.

- B. Emigh, R. An, **E. M. Hsu**, T. H. R. Crawford, H. K. Haugen, G. R. Wohl, J. E. Hayward and Q. Fang, "Porcine cortical bone ablation by ultrashort pulsed laser irradiation", J. Biomed. Opt. **17**, 0128001 (2012)

  I was involved in the early stages of the project where optimization of the laser irradiation scheme was developed, including selection and prototyping of a sealed container for the sample, and operation of the laser micromachining setup. I was also involved in the preparation of the submitted manuscript.

- **E. M. Hsu**, N. A. Mailman, G. A. Botton and H. K. Haugen, "Microscopic investigation of single-crystal diamond following ultrafast laser irradiation", Appl.

Phys. A **103**, 185 (2011)

I carried out ultrafast laser irradiation of samples, and was involved in post-analysis discussions and preparation of the manuscript.

- M. Budiman, **E. M. Hsu**, H. K. Haugen and G. A. Botton, "Cross-sectional study of femtosecond laser bulk modification of crystalline α-quartz" Appl. Phys. A **98**, 849 (2010)

I carried out ultrafast laser irradiation of samples, and was involved in post-analysis discussions and preparation of the manuscript.

- **E. M. Hsu**, T. H. R. Crawford, C. Maunders, G. A. Botton, H. K. Haugen, "Cross-sectional study of periodic surface structures on gallium phosphide induced by ultrashort laser pulse irradiation", Appl. Phys. Lett. **92**, 221112 (2008)

I carried out the ultrafast laser irradiation of the samples, subsequent optical and scanning electron microscopy analysis, and preparation of the manuscript. While the experiments and analysis began before the official commencement of my Ph.D. program, follow-up work and the writing took place within the time frame of my Ph.D. program.

- T. H. R. Crawford, J. Yamanaka, **E. M. Hsu**, G. A. Botton, H. K. Haugen, "Femtosecond laser irradiation of metal and thermal oxide layers on silicon: studies utilising cross-sectional transmission electron microscopy", Appl. Phys. A **91**, 473 (2008)

Assisted in material irradiation with frequency-converted (400 nm) ultrafast laser pulses and subsequent electron microscopy analysis.

Chapter 1

Introduction

Ultrashort laser pulses are generally accepted as laser pulses with durations on the order of a few picoseconds or shorter (10^{-12} s). This time scale is typically shorter than the electron-phonon coupling time of a given material, providing ablation and micromachining capabilities that were not accessible with more conventional long-pulse lasers. For example, the ultrafast laser energy deposition is completed before material heating, yielding ablation and micromachining features with minimized collateral thermal damage. On another hand, the electronic absorption mechanism in transparent materials is a deterministic process with ultrashort laser pulses, resulting in well defined ablation thresholds. This is contrary to the statistical threshold nature when longer pulses are used. The combination of the above factors leads to the capability to produce features with high spatial resolutions that can be finer than the diffraction-limited laser spot size.

Interactions of ultrashort laser pulses with materials have also been observed to generate coherent and pseudo-coherent surface structures. For example, periodic ripples have been observed with spatial periods somewhat below the irradiation laser

wavelength, and substantially below the laser wavelength in materials irradiated with ultrashort laser pulses. Conical structures and spikes have also been observed.

While novel applications have been achieved with ultrashort-pulse laser ablation, the exact ablation mechanisms have been under discussion in the literature. In theoretical modeling of nanosecond laser pulse interaction with materials, where the pulse duration is orders of magnitude higher than the electron-phonon coupling time, thermal excitation and electron-lattice equilibrium can be assumed to be instantaneous relative to the pulse duration. However, this is not the case with ultrashort laser pulses. Modeling of ultrashort-pulse laser ablation of materials requires separate treatments of electron and lattice temperatures, as well as consideration of the highly non-equilibrium temperature and density conditions due to ultrafast laser energy deposition. On account of these challenges, in conjunction with the requirement of high temporal resolution due to the ultrafast events, modeling of ultrashort-pulse laser ablation calls for extensive computing powers, and typical simulation results are those of a limited "slice" of the sample, providing limited, while useful, information.

In the electronics and optoelectronics domain, silicon has a very broad range of applications, and is considered a relatively mature technology. This arises from the abundance of the material, and the maturity in silicon technologies over time has allowed the ability to grow and control high quality samples. Silicon was chosen as the material of choice for the exploratory work in this thesis due to its technological importance, as well as the depth and breadth of existing knowledge in the technology.

The unique ablation, micromachining and surface structuring capabilities of ultrashort pulse lasers can be exploited in conjunction with conventional device processing

techniques to improve upon electrical and photonics devices. Meanwhile, characterization of ultrafast laser interactions with materials that have gone through different steps in the conventional processing flow is useful not only to hybridize the two processing techniques but can also shed further insight into the fundamental mechanisms of the ultrafast laser-materials interactions.

The topics summarized in this thesis include different areas of ultrashort pulse laser interactions with virgin and processed silicon materials with conventional fabrication steps, such as ion implantation and oxide growth, exploration work of the fundamental laser-materials interactions inspired by material annealing dynamics, secondary novel findings from such experiments, as well as potential applications of the combinations of the two types of processing techniques. Chapter 2 provides relevant background information to the generation, amplification and diagnostics of ultrashort laser pulses, ablation mechanisms and typical experimental setups common to experiments presented in this thesis. Specific background and experimental considerations, conclusions and suggested future work are presented in the relevant chapters. Chapter 3 presents a series of experiments characterizing the ablation threshold and damage accumulation (incubation) mechanisms. Chapter 4 presents surface morphological findings from specific repeated surface irradiation conditions, while Chapter 5 presents secondary surface morphological findings resulting from *in situ* heating of the samples during the incubation studies; both relate back to experimental work presented in Chapter 3. Chapter 6 presents preliminary results from optical absorption and electronic photoresponsivity measurements from surface texturing of silicon in conjunction with ion-implantation with the goal of improving sub-bandgap absorption in silicon-based devices. The last series of experiments is presented in Chapter 7

showing thresholds and morphological findings of laser irradiation of SiO_2-on-Si structures. An extra chapter is included showing work conducted outside of the silicon theme, studying the interactions or applications of ultrafast laser pulses with various materials, including gallium phosphide, synthetic diamond, quartz, metal-silicon dioxide-silicon structure, and porcine bones. Lastly, a brief summary of the key findings of the experimental results in this thesis is presented in the Conclusions chapter. An appendix is included showing details of wire-like nanostructure formation during high-temperature ablation of silicon.

Chapter 2

Background

This part of the thesis briefly covers background theories related to laser interactions with materials, current proposed ultrafast laser ablation mechanisms, relevant background and experimental work common to multiple experiments, as well as experimental setups and analysis techniques. Background and experimental details specific to particular experiments will be presented as self-contained information in the individual chapters to follow.

2.1 Ultrashort-pulse laser interactions with materials

The term "ultrashort laser pulses" is generally accepted as laser pulses with durations on the order of a few picoseconds or less, shorter than typical electron-phonon interaction time of materials. Consequently, the laser energy absorbed by the electrons is almost entirely confined and instead of dissipated as heat into the material, resulting in minimized collateral heating and related damage (e.g., [2–5]). To further illustrate

5

the dynamics of ultrafast laser ablation, the following subsections describe the interaction of the laser energy with the materials, and the subsequent events taking place in the material.

2.1.1   Absorption mechanisms of laser energy

The absorption mechanisms in materials can be categorized by the electronic structures of the materials. In metals, laser energy is absorbed by free electrons via the inverse Bremsstrahlung process, also known as free-free absorption. In semiconductors, laser energy is absorbed via the excitation of electrons from the valence band into the conduction band. In transparent materials, such as wide-bandgap semiconductors and dielectric materials, initial excitation of electrons requires multiphoton ionization, or may be assisted by intermediate states due to defects or surface states. The excited electrons in the conduction band may absorb laser energy and subsequently cause excitation of other electrons into the conduction band through impact ionization. When a chain of impact ionization occurs, it is referred to as avalanche ionization, and the resulting electron density can be significant. As the electron density reaches a critical value, the material becomes metal-like in absorption [3].

2.1.2   Ultrashort-pulse ablation mechanisms

As mentioned previously in Chapter 1, theoretical modeling of ultrashort-pulse laser ablation is burdened with challenges, and the ablation mechanisms are still being unraveled in the literature. However, research groups are converging on several proposed ablation mechanisms, which will be presented in this section of the thesis. In this section, the "ablation threshold" will follow the common definition of a laser energy or

fluence where significant volume of material is removed. Below this threshold, where the deposited laser energy is relatively low, material removal is mostly achieved via subsequent thermal evaporation at the surface. Near and above the ablation threshold, some mechanisms can be unique to the employment of ultrafast laser pulses, as discussed below. The mechanisms presented here follow the categorization in the simulation works of [6–10]. These mechanisms are also postulated in experimental works such as [11] and [12], as examples, despite different classifications of the qualitatively identical mechanisms.

Near the ablation threshold, the ultrafast deposition of laser energy results in rapid confined constant volume heating without melting in this time frame, leading to development of two compressive waves being launched, respectively towards the surface and into the bulk. Upon incidence on the surface, the compressive wave is reflected back towards the bulk as a tensile wave. The amplitude of the reflected tensile wave is weaker than the original compressive wave, indicating that energy is lost to the creation of surface deformations and defects. The reflected tensile wave follows the compressive wave originally launched into the bulk, causing mechanical failure and leads to the ejection of the top layer of the material. The above mechanism is referred to as spallation [7, 8, 10, 13, 14]. The spallation process requires ultrafast laser energy deposition to create the initial stress confinement, and occurs in near-threshold laser fluence since at higher fluences softening of the material damps the propagation of the pressure wave.

As the laser fluence is increased, constant volume heating to a high temperature following ultrafast laser energy deposition pushes the material into a metastable liquid-vapour state, or a superheated liquid. Homogeneous nucleation occurs with

nucleation bubbles developing spontaneously. In conjunction with the expanding material, due to the initial thermal confinement, the nucleation bubbles expand very rapidly, and as they rupture they further propel the expanding liquid, causing ejection of the material [7–10, 12, 14, 15].

At even higher laser fluences, the material is pushed into a supercritical fluid state quickly. The high thermal and mechanical stress causes the material to break up before it cools to a superheated liquid. Thus, the fragmentation process and homogeneous nucleation process are mutually exclusive. Fragmentation occurs when the gradient of mechanical stress is locally enhanced by the expansion of the fluid, finally causing the formation of new surfaces, leading to the break-up of the material. From an energy standpoint, fragmentation occurs when the energy of newly formed surfaces is more favorable than the elastic energy existing in the material [6–10].

Lastly when the deposited laser energy exceeds the binding energy of the electronic bonds, the material can be atomized, forming an ejection of a plume consisting of atoms and very small clusters in a process referred to as (non-thermal) vaporization [6, 7].

In a typical situation, there is a distribution of laser intensity across the cross-section of the beam, as well as a variation of the deposition as a function of the sample depth. The ablation mechanism at play would be dominated by the local incident and deposited laser fluence. The above statement should be a reasonable extrapolation from the simulation work in [10], which shows a depth distribution of the main proposed mechanisms as a function of depth at different laser fluences.

One of the other material removal mechanisms at lower laser fluence is Coulomb explosion, although this is not considered a universal mechanism. In this scenario the

laser energy deposited is adequate to excite and remove electrons from the material, leaving behind a net positive charge at the near-surface region. The high density of positive ions repel strongly, and destabilize the crystal lattice with enough force to eject the material from the surface [16, 17].

Due to the high peak intensity and the confinement of the deposited energy with the ultrashort pulse durations, the material temperature following energy deposition can initially rise as high as $\sim 10^3$-10^4 K, leading to a confined pressure on the order of a few tens of GPa (e.g., [15]), and a fast ejection speed of $\sim 10^3$ m/s (e.g, [8]).

2.1.3   Time scale of ultrafast laser ablation events

The above ablation mechanisms occur following the initial incidence and energy absorption of the laser pulses. To put the time frame into perspective, when a material is irradiated with a laser beam, absorption of the energy via electronic excitation occurs in the tens to a hundred femtosecond time frame. Heating of the lattice through electron-lattice coupling occurs on the order of hundreds of femtoseconds to a few picoseconds. Highly non-equilibrium conditions associated with homogeneous nucleation and fragmentation occur on a time frame of a few tens of picoseconds or less. Conversely, when lower energy intensities are used, heterogeneous nucleation occurs on the hundreds of picoseconds time scale. Ejection of the material continues for a few nanoseconds. Cooling of the material through thermal conduction occurs in tens of nanoseconds, and finally the material solidifies within a hundred nanoseconds (see, e.g., [3, 15]). Figure 2.1 is an adaptation of an illustrated summary from [3] of the time scale of events following the incidence of a ~ 100 fs laser pulse.
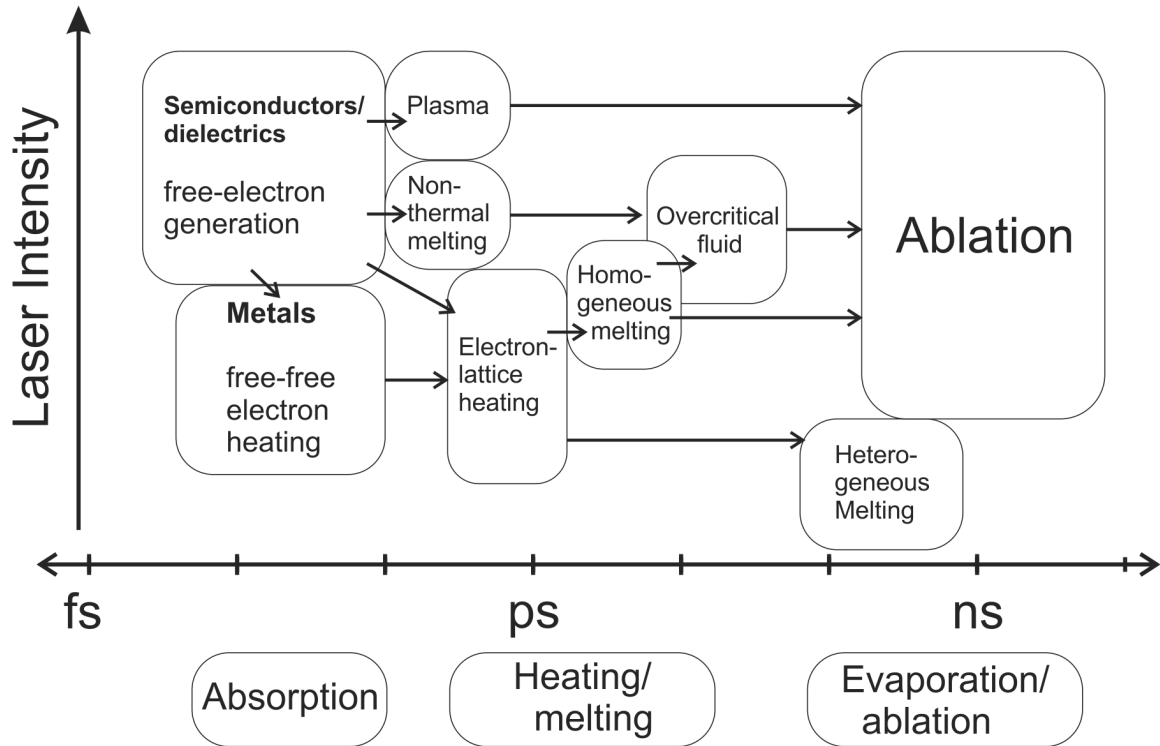
Figure 2.1: Illustrated time frame summary of absorption, heating, melting, thermal evaporation and ablation events for metals, semiconductors and dielectrics following the incidence of a ~100 fs laser pulse at various intensities. This figure is adapted from [3].
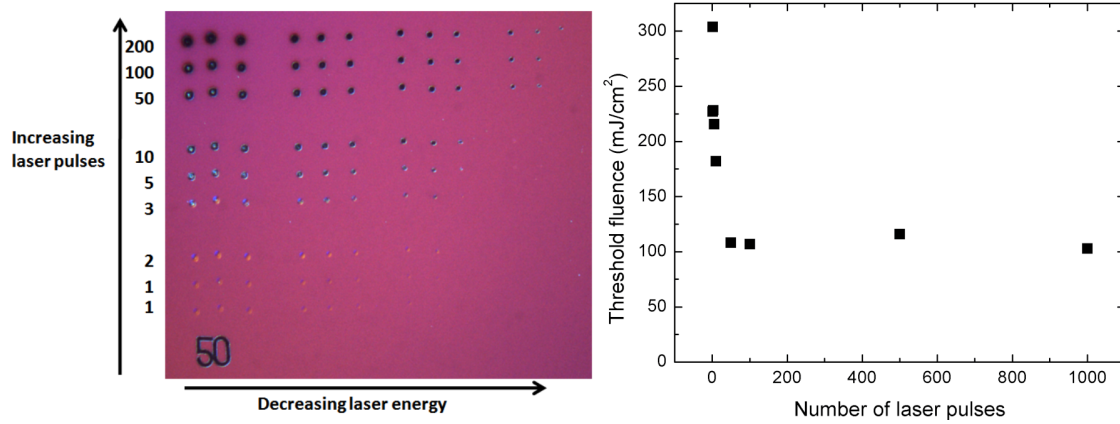
Figure 2.2: Examples of incubation behavior, observed as a reduction in the ablation threshold with increasing number of laser pulses. Left: areal optical microscope image of laser irradiated target sites, showing low pulse energies creating ablation craters with increasing number of laser pulses. Right: typical behavior of extracted threshold fluences as a function of the number of laser pulses.

2.1.4   Incubation behavior in laser ablation of materials

One phenomena observed in material ablation with laser pulses is the incubation behavior, describing a reduction in the per-pulse fluence required to create damage as the number of pulses used to irradiate the material increases. Figure 2.2 shows examples of the observations of incubation behavior.

The early studies of incubation behavior was prompted by the observation of metallic mirrors being damaged in prolonged usage, due to cumulative damage from being exposed to a high number of laser pulses. In such studies the source of the cumulative damage was attributed to an accumulation of plastic slip deformations resulting from material fatigue due to the repeated thermal cycling, which requires considerably less laser energy to create than for the material to ablate. As this type of deformation accumulates, an overall roughening of the material surface occurs, increasing surface absorption of laser energy and accelerating the damage accumulation

11

process [18]. Details of quantitative characterization of the incubation behavior used in this thesis will be presented in Section 2.3.3. The empirical equation relating the multiple-shot to single-shot threshold fluence in the original study is [18]:

$$\phi_{\text{th}}(N) = \phi_{\text{th}}(1) \times N^{\xi-1} \tag{2.1}$$

where N is the number of laser pulses, $\phi_{\text{th}}(1)$ and $\phi_{\text{th}}(N)$ are the single- and N pulse fluences, respectively, and ξ is the incubation coefficient. Equation 2.1 was first presented in nanosecond pulsed laser irradiation of metals in [18], based on empirical treatment. The equation has an analogous form to the equation modeling damage caused by mechanical-fatigue accumulation. In fact, it was shown that the laser incubation coefficient from Equation 2.1 can be used to derive several coefficients describing the mechanical properties of the material, such as cyclic strain-hardening, fatigue-strength, and fatigue-ductility exponents. This model and a modified form of the model was later adopted to ultrashort-pulse laser irradiation of different material systems with good agreement (e.g., [19–32]). However, due to the differences in the electronic structures in metals, semiconductors and insulators, the underlying mechanism for the observed incubation behavior may be different. There are several other proposed sources of the damage accumulation mechanisms in the above references, including the generation of color centers in dielectrics, and crystallographic or potential chemical changes as a form of energy storage in semiconductors. A modified form of the incubation equation has been presented with an exponential form and takes into consideration that the threshold fluence required to cause damage in materials may not approach zero as the pulse number approaches infinity, as opposed to the original model presented in Equation 2.1, but used an asymptotic baseline instead

(e.g., [1, 22, 33, 34]):

$$\phi_{\text{th}}(N) = \phi_{\text{th}}(\infty) + [\phi_{\text{th}}(1) - \phi_{\text{th}}(\infty)] \times e^{[-k(N-1)]} \qquad (2.2)$$

where $\phi_{\text{th}}(\infty)$ is the threshold fluence required for infinite number of laser pulses, and k is the incubation coefficient for this model.

2.1.5   Generation of coherent structures in materials in ultrafast laser irradiation

A phenomenon that results from laser irradiation of materials is the generation of coherent structures, observed since the early days of laser-material interactions [35]. These ripples have a spatial periodicity on the order of the irradiating laser wavelength. The generation of these structures were attributed to the surface scattering of the laser energy with the incoming laser beam itself, creating a lateral spatial modulation in the deposited energy into the material, thus resulting in periodic structures (e.g., [36–42]). The experimental framework and theoretical model by the effort of Sipe *et. al.* ([38–42]) are well accepted in describing the ripple formation as a general description and has been referred to as Sipe-theory.

However, new types of periodic structures have been observed occur with the use of ultrashort laser pulses. These types of ripples primarily form on materials where the bandgap is above the irradiation photon energy. Such structures include surface ripples with periodicities that are substantially below the irradiation laser wavelength (e.g., [24, 43–66]). Several proposed formation mechanisms are proposed in the above references, and are still under debate in the literature. Detailed discussions will not be

included in this thesis. Periodic modifications of materials have also been observed in the bulk when the ultrafast laser beam is focused into the material below the surface (e.g., [67–71]).

Another type of surface structuring is the formation of quasi-periodic conical structures, which can be generated with pulsed laser irradiation of silicon [5, 72–103]. Note similar structures were generated on germanium, which is crystallographically similar to silicon [80, 81].

While the physics of the formation mechanisms of the coherent structures resulting from ultrafast laser processing is not yet fully understood, there are application implications of these structures as well. For example, when using ultrafast laser systems to process microfluidic channels or micro-/nano-electromechanical system structures, having periodic surface corrugation can create undesired effects. On another hand, the generation of these structures may be exploited to modify material properties, such as modified thermal transport, or optical absorption at the material surface. (See, e.g., [75, 78, 82, 86, 87, 90–93, 96–102].) Whatever the desired outcome is, characterizing the formation conditions and understanding the generation mechanisms will aid the realization of applications.

2.2   Experimental setup

This section will describe the experimental setup of typical ultrafast laser ablation and micromachining experiments presented in this thesis, including the ultrafast laser system, micromachining setup and diagnostic techniques. Experimental details specific to particular experiments will be presented in the relevant chapters.

2.2.1   Ultrashort-pulse laser systems

The ultrashort laser system used was a commercial (Spectra Physics) titanium:sapphire based chirped-pulse-amplifier system. In this system, a Millennia V diode-pumped neodymium yttrium vanadate (Nd:YVO$_4$) laser, frequency doubled from a wavelength of 1064 nm to 532 nm pumps a Ti:sapphire oscillator (Tsunami), which in turn produces approximately 9 nJ ultrashort laser pulses at a repetition rate of 82 MHz, with a ~90 fs pulse duration, and a wavelength centered near 800 nm with a FWHM bandwidth of about 13 nm. The laser pulses output from the Tsunami have low pulse energies, and for ablation and micromachining applications, amplification of these pulses is required. Due to the short pulse durations, even a pulse with a relatively weak energy can have a considerably high intensity. Amplification of such pulses directly can lead to damage to the optical elements in the amplifier, as well as undesired nonlinear effects in the amplification cavity. To work around such issues, a chirped-pulse-amplification scheme was introduced where a pulse is first stretched in time prior to amplification to reduce the instantaneous intensity at any given time, and subsequently re-compressed following amplification. The pulse stretching scheme introduces a temporal change of wavelength components in the pulse, referred to as "chirp". The stretcher-amplifier-compressor combination is housed in a Spectra Physics commercial unit (Spitfire LCX), which is pumped by an Evolution diode-pumped neodymium yttrium lithium fluoride (Nd:YLF) laser that is frequency doubled to 531 nm, at a repetition rate of 1 kHz. The Spitfire typically outputs ~400 μJ laser pulses with a duration ~150 fs. Figure 2.3 summarizes functions of different elements of the laser system, while the following subsections describe the details and operations of each element.
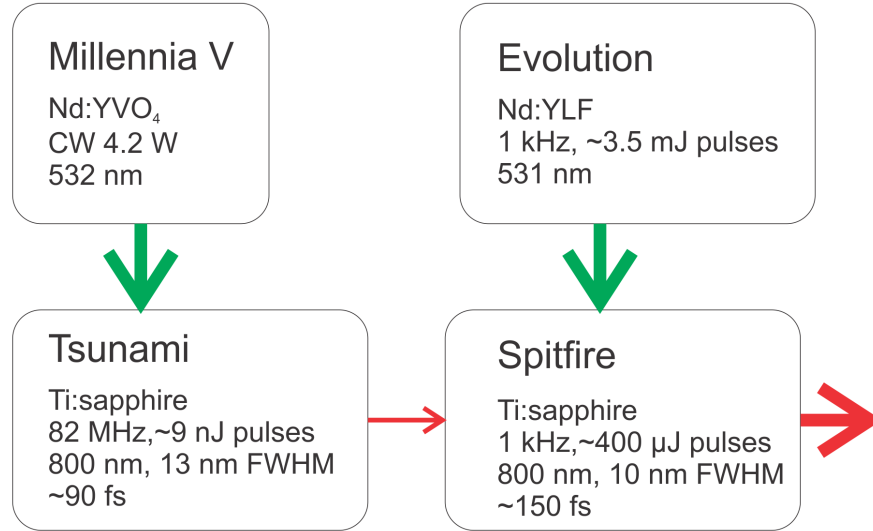
Figure 2.3: Spectra Physics commercial chirped-pulse amplifier system typically used in experiments described in this thesis.

2.2.2   Micromachining setup

Following transport of the beam to the experimental area via highly reflective mirrors, the beam is typically reflected off a 20% beam splitter, such that the energy is adequate for most experiments while the intensity of the beam propagating through subsequent optics is kept low to avoid nonlinear effects. Following the beam splitter, the laser energy is initially manually attenuated using a combination of a rotating half-wave plate and thin-film polarizers. When a linearly polarized beam enters a half-wave plate, its polarization is rotated about the optical axis of the birefringent crystal such that the output polarization is linear but rotated in the plane perpendicular to the direction of propagation. By varying the rotational orientation of the optical axis of the half-wave plate relative to the incidence electric field, one can vary the amplitude of the electric field component making it through the polarizer. While calcite-based polarizers provide a better distinction ratio than thin-film polarizers,

thin-film polarizers were employed to minimize the amount of dispersive material the ultrashort laser pulses travel through, and to avoid nonlinear effects that can take place due to the high intensity associated with the ultrashort pulse durations.

In the earlier experiments, further automated attenuation is achieved through neutral density filters housed in filter wheels secured to computerized rotators to obtain different combination of optical densities (O.D.'s). With this setup, one could employ optical densities of 0.0 - 2.9 in incremental steps of 0.1. Optical densities of a given material are describes as:

$$P_{out} = P_{in} \times 10^{-O.D.} \tag{2.3}$$

where P_{in} and P_{out} refer to the optical power before and after the material (i.e. neutral density filter), respectively.

An inherent shortcoming of using the neutral density filters is the reflective nature of the metallic filter coatings, where higher-order reflection may be an issue. For example, if a secondary reflection of 1% trails the main pulse as a result of propagating through a neutral density filter, at high energy experiments the secondary satellite pulse may have adequate energy to cause undesirable material changes. To eliminate the generation of satellite pulses from these filters, the filters were retired from the experiment setup, and were replaced with a second series of half-wave plate and polarizer combinations. Including the previously described initial manual attenuation, the entire attenuation line now includes a thin-film polarizer that is used first as an initial polarization filter to suppress polarization components orthogonal to the main pulse that may be accentuated due to the polarization rotation through the half-wave plate. A manual half-wave plate and a thin-film polarizer are then used to

provide the first stage of manual attenuation, followed by a half-wave plate mounted in a motorized rotation mount and a thin-film polarizer for automated attenuation control. Finally an anti-reflection coated Glan-laser calcite polarizer is used as the final stage of polarization filter with a high distinction ratio. When a very low laser energy is desired from a half-wave plate and thin-film polarizer combination, we will be approaching a null of the polarizer. For a polarizer with a low discrimination ratio, such as the thin-film polarizer with a ratio of 95:1, the resulting beam can have relatively impure polarization. A calcite-polarizer, having a maximum discrimination ratio of 10^5:1, provides an output beam with a significantly improved polarization purity. At such low energies nonlinear effects in the calcite polarizer are not expected to be significant.

Following the attenuation setup, the laser beam is then delivered to a stainless steel micromachining chamber. Stainless steel is used to provide adequate attenuation to x-rays that may be generated when the laser irradiation is performed on high-Z targets, or when the laser intensity is high [104]. A hand held radiation detector is used regularly to check for x-ray in the vicinity around the sample chamber during the micromachining process. The micromachining chamber has adequate sealing to maintain a rough vacuum on the order of tens of mTorr ($\sim$0.05 mbar or so) when continuously pumped with a roughing pump. Ablating materials in vacuum has two benefits. First, the substantial reduction of the number of air molecules in the chamber increases the mean free path of the ablated materials, allowing the debris to be ejected farther from the sample surface and minimize re-deposition of the debris. Second, by evacuating the chamber any possibly hazardous or harmful debris can be evacuated. The debris that is not pumped away from the chamber will coat the

chamber, which can be subsequently cleaned in a fume hood, thus minimizing airborne concerns from the ablation debris. For relatively large-volume ablation, a series of bleed-purge cycles with decreasing bleeding speed are carried out to further evacuate loose debris. In such cases a fine particle-mask is worn upon opening of the chamber. A foreline trap is used between the vacuum pump and the micromachining chamber, while the exhaust side of the vacuum pump is connected to the fume hood system of the building with an oil mist filter in place. The chamber pressure is monitored using a Pirani vacuum gauge. Unless otherwise stated, experiments presented in this thesis are performed in a rough vacuum of ~35-50 mTorr (0.05-0.07 mbar). In some experiments it may be desirable to use an ambient gas, either flowing or still, other than the atmosphere or a rough vacuum, and the micromachining chamber is also tapped to allow gas line feedthroughs to be employed in such experiments. This can be useful if a reactive ambient or an inert atmosphere is desired. The micromachining chamber is mounted on two computerized translation stages to allow controlled movements in the x- and y- directions. The laser beam is brought to a focus with either a microscope objective or a lens, through a window on the micromachining chamber lid into a target placed inside the chamber. The thickness of the window was chosen as the minimum thickness required to prevent deformation under vacuum such that nonlinear effects is minimized through the window. The window is also placed within the first half of the working distance of the focusing element to keep a low intensity of the converging beam through the window. The focusing element is mounted on a manual and a computerized translation stages to allow controlled movement in the z-direction.
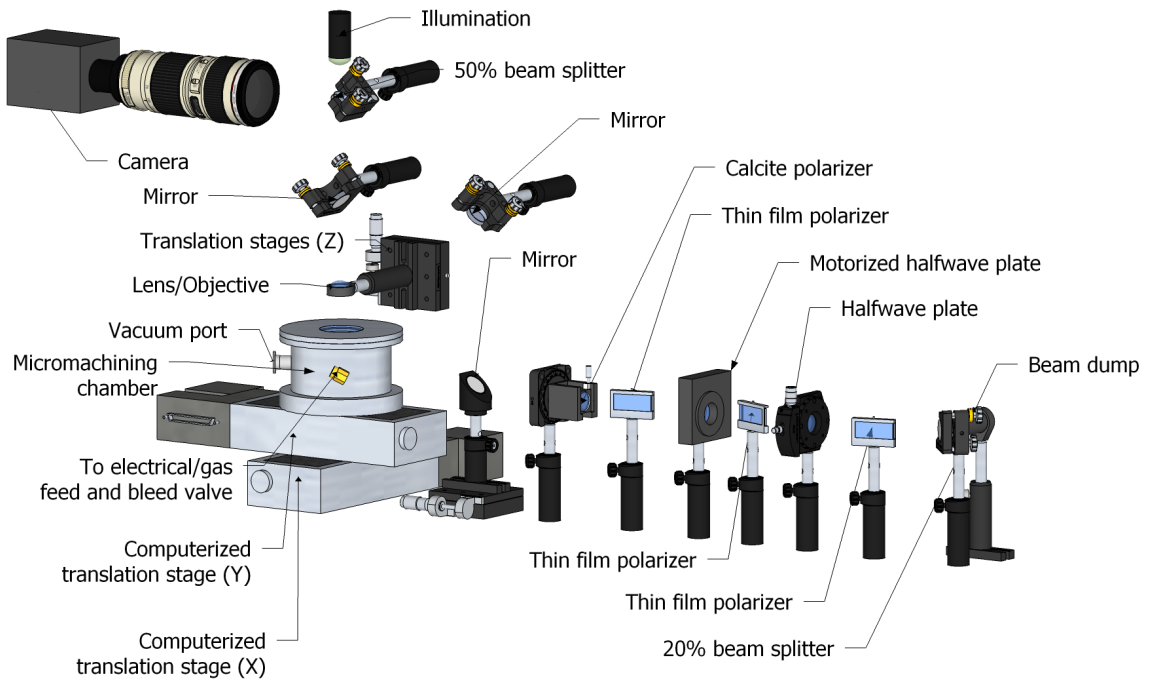
Figure 2.4: Primary elements of the micromachining setup. Shown here are a beam splitter for initial attenuation (far right), a beam dump to capture the unused beam from the splitter, a series of polarizers and half-wave plates for manual and automated attenuation, micromachining chamber with vacuum port, electrical and gas line feedthrough, computerized translation stages, and the viewing system.

2.2.3   Samples employed in experiments

Unless otherwise stated, the samples used in this thesis were boron-doped p-type CZ silicon, with typical wafer thickness of 505-545 μm and resistivity of 15-31 Ω·cm, courtesy of Professor Andrew Knights and commercially available through MEMC Electronics Materials SDN.

2.2.4   Diagnostics of ultrashort laser pulses

In laser-material interaction experiments, diagnosis of the laser pulses is required to understand how the laser pulses are interacting with the materials. This is particularly important when quantitative experiments are being performed. Laser pulse parameters to characterize include the spectral, spatial and temporal intensity distribution, spatial and temporal frequency variation (also known as chirp), as well as pulse-front tilt. Due to the short pulse durations, there are inherent challenges associated with the measurements of some of the above mentioned parameters.

Spectrum

The spectrum of the laser system can be measured simply using a spectrometer. In a typical commercial spectrometer, a diffractive element is used to spatially separate the spectral components of the incoming beam. An imaging array (e.g. charge-coupled device (CCD) sensors) can then be used to image the spatial distribution of the spectrum to obtain the intensity at each spectral component. This technique requires the spatial positioning and the spectral sensitivity of the imaging element to be well calibrated. In the experimental work presented in this thesis the laser intensity spectra were obtained using Ocean Optics spectrometers (typically a PC2000 model,

and an USB2000 model was sometimes used to obtain the spectrum of frequency-doubled 400 nm light).

Spatial intensity distribution

The spatial intensity distribution of the beam can simply be imaged using a 2D imaging device, such as a CCD imaging element. Such a device is also a powerful tool for fine beam alignments as well. In the experimental work presented in this thesis the laser spectra were obtained using an Ophir Optronics BeamStar CCD camera.

Pulse width

Measuring the pulse width of ultrashort laser pulses poses several challenges, since the pulse durations can be much shorter than the response time of any electronic photodetectors. In typical micromachining experiments presented in this thesis, pulse durations are determined using a second-order non-collinear autocorrelator. In such an autocorrelator, a pulse is split into two parts using a beam splitter. The two "copies" of the pulses propagate through separate optical paths, one of which is able to translate to generate a relative delay of one pulse relative to the other with the use of a translation stage. The two beams are then routed back to propagate through the beam splitter in parallel into a focusing lens. At the focus of the lens, the two pulses cross one another inside a frequency-doubling crystal (500 μm thick potassium dihydrogen phosphate (KDP) crystal), such that a second harmonic (frequency-doubled) pulse is generated and propagates along the forward direction bisecting the two intersecting beams (Figure 2.5). The intensity of the frequency-doubled pulse corresponds to the temporal overlap of the two fundamental pulses, and is detected using a photodiode.

The relative delay of the two pulses are changed such that they "slide past" each other in time, and the pulse width of the fundamental pulses can be extracted from the resulting second harmonic intensity as a function of the relative delay. Residual fundamental beams and the respective frequency-doubled components are blocked out so that photodiode detection only monitors the frequency doubled component traveling in the bisecting axis.

The main drawback with the autocorrelation technique is the ambiguity of the resulting autocorrelation trace, in that the trace is always symmetric in time due to the nature of autocorrelation. Also there are virtually infinite possibilities for the temporal intensity envelope that the laser pulse can have that may lead to the same autocorrelation trace; an assumption of the temporal pulse shape has to be made to extract the pulse intensity envelope from the autocorrelation trace [105]. Often a hyperbolic-secant-squared or a Gaussian temporal profile can be reasonably assumed.

Other techniques that are occasionally employed to measure the pulse duration include GRENOUILLE and tilted-front-pulse autocorrelation, as discussed below.

Pulse-front tilt

Due to dispersion effects, it is possible for a pulse front to not be perpendicular to the direction of propagation. This is referred to as a tilted pulse front. A pulse-front tilt can result in an altered effective pulse duration when focused, which can create errors in characterizations. In the Photonics Research Laboratory, two instruments are available to characterize pulse-front tilt, namely the tilted-front-pulse autocorrelator [106], and GRENOUILLE (GRatings Eliminated No-nonsense Observation of Ultrafast Incident Laser Light Electric-field) [105, 107].
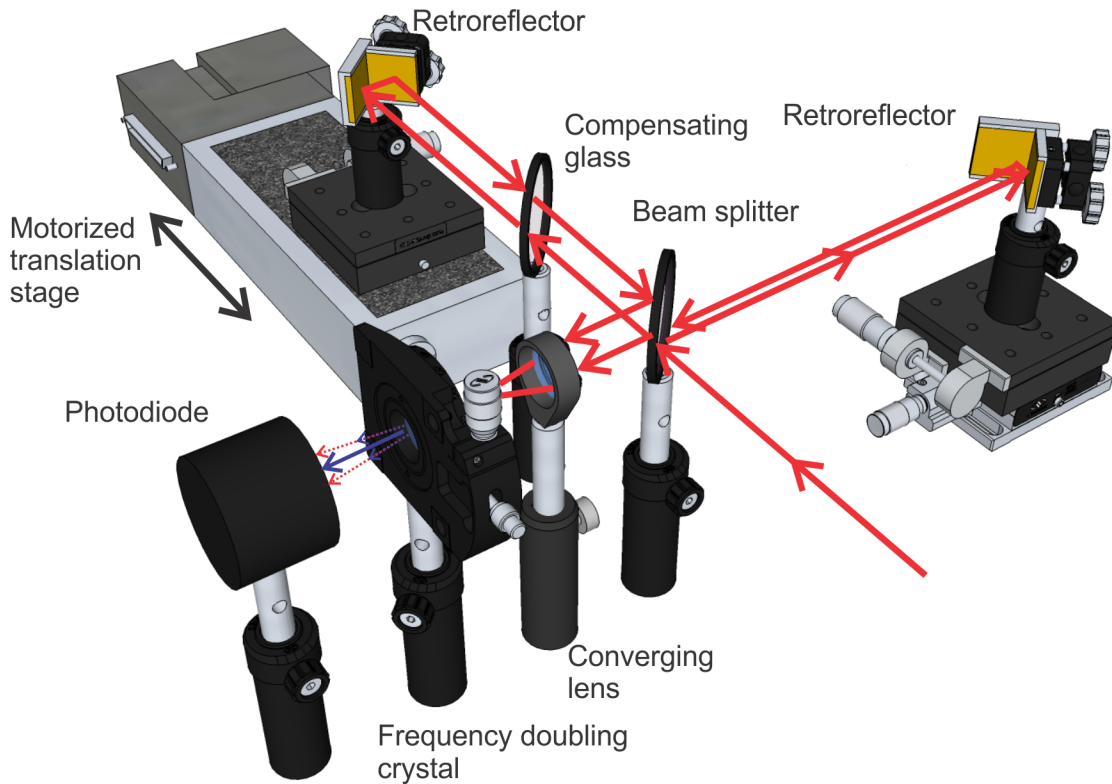
Figure 2.5: Schematic representation of the second order non-collinear autocorrelator setup. The input beam (bottom right corner) enters the setup and is split into two paths. The two beams are retroreflected to propagate in parallel through a converging lens. The lens focuses the two beams into a frequency doubling crystal, where a frequency doubled component propagating along the bisecting axis of the two beams impinges on a photodiode for detection.

SHG crystal
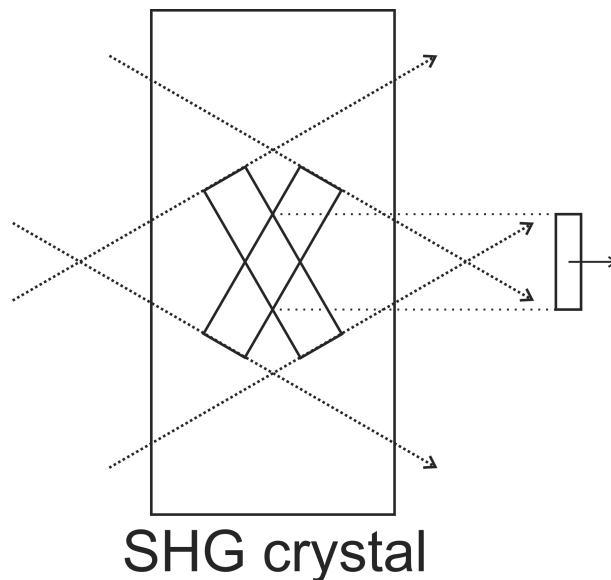
Figure 2.6: Geometry of single-shot autocorrelation, showing two intersecting beams or beamlets in a second harmonic crystal generating a frequency-doubled output propagating along the bisection line with its width corresponding to the pulse duration (i.e., "thickness" of the beamlets). In the case of GRENOUILLE, the beamlets are generated from propagating the incoming beam through a Fresnel bi-prism.

GRENOUILLE

GRENOUILLE is a commercially available unit through Swamp Optics that is able to extract pulse information such as pulse width, temporal and spatial chirp as well as pulse-front tilt [105, 107]. A GRENOUILLE uses optical geometries that generate a spectrogram (a plot of wavelengths versus time) by cleverly using the horizontal geometries as a single-shot autocorrelation while using the vertical geometries to act as a second-harmonic spectrometer.

The horizontal optical geometry uses a Fresnel bi-prism to split a pulse front to two beamlets that intersect in a second-harmonic crystal. A second-harmonic beam is generated in the forward direction, and the width of the generated second harmonic corresponds to the pulse duration, as depicted in Figure 2.6.

In the vertical optical geometry, the beam is focused into a line-focus through a cylindrical lens into the second harmonic crystal. The crystal thickness is chosen to have a very small bandwidth such that phase matching conditions at different beam propagation angles (due to focusing of the beam into the crystal) is optimized for different wavelengths. The resulting spatial distribution of the second harmonic intensity will then correspond to the spectral contents of the original pulse.

Combining the two dimensions of the geometries, a spectrogram can be constructed directly using a 2-dimensional CCD imaging element. Since in a spectrogram frequency information as a function of time is available, temporal chirp can be extracted. The symmetry of the optical geometries results in symmetrical traces, so the sign of the temporal chirp is not extracted directly. However one could insert an optical element with a known dispersion sign (e.g., a thin glass plate) and observe whether the temporal chirp is enhanced or compensated, thus extracting the sign of the original temporal chirp. Pulse-front tilt is detected as a horizontal spatial offset of the resulting trace, since a tilted-pulse front propagating through the Fresnel bi-prism will result in an off-axis "crossing" of the two beamlets in the second harmonic crystal. A spatial-chirp will result in a tilt in the GRENOUILLE trace, resulting from the spatial distribution of the frequency components.

Tilted-front-pulse autocorrelator

A pulse-front tilt refers to a laser pulse with wavefronts that are not perpendicular to the direction of propagation of the pulse. This can result from the beam propagating through a dispersive element at an off-normal incidence.

To extend the discussion on single-shot autocorrelators from section 2.2.4, one of

the shortcoming of a single-shot autocorrelator configuration is the symmetry of the resulting trace. An example of information lost due to this symmetry is the pulse-front tilt. A technique that is able to extract spatial information from a single-shot autocorrelator is to rotate the orientation of one of the two beamlets geometrically through optics such that it is rotated by 90° with respect to the other. With this asymmetric geometry, the autocorrelation scan will provide pulse-front tilt information as a visible tilt in the resulting trace [106].

2.3   Sample analysis and parameters extraction

This section describes analysis techniques used to characterize the samples and features following ultrafast laser irradiation, as well as quantitative treatments to extract relevant parameters for characterization.

2.3.1   Sample analysis techniques

Various microscopy techniques have been employed to characterize the laser irradiated area. These techniques include scanning and transmission electron microscopy (SEM and TEM, respectively), atomic force microscopy (AFM), as well as optical microscopy (OM) with differential interference contrast technique (DIC). On specific samples where cross-sections are required the sample can be cleaved to reveal a rough cross section or focused ion beam (FIB) preparation of cross-section specimens can be carried out. Focused-ion beam milling is a technique that uses an energetic ion beam to mill away material to expose the desired cross-section region. For TEM specimen preparation the milling is carried out on both sides of the desired region

such that a thin "slice" remains. This thin slice can be extracted with the ion beam in conjunction with a manipulator, and further thinning for a thickness suitable for TEM analysis is then carried out once the slice is attached to a TEM grid (for further details see, e.g., [108]).

While optical microscopy does not provide resolution below the order of the illumination (i.e., visible) wavelengths to resolve finer features resulting from laser irradiation of materials, it is very useful in providing a topical survey of features on the near- and above-micrometer scale, such as ablation craters. The DIC-OM technique provides good sensitivity to surface relief due to its short depth of focus. On the contrary, the long depth of focus of an SEM provides more information from features with considerable depth modulation. Careful depth profiling of subtle features can be obtained with an AFM on selected sites, since it has a low throughput. FIB milling of samples allowed preparation of cross-sectional specimen for TEM studies on selected sites where surface relief, morphology, material crystallography, and composition can be examined in detail.

2.3.2   Extraction of incident laser spot size and threshold fluences

Due to the high intensity at the focal volume of the laser pulses, it may be challenging to apply a conventional knife-edge measurement technique to measure the spot size at the laser focus. Alternatively, the focused laser spot size during ultrafast last irradiation of material surface can be extracted using the "D^2 technique" presented below, along with the threshold energy required at the given spot size (thus the threshold

fluence). Within a given irradiation site, multiple features may be observed (e.g., regions with strong material removal, melting, or subtle amorphization), each having a different threshold fluence. With a typical Gaussian spatial intensity distribution of a laser pulse, the different features can be observed with different diameters. Threshold fluences for specific features can thus be extracted (e.g., [109, 110]). The relationship between the incident laser spot size, laser fluence of the incident pulse, and the threshold laser fluence is described by Equation 2.4 [109]:

$$D^2 = 2\omega_o^2 \ln\left(\frac{\phi_o}{\phi_{\text{th}}}\right) \tag{2.4}$$

where D is the measured diameter of a given feature in the crater, ω_o is the $1/\text{e}^2$ radius of the incident spot size, ϕ_o and ϕ_{th} are the peak incident and threshold fluences, respectively. For elliptical craters, the geometric average of the measured major and minor diameters are taken. Note the peak fluence of a pulse is related to the pulse energy as:

$$\phi_o = \frac{2E_o}{\pi\omega_o^2} \tag{2.5}$$

where E_o is the pulse energy. As an initial step, equation 2.4 can be reduced to the form:

$$D^2 = 2\omega_o^2 \ln\left(\frac{E_0}{E_{\text{th}}}\right) \tag{2.6}$$

where E_{th} is the threshold energy.

By plotting the diameter-squared of a given feature in a crater against the natural logarithm of the laser energy employed, the laser spot size incident on the surface can be extracted from the slope of the plot, while the intercept will give the threshold pulse energy required to generated the observed feature. The extracted spot size can

then be applied to the threshold energy extracted to calculate the peak threshold fluence required to generated a certain feature.

Comments on result uncertainties

A challenge in the extraction of the irradiation spot size and the threshold fluence is the associated uncertainties. The uncertainties should provide not only ones related to the measurement equipment, such as the calibration of the power meter and the length scale of various microscopy instruments, but also incorporate ones arising from human input, such as the measurements of crater sizes. In the past, an error of $\pm 30\%$ had been associated with fluence measurements performed on irradiation with tightly focused laser beam using the $5\times$ microscope objective [111]. A more conservative uncertainty margin of approximately $\pm 15\%$ is associated with the error associated with the larger focal spot sizes obtained with the 125 mm focal-length lens used in the majority of the work presented in this thesis. This figure is based on a 5% uncertainty in the energy measurement, and the typical uncertainty in the spot size extraction.

Often in this thesis the single-shot results were obtained from the same experimental session, using the same measurement equipment, as well as consistent measurement techniques on well defined structures. As such, another relevant figure merit arise from statistical variations obtained from a test experiment, where repeated single-shot irradiation on numerous silicon samples cleaved from the same wafer yielded a standard deviation of $\pm 1.5\%$ in the single-shot threshold fluence.

2.3.3   Extraction of incubation coefficient

The D^2 technique can also be applied to multiple-pulse irradiation, however, this should be performed with care. This simple model does not take into account the potential difference in the amount of damage accumulation for different irradiation conditions (i.e., when the pulse energy changes for multiple-pulse irradiation). It also assumes a precise correlation of the locality between the incident laser energy and the observed feature, and does not take into account lateral energy or material transport that may be more significant with higher numbers of shots. (Detailed introduction to the damage accumulation effect is given in Section 2.1.4.) Presumably spatial jitter of the beam can affect some of the assumptions of the incubation model for multiple pulse irradiation. In the work presented in this thesis, the single-shot spot sizes extracted from each respective set of experiments were used in conjunction with the extracted threshold energies for multiple-pulse irradiations fluence calculations. Incubation equations presented in Section 2.1.4 can then be applied to the extracted thresholds for each number of laser pulses for a quantitative incubation characterization. The classical power-law model presented in Section 2.1.4 (Equation 2.1) was chosen as the model to quantify our results since it provided closer fits than the alternative model for dielectric materials in the literature (Equation 2.2).

Typically for most materials the incubation coefficients ξ for the classical power-law model fall into the range of $\sim$0.7-0.9 (e.g., [19–32]). To provide an example for the magnitude of the threshold difference, using $N = 1000$, the range of ξ corresponds to a threshold reduced to 12.5-50% relative to the single-shot threshold.

2.3.4   Effective number of shots for a translating laser beam

When the laser beam is translated across the sample surface, the effective number of shots a given spot is exposed to can be estimated based on a Gaussian intensity distribution of the laser pulse and the accumulated local energy as the beam is scanned over this location [112]. This accumulated energy is dependent on the translation speed of the laser beam, incident laser spot size, and the repetition rate of the laser, which are related through the equation:

$$N_{\text{eff}} = \sqrt{\frac{\pi}{2}} \frac{\omega_{\circ} f}{v} \tag{2.7}$$

where N_{eff} is the effective number of laser pulses (seen by a given position), f is the laser repetition rate in Hz, and v is the translation speed of laser beam. For two-dimensional scanning of the sample surface, a model presented in [113] was used, where the accumulated peak fluence for a given position was simulated based on an overlap factor, which in turn was derived using the spot size, repetition rate, and scanning velocity, using a similar approach as the derivation of Equation 2.7.

Chapter 3

Threshold and incubation behavior in silicon under ultrafast laser ablation

To briefly reintroduce the incubation effect, as mentioned in Section 2.1.4, incubation behavior in the context of laser-material interactions refers to the cumulative damage behavior from sub-single shot ablation threshold pulses where damage still occurs when multiple shots are employed. While a commonly accepted empirical model based on long-pulse laser irradiation on metal targets exists and provides reasonable fits to data obtained with a host of pulsed lasers and material systems, the proposed underlying mechanisms are generally speculative.

This chapter of the thesis reports a series of experiments designed to study the origin of the incubation effect in silicon. The experiments carried out include positron annihilation spectroscopy, characterization of the incubation behavior as a function of the laser repetition rate, as well as sample temperature during laser irradiation.

While the experiments introduced above are quite different, the common underlying effect to be studied is the role of defects in the contribution of observed incubation behaviors. Positron annihilation spectroscopy is sensitive to divacancy density down to $1:10^7$ [114]. Divacancies are stable defects in silicon at room temperature, thus it is feasible to study the divacancies using the positron annihilation technique following the laser irradiation experiment (typically on the order of weeks after the laser irradiation). Monovacancies in silicon, on the other hand, are unstable at room temperature and can have a lifetime in the range of millseconds to seconds [115]. If monovacancies are a significant contributing factor to the observed incubation behavior, by altering the incident laser repetition rate we should be able to observe a change in the incubation effect as the pulse-to-pulse delay is changed. Lastly, since annealing is a typical procedure to recover crystallinity in materials that are damaged, due to either stable or short-lived defects, defect clusters, extended defects or dislocations, elevating the sample temperature can facilitate crystallographic recovery during laser irradiation.

Further background related to crystallographic defects, recovery (annealing), and other considerations relevant to the experiments presented in this chapter are covered in the following section. Subsequent sections to follow present specific experimental details, discussions and conclusions for the respective experiments.

3.1   Defects, annealing, and oxidation considerations in silicon

Defects in silicon play an important role in device processing technologies (see, e.g., [116]). Several topics relevant to the context of ultrafast laser incubation will be

discussed in this section.

For simplicity, a Gedanken model of a perfect crystal lattice may be thought of as a three-dimensional grid of atoms. In reality, defects exist in such a crystal lattice. The simplest types of defects that can exist in the crystal lattice are point defects consisting of vacancies (atoms or ions missing from an expected lattice sites) and interstitials (atoms or ions being "lodged" at a non-expected lattice site) [116]. The vacancies can join to form stable defect complexes. For example, even though monovacancies are considered unstable in silicon at room temperature, a fraction of monovacancies may form divacancies which are stable at room temperature, resulting in lasting crystal disordering.

Ion implantation is a common technique used to introduce dopants into crystalline materials in device processing. An inherent side effect of ion implantation is disordering of the crystal lattice. This is caused mainly by the collision of the energetic implanted ions with the target atoms, displacing the target atoms from their original sites, and possibly causing secondary collisions. The result is defects being generated in the material. The generated vacancies and the interstitials can recombine during the implantation process due to the increased sample temperature from the incident ions, thus reducing the long term disordering. However, as mentioned above, a fraction of the vacancies can survive and form stable complexes at room temperature. At high implantation doses, it is possible for the material to be completely amorphized during the implantation process.

Thermal annealing is often carried out to recover crystallinity damage in the material (e.g., disordering caused by the ion implantation process). At adequate temperatures, specific types of defects may become mobile and dissociate, allowing

recovery of the crystallinity. In silicon, monovacancies are considered unstable at room temperature as they anneal out between $\sim$-200 to -50°C, depending on the charge state. The divacancy is stable at room temperature and anneals out at 300°C [116, 117]. However, more recent studies have shown a possible two-stage anneal process for divacancy or divacancy complexes in silicon, with further annealing stages occurring over 600°C [118–120].

Annealing also induces recrystalization in damaged and amorphized regions where the underlying bulk acts as the seed required for crystal regrowth for the damaged region. As examples, for silicon $\langle 100 \rangle$ at 550°C the epitaxial growth rate is on the order of $\sim$100 Å/min, and at 600°C the growth rate is $\sim$500 Å/min [121, 122].

At elevated temperatures, however, oxidation of the sample surface may become an issue. Annealing processes are often carried out in a controlled and dry atmosphere. In a dry environment the oxide growth rate is much lower than in a humid environment, even in an oxygen-containing ambient. Thus, for thick oxide growth wet oxidation is often carried out, while a dry environment is employed to grow thin oxide layers, or when specific oxide properties from dry oxidation is required, and finally if oxidation is undesired [121, 123].

In the context of laser processing of materials, it is likely for the ion implanted materials to exhibit an altered ablation threshold relative to a virgin sample due to changes in the optical properties [124–126], or amorphization of the material [5, 110, 127]. Even if annealing is capable of recovering crystallinity in the material, the implanted species may be electronically active, resulting in an altered threshold. Therefore, characterization of laser-material interactions at different ion-implantation conditions and annealing may prove to be useful for the combined usage of ultrafast

laser ablation and conventional cleanroom processing. Another use of the annealing process in the context of ultrafast laser ablation may be to recover the crystallinity that may be damaged following laser ablation of the material, which can have implications in device applications as well as fundamental studies of defect generation in ultrafast laser ablation (i.e., incubation effect). If annealing is carried out *in-situ* in the laser micromachining chamber, consideration of oxidation will have to be taken into account in the designing of the setup, as discussed in Sections 2.2.2 and 3.2.1.

3.2   Incubation behavior in silicon at elevated sample temperatures

In semiconductor processing, annealing of the sample is often carried out to recover damaged crystallinity of the material. This is achieved by either providing enough energy for vacancies to be mobile and eventually dissociate, or through solid phase epitaxial regrowth. Studies of laser irradiation at elevated sample temperatures have been reported in the literature in investigations of surface morphology [128–130], ablation rates [129, 131], and damage accumulation mechanisms [132]. The incubation study in [132] focused on the single-to-30 shot 50%-probability damage threshold of silicon under 10-ns Nd:YAG pulsed laser irradiation at 1064 nm, and the authors did not see an effect of temperature on the damage accumulation behavior. Ultrashort pulsed lasers provide an attractive alternative to incubation studies since the damage behavior is deterministic in nature. Also, due to the ultrashort pulse durations the energy deposition is very well defined.

The original intention of this experiment was to carry out ultrafast laser irradiation in stages, with an intermediate anneal stage to study the suppression of the incubation effect introduced by annealing of the sample. However, it was technically challenging to perform two-stage stationary irradiation once the sample is removed from the laser irradiation chamber for annealing, as the current viewing system in the micromachining setup does not allow a high degree of accuracy in the repositioning process to ensure overlap of the target sites between each irradiation stage. Further details and findings from several attempted irradiation schemes are discussed in the introduction of Chapter 4 and Section 4.1. Instead, a heated stage was built to be inserted into the micromachining chamber, so that the samples do not have to be removed between laser irradiation stages for annealing. However, in an enclosed system at partial pressure (i.e., the micromachining chamber) the thermal cycling rate of the sample is limited, and instead of experiments with multiple alternating irradiation and annealing stages, experiments were conducted with the silicon samples irradiated at elevated temperatures.

This section presents the ablation threshold and incubation behavior of ultrafast ablation of silicon between room temperature up to 600°C.

3.2.1 Experimental details

The laser irradiation details are mostly similar to the configuration outlined in Section 2.2.2. Coordination and brainstorming during the development of the heating system received an appreciable amount of help from M.A.Sc. student Bing "Kevin" Liu from the Photonics Research Laboratory, as well as input of ideas and commercially

available options for heating elements from Jim Garrett from the Brockhouse Institute for Material Research and fellow Engineering Physics Ph.D. candidate Gabriel Devenyi, and electrical inspection of the finished setup performed by Peter Jonasson, Lab Coordinator of the Department of Engineering Physics.

Several iterations of a heated micromachining stage had been attempted. The first prototype was fabricated out of aluminum for low-temperature ($\leq 300°$C) experiments. As higher surface temperatures were eventually desired, copper was chosen as the material for the stage. The stages were custom fabricated to accommodate a $1/4''$ nickel-chromium wire based commercial cartridge heater along its radius. The heated portion of the stage is $\sim 1/2''$ in thickness, and $1''$ in diameter. The stage was insulated from a mounting base with a $1/2''$-thick firebrick, and the mounting base was secured to the bottom of the micromachining chamber through a ~ 5 mm ceramic slab. While both copper and silicon have relatively high melting temperatures ($1085°$C for copper, and $1414°$C for silicon), the eutectic point of the copper-silicon binary system is $802°$C. Solid diffusivity and silicidation are also known issues in copper-silicon interfaces [133]. For experiments using a copper stage a 25 μm thick tantalum foil was used as a barrier material between the copper stage and the silicon samples to work around diffusion and alloying issues that can arise from copper-silicon interfaces, especially at high temperatures.

Temperature control was achieved via the use of a commercial temperature controller with an internal relay. The output of the temperature controller was plugged into a line-voltage power analyzer to monitor the power delivered into the heating circuit. An inline variable transformer was used to adjust the power to the heater. For low temperature set points a lower power setting prevents the temperature from

overshooting. Temperature feedback for the controller was achieved with a K-type thermocouple secured ~5 mm above the stage surface onto a screw secured into a tapped hole on the stage, such that the thermocouple was not in contact with the top surface of the stage. The thermalcouple was routed downwards to provide a firm pressure on the sample surface. A second K-type thermocouple was inserted into a small hole in the side of the heating stage to monitor the temperature of the stage to prevent damage to components. A wire feedthrough was fabricated to route the wires into the micromachining vacuum chamber. The feedthrough was made out of a bored national pipe thread to Swagelok® adapter filled with two-part epoxy. Outer sheaths of multiply-insulated wires were removed before insertion into the feedthough, and single-strand wires were used for all connections to maintain a good vacuum. To prevent melting or possible outgassing of electrical tapes in a heated vacuum environment, electrical insulation of the wire joints were achieved instead by encapsulating the joints with ceramic beads, and subsequently enclosing them in fiberglass sleeves secured in place with strands of copper wires. All of the parts were pre-baked to at least 400°C prior to the experiments.

Laser irradiations were carried out with a protective argon ambient. The micromachining chamber would first be pumped down to about 0.07 mbar, and subsequently backfilled with argon gas flowing at a rate of ~9 cm^3/s, resulting in a chamber pressure of ~25 mbar, as estimated using the N$_2$ equivalent signal calibration data provided by the Pirani gauge manufacturer. The typical heating rate at this ambient condition is on the order of ~30°C/min. Once each sample surface reached the temperature set point, a 10 min wait was carried out for each sample before commencing the laser irradiation. Each set of laser irradiations took about 10 min. Following the laser
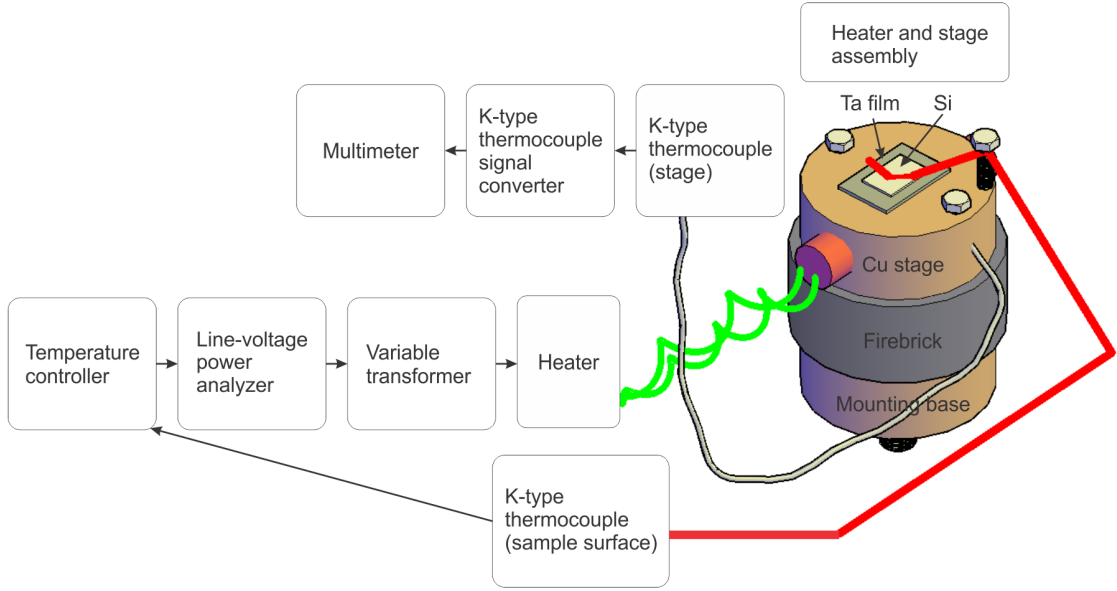
Figure 3.1: Schematic diagram of the overall sample heating system. The heater and stage assembly diagram was largely prepared by M.A.Sc. student Bing "Kevin" Liu from the Photonics Research Laboratory.

irradiation and shutting off the heater, the argon flow was increased to ∼55 cm^3/s to facilitate quicker cooling, resulting in a chamber pressure of ∼465 mbar. The typical temperature variation from the set point was ±2°C. The exterior of the laser micromachining chamber was cooled with active heat-sink cooling.

Laser irradiations were carried out with a 75 mm plano-convex lens. With this lens a spot size of 11.7 μm 1/e^2 radius was extracted using the D^2 technique ([109]). Each set of laser irradiations employed pulse energies ranging from 160 nJ to 1.4 μJ, and the number of laser pulses $N = 1, 1, 2, 3, 5, 10, 50, 100, 500,$ and 1000 were used. The single-shot ($N = 1$) irradiation was repeated to provide more data points for parameter extractions. The same sets of irradiation conditions were carried out at room temperature, and for 100-500°C at 100°C increments, and again for each sample after it had cooled down to near room temperature. This is to ensure that the

observed changes at elevated temperatures did not result from permanent changes from the initial state of the sample (e.g., due to unlikely pre-existing damage to the wafers that are recovered at high temperatures).

Analysis of the irradiated sites were carried out using optical microscopy with differential interference contrast (DIC-OM) technique in conjunction with the D^2 technique ([109]), as described in Section 2.3.2. For multiple shot irradiations, the extracted threshold energy for each number of shots was fitted with the extracted single-shot spot size from the respective set of data for fluence calculations (i.e., from the same set of irradiations). In general there is a tendency for the extracted spot size for multiple-shot irradiation to be larger, potentially due to lateral energy or material transport, non-uniform incubation effect across the beam profile, or spatial jitter of the beam. To provide an example, at room temperature the extracted spot size for N=1000 can be as much as 15% larger than that extracted from single-pulse irradiation. At elevated temperatures this effect is further exaggerated (up to an extracted N=1000 spot size that is 35% larger than the N=1 spot size at 500°C). This affects the quantitative outcome of the numerical analysis. Examples of this effect will be demonstrated in the following discussions. Measurements were made to identifiable features where significant material removal had occurred, indicating an ablation event (i.e., ablation crater rim for low numbers of shots, or a distinct boundary within which a significant crater depth is observed).

3.2.2   Results and discussions

The single-shot ablation threshold for silicon obtained from this experiment was determined to be 304 mJ/cm^2, comparable to values reported in the literature (e.g.,
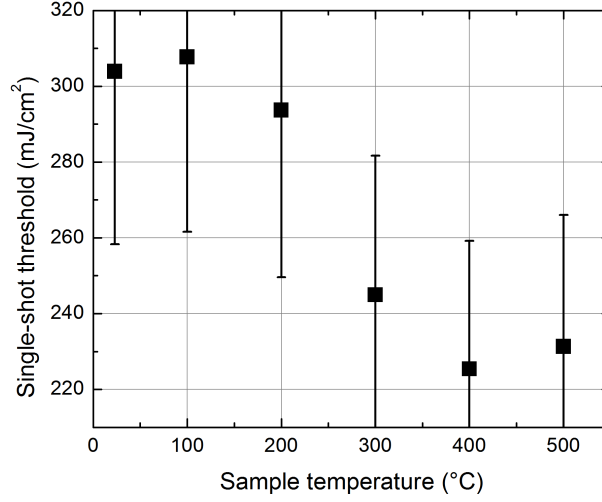
Figure 3.2: Single-shot thresholds as a function of sample surface temperature. For details of the error considerations refer to the discussions in Section 2.3.2.

[26, 110, 134, 135]). As the number of laser pulses N increased, the threshold decreased as expected, showing an incubation effect. The extracted incubation coefficient ξ for the power law model (for details see Section 2.1.4) was determined to be 0.84, in agreement with the reported value in the literature using ultrafast laser irradiation (ξ=0.84 in [136]).

As the temperature of the sample surface was increased, the single-shot threshold fluence demonstrated a tendency to decrease. However, within uncertainty the data points suggest a slight tendency to plateau below 100°C and above 400°C. Figure 3.2 shows the extracted single-shot threshold fluence as a function of temperature.

At higher temperatures and higher numbers of irradiation pulses (above a few tens of shots), extracted thresholds indicate that a higher fluence tends to be required to cause an ablation event. The suppression of single-shot thresholds and the increase of higher N multiple shot thresholds can be seen in the extracted threshold fluences as a function of numbers of shots for different temperatures (Figure 3.3). The same set of
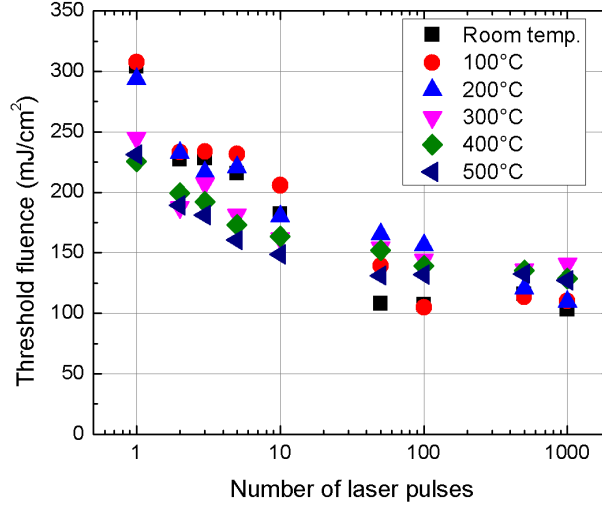
Figure 3.3: Single- and multiple-shot thresholds at different sample surface temperatures.

laser irradiations on each sample following cooling to near room temperature yielded the same threshold and incubation results as the benchmark room temperature sample without heating.

The combination of the general decreased single-shot thresholds and increased multiple-shot thresholds with increasing temperature together contributed to a reduction of the incubation effect. This is demonstrated in Figure 3.4, where each of the data sets presented in Figure 3.3 is normalized to its respective single-shot threshold fluence to facilitate comparison of the threshold suppression with increasing N at different temperatures.

The incubation coefficients were used as a quantifiable figure of merit for comparison of the temperature data, and are summarized in Figure 3.5. Note that since the incubation coefficient ξ appears in the power-law equation as 1-ξ in the numerator, and an incubation coefficient of 1 indicates a lack of incubation effect, while a smaller value will indicate stronger incubation. As shown in the figure, the incubation effect
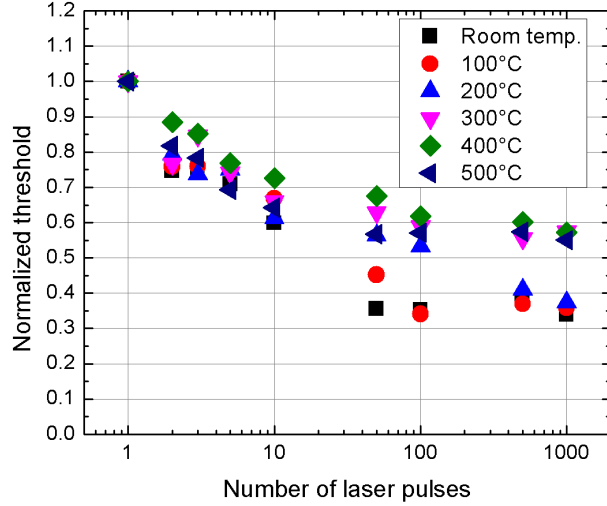
Figure 3.4: Normalized single- and multiple-shot thresholds at different sample surface temperatures, to better demonstrate the evolution and suppression of the incubation effect at different temperatures. Two general regimes can be identified; temperature below 100°C, and temperatures above 300°C, with the 200°C data set as the transition.

decreases for temperatures above 100°C, and plateaus at a nominal value of ∼0.93 for temperatures above 300°C. A previous experiment carried out on a copper stage with no barrier tantalum film showed the same qualitative behavior out to 600°C. The purpose of the tantalum film was discussed above in Section 3.2.1, and further in Appendix A.

The threshold behavior as a function of laser pulses in room temperature irradiation sample showed typical incubation behavior observed for silicon. The threshold fluences can be compared to ablation, melting or amorphization threshold fluences reported in the literature summarized in Table 3.1 (based on the summary presented in [110] and [137], and additional references).

Table 3.1: Single-shot ablation, melting and/or amorphization threshold fluences for silicon. All units in mJ/cm^2 unless otherwise specified.

$\phi_{\text{th,ablation}}$	$\phi_{\text{th,melting}}$	Sample type	Reference	Comments
170 (25 fs) 280 (400 fs)		(111)	[134]	Peak fluence presumed.
458		(100)	[138]	Ablation rate.
300		(100)	[139]	
	170	(100) or (111)	[140, 141]	Transient reflectivity. Fluence type N/A.
	260	(111)	[136]	
520	270	(111)	[110]	
550	260	(111)	[24]	
300	150	(100) and (111)	[11]	TOF Mass. Spec.
∼300	∼150	(100)	[139]	
310	160	N/A	[142]	Absorbed fluence.
3.7 eV/atom (20 fs) 6.2 eV/atom (500 fs)	2.6 eV/atom (20 fs) 5.4 eV/atom (500 fs)		[134]	Theoretical. .
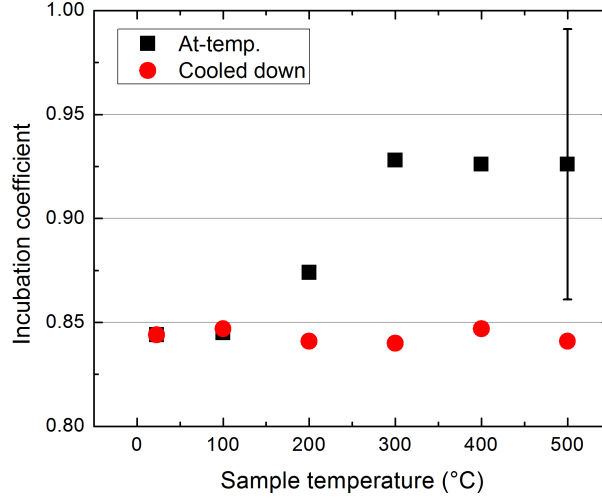
Figure 3.5: Extracted incubation coefficients at different sample surface temperatures. Two general regimes can be identified; temperature below 100°C, and temperatures above 300°C, with the 200°C data point as the transition. An example of the error bar is shown. Errors were calculated based on propagation of uncertainties associated with the threshold fluences (details in Section 2.3.2).

While there is a distribution of the reported thresholds, aside from the simulation work in [134] experimental work presenting both melting and ablation thresholds showed that the melting threshold is roughly on the order of half of the ablation threshold. Once melting occurs, amorphization can take place due to the rapid cooling rate of the material following ultrafast laser energy deposition (e.g., [110, 136, 143]). This occurs as the resolidification front in the material progresses at $\gtrsim$1-25 m/s, where nucleation of the crystalline phase does not have adequate time to occur through the melted layer. This is true for fluences employed between the ablation and melting thresholds [143]. Using an approximate single-shot melting-to-ablation threshold fluence of 0.50, an incubation coefficient of 0.84 as extracted from this work and [136], solving Equation 2.1 for N yields a single-shot melting threshold which corresponds to the ablation threshold of N=76. Therefore single-pulse irradiation with pulse fluences

between $\phi_{\text{th}}(1)$ and $\phi_{\text{th}}(76)$ (or equivalently, $\phi_{\text{th,ablation}}$ and $\phi_{\text{th,melting}}$) is expected to cause amorphization in a thin surface layer. Each subsequent pulse with the same fluence following this pulse would then be expected to cause a remelting-refreezing cycle in the same target site. This condition would be true for the threshold conditions for $1{<}N{<}76$, and the observed incubation behavior would arise from damage accumulated in the repeated melt-freeze cycles. This could occur either through increased disordering of the crystallinity of the affected region, or changes in the interacting volume due to material changes. The latter may be linked to the difference in the absorption between crystalline and amorphous silicon. A simplistic calorimetry estimate yields a 20% reduction in the energy required to melt amorphous silicon relative to crystalline silicon. Further reduction in the energy required can be expected from the optical constants of the amorphous and crystalline material, as summarized in [110] (using [5] and [127]). At 800 nm the absorption coefficient and refractive index for crystalline silicon are $0.1{\times}10^4$/cm and 3.693 respectively, while for amorphous silicon they are $2.47{\times}10^4$/cm and 3.904. The general decreasing trend of the single-shot threshold fluence as temperature increases may be linked to increasing absorption at elevated temperatures. To provide a rough idea, the linear absorption coefficient of silicon reaches several times higher in the mid hundreds of degrees Celsius range compared to room temperature [144–147], and the two photon absorption at $\sim$200°C is about twice that of room temperature [148]. Another contributing factor to the decreased single-shot threshold is the temperature differential between the initial sample temperature and the relevant material removal temperatures (i.e., melting, ablation and boiling temperatures). To provide an idea, the melting point of silicon is $\sim$1410°C, and an ablation threshold of roughly twice the melting threshold has been reported

[110]. At this point, the origin of the plateauing behavior is unclear and warrants further studies. From Figures 3.3 and 3.4, the suppression of the incubation effect at higher temperatures was not significant for pulse numbers below a few tens of shots, and quoting a N-to-1 threshold ratio as a figure of merit may not accurately describe the (lack of) suppression of incubation effects at high temperatures. This may be due to the interplay of the time frames for relevant events at this specific laser repetition rate (i.e., damage accumulation, and possible defects and crystallographic damage recovery). The suppression of the incubation effect can be put into the context of the crystallographic properties of silicon and knowledge of its defects. In silicon, dissociation of divacancies occurs at 300°C (e.g., [116, 149]). Although a more recent study suggests a two-stage annealing of residual divacancies with a second stage at 600°C, and at even higher temperatures no signal resulting from defects was observed [120]. In terms of crystallographic regrowth, the solid phase epitaxial regrowth rate of silicon [100] direction at 500°C is ~10Å/min from the crystalline-amorphous interface, and follows an Arrhenius temperature dependence [121, 122]. Figure 3.6 shows the estimated regrowth rates at the temperature range used in this experiment, as reproduced from [122]. While the lower range for silicon $\langle 100 \rangle$ at temperatures used in this experiment is lower than the typical temperatures where the Arrhenius model is applied (typically above 600°C), the reproduction is intended to show negligible regrowth rates at the lower temperatures used in this experiment.

While typical deposition of ultrashort pulse laser energy can lead to a very high, rapid increase of sample temperature [3, 9, 10], the subsequent cooling of the target also occurs in a very short time frame [3, 9, 12]. This would not allow time for significant crystallographic recovery during the cool down period and between the
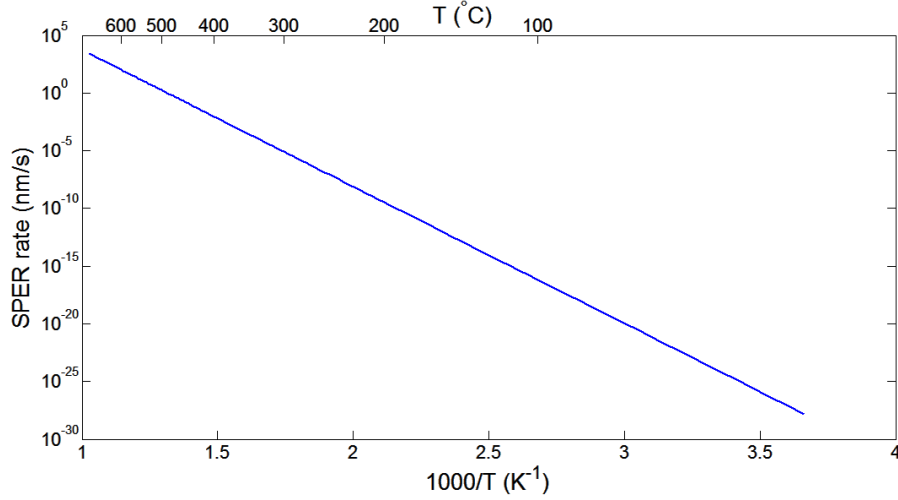
Figure 3.6: Estimated solid phase epitaxial regrowth rate in the silicon [100] direction for relevant temperatures to this experiment, reproduced after [122]. While the lower temperature range is lower than where the Arrhenius model is typically applied, the results here show negligible regrowth rates at lower temperatures used in the experiments.

pulse-to-pulse delay of 20 ms. However, the high temperature may promote faster dissociation of defects, leading to a suppression of accumulated damage between each pulse. While crystallographic regrowth is not expected to be significant during the pulse-to-pulse delay, a higher number of shots will require a longer laser dwell time (e.g., at 50 Hz irradiation, 1000 shots would take 20 seconds) and recovery of damage induced by the early pulses may come into play. The data suggests that the incubation effect as well as its suppression at higher temperatures both have a tendency to saturate, and the combination of irradiation conditions and sample temperature may favor one over another. Permanent changes of the samples resulting from the heating was ruled out as a contributing factor to the observed threshold behavior, since the same threshold and incubation behavior were obtained between an unheated room temperature benchmark sample and on each heated sample after cooling down to

near room temperature.

As mentioned in the background chapter, spot sizes extracted for higher numbers of shots or at different conditions (i.e., elevated temperatures, longer pulse durations) may sometimes be somewhat different (typically larger) than that extracted using the single-shot data. Alternative analysis carried out using spot sizes extracted for each number of shots, rather than using the respective single-shot spot size for each series, leads to qualitatively similar but a relatively more subtle outcome. To provide a quantitative example, Figure 3.7 shows the threshold fluences for different numbers of laser pulses at 200°C, fitted using the individual spot sizes extracted for each N, compared to the same data fitted using the single-shot spot size. The increase of the extracted spot sizes with increasing N will result in a lower fluence value. Fitting to such a set of data will then result in a seemingly stronger incubation effect (or a smaller value of the incubation coefficient). This is demonstrated in Figure 3.8; for each sample temperature the extracted incubation coefficient from the same set of threshold energy data is lower when fitted with individual spot sizes. The enlargement of the extracted spot size tends to be increased at higher temperatures, likely causing the decreasing trend observed above 300°C. The decision on the suitable analysis technique will require further understanding of the ablation mechanisms, damage accumulation dynamics, and careful diagnostics to identify or eliminate the possibility of a contribution from the experimental setup.

3.2.3 Conclusions and future work

Within the temperature range employed in this experiment, the results of this experiment showed that a suppression of the incubation effect occurs above 100°C. This
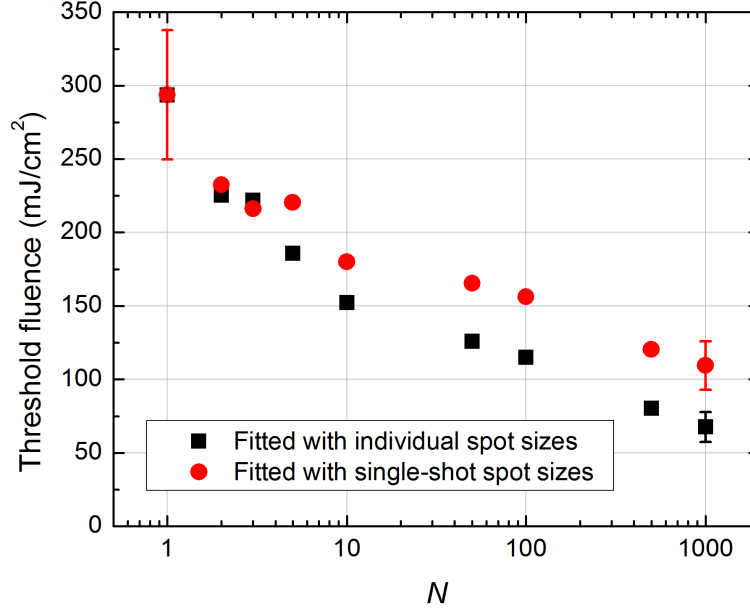
Figure 3.7: Threshold fluence as a function of numbers of laser pulses at 200°C, fitted with individual spot sizes (squares), and single-shot spot sizes extracted for each series (circles) for comparison.

suppression plateaus with temperature above 300°C up to 600°C. The behavior of the extracted thresholds suggest that both the incubation effect and its suppression at elevated temperatures have a tendency to saturate, and the interplay between irradiation conditions and sample temperature may favor one over another. Possible permanent changes made to the sample due to the heating was ruled out as a contributing factor to the observed thresholds and incubation behavior since irradiation following cooling down of each heated samples yielded the same results as the unheated room-temperature benchmark sample. The results of this work can be put into the context of crystallographic properties of silicon and knowledge of its defects. The suppression of the incubation effect likely arises from the recovery of the damage to the crystal structure generated by the laser energy. Future work on expanding the temperature range, characterizing the degree of recovery at different
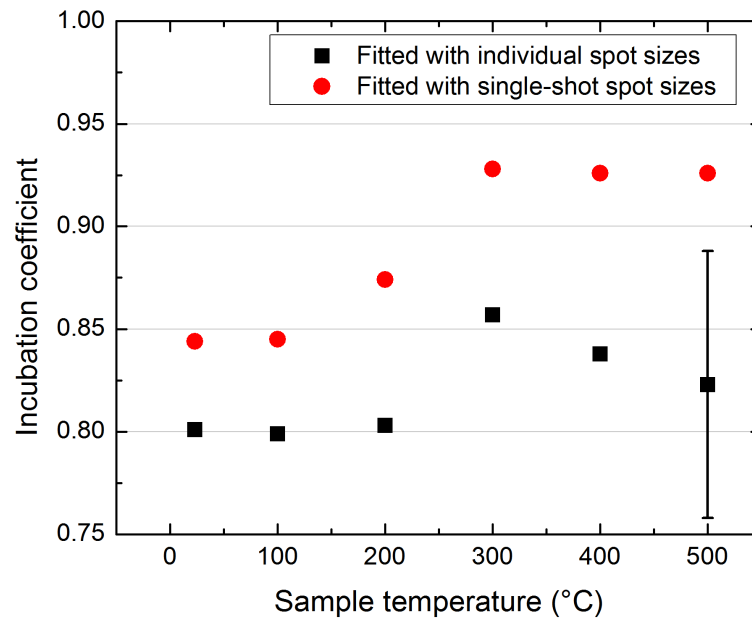
Figure 3.8: Incubation coefficients extracted using different spot-size fittings for different sample temperatures. An example of the error bar is shown. Errors were calculated based on propagation of uncertainties associated with the threshold fluences (details in Section 2.3.2).

heating conditions (i.e., analogous to isochronic and isothermal annealing experiments in the literature), as well as combined simulation of silicon defects and laser ablation dynamics may provide valuable insights into the incubation effect.

3.3 Positron annihilation spectroscopy studies of incubation mechanisms in silicon

Positron annihilation studies were made available through the affiliation of Professor Andrew Knights at McMaster University with the Positron Laboratory at the University of Bath, U.K. Providing details of the positron annihilation technique is beyond the scope of this thesis. Instead, readers are referred to, e.g., [114, 150]. As mentioned in the introduction to this chapter, positron annihilation spectroscopy is sensitive to divacancy density down to $1:10^7$, and thus is a suitable tool to detect subtle defect generation in sub-threshold ultrafast laser irradiation. The adaptation of position annihilation technique to study the accumulation of laser-induced defects is novel.

3.3.1 Experimental details

To prepare samples suitable for the positron annihilation spectroscopy (PAS) work, the focused laser beam used for sample processing was scanned over the sample surface to cover a $\sim 1 \times 1$ cm^2 area on each sample. The development of the micromachining instrumentation was geared for small scale processing in mind, and large-area processing and larger throughput was not emphasized. As such, the longest focal length that can be conveniently used in our micromachining setup is a 125 mm focal length

lens, providing a spot size of $\sim$20 μm $1/e^2$ radius at the time these experiments. As a compromise between uniform sample coverage and time spent on each sample, the laser beam was scanned in lines across the sample at 1000 μm/s with a 20 μm line-to-line spacing. A reference energy $E_{\text{ref}}\sim$1 μJ was taken as the energy required to cause a visible change (discoloration, usually indicative of amorphization of the material) on the surface under the viewing system and the subsequent brief microscope examination. Several samples were irradiated, each with a different energy level relative to E_{ref}, including 1%, 10%, 25%, 50%, 77%, 90%, 95%, 100%, and 130% of E_{ref}. Due to the large spot size of the positron beam (millimeters in diameter), the results can be considered as an spatial average over the irradiated area.

3.3.2   Results and discussions

The positron annihilation spectroscopy results are summarized based on a figures prepared by the Positron Physics Laboratory at the University of Bath (Figure 3.9 and 3.10) for selected samples. The fitted positron diffusion lengths L are also included in this figure. It can be seen that the samples irradiated at 77% and 90% of E_{ref} showed similar behavior in the positron results, with a fitted diffusion length of L=190 nm. For irradiation at 95% of E_{ref}, the fitted positron diffusion length is 150 nm, and at E_{ref} the fitted positron diffusion length is 90 nm. The results suggest that the positron diffusion behavior is changed at a very near surface region, where material modifications due to the laser processing is expected to occur. Etching of the sample irradiated at E_{ref} with HF changed the positron signal more dramatically from the bulk condition, as can be seen in the figures, indicating that the changes are in the silicon surface and not in the oxide layer. In a follow-up experiment, PAS was carried

out on a new set of laser irradiated samples, including one conducted at 130% of E_{ref} where more obvious surface changes were visible by eye (in the form of gentle surface rippling, as inspected using optical microscopy), and a pristine silicon sample as a benchmark. The difference in the PAS signal for the E_{ref} samples from the two sets of data may be due to the small difference in the energy calibration between the experiments. The follow-up work is summarized in Figure 3.10. It can be seen that the sample irradiated with 130% E_{ref} showed a convincing signal indicating surface modification. The Positron Physics Laboratory at the University of Bath fitted the data with a ~350 nm defect layer with a ~20 nm positron diffusion length, and reported the likelihood of nano-voids or larger scale disorder over divacancies or amorphous silicon. It should be pointed out that the fitting was performed assuming uniform conditions in the material, whereas a more sophisticated fitting scheme modeled after a thin modified surface region and unmodified bulk material below could be carried out for a more quantitative defect analysis in the future.

3.3.3   Conclusions and future work

Preliminary positron annihilation spectroscopy results suggest a slightly detectable change of divacancy concentration at the surface of the sample for pseudo-uniform irradiation at and above 90% of E_{ref}, where E_{ref} is the energy where visible modification to the sample surface occurs under the same irradiation conditions. The results are consistent with a shallow modified layer generated by ultrafast laser irradiation of materials. The obvious discernable changes in the E_{ref} sample after a hydrofluoric acid etch, as well as in the 130% E_{ref} sample indicate surface modifications likely in the form of nano-void or larger-scale disordering over divacancies and amorphous
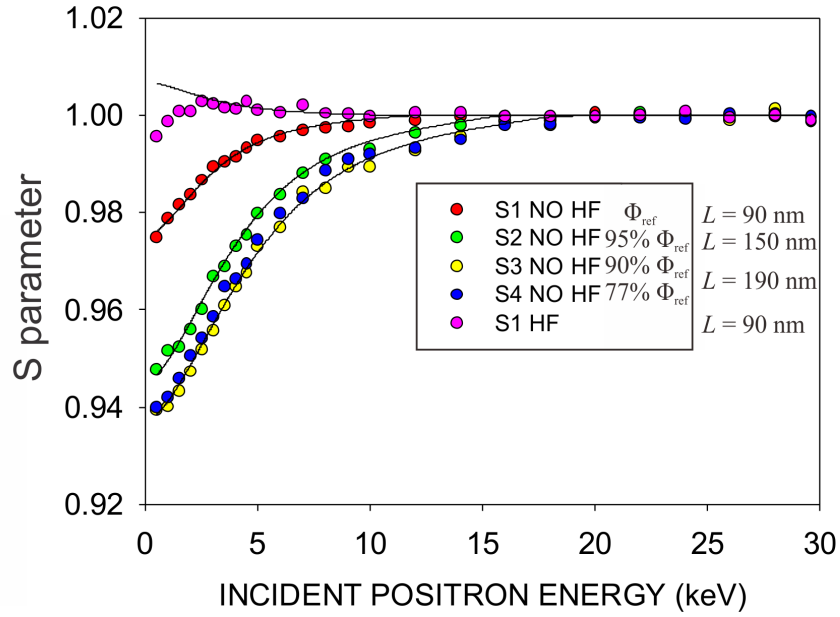
Figure 3.9: PAS results of samples irradiated at different fractions of $E_{\mathrm{ref}} {\sim} 1\ \mu$J where discoloration just occurs on the sample surface, as indicated in the legend. Also shown are the fitted positron diffusion lengths L, indicating the existence of increased surface defect density.
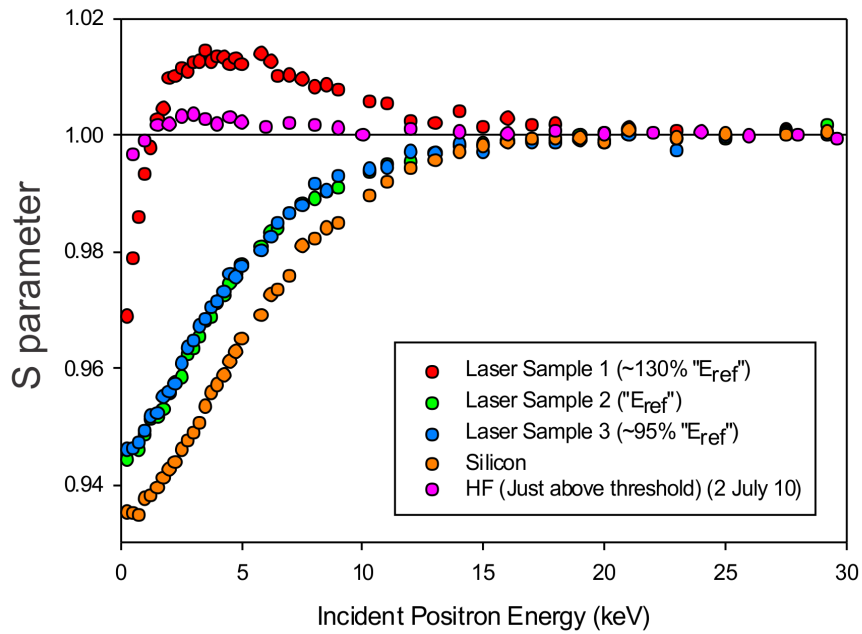
Figure 3.10: Follow-up PAS results of samples irradiated at different fractions of E_{ref} where discoloration just occurs on the sample surface, as indicated in the legend. Also shown are the signal from a pristine silicon sample, and HF-etched E_{ref} data from Figure 3.9 ("HF (Just above threshold)(2 July 10)") for comparison.

silicon. A more sophisticated fitting scheme to account for a shallow modified layer on top of an unmodified bulk should be employed in future work for a more accurate characterization of the defect density and distribution. The results combined with the high-temperature experiments point to the role of defects in sub-threshold damage accumulation. Results from a more systematic study combined with repeated laser irradiation (on a pre-irradiated and characterized sample) may yield important insights into the origin of the incubation effect.

3.4 Incubation behavior in silicon as a function of laser repetition rate

As presented in Section 3.3, preliminary positron annihilation spectroscopy studies in the laser processed samples showed subtle changes in the divacancy concentration at the surface region. This section describes efforts in investigating the dynamics of defect accumulation during ultrafast laser irradiation. As mentioned in the introduction of this chapter, monovacancies have lifetimes on the order of milliseconds to 2 seconds in silicon in room temperature. By studying the threshold behavior as a function of laser repetition rate, an incoming laser pulse would presumably be interacting with a different monovacancy density, if present, as a result of the preceding laser pulse and changes in the incubation effect can be observed.

3.4.1 Experimental details

In typical laser irradiations where low numbers of laser pulses are desired, a mechanical chopper is used to reduce the pulse repetition rate to 50 Hz, thus allowing the

electromechanical shutter enough time delay between pulses to isolate single-pulses. Further delay of the pulses was implemented through software control of the shutter, slowing down the laser repetition rate below 10 Hz (10 Hz is the maximum continuous operating frequency of this specific shutter as per specifications). To investigate the effect of laser repetition rate on the laser incubation behavior, the following pulse-to-pulse delays (repetition rates) were employed: 20 ms, 250 ms, 500 ms, 1 s, and 2 s (50 Hz, 4 Hz, 2 Hz, 1 Hz, and 0.5 Hz). Focusing of the laser pulses was achieved with a 75 mm lens. With this lens a spot size of 11.7 μm $1/e^2$ radius was extracted using the D^2 technique ([109]). Laser energies used ranged from 160 nJ to 1.4 μJ. The numbers of laser pulses employed were 1, 1, 2, 3, 5, 10, 50, 100, and 200 for all of the repetition rates, and an additional 500-shot irradiation was carried out at 50 Hz. As indicated, single-shot irradiation were carried out twice to provide extra data points for the D^2 analysis.

Laser irradiation at different repetition rates was carried out at room temperature and at $\lesssim 300°$C. Details of the heating setup are presented in Section 3.2. It should be noted that for this experiment only, the temperature monitoring scheme was still under optimization and the sample surface temperature was estimated using the subsequently observed temperature differential between the internal region of the stage and the sample surface. Results presented in Section 3.2 suggest a change in the incubation behavior is expected in this temperature range for irradiation at 50 Hz.

3.4.2   Results and discussions

Details of the data analysis, extracted parameters and qualitatively similar results and relevant discussions are presented in Sections 2.3.2 and 3.2.2. Instead, in this section
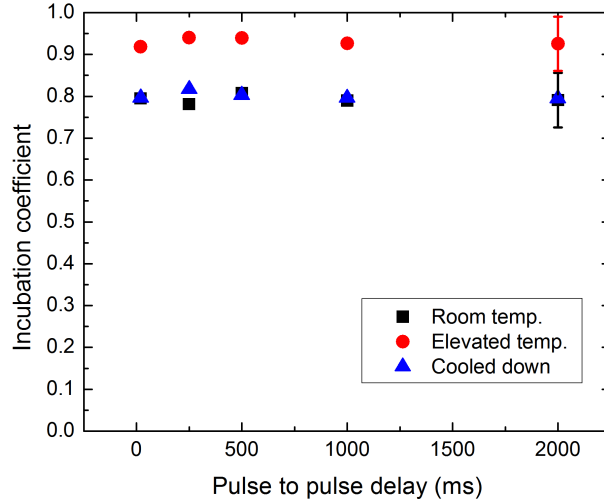
Figure 3.11: Extracted incubation coefficients at different laser repetition rates for irradiation carried out with sample surface at room temperature, and $\lesssim 300°$C, as well as irradiation on the same sample following a cool down to near room temperature. Examples of the error bars are shown. Errors were calculated based on propagation of uncertainties associated with the threshold fluences (details in Section 2.3.2).

only the incubation coefficients obtained from irradiation at the two temperature points will be presented.

The results show that while there is a suppression of the incubation effect at elevated sample temperature, at an estimated $\lesssim 300°$C, there is not a significant dependence of the incubation behavior on the laser repetition rate at this temperature, nor at room temperature in the unheated sample. The threshold and incubation behavior in irradiations carried out following the cool down of the heated sample is identical within experimental uncertainty to that of the unheated room temperature benchmark sample, as also shown and discussed further in Section 3.2.

The results suggest that if defects are contributing to the damage accumulation leading to the observed incubation effect, the defect lifetime does not change significantly in the range of 20 ms to 2 seconds.

3.4.3   Conclusions and future work

Within the irradiation conditions employed, the results of this experiment showed no changes in the incubation behavior between laser repetition rate in the range of 50 Hz to 0.5 Hz at room temperature and at an elevated sample temperature of $\lesssim 300°$C, as estimated using the near-surface stage temperature reading. This suggests a lack of a lifetime component to the contributing damage accumulation between 20 ms and 2 seconds. Future work in pursuing the repetition rate dependence of the incubation effect should employ a higher range of repetition rates, ideally with a shorter pulse-to-pulse delay, as well as carrying out the experiment at more sample temperatures.

3.5   Threshold behavior in ion-implanted silicon

In semiconductor device fabrication, the materials being processed are at times altered from the as-grown state. For example, ion implantation is often used to introduce dopants into materials to alter the electronic properties. In silicon based devices, implantation of phosphorous can be used to generate an n-type doping, while boron can be used to generate a p-type region. An inherent side effect of the ion implantation process is disordering of the crystal lattice resulting from the damage caused by the implanted ions. An annealing stage is often carried out following ion implantation to allow recovery from this disordering to regain crystallinity of the material. While ultrafast laser processing of material provides unique capabilities over other material systems and conventional photolithographic device fabrication techniques, conventional clean room techniques are still required to fabricate devices from the ultrafast laser processed samples. In the effort to employ ultrafast lasers in conjunction with

conventional fabrication techniques, it will be necessary to gain an understanding of ultrafast laser interactions with materials at the different altered states in the process flow. The introduction of dopants and disordering of the crystallographic structures resulting from ion implantation can alter the ultrafast laser modification and ablation thresholds. This may result as an interplay between the mechanical, electronic and optical properties in an ion-implanted sample. This section presents results of ultrafast laser ablation of ion-implanted silicon samples.

A bundle of simulation software popularly used in the ion implantation community to estimate the outcome of ion implantation is "The Stopping and Range of Ions in Matter", or SRIM, with the core being a program called "Transport of Ions in Matter", or TRIM, were developed by James F. Ziegler and Jochen P. Biersack in 1983, and has been continuously improved since (e.g., [151]). These simulation tools were used to estimate the distribution of implanted ions and the resulting damage for implantation conditions employed in this series of experiments.

3.5.1   Experimental details

Low energy ion implantations (e.g., up to a few tens of keV's) were carried out at the Centre for Emerging Device Technologies facility at McMaster University, while high energy implantations were carried out at the Tandetron Laboratory at the University of Western Ontario. Table 3.2 summarizes the implanted ion species, ion energies and doses employed for this series of experiments. The Ar and Si implantations were carried out to characterize the ablation thresholds for samples with an amorphized surface layer, as low energy, high dose implantation results in a high damage concentration in a shallow region. The goal of the phosphorous implanted sample series is
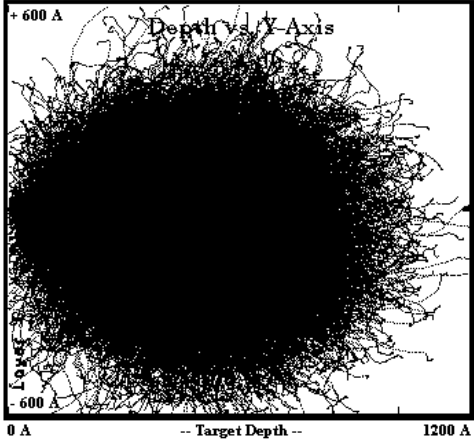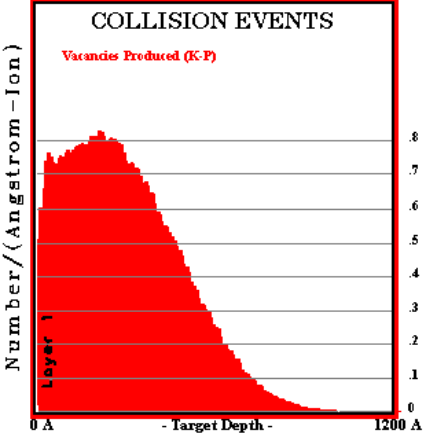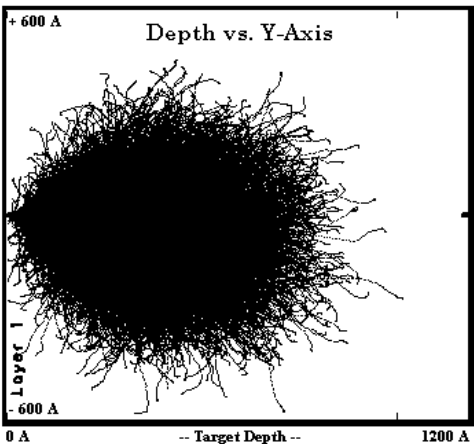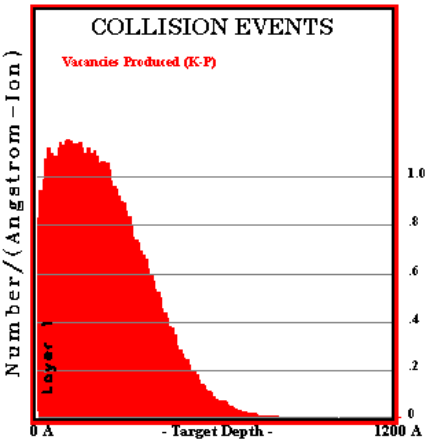
Table 3.2: Implantation species and conditions employed for this series of experiments.

Ion species	Voltage (keV)	Dose (ions/cm^2)
Si	30	1×10^{15}
Ar	30	1×10^{15}
P	500	1×10^{13}
P	500	1×10^{14}
P	500	5×10^{14}
P	500	1×10^{15}
P	1000	1×10^{15}
P	1500	1×10^{15}
P	2000	1×10^{15}
B	500	1×10^{13}
B	500	1×10^{14}
B	500	5×10^{14}

to study the potential threshold dependence on the implantation depth (i.e., implantation energy) and damage concentration (i.e., ion dose), while the boron-implanted series aims to study the dependence on the damage concentration (i.e., ion dose) at a different depth relative to the phosphorous implanted case.

The simulated ion distribution and resulting damage profile for the ion implantation conditions employed in this series of experiments are presented in Table 3.3.

Table 3.3: TRIM simulation results showing outcomes of various ion implantation conditions to provide estimations of the ion ranges and the distributions of generated vacancies.

Silicon ions		
Ion energy	Ion trajectory	Vacancies distribution
30 keV		
Argon ions		
Ion energy	Ion trajectory	Vacancies distribution
30 keV		

Phosphorous ions		
Ion energy	Ion trajectory	Vacancies distribution
500 keV		
1 MeV		
1.5 MeV		

Ion energy	Ion trajectory	Vacancies distribution
2 MeV		
	Boron ions	
500 keV		
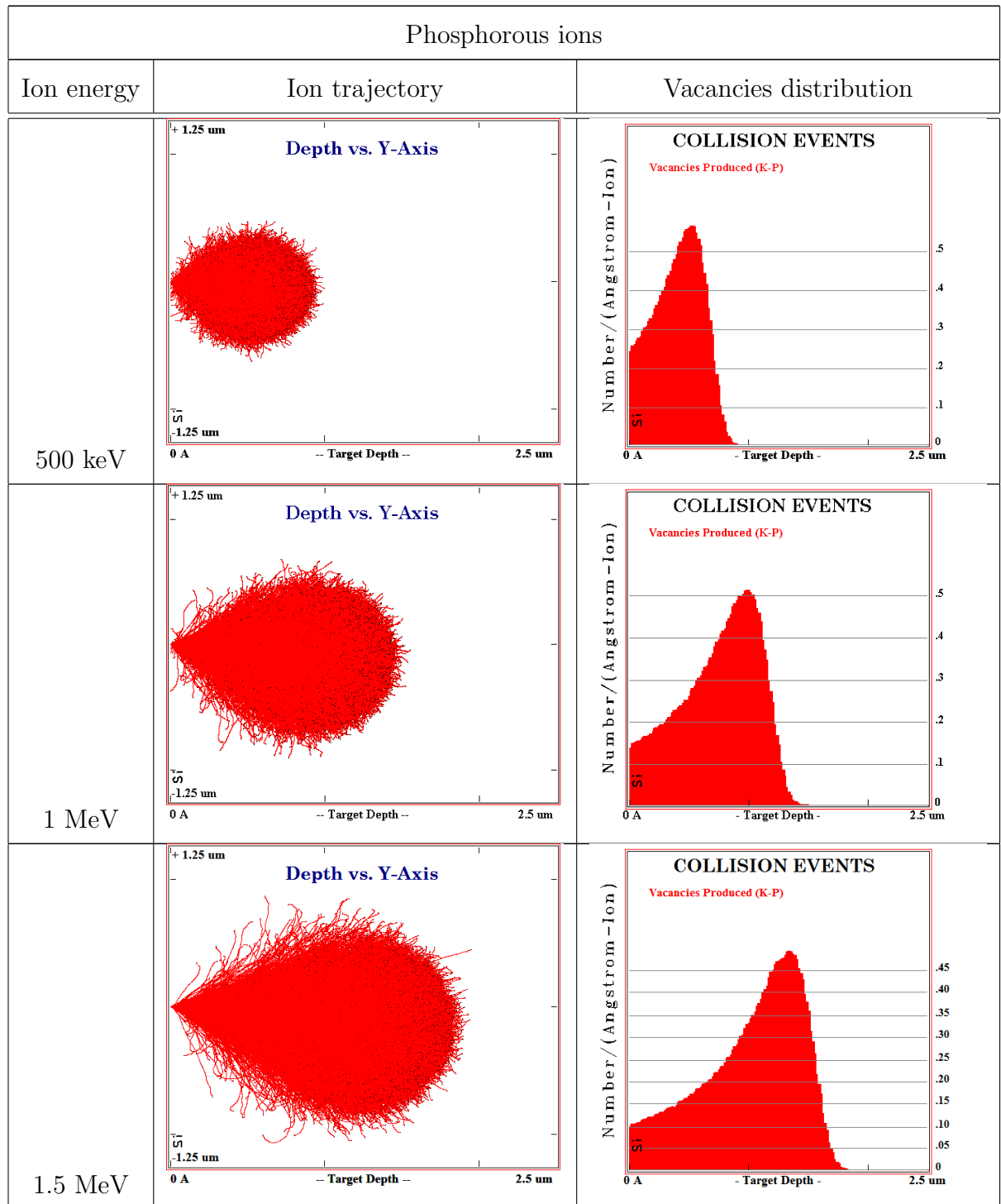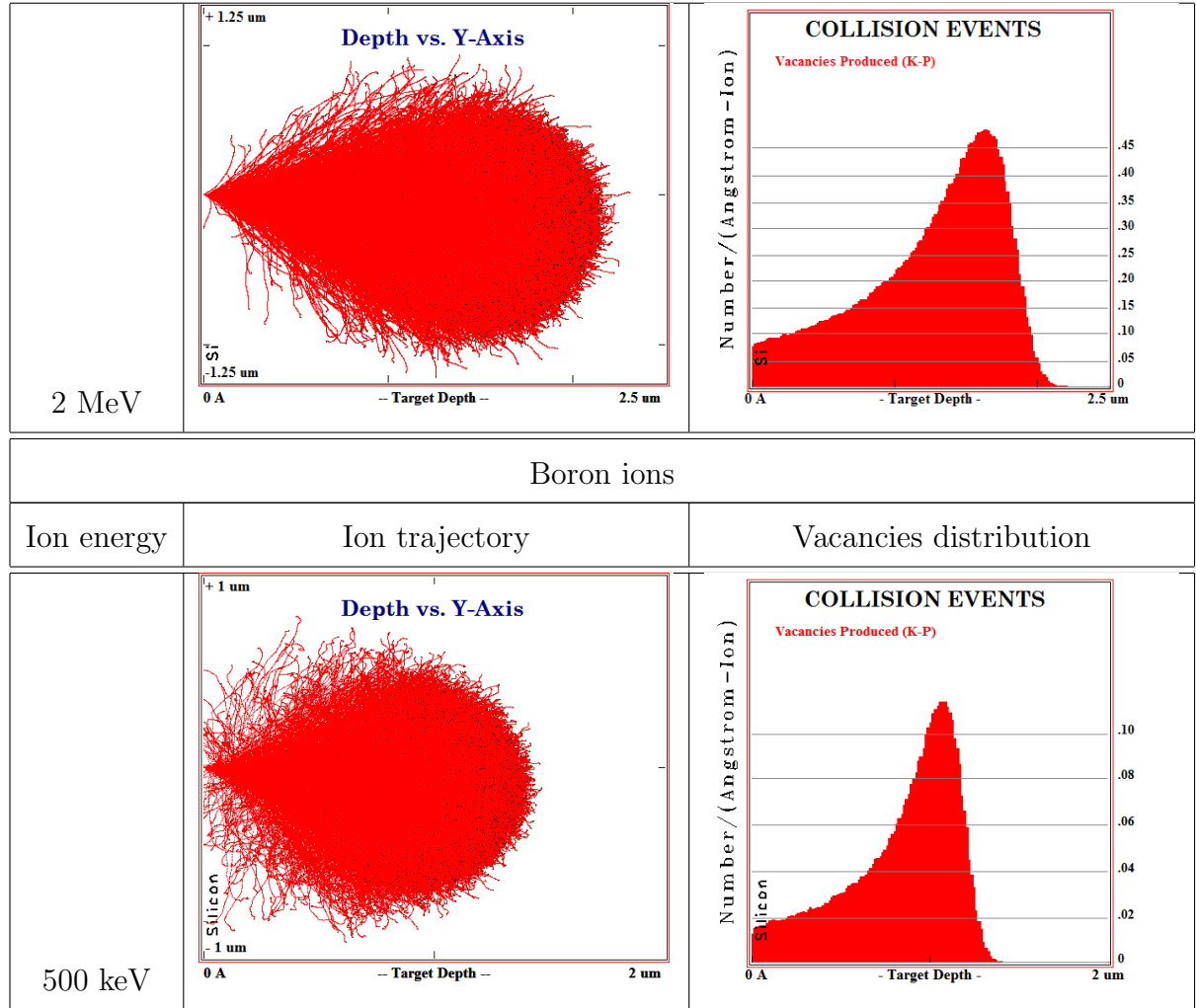
Laser irradiations were carried out using approaches mostly similar to descriptions provided in Section 2.2.2. Laser energies employed for this series of experiments ranged from several times the ablation threshold to below the ablation threshold. Stationary irradiations were carried out at 50 Hz with a 125 mm focusing lens. This lens yielded a spot size of $\sim$20 μm in $1/e^2$ radius. Single-shot ablation thresholds were then extracted using the D^2 technique as presented in Section 2.3.2, and the results

are presented in this thesis. To facilitate comparison of the relative changes in the thresholds, the results from each series of experiments will be normalized to the single-shot threshold obtained from the non-implanted silicon samples used as a benchmark for each series. This was done since the single-shot threshold fluence for virgin silicon can vary on the order of 5-10% from experiment to experiment, while the variation of samples processed in the same experiment is much smaller (repeating single-shot irradiation over numerous samples on the same experiment yielded a variation of 1.5%). While experimentally this type of statistic may be expected, looking for subtle changes in samples with different implantation conditions can be misleading if absolute quantities from different series of experiments are compared. As such, experiments were, and should be, conducted such that each series of samples are compared to a virgin benchmark sample from the same experiment, and normalization of each series should be used to compare the relative changes.

3.5.2   Results and discussions

Using TRIM calculations, in the case of Ar and Si ion implantations the shallow near-surface layer of the silicon samples is expected to be amorphized. The single-shot ablation thresholds were extracted and averaged over two sets of experiments using the D^2 technique. The extracted ablation thresholds are 350 mJ/cm^2 for virgin silicon, and 266 mJ/cm^2 for the Ar- and Si-implanted samples. The results are summarized in Figure 3.12.

Multiple-pulse ablation thresholds for the virgin silicon samples, Si-ion implanted, and Ar-ion implanted samples are shown in Figure 3.13. Incubation behavior is observed in all three samples.
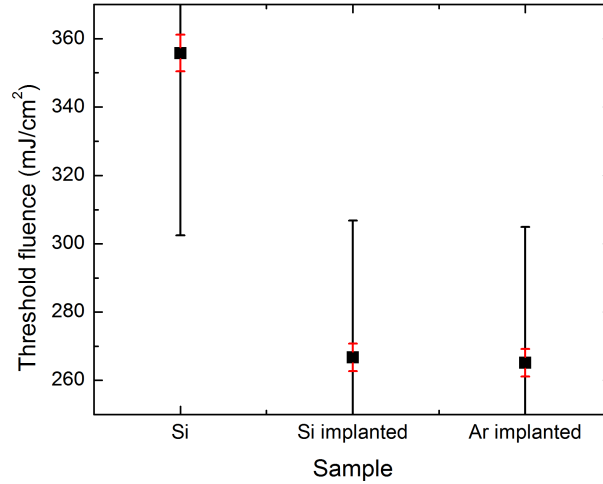
Figure 3.12: Averaged single-shot laser ablation thresholds for virgin silicon, and silicon and argon ion implanted samples. Ion implantations were carried out at 30 keV and each with a dose of $1 \times 10^{15}/cm^2$. The 15% error associated with the absolute value, as well as the 1.5% error figure, as discussed in Section 2.3.2, are provided.
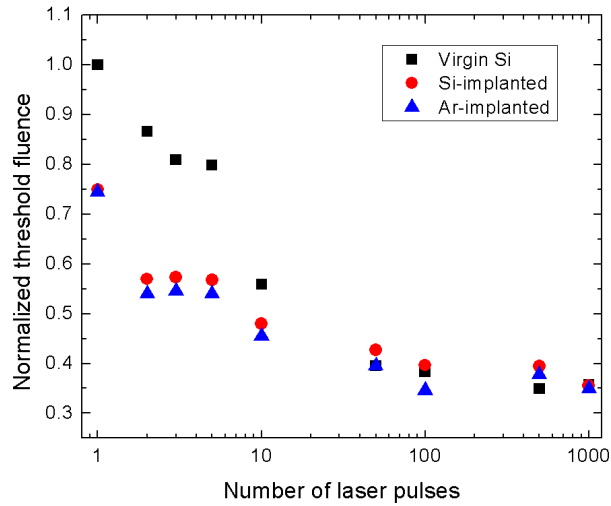
Figure 3.13: Normalized multiple-shot thresholds for virgin silicon, and silicon and argon ion implanted samples. Data points were normalized to the single-shot threshold for the virgin silicon sample. Associated error is estimated to be 15% of the extracted values.
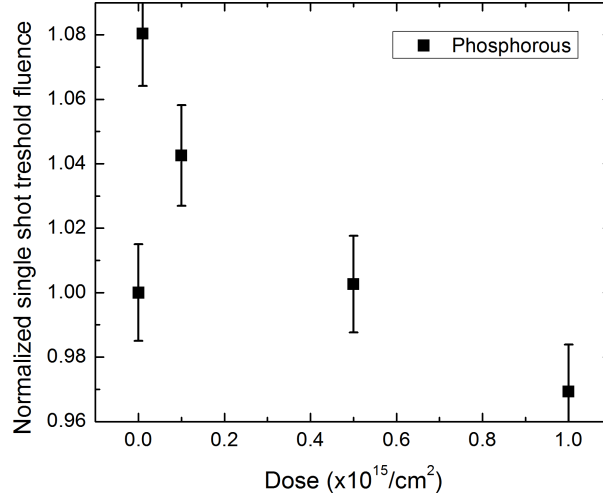
Figure 3.14: Normalized single-shot threshold behavior at various phosphorous doping doses implanted at an ion energy of 500 keV. Details of uncertainty considerations are provided in Section 2.3.2.

The single-shot threshold behavior as a function of implantation dose for phosphorous implantations however showed an initial increase in the threshold fluence with an implantation dose of $1 \times 10^{13}/cm^2$, and a decreasing trend with increased implantation dose from there on (Figure 3.14).

Figure 3.15 summarizes the normalized single-shot threshold fluences for samples implanted with phosphorous at different ion energies at a fixed implantation dose of $1 \times 10^{15}/cm^2$. Without more data points it is difficult at this point to determine the behavior of the single-shot ablation threshold as a function of ion implantation energies.

The single-shot threshold for samples implanted with boron, however, showed an increasing trend with increasing dose, in contrast to the phosphorous implantation at the same dosage implanted at the same ion energy (500 keV) (Figure 3.16).

It should be pointed out that the implantation depth for boron and phosphorous is considerably different, as shown in the TRIM simulation results (Table 3.3). A
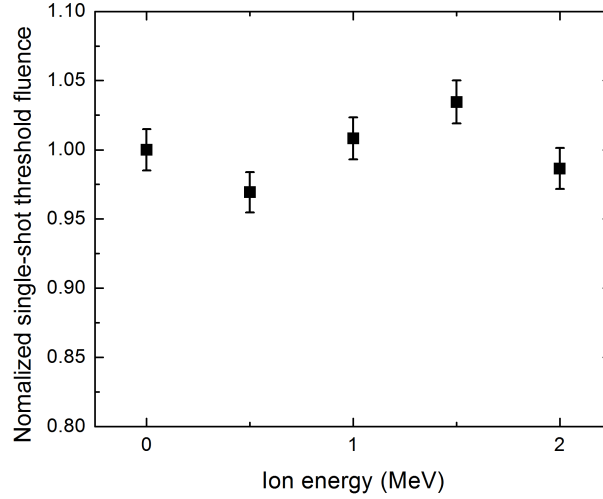
Figure 3.15: Normalized single-shot threshold behavior at various phosphorous doping ion energies at a fixed dose of $1 \times 10^{15}/\text{cm}^2$. The 0-MeV data point refers to the virgin silicon benchmark sample. Details of uncertainty considerations are provided in Section 2.3.2.
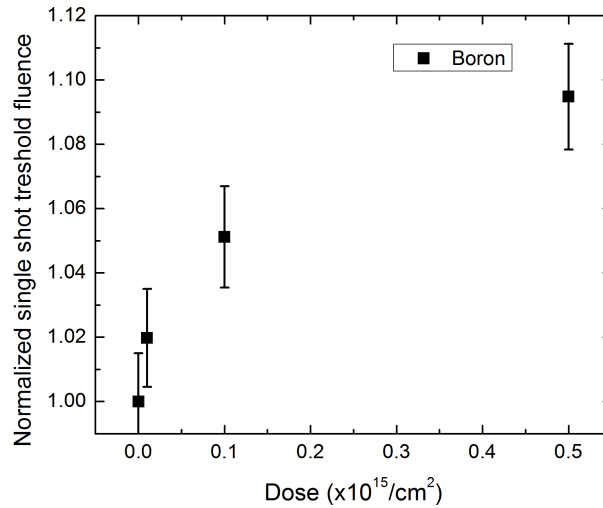
Figure 3.16: Single-shot threshold behavior at various boron doping doses implanted at an ion energy of 500 keV. Details of uncertainty considerations are provided in Section 2.3.2.

sensible comparison would be to estimate an optical penetration depth, and determine the total damage caused by the ion implantation based on TRIM simulation results for the boron and phosphorous implantations within this depth. Typically a simple estimate of the effective optical penetration depth is (e.g., [140, 152]):

$$\alpha_{\text{eff}} = \alpha_{\text{lin}} + \beta I_o(1 - R) \tag{3.1}$$

where α_{eff} is the effective absorption coefficient, α_{lin} is the linear absorption coefficient, β the two-photon absorption coefficient, I_o the laser intensity, and R the small signal reflectivity.

Using values from [127], typical values of $\gtrsim$ 100s of nanometers are obtained for α_{eff} for semiconductors. However in [127] the measurements were performed using spectroscopy techniques, and the high intensities associated with the ultrafast laser pulses can facilitate higher order and other absorption mechanism(s) rather rapidly (e.g., [141]). Experimentally extracted effective penetration depths for ultrafast laser ablation of semiconductors from the literature using Equation 3.2 tend to be on the order of a few tens of nanometers, about an order of magnitude lower than the estimation provided using Equation 3.1 ([141, 153] for silicon specific discussions, and [25, 44, 154] for other semiconductors). The theoretical work of [141] presented a model that takes the transient state of the material following ultrafast laser energy into account (Equation 3.2), and yielded good agreement with the extracted effective optical penetration depths of ultrafast laser pulses in semiconductors in the above referenced experimental work.

$$L = \alpha_{\text{eff}}^{-1} \ln(\phi_o/\phi_{\text{th}}) \tag{3.2}$$
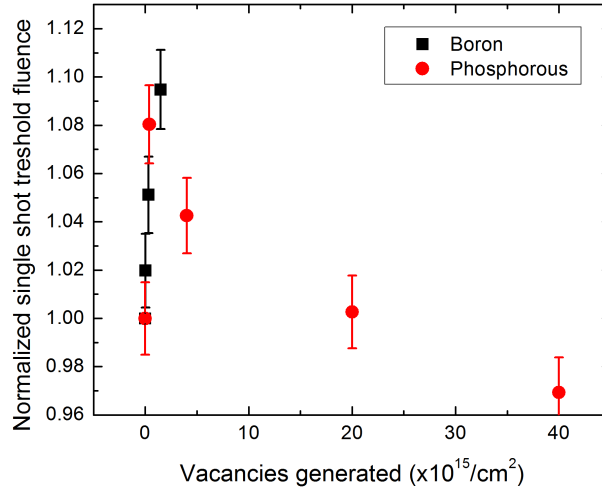
Figure 3.17: Single-shot threshold behavior as a function of total damage generated ($/cm^2$) in a 20 nm depth layer for various boron and phosphorous doping at 500 keV. Details of uncertainty considerations are provided in Section 2.3.2.

where L is the ablation depth per pulse.

Simulations for the phosphorous and boron implantation at the energy employed were carried out with TRIM to obtain the number of vacancies generated (per ion) at a depth of 20 nm. For boron implantation at 500 keV the damage yield in this depth is $\sim$3 vacancies/ion, and for phosphorous implantation the damage yield at this depth is $\sim$40 vacancies/ion. Figure 3.17 presents the single-shot thresholds for boron and phosphorous implanted samples as a function of total vacancies generated in a 20 nm layer.

The reduction of single-shot thresholds in silicon-implanted and argon-implanted samples was expected, since the ablation threshold of amorphous silicon is expected to be lower than that of crystalline silicon due to a stronger optical absorption at 800 nm (see Section 3.2.2 for discussions). The behavior of multi-shot thresholds from the same samples for $N \geq 50$ showed similar thresholds for all three samples, suggesting the damage accumulation mechanism in the incubation effect may be analogous to

surface amorphization caused by ion implantation on some level, and that it takes several pulses (i.e., $N \lesssim 50$) for the material to behave as an amorphized material. The observed single-shot threshold behaviors for the different ion implantation scenarios may be a result of the interplay of several factors. Amorphization of silicon will ultimately lead to a higher absorption coefficient than that of crystalline silicon (e.g., [155]). To provide an idea, the absorption coefficient of amorphous silicon is 2.47×10^4 cm^{-1} at 800 nm, while for crystalline it is 0.10×10^4 cm^{-1}. This effect would dominate over the simple estimated change in the reflectivity due to the different refractive indices of the amorphous ($n = 3.904$) and crystalline ($n = 3.693$) silicon. The above absorption coefficient and refractive indices are obtained from [155] and references therein. From this one would expect the single-shot ablation threshold to decrease as the implantation dose increases (i.e., degree of crystallographic disordering approaches amorphization of material). However, other possible factors may be at play. For example, depending on the depth of the ion distribution, one could obtain a structure analogous to a multi-layer thin-film optical system with each layer having a different refractive index (i.e., within the limits of the refractive indices of crystalline and amorphous silicon, as well as possible modifications due to the implanted ion species). Optical interference effects have been observed in ion-implanted materials in reflectivity studies, showing an oscillating reflectivity change on the order of $\pm 5\%$ as the function of light wavelength (e.g., [124–126]). Other material considerations may be the chemical or mechanical modifications due to the implantation (i.e., eventual modifications to the mechanical strength [156, 157]).

3.5.3   Conclusions and future work

The preliminary results of this series of experiments showed a dependence of single-shot threshold fluences of ultrafast laser ablation of silicon on ion implantation parameters. The single-shot ablation threshold of amorphized material is reduced by 20-25% from that of the pristine silicon. However, there can be a tendency of the single-shot threshold to increase with partially amorphized material, as seen in the cases of boron and phosphorous implantation. At a fixed dose with phosphorous implantation, the implantation energy also has an effect on the single-shot ablation threshold. Future work should be carried out to reproduce the experiments to develop a statistical data set, and various material characterization techniques should be carried out to determine the contributing factor or factors at play to yield the threshold behaviors we observe. The results of this work is a very preliminary step towards subtle material modification based applications (e.g., micro-scale defect engineering), and eventual future work can shed insight into both the material structures following ion implantation as well as ultrafast laser-material interactions and absorption mechanisms, which itself is a topic warranting further elucidation in the literature.

Chapter 4

Near-threshold surface behavior from large-area pseudo-uniform irradiation

This section primarily presents studies on near-threshold irradiation induced ripple-patterns that are novel in addition to femtosecond-laser induced ripple structures reported in the literature. Relevant general background on laser induced periodic structures is presented in Section 2.1.5.

In the preliminary stages of the experimental design for the initial multistage laser irradiation-annealing experiment for incubation studies (as discussed in Section 3.2), several irradiation geometries were tried in order to establish an optimal (re)irradiation scheme prior to and following the annealing stage. The challenge with multiple-stage irradiation with stationary irradiation was ensuring overlap of the target sites between each laser irradiation stage. Other irradiation schemes attempted to

work around this overlap accuracy issue with stationary irradiation included irradiating sets of linear grooves at varying energies and speeds such that the lines irradiated at later stages (i.e., following an annealing stage) are orthogonal to the lines from the previous stage, and the intersecting regions of the lines will be used for the incubation studies. However due to the subtlety of the features and slightly statistical nature of very-near threshold conditions, observation of material changes at the limited areas at interacting sites was challenging.

An alternative scheme was to employ large-area pseudo-uniform irradiation using overlapping line scans of the laser beam with sub-threshold energies such that there would be ample area for the subsequent irradiation target regions to coincide. To characterize the laser-material interactions during the preliminary testing of the large-area irradiation, irradiated regions were studied in detail to examine the surface modifications for the near-threshold conditions for this irradiation scheme. A search in the literature for references on similar irradiation scheme using ultrafast laser had not been successful.

This section presents the observed surface features from repeated surface irradiation with sub- and near-threshold laser energies.

4.1   Experimental details

The irradiation scheme employed in this series of experiments was the standard geometry described in Section 2.2.2. A $5\times$ microscope objective was used to focus the laser pulses. The spot size using this objective was approximately 4.3 μm, as extracted using the D^2 technique ([109]). The beam was translated at a speed of 500 μm/s ($N_{\rm ref}$ of 11 per line scan), and the line-to-line spacing was 4 μm. The

lines are scanned at alternating directions along the y-axis as viewed on the sample (where the sample surface lies in the x-y plane, and the z-axis would be normal to the sample surface), and the starting points of each pass were at the bottom left in the images, where a "pass" refers to an area covered with overlapping line scans once. E_{ref} of 48 nJ was assigned as the energy where laser irradiation appeared as darkened regions in the micromachining viewing system, indicating significant material removal (subsequent analysis showed more pronounced ripple structures at this energy). Large areas were then irradiated with the same geometry at 50%, 70% and 90% of E_{ref} to cover 800 μm×800 μm areas as a "first pass". Second large-area irradiations, "second pass", were carried out at 30%, 50%, 70% and 90% of E_{ref} covering 600 μm×600 μm areas to overlap within the area irradiated at the first pass to create different energy combinations between the two passes, thus probing the effect of varying the accumulated and subsequent irradiation energies. To promote better uniformity to the irradiated regions, follow-up experiments used equal spacings between the spot-to-spot displacement for each line and the line-to-line spacing. For example, given that the laser repetition rate is 1 kHz, a line-to-line spacing of 2 μm would be used for a 2000 μm/s translation speed, and for a 1 μm line-to-line spacing a speed of 1000 μm/s would be used. Using the model presented in [113], where the accumulated fluence from two-dimensional scanning of the laser beam was derived based on the Gaussian spatial energy distribution, the effective numbers of laser pulses were 8 and 35, respectively. Surface analysis was carried out in an optical (with differential interference contrast (DIC)), scanning electron, and atomic-force microscopy techniques. Selected sites were chosen for transmission electron microscope (TEM) studies using focused ion beam (FIB) milling for sample preparation. Unless otherwise stated,

results reported are carried out with the 5× microscope objective.

4.2   Results and discussions

Figure 4.1 shows results of pseudo-uniform large-area irradiation observed using differential interference contrast optical microscopy (DIC-OM). Each "pass" consists of line scans of the 5× microscope objective-focused laser beam at a speed of 500 μm/s, with a 4 μm line-to-line spacing. As shown in Figure 4.1, a single-pass irradiation at 90% of E_{ref} was adequate to generate discoloring on the sample surface, likely due to gentle material modifications. The starting points of the line scans showed stronger modification/material removal due to dwelling of the laser beam during acceleration and deceleration of the line scans. No obvious modifications were observed using DIC-OM at single-pass irradiation at 50% and 70% of E_{ref}. A first-and-second pass energy combination of 70%+70% E_{ref} showed subtle discoloration in the overlapped region. As a single 90% E_{ref} generated a discolored area, and following up with a 70% E_{ref} second pass generated further discoloration. Discoloration was observed in the overlapped region of 50%+90% E_{ref} irradiation. Signs of stronger ablation (sporadic darkened regions due to more pronounced rippling structures) can be observed in irradiation carried out at 70%+90% E_{ref}, and at 90%+90% E_{ref} the overlapped regions from the two passes showed mostly darkened (rippled) regions. Higher magnification DIC-OM images for selected irradiation conditions are shown in Figure 4.2.

The results from the two-pass irradiation shown in Figure 4.1 showed that the cumulative incubation effect depends on the specific energies used for each pass. This is deduced from the observed difference in the resulting surface feature for the same cumulative energies (i.e., 90%+70% E_{ref} irradiation compared to 70%+90% E_{ref}), and

may speak for a possible difference in the energy deposition and damage accumulation depths into the material at different incident energies. In conjunction with future simulation and high resolution microscopy work the results of this work may help elucidate the origin of the incubation effect. Despite the time consuming nature of this irradiation scheme, this irradiation geometry may be useful for deployment in high-temperature studies presented in Section 3.2.

For experiments using 1 μm pulse-to-pulse and line-to-line spacings (i.e., translating at 1000 μm/s, with a 1 μm line-to-line spacing), due to the faster translation rate, higher energies were required to create observable surface changes. These changes include surface spotting and rippling, which appear to be generated sporadically. Atomic force microscopy (AFM) showed the ripple modulation depth to be on the order of a few nanometers. Figure 4.3 presents examples of such observed features. The observed ripples have a periodicity of $\sim$750 μm, in the range of typically observed periodicities for low-spatial frequency laser-induced periodic surface structures ("LSF-LIPSS", or LSFL).

To work around the requirement of needing higher energies to create observable features, which tend to show stronger signs of material removal and could potentially work against our goal of observing subtle damage accumulation and very-near threshold damage, irradiation at lower energies over the same area with multiple passes were carried out. It was then observed that irradiation with below-threshold pulse energies can generate spotting and ripple structures with increasing numbers of passes. Depending on the laser energy employed, repeated irradiation can generate discoloration spotting, which can expand to larger area discoloration and ripple structures. Figures
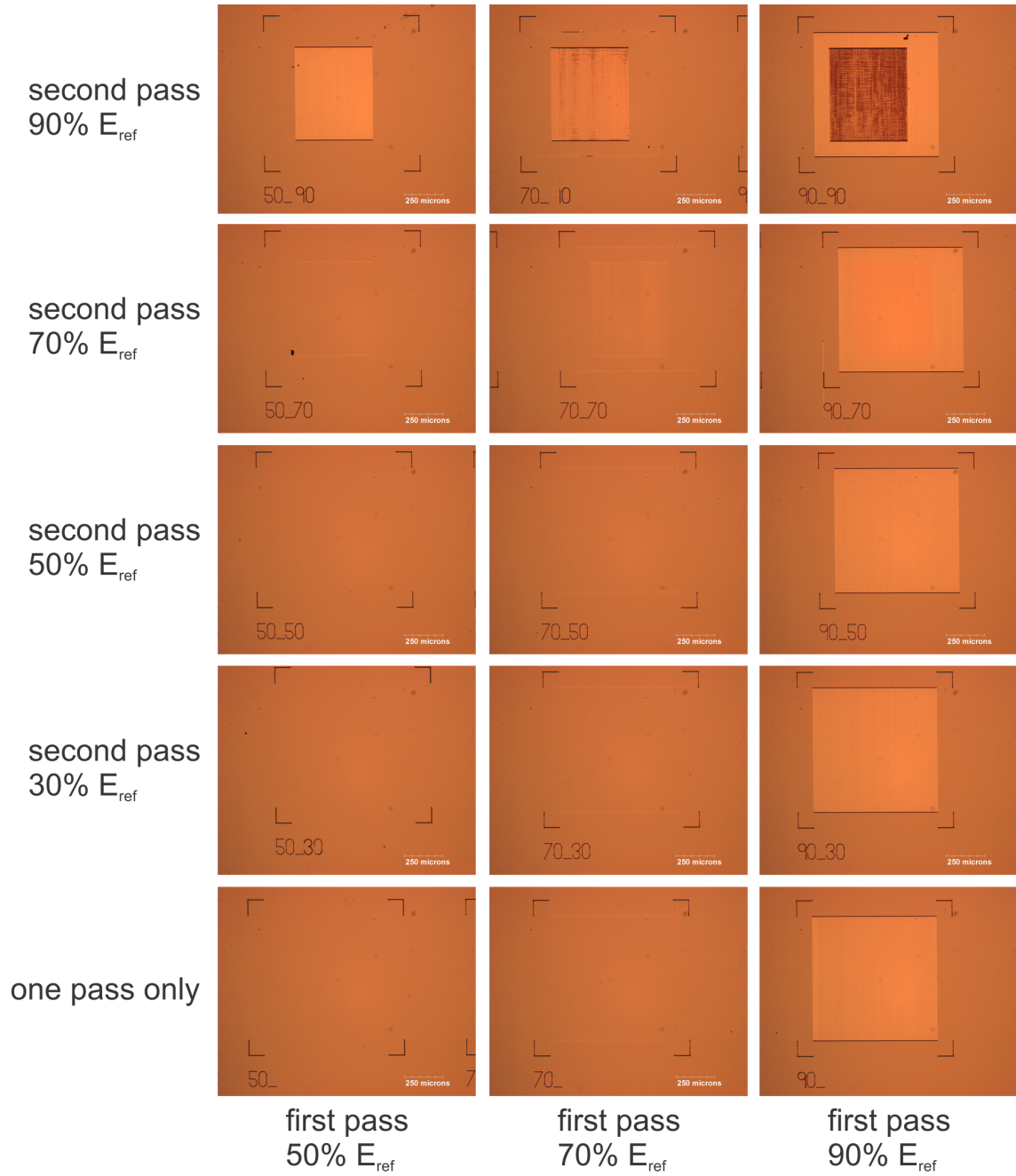
Figure 4.1: Overlapping large-area irradiation results at different levels of E_{ref}=48 nJ. The points of the corner markers (right angle brackets) mark 1×1 mm^2 areas. Sizes and positioning of the irradiated areas for the two passes are best represented in the 90%+90% E_{ref} region (top right, first pass: light shaded square; second pass: dark rectangle within). The electric field is horizontal relative to the figure orientation.
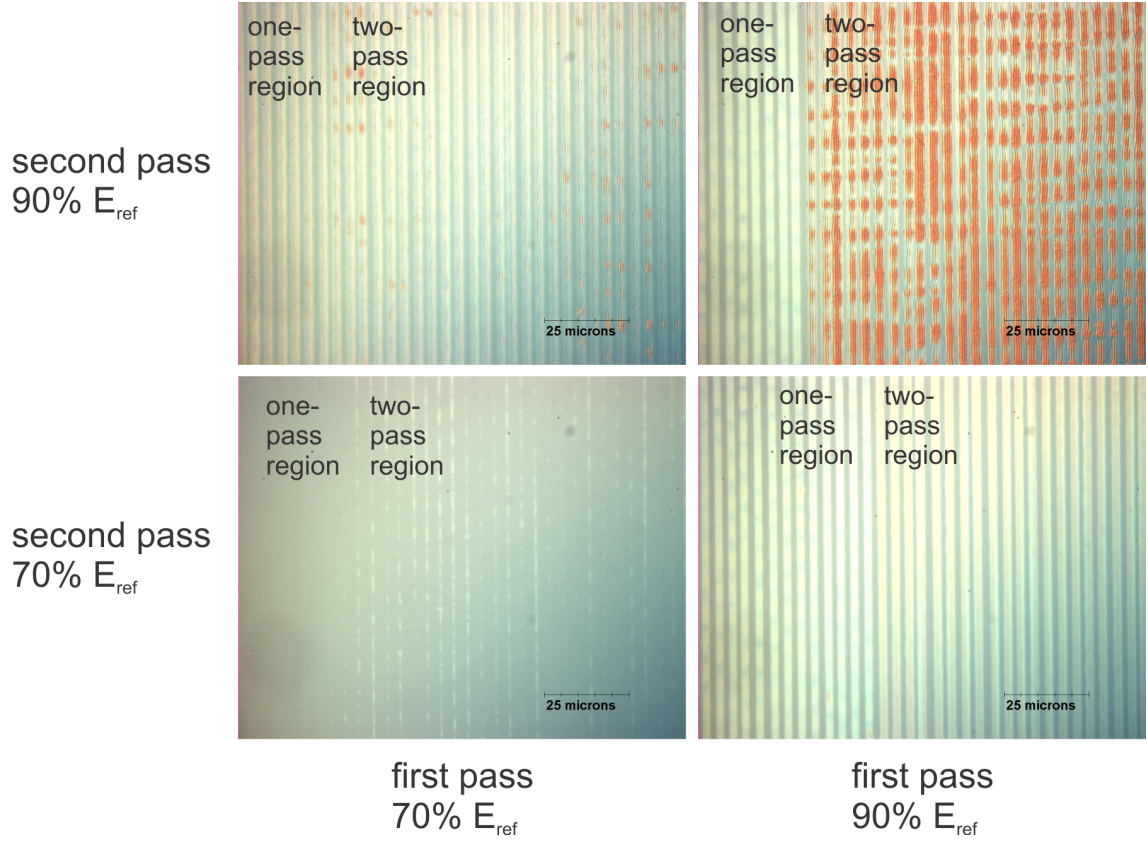
Figure 4.2: Higher magnification of overlapping large-area irradiation results at different levels of E_{ref}=48 nJ. Images were acquired using DIC-OM. E_{ref} was assigned as the energy where laser irradiation yielded darkened regions, indicating significant material removal (ripple structures). Images taken from the boundaries of single-pass and two-pass irradiation from the same irradiated target sites shown in Figure 4.1, as indicated. The electric field is horizontal relative to the figure orientation.
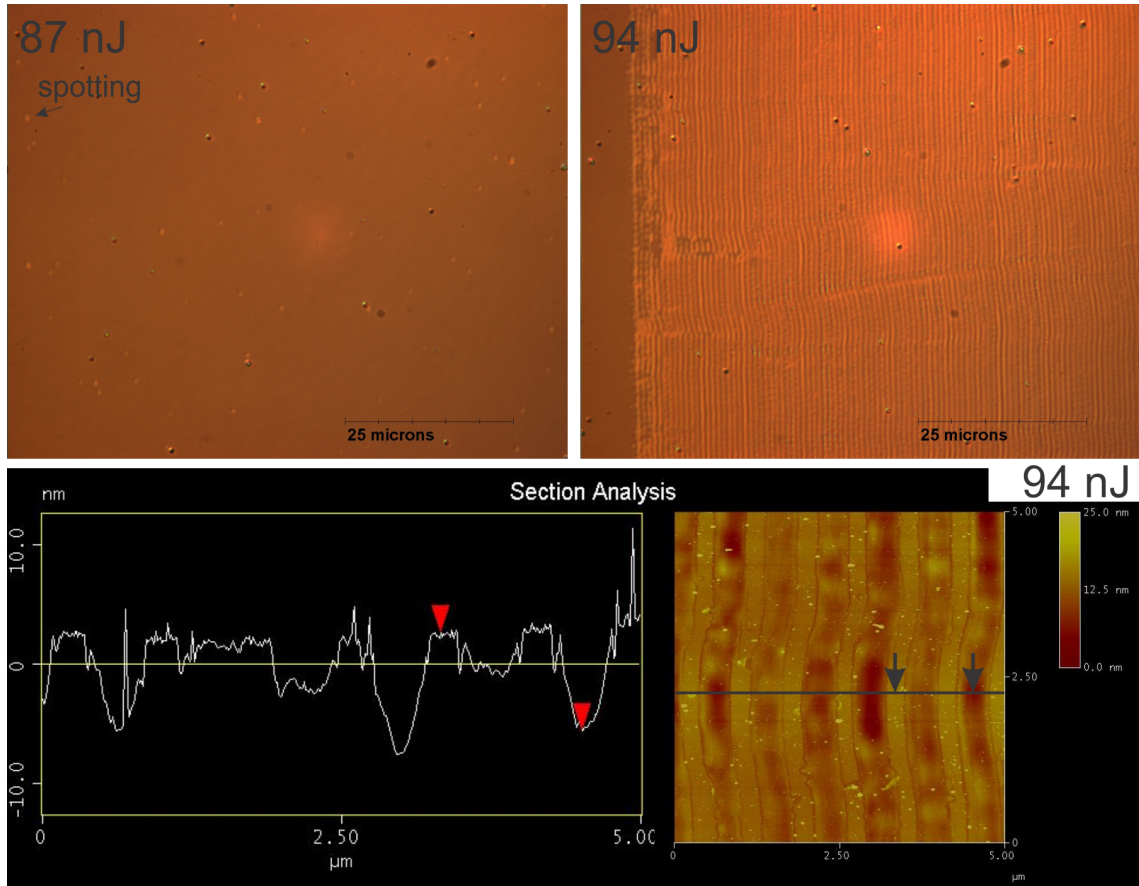
Figure 4.3: OM-DIC images and AFM results of sites irradiated with single-pass 1 μm pulse spacings at selected energies. Sporadic spotting was observed for irradiation carried out with 87 nJ pulses (top left, with an arrow pointing to an example), while irradiation with 94 nJ pulses generated rippling structures (top right). AFM results of the rippling structures showed the modulation depth of the ripples to be a few nanometers. The electric field is horizontal relative to the figure orientation. The spacing indicates LIPSS formation rather than grooves formed by each individual line scans of the laser beam.

4.4, 4.6 and 4.8 show the evolution of surface structures resulting from different numbers of passes irradiated at the same energy (Figure 4.4), as well as frame captures of video recordings at different stages of the multi-pass irradiation at selected energies (Figures 4.6 and 4.8).

A FIB-TEM specimen was prepared out for 20-pass irradiated region shown in Figure 4.4 to conduct a cross-sectional study of the different features, as well as crystallographic examination of near-surface regions. The overall morphology observed in DIC-OM and SEM, the cross-sectional profile obtained from FIB milling and a high resolution TEM micrograph are shown in Figure 4.9. Regions where LSFL formation (spatial period of ~700 nm oriented perpendicular to the incident electric field) did not occur showed subtle periodicities oriented primarily perpendicular to the LSFL structures (spatial period of ~400 nm), overlain with even finer periodic structures parallel to the LSFL (not resolved from current micrographs). Initial TEM characterization showed crystalline silicon in the bulk with a surface cap layer of a few tens of nanometers thickness composed of amorphous or polycrystalline silicon.

Detailed studies of the discoloration spots using scanning electron microscopy showed periodic surface patterns as shown in Figure 4.10. While the irradiation conditions are similar to Figure 4.9, the difference in the feature appearances is attributed to a small percentage difference in the power calibration between experiments, as it has been observed in this series of experiments that a subtle change in pulse energies can alter the overall outcome of the irradiated area. There are periodic substructures within the spotted region, with the ripples oriented primarily parallel to the incident electric field (horizontal relative to the images), and an approximate spatial period of 165 nm. A FIB-TEM specimen was obtained from such structures and showed an
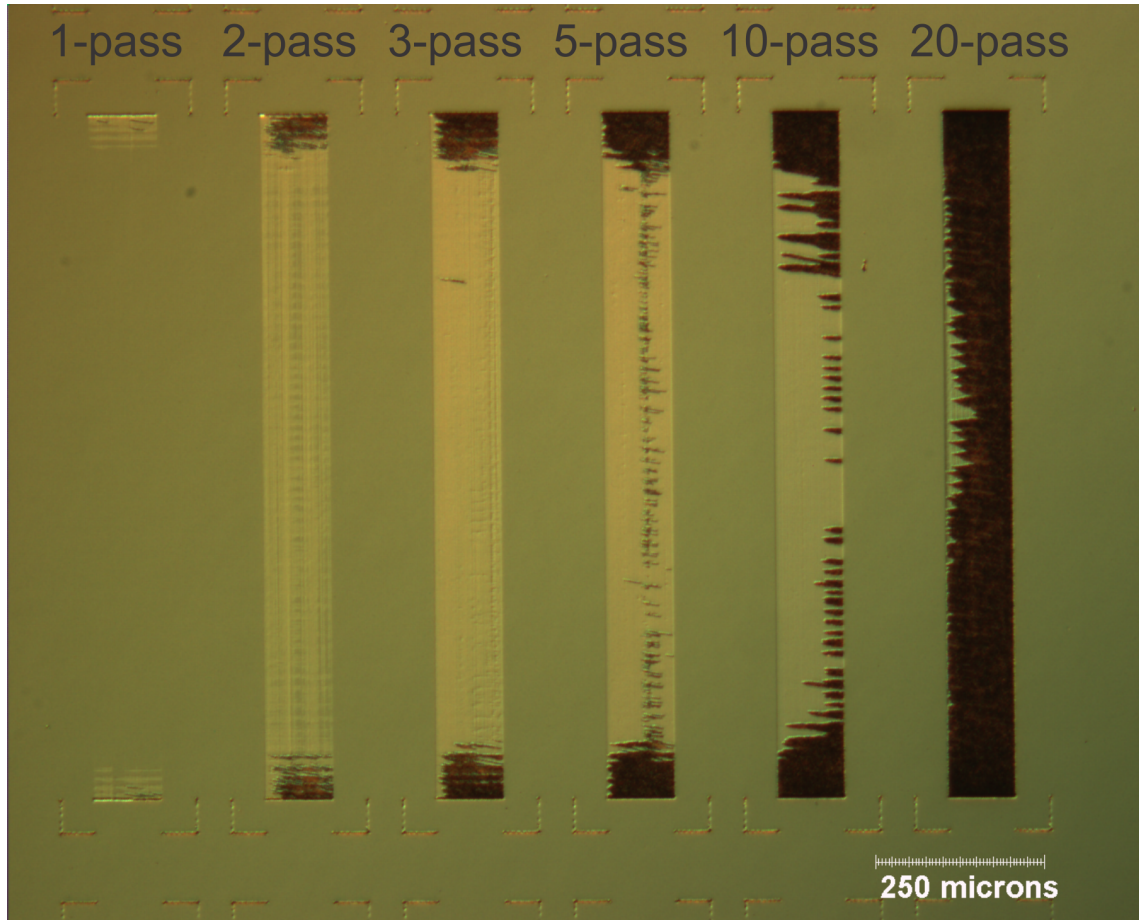
Figure 4.4: Areas irradiated with 1 μm pulse-to-pulse spacing with 42 nJ pulses at the indicated numbers of passes. Each pass starts at the lower left corner of the irradiated area, and consists of the laser beam line-scanned at alternating up-down directions (as viewed in the above image). The stronger modifications at the start and end of the line scans (top and bottom of the irradiated areas) are due to dwelling of the laser beam as the line-scan accelerates and decelerates. The electric field is horizontal relative to the figure orientation.
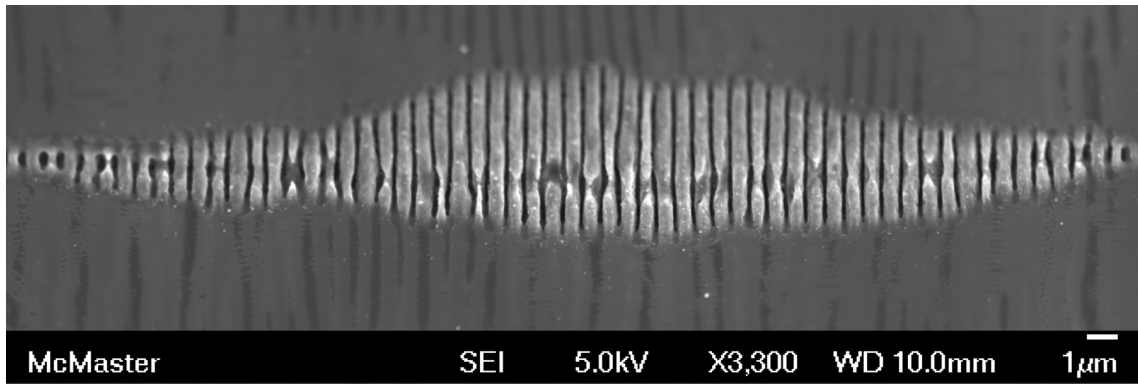
Figure 4.5: SEM image of structures evolved during a 60-pass areal irradiation with 32 nJ pulses with 1 μm spacing in the x- and y-directions. Irradiation was carried out such that the starting point of each pass begins at the alternating bottom left and right corners. Each pass consists of lines scanned at alternating up-down directions. An area of discolored structures evolved with increasing number of passes (lighter area in the frame-capture images, Figure 4.6). The ripple formation area (higher-contrast area in this image, and dark region in Figure 4.6) also expands with a increasing number of passes. SEM image shows the rippled area and surrounding surface morphology following 60 passes. The electric field is horizontal relative to the figure orientation.
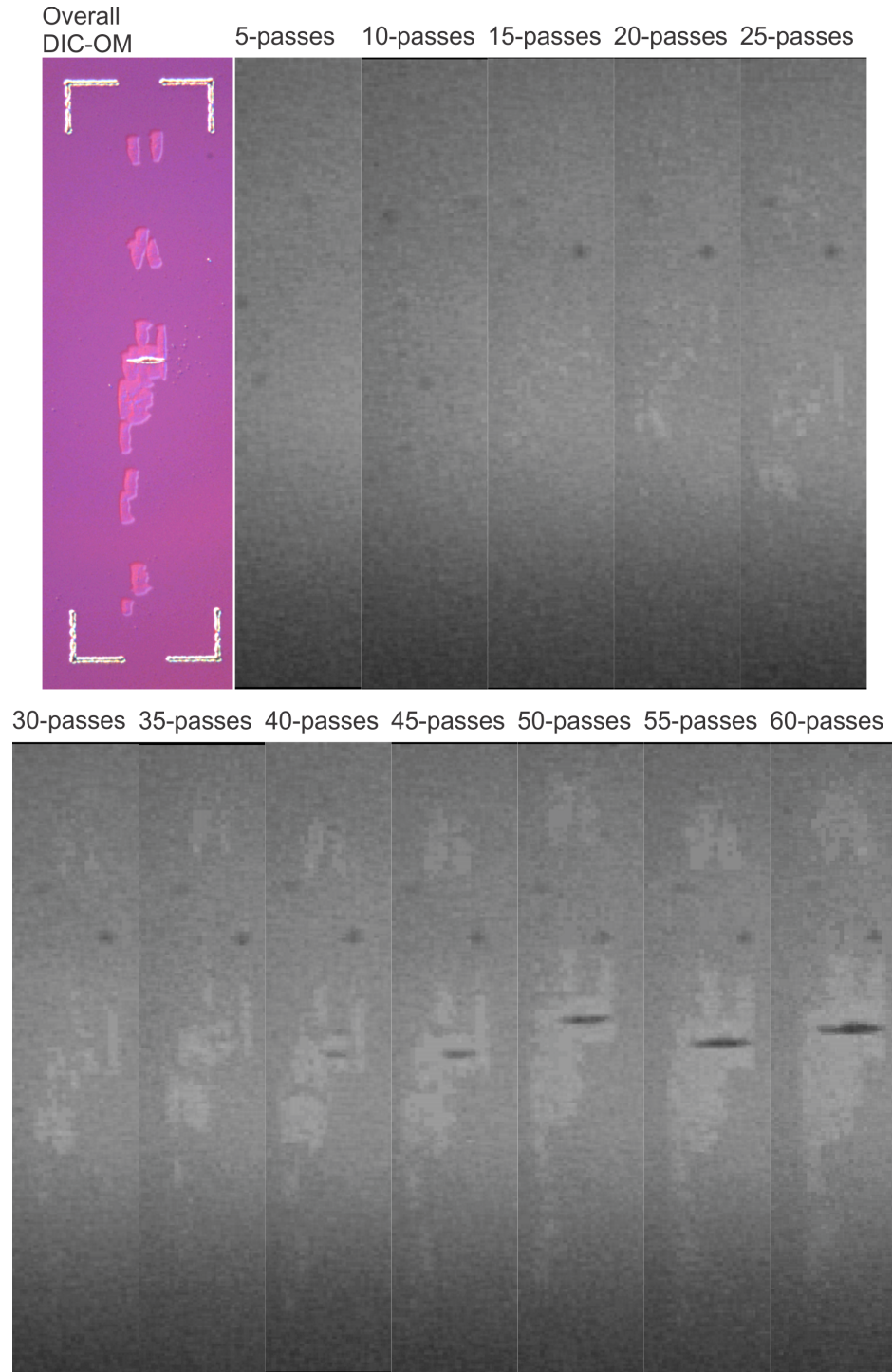
Figure 4.6: OM and video frame-capture images of structures evolved during a 60-pass areal irradiation with 32 nJ pulses. (From the same areal irradiation shown in Figure 4.5.) The electric field is horizontal relative to the figure orientation.
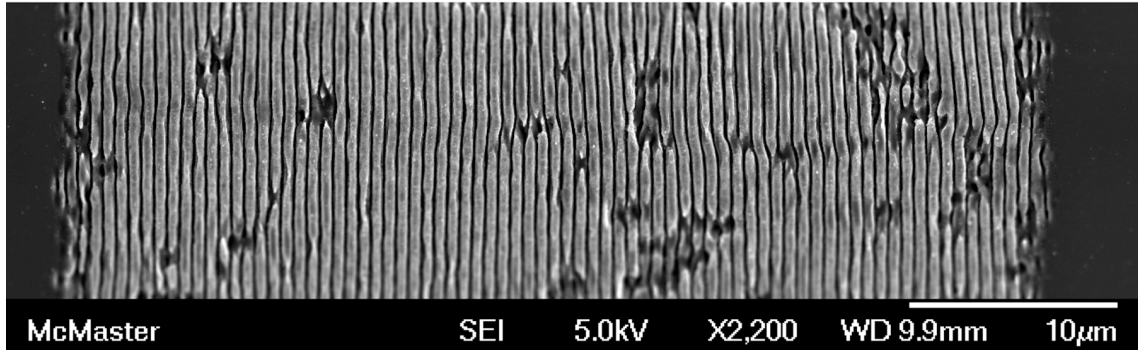
Figure 4.7: SEM image of structures evolved during a 60-pass areal irradiation with 34 nJ pulses with 1 μm spacing in the x- and y-directions. Irradiation was carried out such that the starting point of each pass begins at the alternating bottom left and right corners. Each pass consists of lines scanned at alternating up-down directions. Discolored area covered the irradiated region fully after 5 passes. Ripple formation area (dark lines in the frame-capture images, Figure 4.8) expands with increasing number of passes. SEM image shows the surface ripples following 60 passes. The electric field is horizontal relative to the figure orientation.

amorphous silicon cap layer throughout the FIB sample, suggesting crystallographic changes made to the irradiated area even in regions not exhibiting an observable morphological change using OM and SEM. In the TEM micrographs there are regions with subtle profilometric features, likely from the periodic surface patterns seen in the SEM. Figure 4.10 summarize OM, SEM and TEM observations of the surface features in these spots.

Large discoloration areas showed extended coverage of similar structures compared with the spot-like features, as well as honeycomb-like pattern that showed a coalescing tendency towards deeper ripple formation. Figure 4.11 shows the structural similarities of individual spots, co-joined spots, larger area features evolving into ripple-like patterns, and typically observed deeper ripple patterns (i.e., LSFL) at various irradiation conditions.
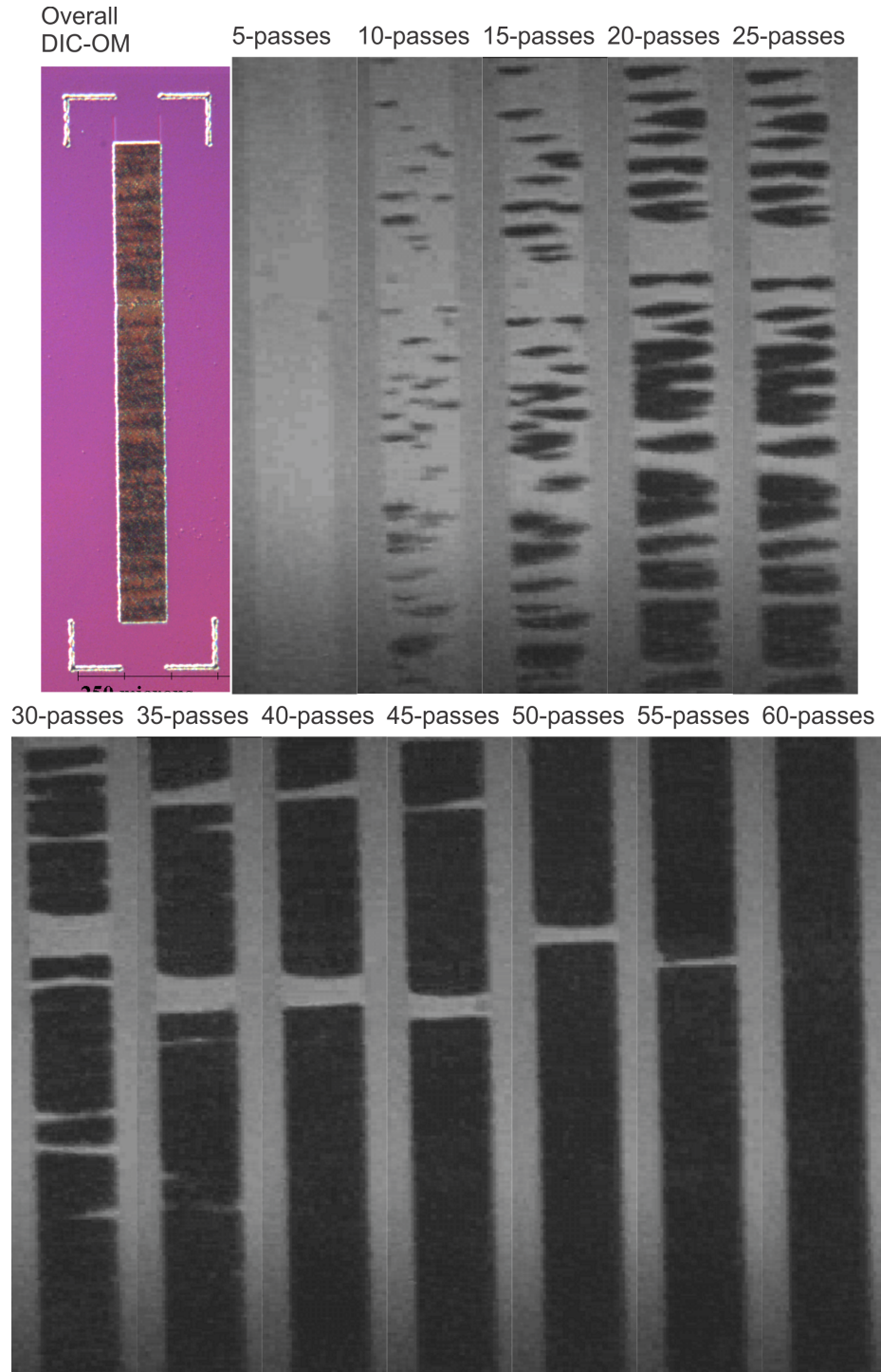
Figure 4.8: OM and video frame-capture images of structures evolved during a 60-pass areal irradiation with 34 nJ pulses. (From the same areal irradiation shown in Figure 4.7.) The electric field is horizontal relative to the figure orientation.
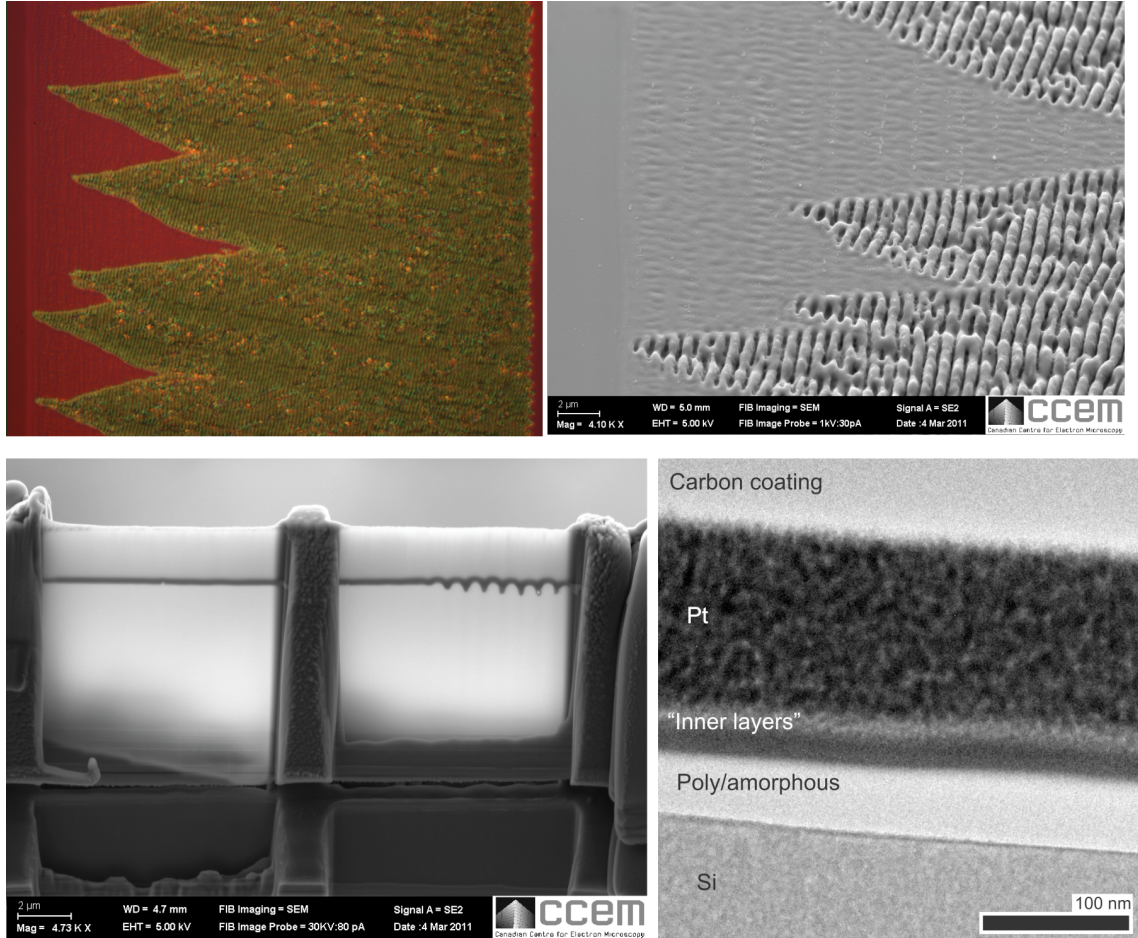
Figure 4.9: OM (top left) and SEM (top right) top views of ripple structures resulting from 20-pass areal irradiation with 42 nJ pulses having 1 μm pulse-to-pulse spacings, from the same area shown in Figure 4.4. Bottom left shows the SEM of the FIB-prepared cross-section sample. The middle part for the FIB specimen was not thinned in the FIB milling process to provide structural support. Bottom right shows a TEM micrograph of the structures, showing an amorphous or polysilicon cap layer over the surface of crystalline silicon bulk. Other layers on top of this cap layer are protective layers deposited as part of the FIB milling process. The electric field is horizontal relative to the figure orientation.
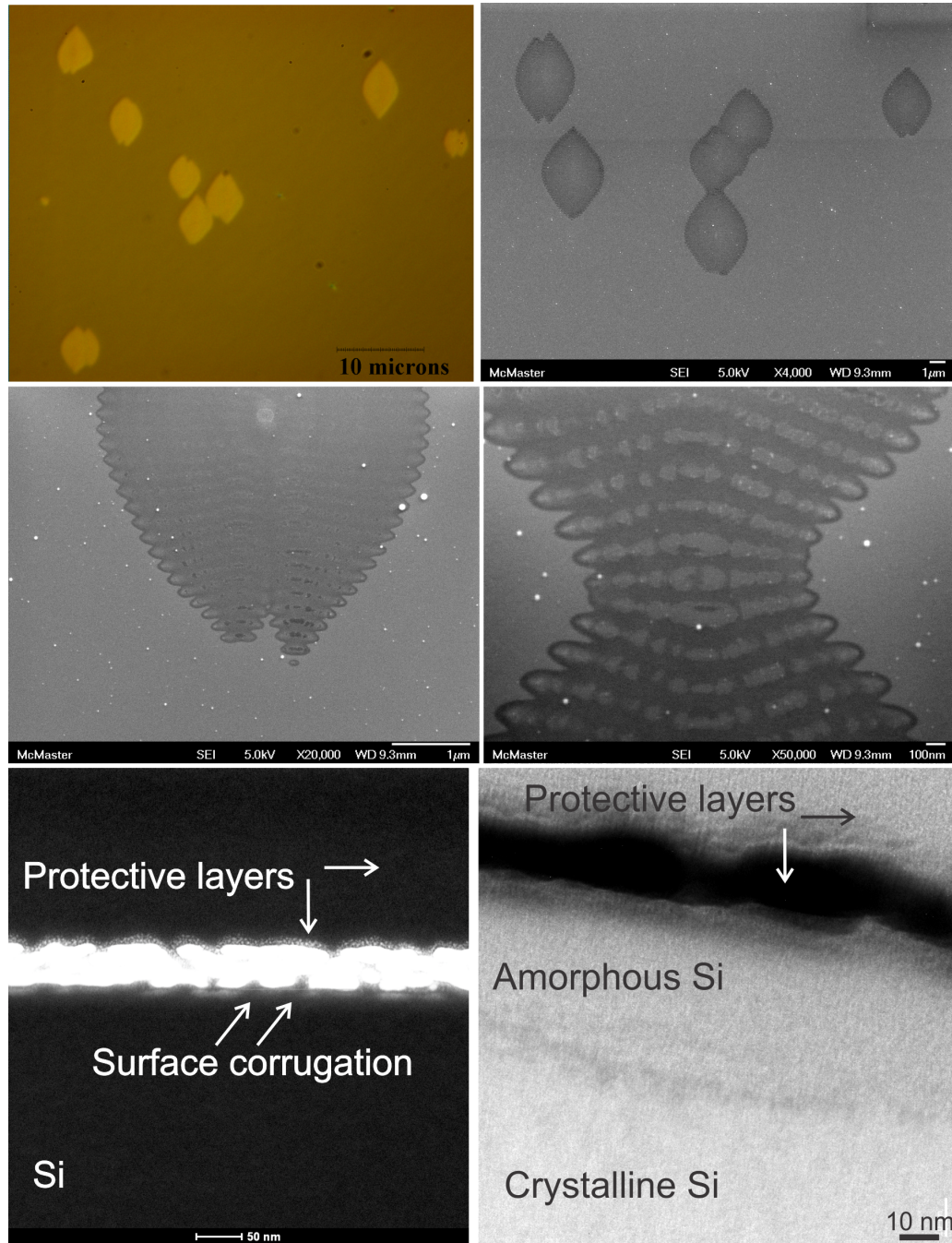
Figure 4.10: OM (top left), SEM and cross-sectional TEM images (bottom two) of 20-pass irradiation with 43 nJ pulses with 1 μm pulse-to-pulse spacings. Sub-structures are observed using SEM in similar discolored spots seen in the OM. Cross-sectional TEM images from such structures showed subtle surface corrugation that are likely related to the periodic sub-structures, and an amorphous cap layer over the irradiated region. The electric field is horizontal relative to the SEM and OM images orientation.
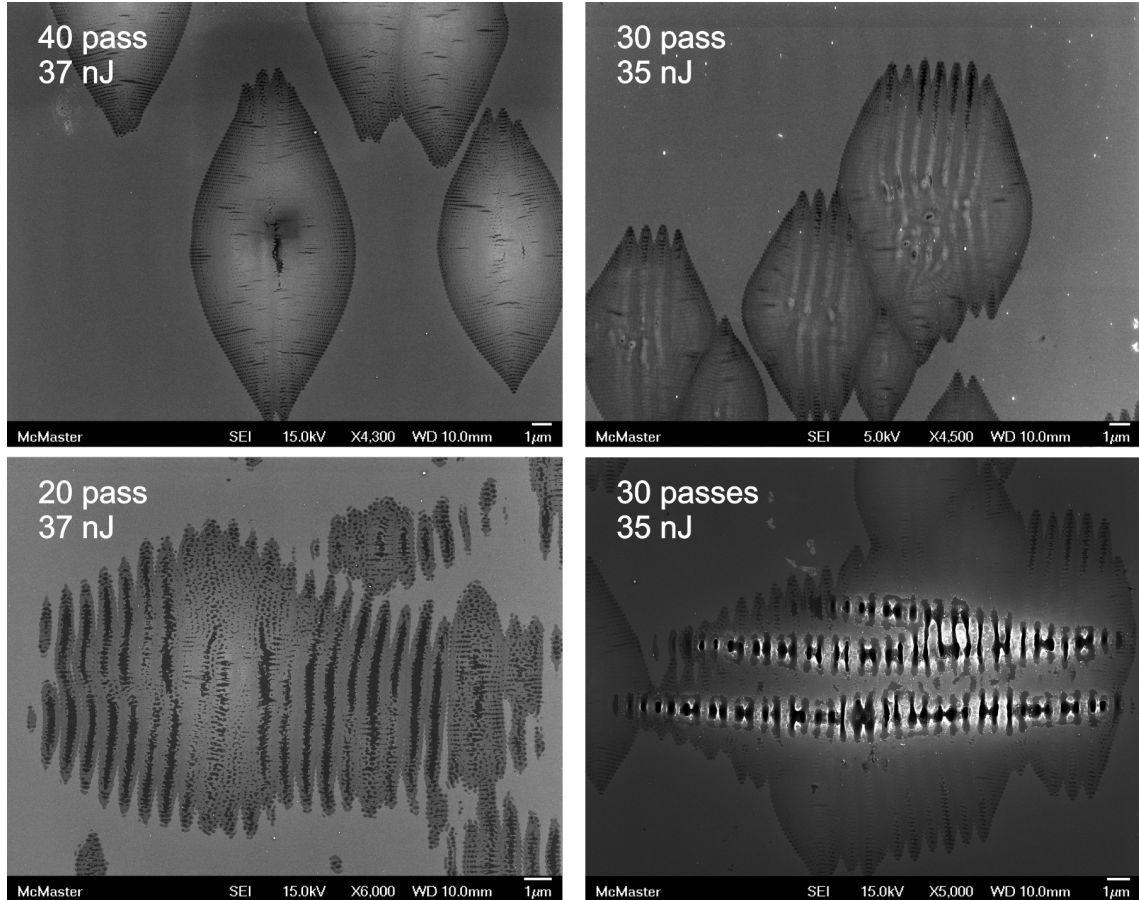
Figure 4.11: Selected regions irradiated with indicated conditions using a 1 μm spacing in both x- and y-directions, showing the qualitative surface morphology of the discrete spots (top left), co-joined spots (top right), larger area coverage, and the possible link to LSFL formation (bottom two). For the bottom right inset, the higher-contrast ripples indicate more significant depth of material removal, and this type of region would typically appear black in low magnification OM. On the contrary, the surrounding region with more subtle contrast in the periodic structures would appear as lighter discolored region in a low magnification OM. The electric field is horizontal relative to the figure orientation.
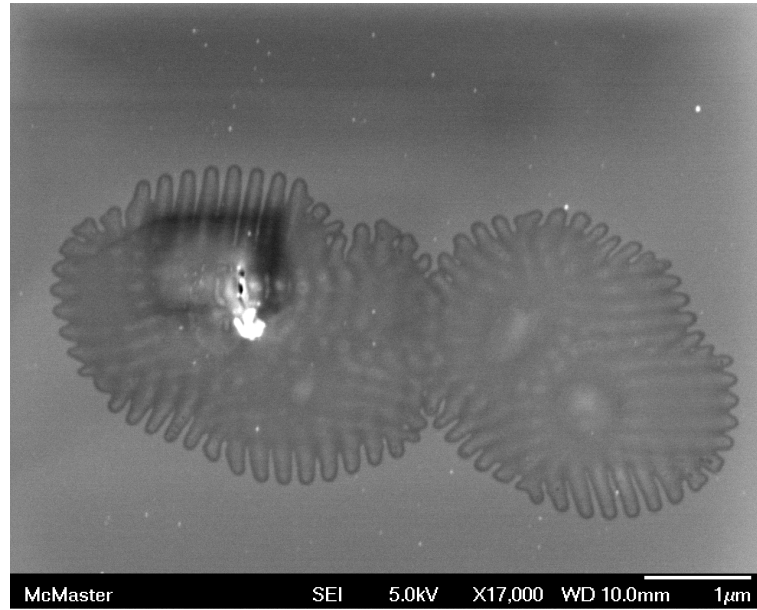
Figure 4.12: Another type of substructure generated in 30-pass areal irradiation using 32 nJ pulses. Irradiations are otherwise identical to those employed in Figure 4.11. Note observations of this type of substructure were not limited to this irradiation condition. The electric field is horizontal relative to the figure orientation.

Another type of pseudo-periodic features observed in the discolored spots occasions consists of larger periodic structures oriented somewhat radially in the spots, as shown in Figure 4.12. The approximate spatial period for this type of structure is 200 nm. Observations of this type of substructures are somewhat scarce, and no clear indication of laser irradiation parameters leading to the generation of this type of structures could be pinpointed.

Figure 4.13 summarizes the type of surface features at different combinations of the laser parameters. The fluence value indicates the lowest fluence where a given structure can be observed at a particular N_{eff}. The N_{eff} per pass is estimated to be 35, using the based on the accumulated fluence as described in Section 2.3.4 (technique adapted from [113]). The summary is for irradiation with 1, 2, 3, 5, 10, 20, 30, and

40 passes from a specific set of experiments to provide an example.

Table 4.1 summarizes the periodicities observed in different periodic sub-structures, as well as example figures.

Table 4.1: Ripple periodicities observed for different surface features at near-threshold conditions. The "Orientation" column indicates the ripple orientation relative to the incident electric field. Irradiation condition shows the relative fluence required to generate the specific feature type. The column Λ indicates the regime of period found in the observed feature. The "Figures" column points to examples of microscopy image(s) for each feature.

Feature	Orientation	Relative fluence	Λ (nm)	Figures
Spots	$\sim\parallel \vec{E}$	Lowest	~165	4.10, 4.11
Spots	Radial	Moderate	~200	4.12
Discoloration	$\parallel \vec{E}$	Moderate high	~400	4.9
Subtle-ripples	$\perp \vec{E}$	Moderate high	~765	4.5, 4.11
Ripples	$\perp \vec{E}$	Highest	$\sim575\text{-}700$	4.7, 4.8, 4.9, 4.11

In terms of ripple formation, the evolution of surface structures from discolored spots with periodic sub-features to larger areas patterns and ripples with further processing (either higher fluence or more numbers of passes) may provide valuable insights into the origin of ripple formation. The fact that crystallography studies carried out with high resolution TEM did not show a significant difference in the regions with and without periodic sub-structures likely suggest melting and refreezing was not significant in ripple formation, and might suggest optical energy distribution and feedback mechanisms in the formation of ripples. The sub-structures observed in the discolored spots that are oriented primarily perpendicularly to the incident electric field point to a likelihood of an optical phenomenon. Meanwhile, the radial sub-structures observed in some discolored spots may point to an optical scattering or absorbing center from surface debris or defects. The sporadic locations of the onset
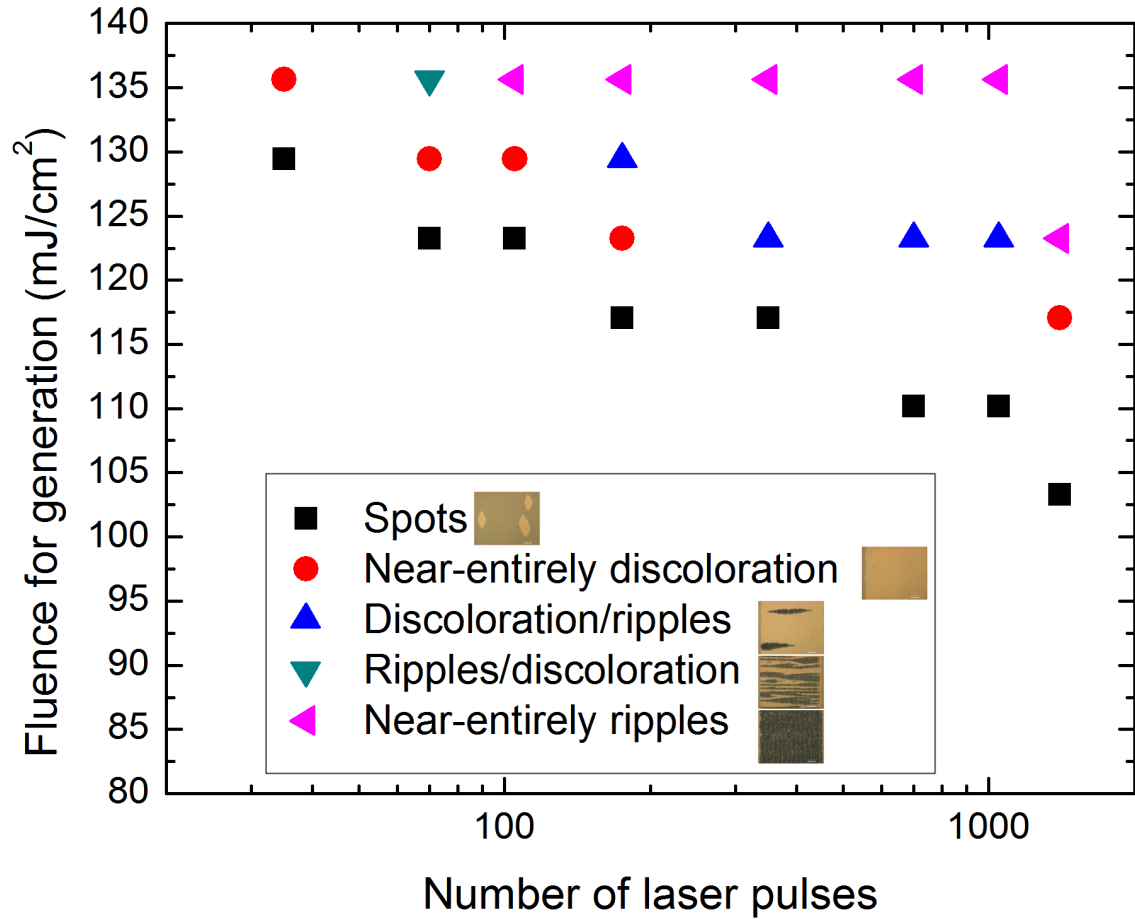
Figure 4.13: Observed surface features as a function of laser parameters. The fluence value indicates the lowest fluence where a given structure can be observed at a particular N_{eff}. The estimated N_{eff} per pass is estimated to be 35, and the summary is for irradiation with 1, 2, 3, 5, 10, 20, 30, and 40 passes. "Spots" indicates observations of discolored spots, "near-entirely discoloration" indicates a near-complete coverage of discolored material, "discoloration/ripples" indicate a mix of discolored material and ripples with majority of the area being discolored material, "ripples/discoloration" describes similar material with the reversed coverage ratio, and "near-entirely ripples" indicate near-complete ripple coverage of the irradiated regions. Insets of OM examples for each classification are provided in the legend, where the width of each OM image is roughly 50 μm. The electric field is horizontal relative to the figure orientation.

of these discolored spots may speak for a combination of surface conditions and the fluctuation of the pulse-to-pulse laser energy. Once subtle surface modifications occur, absorption is likely enhanced locally, leading to the observed "growth" and coalescence of the discolored spots with repeated irradiation, and finally more significant material removal leading to the observations of deeper ripples. Overall the observed LSFL have the tendency to be more regular (in terms of straightness, discontinuities and bifurcations) than, for example, irradiation at higher fluences in stationary targeting (e.g., compared with the room temperature irradiation cases in Chapter 5). In fact, in this regard the surface morphology more closely resembles another type of ripples that are substantially below the irradiation wavelength than LSFL appearance, as further introduced in Section 5.2. This is likely be due to the relatively near-threshold conditions used in this series of experiments, leading to gentler ablation in terms of hydrodynamics of the material removal events.

4.3 Conclusions and future work

The results from this work provided insights into the incubation mechanisms as well as the formation mechanisms of laser induced surface ripples.

In terms of incubation effect, large-area irradiation with two repeated coverage of the areas, i.e., two "passes", showed that the different energy combinations used for each pass can result in different outcome, despite the same total cumulative energy following the two passes (e.g., 70%+90% E_{ref} compared to 90%+70% E_{ref}). This points to the likelihood of different energy deposition or damage accumulation depths when the incident laser energy is changed. Future studies can incorporate simulations into defect characterization techniques, such as positron annihilation spectroscopy

studies (see Section 3.3), and Hall effect studies, to provide further information into the damage accumulative behavior in solving the origin of incubation effect.

Observations of subtle surface features with repeated low-energy irradiation such as discolored spots with periodic sub-structures are shown to expand in areal coverage. The primary type of sub-structure observed in these discolored spots are periodic structures oriented primarily parallel to the incident electric field and having a spatial periodicity of ∼165 nm. Another type of sub-structures observed are oriented radially in these spots and have an approximate spacing of ∼200 nm. With adequate repeated irradiation over the same area or adequate pulse energies these structures can form subtle ripple patterns with comparable periodicity to LSFL. Future work can include the study of surface profile and depth of these structures to aid the determination of the formation mechanisms. Finally with further irradiation the formation of deeper periodic structures with true LSFL periodicities were observed. It is important to point out, however, that these LSFL seem to have a high aspect ratio in these early observations, and resemble appearance more typical of HSFL (e.g., [47]). This is in contrast to typical LSFL appearance in silicon with similar irradiation conditions, where the ripples appear with more irregularities, bifurcations, and evidence of melting (e.g., [158]). A report on HSFL formation in silicon with high repetition rate (82 MHz) ultrashort-pulse irradiation showed qualitatively similar regularities in ripples observed in this thesis [57], suggesting that highly repetitive, relatively gentle irradiation is likely to form ripples with less irregularities. This is consistent with the theoretical prediction that a melt phase is necessary in ultrashort-pulse ablation of silicon [10], and the use of higher fluence pulses encourages the redeposition of the melted material [138]. Crystallographic investigations in

cross-sectional FIB-TEM studies showed similar crystallographic structures for areas with and without the formation of the spots and substructures, suggesting similar ablation and cooling dynamics in the regions, and the modulation may arise from optical effects or feedback once subtle structures began to form. Future work can include detailed crystallographic studies to relate different types of surface structures and sub-structures to help elucidate the formation of ultrafast laser induced surface structures. The linkage between the formation of LSFL in repeated irradiation of regions with fine sub-structure formation should also be tested.

Chapter 5

Ultrafast laser induced ripples in silicon at elevated temperatures

A supplemental finding from carrying out ultrafast laser irradiation of silicon at elevated temperatures was the evolution of different laser-induced periodic surface structures as a function of temperature. Ripple formation observed at elevated temperatures is qualitatively different those those typically obtained in room temperature as discussed in Section 2.1.5. This section of the thesis presents the morphological and crystallographic studies of ripples formed under ultrafast laser irradiation at different sample temperatures.

5.1   Experimental procedures

The laser irradiation configurations and conditions were identical to the high-temperature experiment series reported in Section 3.2.1. Following the laser irradiation, analysis of

the surface morphologies were carried out using an optical microscopy (OM) with differential interference contrast (DIC) technique, scanning electron microscopy (SEM), as well as focused ion beam (FIB) preparation of cross-sectional specimen for transmission electron microscopy (TEM) studies. The length scale calibrations of each microscopy technique were checked from time to time by comparing measurements made from the same site to ensure each calibration was correct (e.g., within a couple percent for well calibrated instruments). A subset of the irradiation conditions most representative of the laser induced period surface structures (LIPSS) evolution were studied in detail for each temperature (pulse energy ranging from ∼310 nJ to ∼870 nJ, and number of laser pulses N=1, 1, 2, 3, 5, 10, 50 and 100).

5.2   Results and Discussions

Regular ripples (low spatial frequency LIPSS, or LSFL) observed at room temperature appeared rough, with discontinuity boundaries oriented somewhat parallel to the incident laser electric field. At low energies these discontinuity boundaries have the tendency to be oriented at small alternating angles (e.g., somewhat of a zigzag pattern) relative to the laser electric field. Examples of such boundaries at room temperature are shown in Figure 5.1 at N=3 and Figure 5.2 at N=10. At regions irradiated with higher local fluence, formation of flatter (relative to LSFL) disordered features tend to be favored (e.g., Figure 5.1, room temperature, N=10, 50 and 100). At intermediate fluence regions, larger fragmented structures are formed. These structures are on the order of 1-2 μm in size, and have a somewhat subtle tendency to be oriented parallel to the incident electric field (e.g., Figures 5.1 and 5.2, room temperature, N=50 and 100). There is a general tendency for the ripple periodicity Λ
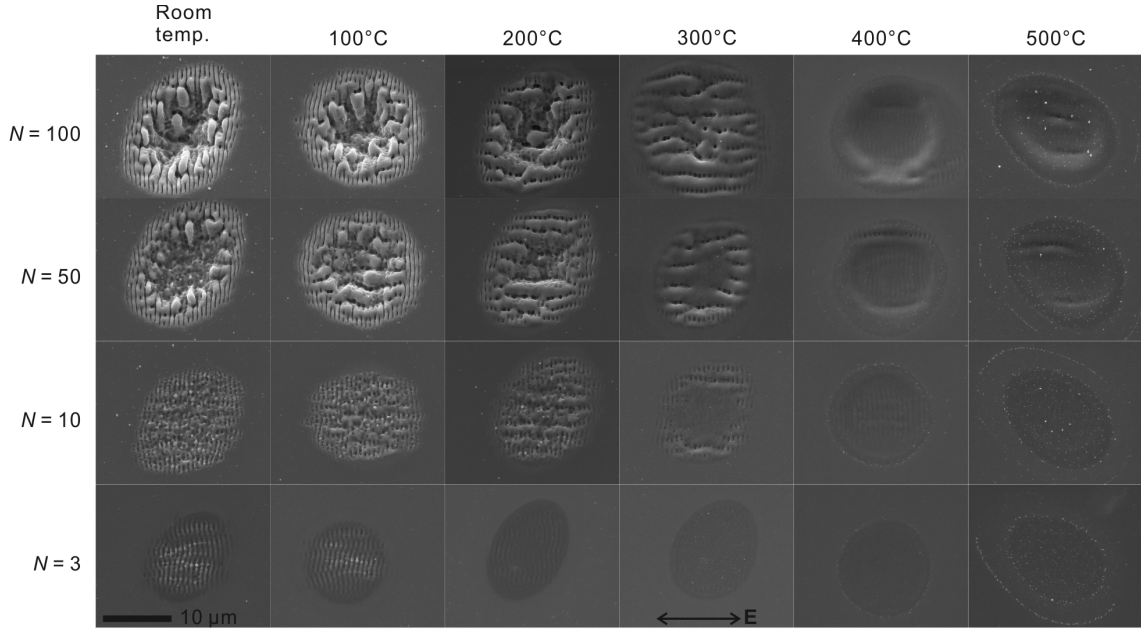
Figure 5.1: SEM top view images of sites irradiated with ∼865 nJ pulses at the indicated numbers of shots N and temperatures, summarizing the evolution of surface morphologies.

to decrease with increasing number of laser pulses and decreasing laser pulse energy. At higher energies and low numbers of shots, the observed LSFL periodicity is as high as ∼735 nm, and with increasing number of shots and/or decreasing energy, the periodicity decreased towards a lower limit in the range of 655-675 nm. The obtained LSFL periodicities are in agreement with the typical range 0.62-1.00 of the irradiation wavelength, depending on the combination of fluence and number of laser pulses, as summarized in the literature (e.g., [24, 49, 60, 159]). Figure 5.3 summarizes the ripple periodicity trends for different combinations of laser shot number and pulse energies at room temperature.
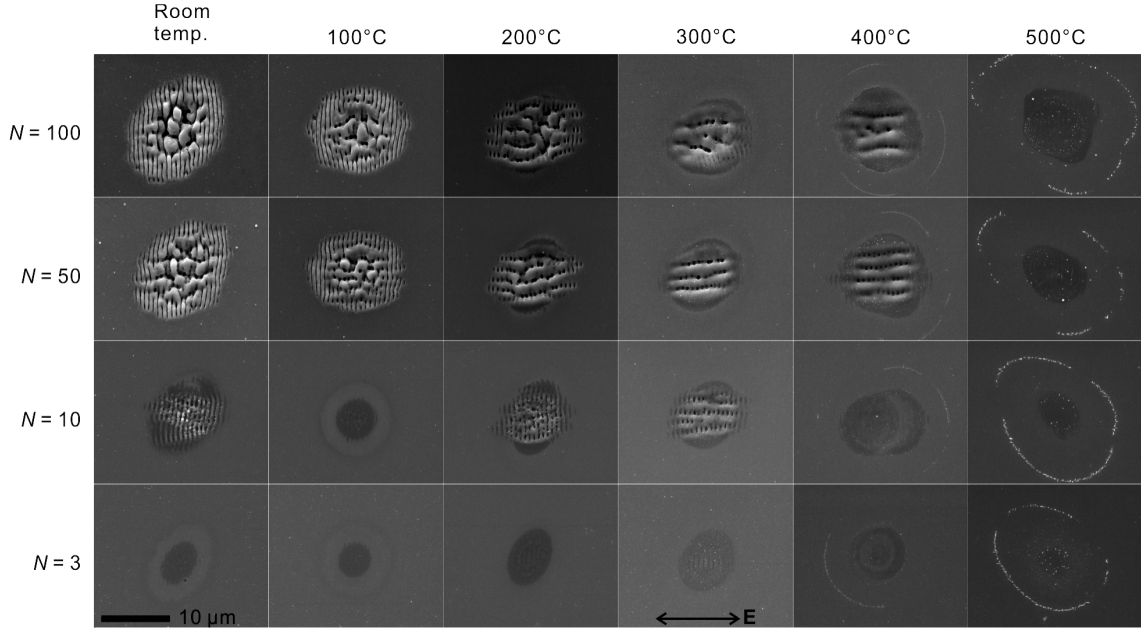
Figure 5.2: Topical SEM images of sites irradiated with ~505 nJ pulses at indicated numbers of shots N and temperatures, summarizing the evolution of surface morphologies.
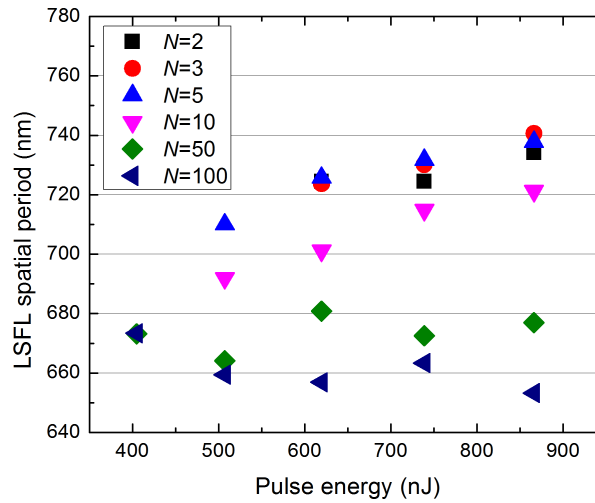
Figure 5.3: LSFL periodicity at various combinations of pulse energies and numbers of laser pulses employed at room temperature.

At near-threshold conditions, often discolored structures are observed at a somewhat flat surface, suggesting subtle material modifications without significant removal. At times ripple patterns with a periodicity at roughly half of the incident laser irradiation wavelength can observed at near-threshold conditions ($\Lambda \approx$530 nm), as well as fine ripples with spatial periods substantially below the laser irradiation wavelength (on the order of $\sim$205 nm, in the regime of ripples typically classified as high spatial frequency LIPSS, or HSFL), with both types oriented parallel to the laser electric field. Small sporadic spots can also be observed at the low local fluence regions of sites irradiated with low energies, and these spots have the tendency to coalesce into the regular LSFL-like patterns, much like observations made with repeated irradiation with a scanning beam (Section 4). Examples of the near-threshold ripples are presented in Figure 5.4. Follow up work showed that these features can be formed over larger areas under translational irradiation.

As the sample temperature increased, the propensity for LIPSS formation decreased. At low numbers of shots where shallow LIPSS formations can be observed at room temperature, smooth craters were observed instead at higher temperatures under SEM observations. The morphology of the LIPSS also appeared to be smooth relative to structures observed at room temperatures. The periodicity of the ripples relative to the number of laser pulses employed and laser pulse energy tend not to show an obvious trend at higher temperatures, as the morphology changed, and the periodicity measurements were somewhat statistical in nature. The fragmented structures at room temperature have to tendency to form continuous structures instead, and with similar laser irradiation conditions at 300-400°C, continuous above-wavelength ripples oriented parallel to the incident laser electric field were observed with a spatial
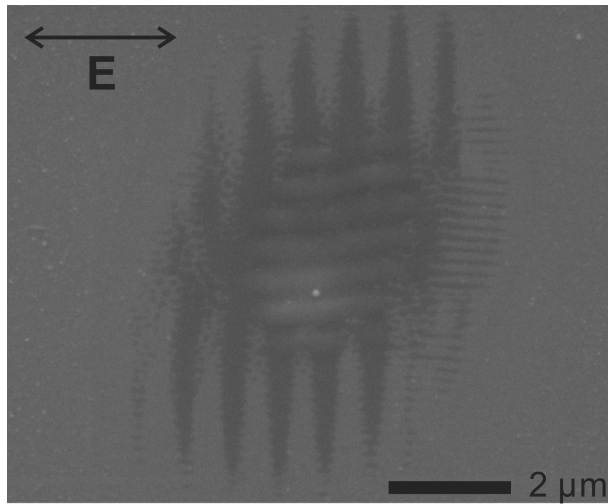
Figure 5.4: SEM image of near-threshold irradiation results with 100 near threshold (312 nJ) pulses at room temperature. Observed here are ripple patterns oriented perpendicular to the incident laser electric field with an average periodicity of ∼700 nm, close to that of LSFL, as well as ripple patterns oriented parallel to the incident laser electric field on the order of half of the laser wavelength at ∼530 nm and substantially smaller than the laser wavelength at ∼205 nm. Also observed are spots at low-fluence regions that typically show a tendency to coalesce into ripple patterns.

period of ∼2200 nm. These ultra-low spatial frequency LIPSS (ULSFL) appear to be overlain continuously on LSFL. The observations of structures that show a qualitative resemblance to this type of ULSFL are reported in the literature for room temperature irradiations (e.g., [53, 160]), but it is not as commonly reported as LSFL. At 500°C LIPSS formation in general became very subtle, and smooth craters are mostly observed with sporadic ripples formation at small areas and faint ripple patterns showing up as a discoloration. A previous experiment conducted with the sample surface at 600°C using a copper stage with no barrier material showed primarily smooth craters with relative shallow features showing a LIPSS periodicity.

Cross-sectional TEM of ULSFL generated with fifty 560 nJ pulses at 400°C was conducted on a FIB-prepared specimen. A topical SEM view and cross-sectional TEM micrograph of this site are presented in Figure 5.5. In the TEM micrograph residual strain in the crystal can be seen as the banding.

High resolution TEM images from the same specimen at near-surface regions suggested that in most of the regions where ULSFL formed, crystalline silicon extends all the way to the very surface of the sample (Figure 5.6). At the periphery of the crater where the resulting surface morphology is relatively smooth (Figure 5.7), and at very few local regions in the ULSFL formation, a thin amorphous layer (<10 nm) is observed. While observations of a thin amorphous layer are generally made following ultrafast laser ablations (at room temperature), the typical thickness of the amorphous layer tend to be on the order of tens of nanometers.

The diminishing tendency of LIPSS to form may be considered consistent with the reported reduction of surface roughness following ultrafast laser ablation of materials at elevated temperatures reported in the literature [129, 130]. As the initial sample
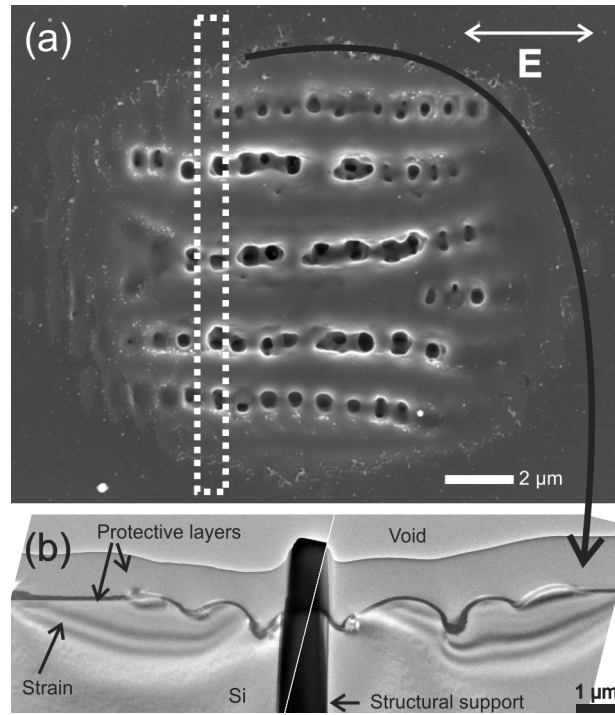
Figure 5.5: (a) SEM top view and (b) cross-sectional TEM view of ULSFL generated with fifty 560 nJ pulses at 400°C. The images are oriented such that the top of the SEM view in (a) corresponds to the right side of the TEM cross-section in (b). The dark column in the center of the TEM specimen is material that was not thinned down during the FIB milling process to provide structural support to the lamina thus preventing the sample from buckling. Also shown the TEM micrograph are banding resulting from residual crystallographic strain, and protective layers that are deposited during the FIB milling process.
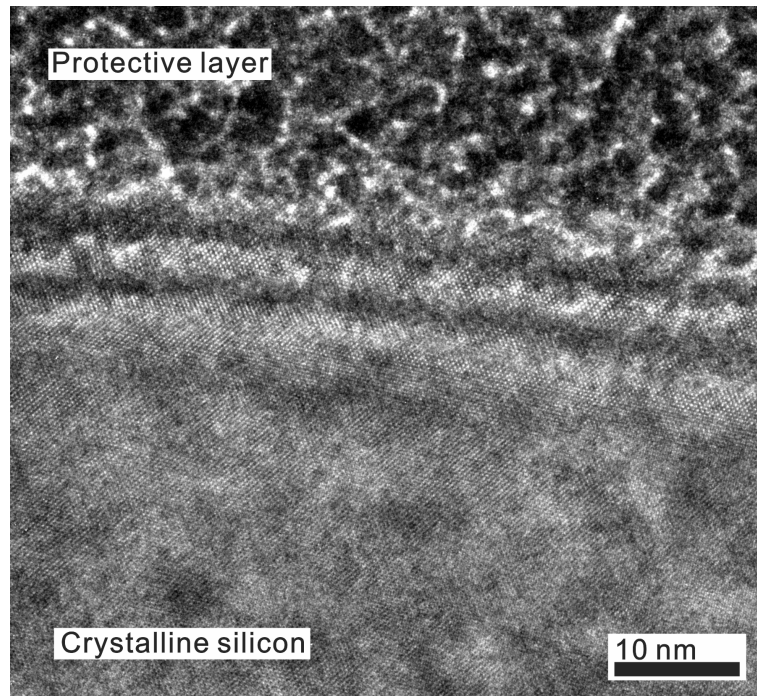
Figure 5.6: High resolution TEM micrograph of the ULSFL region generated at 400°C, from the same TEM specimen presented in Figure 5.5, showing crystalline silicon extending continuously to the sample surface. The banding at the very top surface region is attributed to the contouring of the surface into the depth of the TEM specimen.
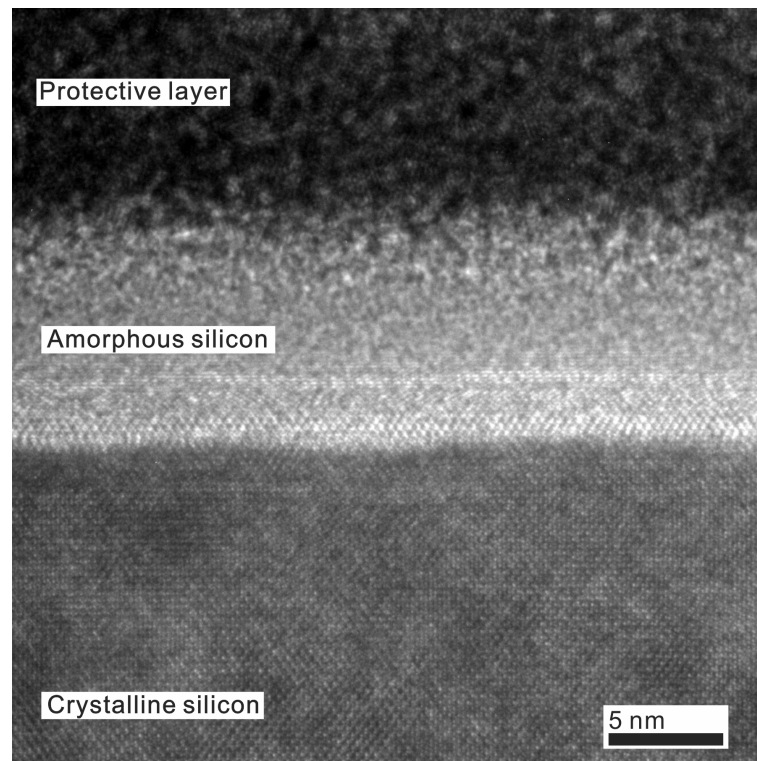
Figure 5.7: High resolution TEM micrograph of the periphery region of the crater from the same TEM specimen presented in Figure 5.5 (irradiated at 400°C), showing a thin amorphous silicon cap layer.

temperature is increased, the temperature differential required to generate material removal is decreased (i.e., relative to melting, evaporation and ablation temperatures), and presumably a somewhat different ablation process may be obtained. Similarly, the temperature gradient between the laser target region and the surrounding bulk material (as well as the final temperature the material would reach following cooling of the target site) is reduced with a higher sample temperature, likely altering the hydrodynamics of the affected material due to the laser energy deposition. The lack of a thin amorphous cap layer in the central region of the crater in the TEM studies was unlike typical observations of material surface following ultrafast laser ablation at room temperature, where an amorphous cap layer has been observed from ultrafast irradiation of materials [47, 48, 110, 111, 136, 143, 153, 158, 161–165]. This may be due to a combination at least two factors: It has been reported in the literature that recrystallization of silicon into poly-crystalline can occur in the center regions of ablation craters, during the refreezing of the material following laser melting, when the incident peak laser fluence is adequately high (∼12% above the single-shot ablation threshold) [110]. Also, the slower cooling rate due to the high substrate and ambient temperature may promote further recrystallization of the melted material. The solid phase epitaxial regrowth rate is small at 400°C, as shown in Figure 3.6 based on [122] (on the order of ∼0.01 nm/s, refer to Section 3.2.2 for discussions on the applicability of the estimate to low temperatures). This epitaxial regrowth rate may account for the recovery of a thin amorphous layer during the course of the experiment where the sample surface is held at the temperature set point (about 20 minutes, not considering the ∼30°C/min ramp up time, or the cooling time following laser irradiation). However, even as a simple estimation, this expected epitaxial regrowth rate would

not account for the observed single-crystalline structure continuous from the bulk at the cores of the ULSFL, which see a depth modulation on the order of a micrometer. The continuous crystallographic structure speaks against the likelihood of their formation arising from mechanisms that are observed in a melted material, such as capillary or acoustic waves, since even in a recrystallized material from a melt, full recovery of the crystallinity is not expected. The above wavelength periodicity is atypical of ripples generally observed. Classical theory of ripple formation (e.g., [40]) excluded the formation of above-wavelength ripples. However, in recent theoretical works based on finite-difference time-domain calculations of inhomogeneous energy deposition, as well as using a Gaussian surface roughness spectrum to supplement the classical theory, it was found that above wavelength surface ripples with orientation parallel to the incident electric field is possible [166, 167]. Future work should be conducted to further investigate the sources of these ULSFL formation.

5.3   Conclusions and future work

Within the subset of the laser irradiation conditions studied, at room temperature LIPSS periodicity has a tendency to decrease with increasing number of shots and decreasing pulse energy, ranging from a highest observed periodicity of $\sim$735 nm to a lower limit in the range of 655-675 nm. At elevated sample temperature the propensity for LIPSS formation tends to diminish. Formation of ULSFL oriented parallel to the incident laser electric field having an approximate spatial period of 2200 nm was the most pronounced at 300-400°C. Qualitatively, these ULSFL may be linked to formation of large, fragmented structures observed at room temperature under similar laser irradiation conditions. The macroscopic and microscopic results of

this work can provide insights into the role of hydrodynamics to aid the elucidation of ultrafast laser induced LIPSS formation mechanisms as well as ultrafast laser ablation dynamics. Future work on expanding the laser irradiation conditions to a broader energy range in conjunction with simulation work may be valuable. The results of this work may also be valuable for applications where surface morphology following laser micromachining is important.

Chapter 6

Ultrafast laser texturing of silicon surface for photonics devices

Laser texturing of material surfaces has received a renewed interest in the more recent years of laser-material interactions with the popularization of unique ultrafast laser induced surface structures. More details on ultrafast laser induced surface structures are discussed in Section 2.1.5.

There are reports of improved above and below bandgap optical absorption of silicon surfaces textured uniformly with conical structures (e.g., [78, 82, 86, 90, 92, 96–102]. It was found that ultrafast laser induced spikes take on a somewhat different morphology in a reactive ambient with SF_6 gas, and the below bandgap absorption was further improved ([78, 82, 86, 90, 92, 96–100]). The absorption mechanism for below-bandgap wavelengths was attributed to the doping of the sulfur from the ambient gas into the shallow near-surface layer of the micromachined silicon surface. Photodetection at below-bandgap wavelengths from devices based on such structures was demonstrated, showing a photoresponsivity with gain when n-type substrates were

used [91, 93]. This type of structure was subsequently referred to as "black silicon" (e.g., [99, 168]) due to its physical appearance and optical properties. Nanostructured-debris generated over femtosecond laser processed regions of parallel grooves on silicon surfaces also showed a reduction in the specular and hemispherical reflectance by a factor of 3.5 in the visible spectrum, and 7 in the ultra-violet range [169, 170].

This chapter presents results from early attempts to create textured silicon with improved sub-bandgap absorption using ion implantation as an alternative technique of introducing sulfur into the textured region. Ion implantation can potentially provide better control of the depth profiling and concentration of the dopants for tailoring the absorption characteristics and performance of the subsequent devices.

6.1 Laser irradiation conditions for surface texturing of silicon

Early efforts in this project emphasized the optimization of the laser irradiation conditions for surface texturing of silicon. Laser parameters explored include laser pulse energy, translation speed of the laser beam, translation direction relative to the laser electric field polarization, line-to-line spacing for optimal pseudo-uniform coverage of large area patterning, and ambient conditions to optimize the ablation debris management. The basic experimental setup is described in Section 2.2.2. Specific experimental conditions will be discussed below.

For all experiments described in this chapter a 125 mm focal length plano-convex lens was used. This lens provides the longest focal length that can be conveniently used in the current micromachining setup without reconfiguration. It is chosen to yield

a larger incident spot size on the samples to facilitate more efficient large-area coverage. The incident spot size ($1/e^2$ radius) obtained with this lens is ∼17 μm. Typical laser pulse energies explored range from ∼500 nJ to 10 μJ, and the laser beam scanning speed ranged from 10-500 μm/s. Once an optimal energy range and translation speed combination was identified, overlapping lines with line-to-line spacings ranging from 10-30 μm were tested to determine the optimal spacing for uniform large-area coverage. The ambient pressure, using N_2 as a backfilling gas, was also explored to provide a better handle on controlling of the micromachining debris trajectory. It should be noted that an additional procedure for debris control with large-volume ablation (as described in the Section 2.2.2) was carried out for this series of experiments. As the ambient pressure is increased (using a nitrogen-flow), redeposition of the debris on the sample surface became an issue. Instead, the optimal irradiation conditions in the context of debris control was to pump the chamber down to a rough vacuum of ∼0.07 mbar. To prevent the debris from collecting on the chamber window, resulting in significant screening of laser energy as the machining process carried on, a 100 μm thick microscope cover slip was secured on the underside of the lid to use as a shield for the optical window. In a large-area irradiation process, a pause is programmed to occur every ∼30 minutes to allow the operator to replace the coverslip with a fresh piece. Once the optimal laser irradiation conditions were established, for optical absorption and preliminary device-fabrication testing 5×5 mm^2 areas were irradiated to generate pseudo-uniform coverage with the conical structures. Analyses of the resulting morphologies were carried out using optical microscopy and scanning electron microscopy.

Following identification of the optimal laser irradiation parameters for large area

irradiation, ion implantation of sulfur was carried out by Dr. Andrew Knights at the Centre for Emerging Device Technologies (CEDT) facility of McMaster University. The ion implantations employed for optical absorption measurements were carried out at 15 keV, at doses of $1.00 \times 10^{15}/\mathrm{cm}^2$ and $1.05 \times 10^{15}/\mathrm{cm}^2$.

The optical absorption measurements were carried out with a 2″ Spectraflect coated LabSphere general purpose integrating sphere with four 1/2″-diameter ports. Several different configurations were attempted for measurement geometries, in collaboration with M.A.Sc. student Bing "Kevin" Liu from the Photonics Research Laboratory. The final iteration allowed the samples to sit flush with the port of the integrating sphere housing with a laser beam incident on the sample at 45° to test for scattered and specular reflection as well as direct and scattered transmitted light to characterize absorption from the textured surface. The measurement geometries are presented in Figure 6.1. To prevent the non-textured silicon surface area from interfering with the measurements, port reducers were fabricated out of stainless steel sheets each drilled with a 5 mm-diameter hole to act as reduced integrating sphere sample ports such that only the textured silicon surface is exposed to the interior of the sphere surface. The port reducer sheets were painted with a flat acrylic primer to provide a relatively high reflectance diffusing surface (tested to have a reflectance of approximately 90% of the Spectraflect coating at 1550 nm) to mimic the interior of the integrating sphere. The light source used was an ILX Lightwave 7900B 1550 nm source, and the detecter used was a Newport 1830-C Power Meter.

As shown in Figure 6.1, the transmittance of the samples was measured with the sample mounted at the entrance port of the sphere. Minor translational adjustments of the sphere were made to ensure that the incoming laser beam is not clipped by the
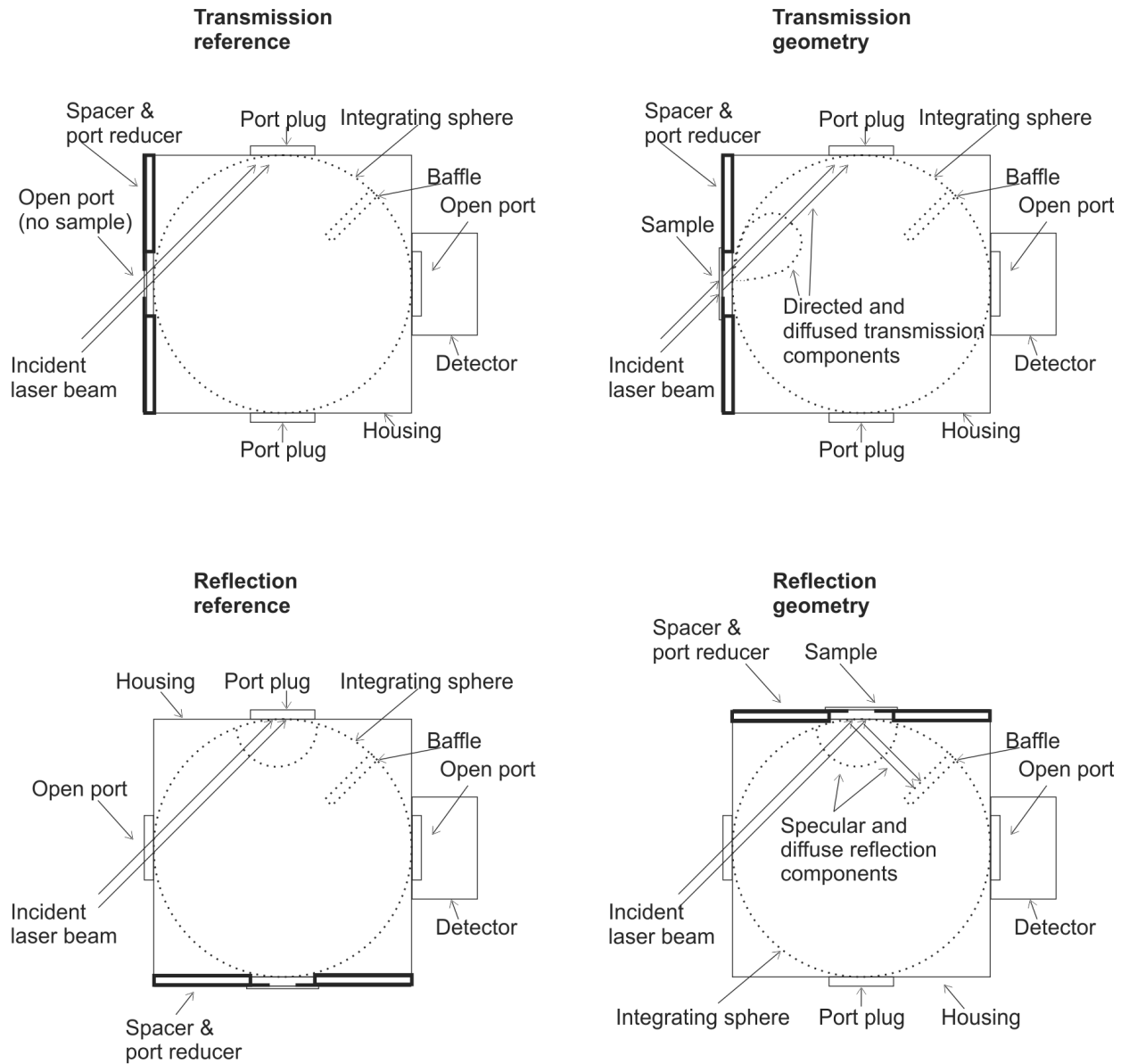
Figure 6.1: Integrating sphere measurement geometries for transmittance and reflectance measurements. The port plugs are factory-made plugs with the inside surface painted with the same Spectraflect coating as the interior of the sphere. An interior baffle of the sphere is oriented to block the direct line-of-sight between the incident surface of the laser and the detector.

integrating sphere port due to a small offset of the beam due to the sample thickness. The transmittance measurements were normalized to the transmission reference with the custom made port reducer in place without a sample (as shown in Figure 6.1) to ensure the small added reflectance from the port reducer is taken into account. Similarly the reference for the reflectance measurement was taken with the incident laser beam incident on a port plug with the sample placed at another free port of the sphere. The reflectance of the sample, taken with the sample placed at the incident port of the laser beam, is normalized to the reflectance reference measurement. This technique ensures that the overall average reflectance of the sphere remains the same and the normalization will yield the true reflectance of the sample only, and is referred to as the comparison sphere technique. Further details of integrating sphere background and measurement geometries can be found in the literature and application notes through manufacturers (e.g., [171–174]). Measurements were taken with the laser beam incident both on the front (laser textured side) and the back (rough-backside of the wafers as received from the supplier) surfaces for the extraction of the absorption of the laser textured surface region.

The reflectance, transmittance, and absorption of each interface was calculated by treating the measured total reflectance and transmittance from the sample as a practically-infinite series of multiple reflections from the front and back surfaces of the sample. An unprocessed silicon sample was also measured as a benchmark, where the initial assumption was made that neither surface of the plain silicon was optically absorbing, and that the scattered light from the unpolished backside of the wafer was captured by the integrating sphere entirely. The obtained single-surface reflectance and transmittance of unprocessed silicon was then applied in the calculations for the

non-textured backside of the samples in the extraction of reflectance and transmittance of the laser microstructured surfaces. Typically for each sample the calculations were performed on both front-side incidence and backside incidence geometries, and the calculation results are averaged results from the two geometries.

6.2   Results and discussions

The resulting surface texture depends primarily on the combination of laser energy and the number of pulses a given location is exposed to (i.e., translation speed of the beam). An estimation technique for the effective number of shots a given spot is irradiated with is provided in Section 2.3.4. Weaker per-pulse and accumulated energies tend to generate shallower feature (ripples), while high cumulative fluences (i.e., high per-pulse fluence and slow translation speed) yielded deep trenches. At moderate fluences, increasing the translation speeds yielded conical structures, and even faster machining speeds generated relatively flat but roughened surfaces. Figure 6.2 summarizes the surface morphologies obtained at several selected combinations of pulse energies and irradiation speeds. Scanning the laser beam in directions parallel and perpendicular to the incident laser electric field did not result in a significant difference in the surface morphology. The optimal laser irradiation condition for the generation of conical structures was $\sim$6.05 μJ pulses at a translation speed of 100 μm/s (N_{eff} $\sim$215 per line scan). Large conical structures were chosen as the surface morphology since it provides a large material surface area (i.e., for potential optical and photonics device applications) for a given laser irradiated area. The typical dimensions of these conical structures are on the order of $\sim$15 μm for the width of the base and $\sim$20 μm for the depth, as shown in a SEM image of a cleaved

500 um/s

300 um/s

100 um/s

50 um/s

10 um/s

10.05 μJ   6.05 μJ   2.13 μJ   1.63 μJ   1.11 μJ
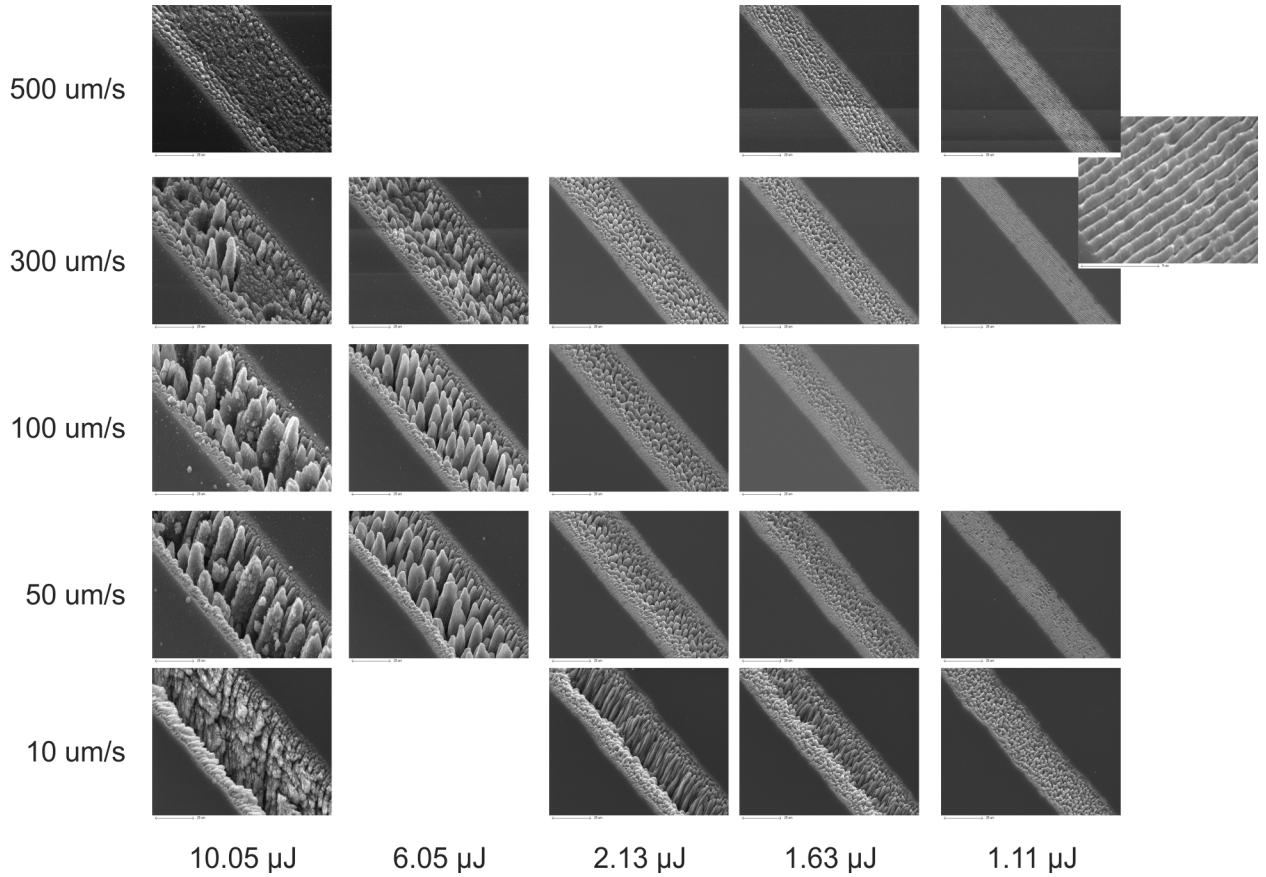
Figure 6.2: Surface morphologies resulting from selected laser irradiating conditions.

cross-section of a pseudo-uniform large area irradiated region in Figure 6.3.

The line-to-line spacing for optimal large-area coverage was determined to be 17 μm, as larger spacings can yield ridges resulting from the weaker wings of the Gaussian intensity profile of the pulse, while smaller spacings generated structures that are qualitatively similar but compromises the throughput of the micromachining processing. Figure 6.4 illustrates the overall effect of the line-to-line spacing on the uniformity of the resulting surface structures.
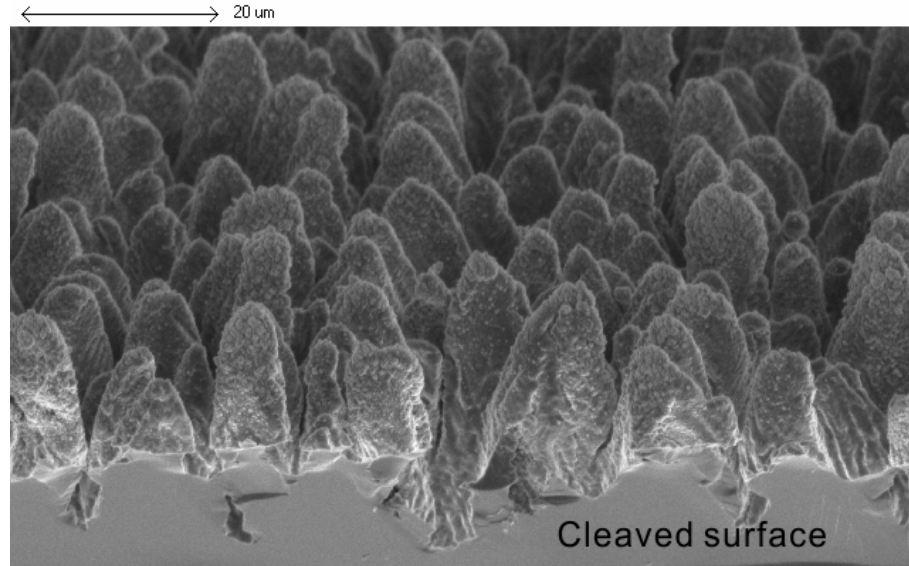
Figure 6.3: Cross-sectional SEM image of a cleaved surface showing the dimensions of the conical structures irradiated with 6.05 μJ pulses translated at 100 μm/s.
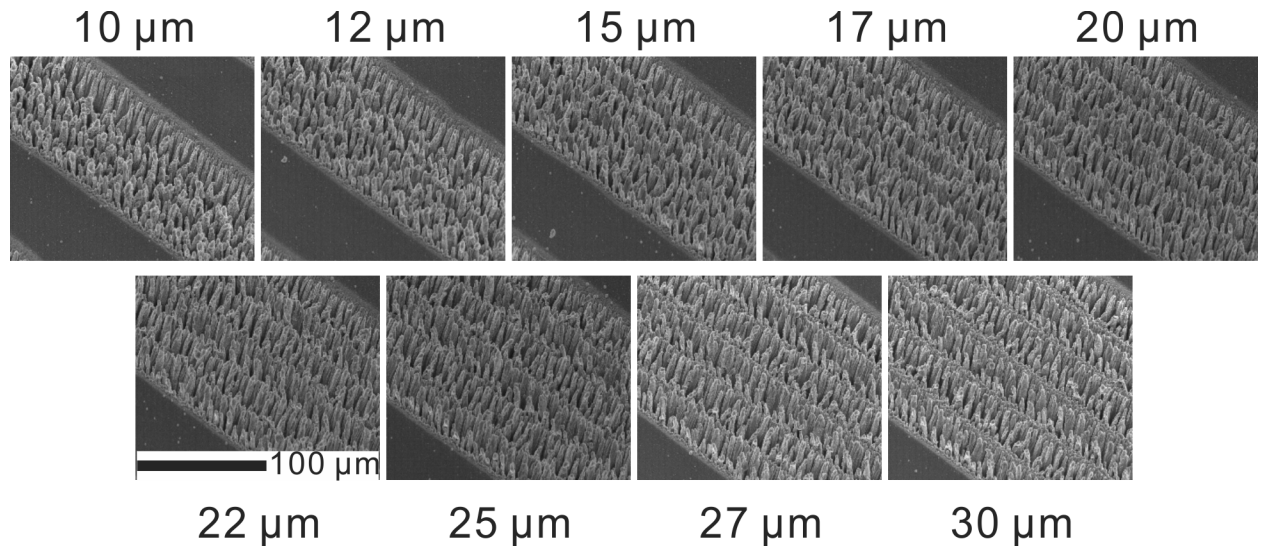
Figure 6.4: Uniformity of surface microstructuring generated by 6 overlapping lines with the indicated line-to-line spacing, irradiated with ~6.05 μJ pulses scanned at 100 μm/s. Large spacings result in non-uniformity in the resulting features, while small spacing reduce the throughput of the laser micromachining process.

Table 6.1: Calculated single-surface reflectance, transmittance, and surface absorption of the microstructured silicon surfaces at 1550 nm. The single-surface refers to the microstructured surface, except for the case of plain silicon where the polished front surface and the unpolished back surface are assumed to have the same reflectance and transmittance.

Sample	$R_{single,calc}$	$T_{single,calc}$	$A_{single,calc}$
Plain silicon	35.68%	64.32%	
Microstructured silicon	25.8%	29.08%	45.13%
S-implanted microstructured silicon 15 keV, $1.00 \times 10^{15}/cm^2$	28.13%	26.43%	45.45%
S-implanted microstructured silicon 15 keV, $1.05 \times 10^{15}/cm^2$	28.49%	25.14%	46.37%

Calculated results for the single-interface absorption for the microstructured silicon surface and plain silicon surfaces are tabulated in Table 6.1. The optical absorption of samples with and without sulfur ion implantation were measured and compared. The results were very similar for samples with and without sulfur implantation.

Preliminary attempts at photodiode fabrication from microstructured silicon implanted with sulfur showed no photoconductivity with sub-bandgap incident laser light irradiation.

The surface morphology obtained from irradiation mostly carried out in rough vacuum are qualitatively different than those carried out in a reactive ambient, such as SF_6, reported in the literature (e.g., [82, 86, 89, 90, 92, 93, 96, 98, 175]). The conical structures obtained through processing in a SF_6 ambient appeared to be skinnier all around with a pointed tip, while the conical structures observed in vacuum from our work appeared to be relatively blunt. Without further characterizations, it would be difficult at this stage to draw comparisons with literature studies where an increased

absorption was achieved with the introduction of sulfur into silicon, either through laser irradiation in a reactive ambient [82, 86, 89–93, 96, 98, 175, 176], or in another study where ion implantation and subsequent laser melting was carried out [177]. The most relevant data in the above references is [175], where it showed the absorptance of 1550 nm light in silicon textured in an SF_6 ambient is $\sim$90%, while texturing in vacuum yielded an absorptance of $\sim$25%, compared to pristine silicon at just over 5%.

In the literature it was reported that while annealing of n-type material provided a gain in photoresponsivity [91], the optical absorption following the annealing actually decreased [86, 89, 90]. This type of photoresponsivity gain was not observed in p-type material, and the gain was attributed to the possible electronic activation of the implanted sulfur in the silicon matrix. It could be possible that without the initial improved absorption following sulfur ion implantation, the annealing step in the metallization process may have decreased or eliminated the optical absorption in the finalized devices. Another possibility is that the environment of the sulfur dopant in the silicon matrix is different when introduced into the silicon during irradiation in a background gas as opposed to through implantation into the sample. Characterization of the optical absorption at different annealing stages may help identify the source of the lack of photoresponsivity.

6.2.1   Debris Considerations

An ancillary result from large area microstructuring of silicon concerns the debris generated from the relatively large volume of material removal. Visually it can be readily observed that the redeposited debris causes interference fringes peripheral to

the laser micromachined area. To facilitate differentiation between the collected debris and the substrate using energy dispersive x-ray spectroscopy (EDX, or EDS), a GaP wafer was placed adjacent to a silicon wafer where large-area microstructuring was carried out. A small gap ($\sim$200 μm) was left between the GaP and the Si samples to prevent possible heat conduction, if it should be a contributing factor in the observed interference fringes. The geometry of the sample placement and resulting visual appearance following surface texturing are shown in Figure 6.5. Figure 6.6 shows the appearance and distribution of the deposited debris at different distances away from the microstructured surface. The resulting EDX spectrum is shown in Figure 6.7. The EDX spectrum showed signal from Ga, P, Si, O and C. Presumably carbon is present in most samples exposed to atmosphere, and from deduction the debris is likely to be silicon and/or silicon-oxide nanoparticles. The photoluminescence (PL) studies were conducted by Professor Andrew Knights on the debris-deposited regions. The photoluminescence spectrum from the deposited debris outside of the microstructured region on silicon shows a blue-shifted signal relative to the porous silicon calibration sample. Annealing the sample at 1100°C quenched and red-shifted the emission peak from the debris. The PL behavior is similar to that of silicon nanoparticles (e.g., [178, 179]). Signal from the microstructured region showed weaker peaks at the same central wavelength, and a similar shift when annealed. The weakened PL peaks from the microstructured regions, the coinciding locations of the peaks as the signal from peripheral debris, and the same behavior before and after annealing suggest that the observed PL activity arises from the debris itself for both regions. The results can be compared to a report of a PL spectrum following ultrafast laser irradiation [87], where the PL spectra were also modified following sample annealing. While annealing the
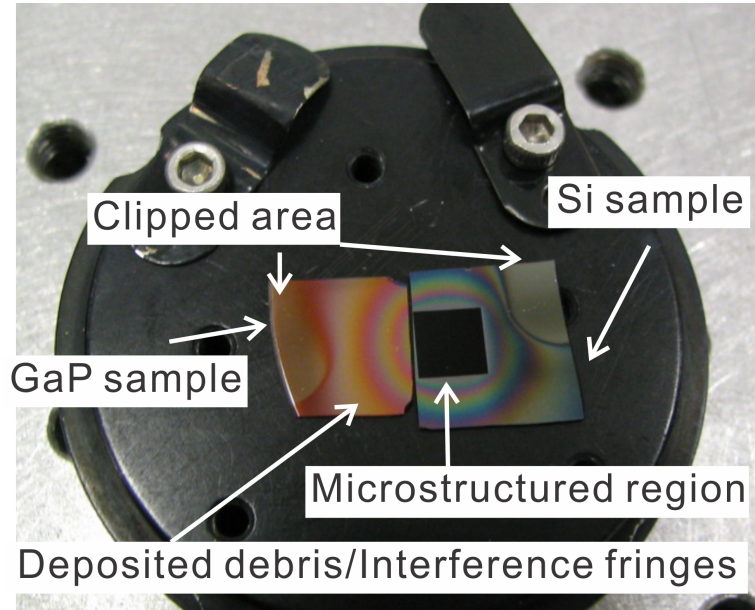
Figure 6.5: Geometry and resulting visual appearance of the debris deposition following large area surface microstructuring of silicon. The microstructured area is 5×5 cm^2.

sample produces a red-shift in the peak of the PL spectrum in both our study and in [87], our work showed a decrease in the PL intensity following annealing, contrary to the findings in [87].

6.3 Conclusions and future work

The results of this work showed optical absorption at 1550 nm from microstructured silicon generated with pseudo-uniform coverage of conical structures. Sulfur ion implantation at 15 keV with a dose of $\sim 1 \times 10^{15}$/cm^2 did not show improvement in the optical absorption. This is contrary to conical structures fabricated using ultrafast
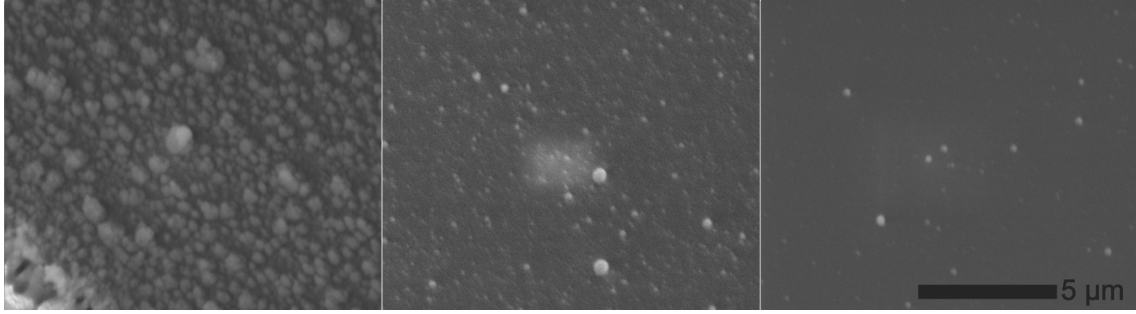
Figure 6.6: SEM images of micromachining debris appearance and distribution adjacent the microstructured surface area (left), and increasing distance from the microstructured area (middle to right, roughly at 2 mm incremental distances away from the microstructured area).
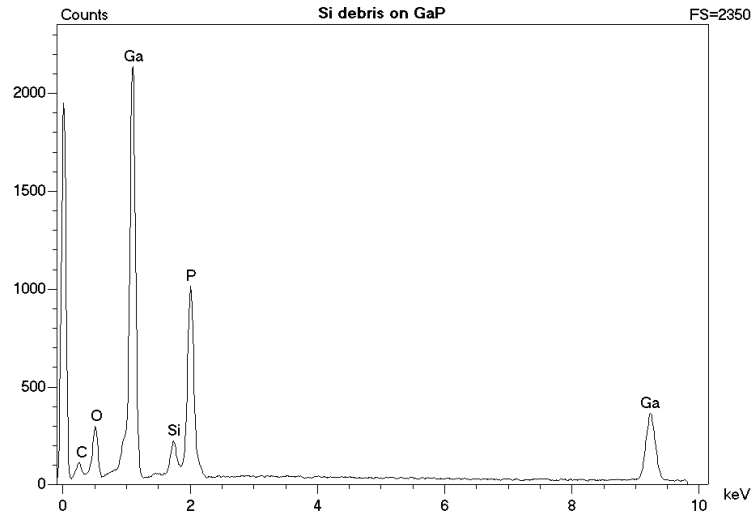
Figure 6.7: EDX spectrum of debris deposited on the GaP sample following large-area surface texturing of silicon, as shown in the geometry presented in Figure 6.5.
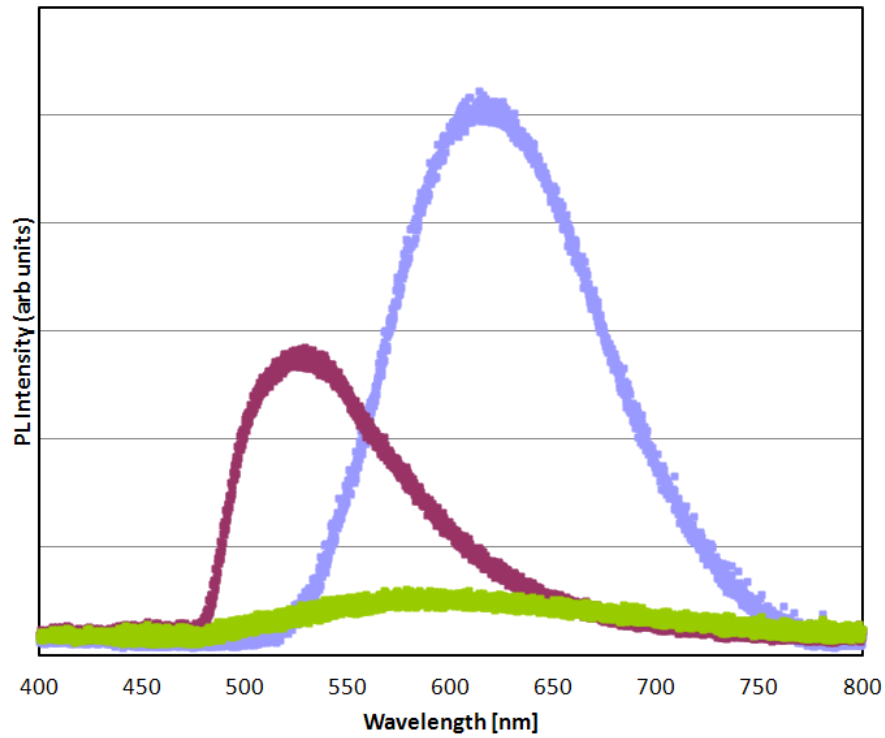
Figure 6.8: PL spectrum of deposited debris at the periphery of the microstructured region on silicon before (purple) and after (green) annealing, compared against a porous silicon calibration sample (blue). Data and figure courtesy of Professor Andrew Knights.

laser irradiation in a sulfur-containing atmosphere as reported in the literature. Attempts at fabricating photodiodes based on the same surface structuring and implantation procedure did not provide a noticeable photoresponsivity at below-bandgap wavelengths. Extensive characterization should be conducted to study and compare the chemical environment of sulfur embedded in the silicon crystal via implantation versus doping achieved using a sulfur-containing ambient gas species, and its effect on the optical absorption. Future pursuit of this work should include both optical and electrical measurements of varying implantation conditions prior to and following different annealing conditions.

Also observed in this work is the photoluminescence signal from the debris generated during the large-area surface texturing of silicon. EDX spectra suggest the debris consists of silicon and/or silicon-oxide particles, while the behavior of the PL signal suggests that the observed signal arises from silicon based nanoparticles. Further studies can be carried out on examining the physical and optical characteristics of the debris to pursue potential applications. The role of the debris in the observed optical properties from the microstructured region should be studied in future work.

Chapter 7

Ultrafast laser ablation of thermal-oxide-on-silicon structures

Silicon dioxide has many essential usages in silicon based devices. The precise material removal mechanisms of ultrashort pulse laser irradiation have shown great potential for processing silicon dioxide-on-silicon structures, as well as selective local removal of silicon dioxide from silicon substrates to (e.g., [180–184]).

Ultrafast laser processing provides unique capabilities compared with other processing techniques and laser systems. The deterministic threshold behavior associated with ultrafast laser processing, for example, can be useful in the context of microfabrication processing. For SiO_2-on-Si structures, ultrafast laser processing may provide maskless, self-aligning fabrication steps. Another possible application is to use the oxide thickness to alter the outcome of the interactions between the ultrafast laser pulses and the underlying bulk material (e.g., by using the oxide layer thickness to enhance or suppress reflectivity of the material or to manipulate the confined pressure at the SiO_2-Si interface). It is also possible to use ultrashort pulse lasers to create

embedded features in such structures (e.g., [185]).

This chapter presents results on stationary and translational irradiation schemes using ultrafast laser irradiation of SiO_2-Si structures. The results presented in this thesis are obtained in collaboration with M.A.Sc. student Bing "Kevin" Liu from the Photonics Research Laboratory. Emphasis was moved away from single-shot laser ablation of SiO_2-on-Si structures following the appearance of similar work in the literature during the course of our experimental work [181–184]. In the above referenced works, detailed studies were conducted on the discoloration, blistering, and rupturing behavior with various SiO_2 layer thicknesses under irradiation of single-pulse laser at different pulse durations and laser wavelengths. It was found that there is a range of laser fluence, depending on the oxide layer thickness, where the SiO_2 layer can be removed without substantial damage to the silicon substrate. For example, in [184] it was shown that with single pulse (150 fs pulse duration) irradiations, a fluence of $\sim$300 mJ/cm^2 can initiate delamination of a 1200 nm oxide film from the silicon substrate, and $\sim$700 mJ/cm^2 of laser fluence is required to cause the oxide blister to rupture. In [182], it was found that the melting and breaking thresholds decrease monotonically with pulse duration between 2 ps to 50 fs, and to remove the oxide layer while leaving the silicon substrate damage-free a maximum fluence of 1.2 J/cm^2 should be employed. However, further investigations of sub-surface crystallinity should be conducted, using FIB-TEM technique for example (analogous to [165]), to examine possible damage that may elude other microscopy techniques (OM, SEM, or even AFM).

7.1   Experimental details

Silicon samples with thermally grown oxide were prepared by Peter Jonasson (Laboratory Coordinator, Department of Engineering Physics) and Thomas Jacob (M.A.Sc. student of Professor Andrew Knights, Department of Engineering Physics) at 1000°C on two part-wafers. Thermal oxide on one sample was grown for 14 min 45 sec, targeting a thickness of 137 nm ($\sim\lambda/4n$), and the second sample for 36 min 40 sec, targeting a thickness of 274 nm ($\sim\lambda/2n$), where λ is the peak irradiation laser wavelength ($\sim$800 nm), and n is the refractive index of SiO$_2$. The calculated reflectivities at 800 nm from such systems are approximately 0.58% and 24.7%, respectively. These are compared to a reflectivity of 32.9% for a bare silicon surface. Subsequent characterization arranged by M.A.Sc. student Kevin Liu measured the actual oxide thicknesses to be 113 nm (using ellipsometry) and 214 nm (using ellipsometry and cross-sectional TEM) for the two samples, yielding calculated reflectivities of 1.9% and 13.3%, respectively.

Laser irradiations were carried out using a 125 mm focal-length plano-convex lens. The typical incident laser spot size on the samples using this lens was calculated to be $\sim$17 μm at 1/e^2 radius at the time of the experiment. Both stationary and translational irradiation were carried out, employing energies ranging from a few times above to below threshold. Translational irradiations were carried out to study the surface morphology that may arise from the SiO$_2$-on-Si structure during the laser writing process. Translations were carried out to machine lines parallel and perpendicular to the incident laser electric field at speeds of 1, 10, 100, 500 and 2000 μm/s.

An initial survey of the resulting morphologies and feature dimensions was largely carried out using optical microscopy (OM). Scanning electron microscopy (SEM) was

used to study the resulting morphology in detail.

7.2   Results and discussions

7.2.1   Single-shot irradiation

Using the D^2 technique, the single-shot threshold for visible modification (discoloration) in the sample with 113 nm of SiO_2 was determined to be 163 mJ/cm^2, lower than that of the sample with 214 nm of SiO_2 sample at 207 mJ/cm^2. For stronger evidence of delamination of the SiO_2 from the underlying silicon, extracted thresholds were 262 mJ/cm^2 for the 113 nm SiO_2 sample and 394 mJ/cm^2 for the 214 nm SiO_2 sample. The results are compared to the extracted single-shot ablation threshold of plain silicon 286 mJ/cm^2 from the same series of experiments. The measured features were based on interpretation of observations under OM using findings in [181]. Single-shot threshold fluences for the different oxide thicknesses and bare silicon are summarized in Table 7.2.1. The results shown are averaged from two experimental runs, where each experimental run would perform two sets of single-shot irradiation for each sample, and the reproduced results are within 15% (typically within a few percent). There is a range of laser fluences for which the single-shot laser irradiation appeared to have removed the oxide cleanly while leaving no observable damage with SEM analysis. At moderately high energies, single-shot laser irradiation yielded craters with radial cracks, with concentric ripples at the periphery of the crater. At even higher local energies, a smooth appearance is observed at the center region of the craters. Figure 7.1 shows examples of different features observed with single-shot irradiation of 113 nm SiO_2-on-Si structures at selected energies.
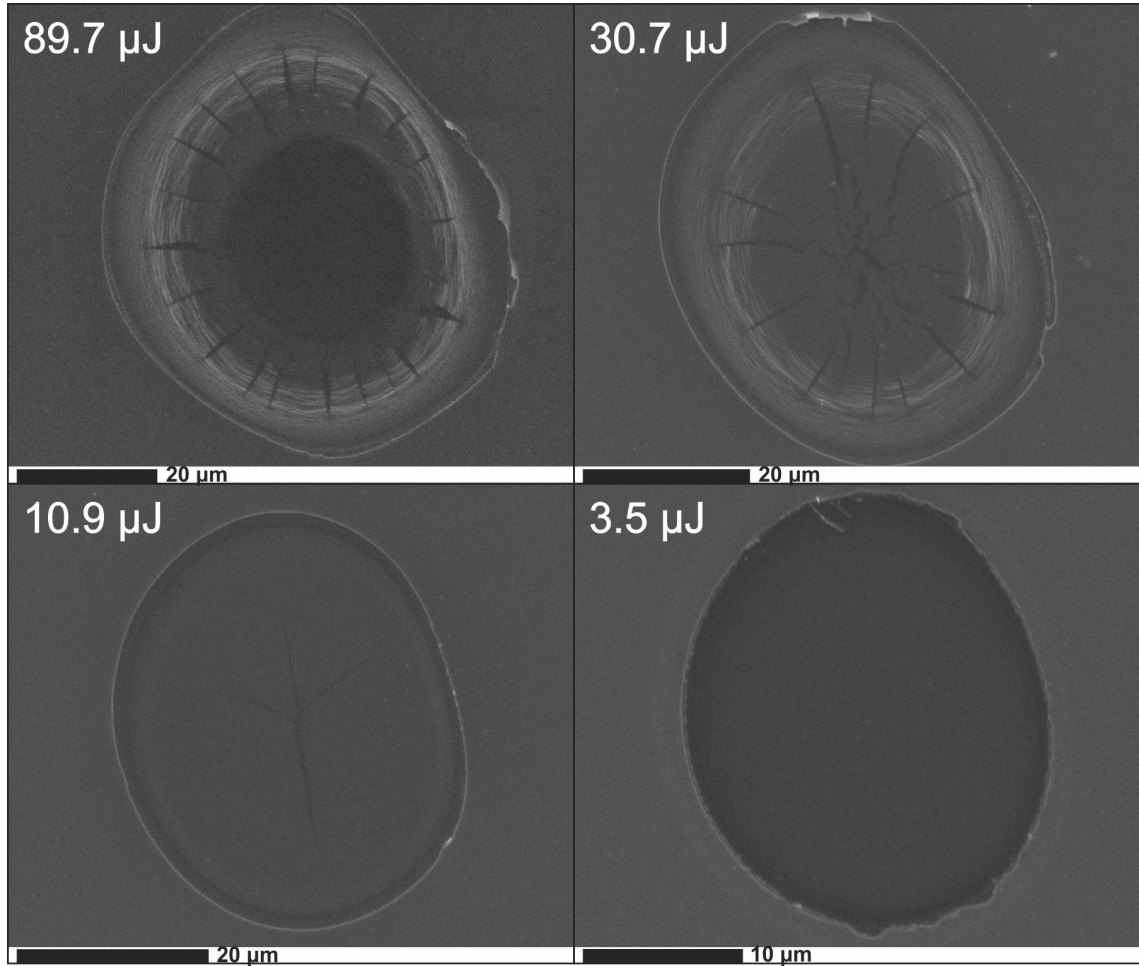
Figure 7.1: Single-shot irradiation of 113 nm SiO_2-on-Si structures at the indicated pulse energies. The outer-most sharp ring surrounding each crater indicate the regions where SiO_2 is removed from the target site. At high energies (e.g., top left) the center of the crater appears smooth and featureless, with radial cracking and concentric rippling at the periphery of the ripples. At lower pulse energies (e.g., top right), the smooth featureless morphology is not observed, and radial cracking extends to the center of the crater. At moderate low energies (e.g., bottom left), a small degree of cracking is observed at the center of the crater. Finally at low energies removal of oxide is obtained without obvious morphological change to the underlying silicon in SEM observations.

Table 7.1: Single-shot threshold fluences to generate a discoloration appearance or delamination of SiO_2 layer/possible ablation of underlying silicon. These values are compared to the single-shot ablation threshold fluence of 286 mJ/cm^2 obtained from the same series of experiments.

Sample	Discoloration threshold	Delamination threshold
113 nm SiO_2 on Si	171 mJ/cm^2	253 mJ/cm^2
214 nm SiO_2 on Si	208 mJ/cm^2	358 mJ/cm^2

The extracted thresholds are comparable to the reported values of $\sim$190 nm and $\sim$280 nm for melting and blistering of a 100 nm thick silicon oxide film on silicon irradiated with 50 fs lasers pulses with a wavelength of 800 nm, respectively [182, 183]. The qualitative behavior of the single-shot thresholds was expected for the different SiO_2 thicknesses, as the SiO_2 layers were grown to target thin-film structures with high-reflectivity ($\lambda/2n$) and anti-reflection ($\lambda/4n$) conditions for the peak incident laser irradiation wavelength, while a thicker layer would provide more mechanical strength as well. The different surface morphologies can provide insights into the ablation mechanisms, as well as the state of the material and the time-frame of events following energy deposition. For example, a smooth feature may indicate local non-thermal melting associated with high energy density. Cracking and concentric rippling indicate a large confined recoil pressure before the removal of the oxide layer, and suggest that energy deposition was primarily in the surface or near-surface region of the silicon as expected. However, it may be premature to conclude that the underlying silicon crystal remained undamaged. In a previous study of ultrafast laser ablation of metals-SiO_2-Si structures, cross-sectional TEM microscopy showed that the removal of a top metal layer can create extensive dislocations in the underlying structure, likely due to propagation of pressure waves into the material, while from the same

target site the underlying material appeared undamaged in SEM microscopy [111].

Comparison of modification or damage generated on a bare silicon surface with the same laser irradiation conditions was difficult. Optical microscopy is typically used as an initial survey since it is sensitive to visible changes made to the sample surface, and damage can be readily identified on bare substrates. However in the cases of SiO_2-on-Si structures, subtle changes may be made at different locations of the layered structure at a lower laser fluence than it would for a bare substrate, which may be accentuated in the optical microscope due to the light interactions with the layered structures.

7.2.2   Translational irradiation

Translational irradiations were able to yield a richness of different morphologies at different laser irradiation conditions, as summarized in Figure 7.2. Types of periodic surface structures observed include ripples with LSFL-type spacing oriented perpendicular as well as parallel to the incident laser electric field, honeycombing structures, and fine ripples. Specific laser irradiation conditions favor different outcomes. A faster translation speed (i.e., 2000 μm/s) yielded primarily LSFL-like ripples ($\gtrsim$660 nm) that are primarily perpendicular to the incident electricfield, while occasionally ripples parallel to the electric field were observed. An overall honeycomb-like structures were observed at 100 μm/s (with a spacing of $\sim$595 nm). At slower translation speeds (10 μm/s and 1 μm/s), parallel ripples show a LSFL-like periodicity ($\sim$700 nm), while structures with very fine spatial periods (on the order of $\sim$200 nm) perpendicular to the laser electric field were also observed (presumably in the underlying silicon). At low energies and a translation speed of 10 μm/s, parallel LIPSS were not observed
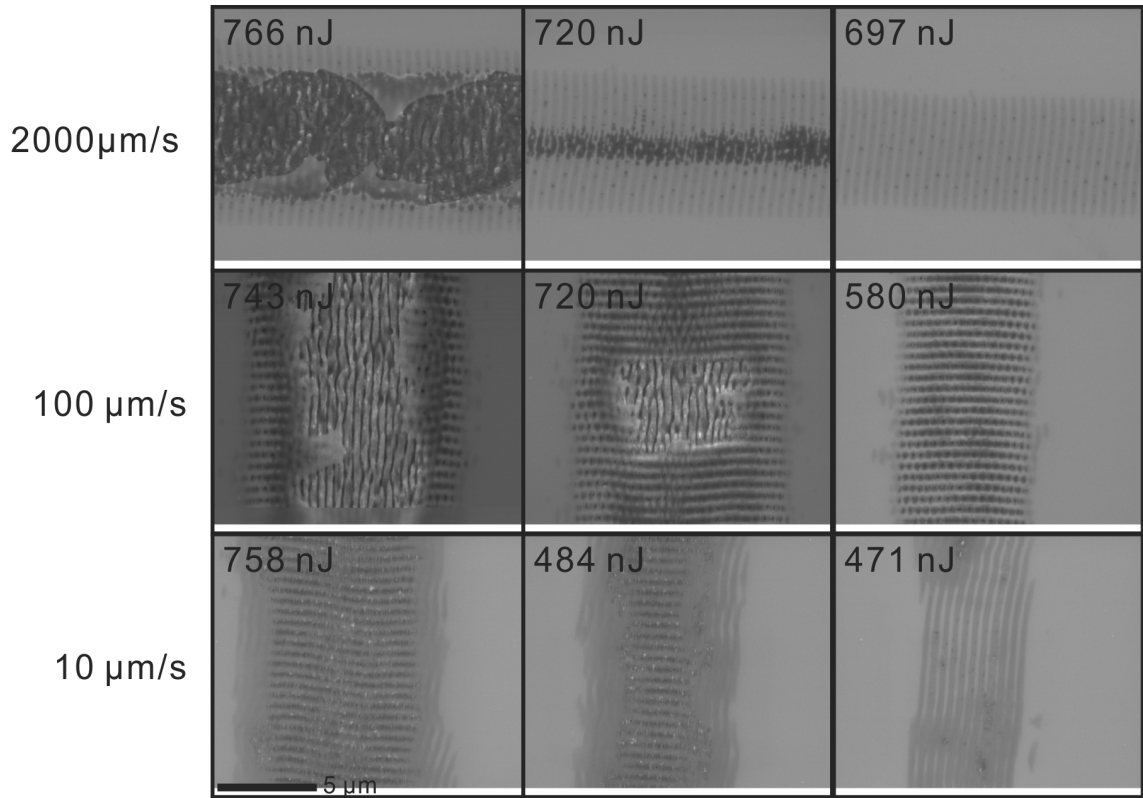
Figure 7.2: SEM images of LIPSS formation under translational irradiation of 113 nm SiO_2-on-Si structure at selected speeds and energies. With a faster translation speed, LSFL-like structures are the primary features observed. With a slower irradiation speed, fine ripples are observed, as are ripple patterns oriented parallel to the laser electric field. Regions where the SiO_2 is removed showed LIPSS qualitatively identical to LIPSS generated in bare silicon.

and the perpendicular ripple pattern reverted back to the regular LSFL-like periodicity. Figure 7.2 presents translational irradiation at selected irradiation conditions summarizing the above observations. In local areas where the SiO_2 layer was removed, qualitatively identical LIPSS to ones generated on bare silicon were observed. Overall, similar structures are obtained between translations parallel or orthogonal to the incident laser electric field.

A FIB prepared specimen for TEM studies was prepared from a site irradiated
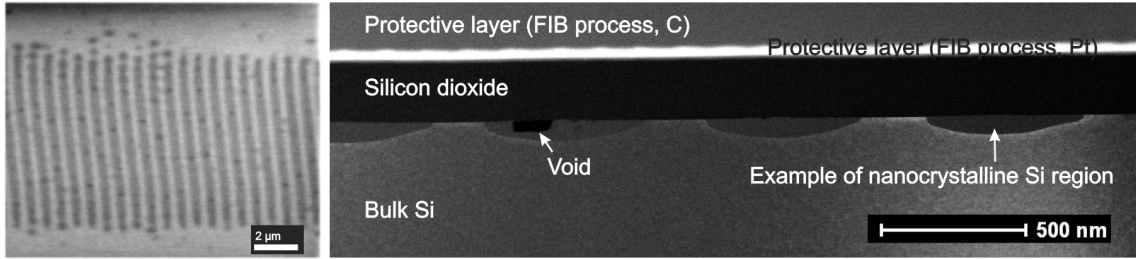
Figure 7.3: SEM top view (left), and cross-sectional TEM image (right) of ripples formed in silicon under a 214 nm oxide layer following 2000 μm/s translational irradiation with 727 nJ pulses. The TEM image is annotated to point out the regions which consist of crystalline bulk silicon, periodically modified nanocrystalline silicon pockets, a void within the modified region, silicon dioxide top layer, and protective layers deposited during the FIB process. The dark spots in the SEM top view are suspected to be voids as observed in the TEM. The TEM investigations were arranged by M.A.Sc. student Kevin "Bing" Liu.

with 727 nJ pulses with the beam translating at 2000 μm/s along the sample with a 214 nm oxide layer. The TEM micrographs showed that the rippled areas consist of pockets of nanocrystalline silicon with sporadic voids likely due nano-explosions. The depth of the modified regions consisting of nanocrystalline silicon is ~75 nm. Figure 7.3 provides an SEM top view and a cross-sectional TEM overview of the generated ripple structures. The crystallography of different regions was confirmed with high resolution TEM as well as electron diffraction patterns. The TEM investigations were arranged by M.A.Sc. student Kevin "Bing" Liu.

In terms of classical ripples (i.e., irradiation with long-pulse lasers) in semiconductors the generated ripples are oriented perpendicular to the incident laser electric field, while ripples oriented parallel to the incident electric field tend to occur in dielectrics [5]. The fact that we observe overlying ripples with orthogonal orientation suggests that the observed surface morphologies under translational irradiation is likely the result of the interplay between laser interactions with the oxide layer and

the underlying bulk structure. Observations of only one type of ripples at low energies (e.g., under 10 μm/s translational speed) indicates that the different threshold energies might exist to generate overlapping structures as in the case in higher energy irradiations. Results from the TEM work indicate that subtle damage can take place on the silicon surface while the oxide layer appears intact. Further characterizations are underway to study the resulting morphologies in detail, and the results should yield insights into the formation mechanisms and the interplay of different types of ripples.

Other than the characterization difficulties observed in the single-shot irradiation case, it was also challenging to conclusively examine the silicon surface, and silicon/SiO_2 interface, for subtle interactions since the oxide layer can mask the details underneath when it is still intact. Scanning electron microscopy was a useful supplementary technique to OM in studying surface morphologies of exposed surfaces in detail. Ongoing and future work should include processing and analysis techniques that can access the underlying silicon surface. For example, HF etching can target SiO_2 while providing good selectivity between SiO_2 and Si. At the same time there are established techniques to selectively etch Si while mostly preserving silicon dioxide, or further FIB-TEM samples can provide valuable insights into the underlying structures.

7.3   Conclusions and future work

Initial results from this work showed a threshold dependence on the thickness of a top thermal oxide layer. Morphology changes as a function of laser energy can provide useful insights into the ablation mechanisms, state of the material, and time

frames of events following ultrafast laser energy deposition. The generation of ripples was observed in a translating irradiation scheme, where both semiconductor-like and dielectric-like ripples are observed. The specific LIPSS type and combinations of LIPSS types depend on the laser irradiation conditions. Further characterizations are underway and are warranted for possible future applications.

By carrying out future characterization of the crystallographic damage in underlying silicon where the oxide is removed, one may correlate the observed damage to the material strengths of silicon and silicon dioxide, and quantify the confined pressure generated from the ultrafast laser energy deposition and provide valuable insight into ultrafast laser ablation mechanisms. In terms of LIPSS studies, on-going and future work include surface contour characterization using atomic force microscopy (AFM), HF dip to selectively remove the oxide layer to expose underlying silicon surface, or selectively etch away the silicon to expose the oxide layer, as well as further cross-sectional TEM work in conjunction with FIB sample preparation. Investigations into the locations of ripple formation (i.e., if ripples are generated at the top, within or below the SiO_2 layer, if there are ripples formed at the SiO_2-Si interface, or if rippling occurs at the near-surface region in the bulk silicon material), larger range of laser irradiation parameters, and different oxide thicknesses will aid the elucidation of the ripple formation mechanisms, provide insights into the possible interplay of the two ripple types in an insulator-silicon layered structure, as well as gaining an understanding into ultrafast laser ablation mechanisms in general. Furthermore, this idea can be extended to laser irradiation of thin silicon-on-insulator structures and specially prepared ultra-thin silicon samples (i.e., using TEM sample preparation techniques).

Chapter 8

Selected studies of ultrafast laser irradiation of GaP, Metal-SiO$_2$-Si, quartz, diamond, and porcine bone

This chapter presents brief introductions, summaries, and discussions of several projects that are outside of the main theme of the thesis. In the first two years of my Ph.D. program my research focused on terahertz (THz)-based research, before reverting back to the main topic of my M.A.Sc. research - laser ablation. My involvement in the collaborative effort started in the first two years of the Ph.D. program on top of the THz-based research. As the results of the projects are published or submitted for publication as journal articles, they will be reprinted in the following sections. The descriptions in this chapter therefore will be brief, and my involvement in each topic will be described.

The topics to be presented in this chapter are published in the following articles:

- **E. M. Hsu**, T. H. R. Crawford, C. Maunders, G. A. Botton, H. K. Haugen,"Cross-sectional study of periodic surface structures on gallium phosphide induced by ultrashort laser pulse irradiation", Appl. Phys. Lett. **92**, 221112 (2008)

  The article is reprinted in this thesis with permission. Copyright 2008, American Institute of Physics.

- **E. M. Hsu**, N. A. Mailman, G. A. Botton and H. K. Haugen, "Microscopic investigation of single-crystal diamond following ultrafast laser irradiation", Appl. Phys. A **103**, 185 (2011)

  The article is reprinted in this thesis with permission. Copyright 2011, Springer-Verlag.

- M. Budiman, **E. M. Hsu**, H. K. Haugen and G. A. Botton, "Cross-sectional study of femtosecond laser bulk modification of crystalline α-quartz" Appl. Phys. A **98**, 849 (2010)

  The article is reprinted in this thesis with permission. Copyright 2010, Springer-Verlag.

- T. H. R. Crawford, J. Yamanaka, **E. M. Hsu**, G. A. Botton, H. K. Haugen,"Femtosecond laser irradiation of metal and thermal oxide layers on silicon: studies utilising cross-sectional transmission electron microscopy", Appl. Phys. A **91**, 473 (2008)

  The article is reprinted in this thesis with permission. Copyright 2008, Springer-Verlag.

- reprinted with permission from: B. Emigh, R. An, **E. M. Hsu**, T. H. R.

Crawford, H. K. Haugen, G. R. Wohl, J. E. Hayward and Q. Fang, "Porcine cortical bone ablation by ultrashort pulsed laser irradiation", J. Biomed. Opt. **17**, 028001 (2012)

The article is reprinted in this thesis with permission from SPIE.

8.1 Cross-sectional study of periodic surface structures on gallium phosphide induced by ultrashort laser pulse irradiation

This project focused on the formation of periodic surface structures on GaP under ultrashort pulse irradiation. The relevant introduction to laser induced surface structures is presented in Section 2.1.5, as well as in the article included below. For this experiment GaP was chosen as the material, due to its bandgap energy being larger than the photon energy of the laser pulses employed, to facilitate the formation of high spatial frequency LIPSS. The key findings of this work shows HSFL can have a very high depth-to-width aspect ratio, with an unmodified crystalline core, an amorphous cap layer, and shed insights into the formation mechanism of HSFL. Future work designed to test the proposed mechanisms in the article in conjunction with the findings of this work can shed further insights into the origin of HSFL formation.

The experimental details, results and discussions are presented in the included article to follow (reprinted with permission from: **E. M. Hsu**, T. H. R. Crawford, C. Maunders, G. A. Botton, H. K. Haugen, "Cross-sectional study of periodic surface structures on gallium phosphide induced by ultrashort laser pulse irradiation", Appl.

Phys. Lett. **92**, 221112 (2008). Copyright 2008, American Institute of Physics). For this project I was the main researching student in carrying out the experiments, analysis, and manuscript preparation. While the experimental work and initial analysis were carried out during my M.A.Sc. program where selected results were presented in the corresponding thesis, the analysis was finalized early in my Ph.D. program as well as the preparation of the manuscript.

Cross-sectional study of periodic surface structures on gallium phosphide induced by ultrashort laser pulse irradiation

E. M. Hsu,[1] T. H. R. Crawford,[1] C. Maunders,[2] G. A. Botton,[2,a)] and H. K. Haugen[3,a)]

[1]*Department of Engineering Physics, McMaster University, Hamilton, Ontario L8S 4L7, Canada*
[2]*Department of Materials Science and Engineering, McMaster University, Hamilton, Ontario L8S 4L7, Canada*
[3]*Department of Engineering Physics and Department of Physics and Astronomy, McMaster University, Hamilton, Ontario L8S 4L7, Canada*

We present cross-sectional transmission electron microscopy studies of laser induced periodic surface structures (LIPSS) formed on gallium phosphide after irradiation with ultrashort laser pulses with a pulse duration of 150 fs and centered at a wavelength of 800 nm. LIPSS with spatial periods (~165 nm) substantially smaller than the incident wavelength are found to have vertical profiles as high as ~960 nm measured from the crest to the trough. The present observations provide important insights into the formation mechanisms of subwavelength LIPSS. © *2008 American Institute of Physics*. [DOI: 10.1063/1.2936865]

High spatial frequency laser induced periodic surface structures (HSF-LIPSS or HSFL) have been recently observed following solid target irradiation with ultrashort laser pulses. HSFL have spatial periods that are substantially subwavelength and have been observed on a variety of sample surfaces following multiple pulse irradiation (see, e.g., Refs. 1–18). In many cases, the laser wavelengths correspond to sub-bandgap energies on the target materials. There are also a few reports of fine periodic structures on metals in the literature (i.e., copper[19] and a brief mention for stainless steel[9]). HSFL appear to be different from low spatial frequency LIPSS (LSFL) that were first observed more than four decades ago.[20] The formation of LSFL is attributed to the interaction of incident light with scattered light at the material surface (e.g., Ref. 21). However, the origin of HSFL is still a topic of debate in the current literature. Proposed mechanisms for HSFL generation include nonlinear interactions,[1,15,16] self-organization,[2–4,17] and extension[5,6] of existing theories (e.g., Ref. 21). Coulombic explosion has also been proposed as an origin of nanostructures.[22] Periodic nanogratings are also observed in bulk fused silica when irradiated with femtosecond laser pulses at a wavelength of 800 nm.[23–26] Relative to the incident laser wavelength, the nanostructures found in Refs. 23–26 have periodic spacings comparable to HSFL found on other material surfaces. A crystallographic study of HSFL may shed valuable insight on their formation mechanism. In this work, we present transmission electron microscopy (TEM) studies on focused ion beam (FIB)-prepared cross-sectional specimens (for details of this technique, see, e.g., Ref. 27) of irradiated regions on GaP samples over which LIPSS are generated.

A commercial titanium:sapphire chirped-pulse amplification system is used to provide laser pulses with a duration of ~150 fs at a central wavelength of 800 nm and a repetition rate of 1 kHz. A description of the experimental setup, including comments on various technical issues, is provided in Ref. 28. Irradiation is performed on double-side polished gallium phosphide (100) samples that are ~430 μm in thickness, with an n-doping of 1.85×10^{16} cm^{-3} and a mobility of 160 cm^2 V^{-1} s^{-1}. Laser pulses are focused perpendicular to the sample surface using a lens with 75 mm focal length. For this irradiation setup, use of the D^2 method[29] yields a spot size of ~13 μm $1/e^2$ radius on the target. Although the D^2 approach was not applied for the two FIB-prepared samples described here, the typical spot size is used to indicate approximate irradiation fluence. A charge-coupled device camera is used prior to the experiment to image the beam profile and a Gaussian beam can be reasonably assumed. Pulse-front tilt is minimized by diagnosing the pulses with a GRENOUILLE (see, e.g., Ref. 30) or a tilted pulse-front autocorrelator (see, e.g., Ref. 31) on a regular basis.

The LSFL observed in this study are similar to that we observed via scanning electron microscopy (SEM) on GaP[14] and other semiconductors[11,12] in our earlier works. In Ref. 11, we have also conducted a TEM study of a FIB-prepared cross-sectional specimen of LIPSS formed on InP. However, it should be pointed out that the cross-sectional study in Ref. 11 was performed on a site irradiated with a low number of pulses (20) at a long wavelength (2050 nm) in comparison to sites studied in this work, and the earlier FIB specimen was not obtained from an ideal location for HSFL observation. LSFL have also been observed on Si in a cross-sectional TEM study on FIB-prepared specimens conducted by Coyne *et al.*[32] The appearance of HSFL observed in this work is qualitatively similar to observations reported in the literature on a wide variety of materials.[1,2,4,5,7–12,14,17]

All LIPSS observed in this work are oriented perpendicular to the electric field of the incident pulses. Figure 1 presents microscopy images of a site irradiated with N =100 pulses with a pulse energy of ~415 nJ, corresponding to an approximate single pulse irradiation fluence of ~160 mJ/cm^2. Figure 1(a) shows an overall profile of the crater. As can be seen more clearly in a plan-view SEM image [Fig. 1(b)], both LSFL and HSFL are formed in this irradiation site with HSFL at the periphery of the site, whereas the central region is occupied by LSFL. Higher magnification images show HSFL [Fig. 1(c)] and LSFL [Fig. 1(d)] in more detail. At this irradiation site, LSFL and HSFL have spatial periods of ~575 and ~185 nm, respectively.

a)Electronic addresses: haugenh@mcmaster.ca and gbotton@mcmaster.ca.
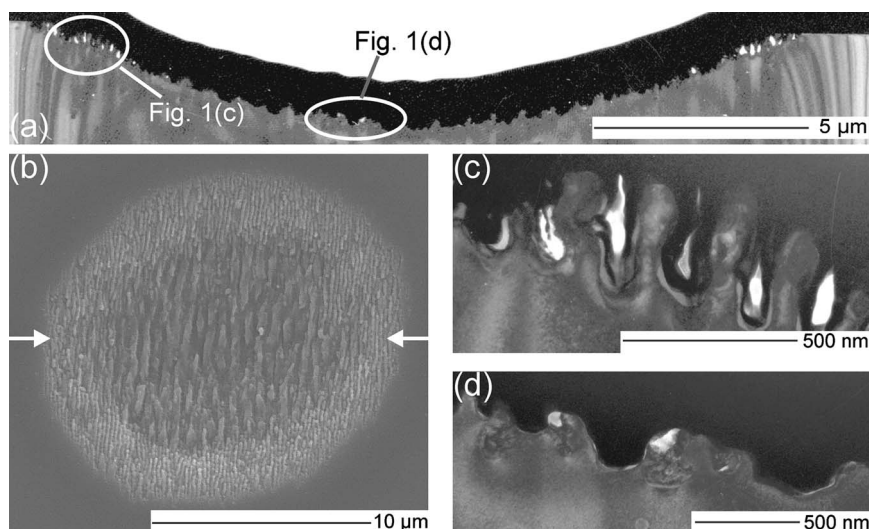
FIG. 1. A site on a GaP sample irradiated with 100 laser pulses, at a pulse energy of ~415 nJ, showing HSFL surrounding LSFL at the irradiation site. (a) Cross-sectional TEM image showing the profile of the crater. (b) SEM image showing LIPSS distribution. Arrows in this figure indicate the location where the FIB cross-section specimen was prepared. (c) High magnification cross-sectional TEM image showing HSFL and (d) TEM image showing LSFL. The locations for images shown in (c) and (d) are indicated in (a). The black regions in the TEM images correspond to a protective layer deposited prior to the FIB milling process, whereas the white regions indicate vacuum.

LSFL with spatial periods somewhat smaller than the irradiation wavelength have commonly been observed (see, e.g., Refs. 4, 5, and 11–15). With a Gaussian beam profile, the spatial separation between LSFL and HSFL indicates that lower fluence favors the formation of HSFL for a given N. This is consistent with our previous observation.[14]

After irradiation by 1000 pulses, only HSFL are observed in the final state of the irradiation sites over the range of energies employed in this experiment (5–460 nJ). For high pulse energies, HSFL are observed on the walls of the resulting holes, though the centers could not be easily imaged using SEM. At lower pulse energies, relatively shallow profiles are obtained where HSFL are present throughout the sites. Figure 2 presents images of sites irradiated with N =1000 pulses at 190 nJ per pulse, corresponding to an approximate single pulse irradiation fluence of ~75 mJ/cm^2. HSFL found at these irradiation sites have an average spatial period of ~165 nm, smaller than that for N=100. A small reduction in the apparent HSFL spatial periods as N increases has been reported previously.[14,15] Electron diffraction patterns reveal that the irradiated surfaces are capped by a layer of amorphized material [Fig. 2(c)], while single crystal material is found in the bulk and the inner region of HSFL. High resolution TEM images (not presented here) show that

the crystal structure and orientation in the bulk and the inner region of the HSFL protrusions are identical throughout, suggesting that the material in the central parts of the protrusions is not modified by the irradiation process.

The cross-sectional images show that HSFL can have a substantial height to width ratio with the tallest protrusion reaching ~960 nm in height. In comparison, the widths of HSFL protrusions are ~85 nm on average. This indicates that these HSFL are planarlike structures, not unlike the nanostructures observed in bulk fused silica.[23–26] In Ref. 26, the periodic planar structures are attributed to local field enhancement during inhomogeneous breakdown. The formation of planar structures is proposed[26] to arise from nanoplasmas growing into nanoplanes when a linearly polarized laser source is used. This model also associates the spacing that is close to one-half of the irradiation wavelength in the medium to the mode supported by a planar waveguide. In this present work on GaP, the spatial periods of HSFL are somewhat larger than the expected second harmonic wavelength in the material. Spatial periods of HSFL being greater than the expected second harmonic wavelength in the solid has been attributed to a refractive index reduction upon irradiation by ultrashort laser pulses.[1] It can also be noted that once the HSFL protrusions have begun to form, the effective refrac-
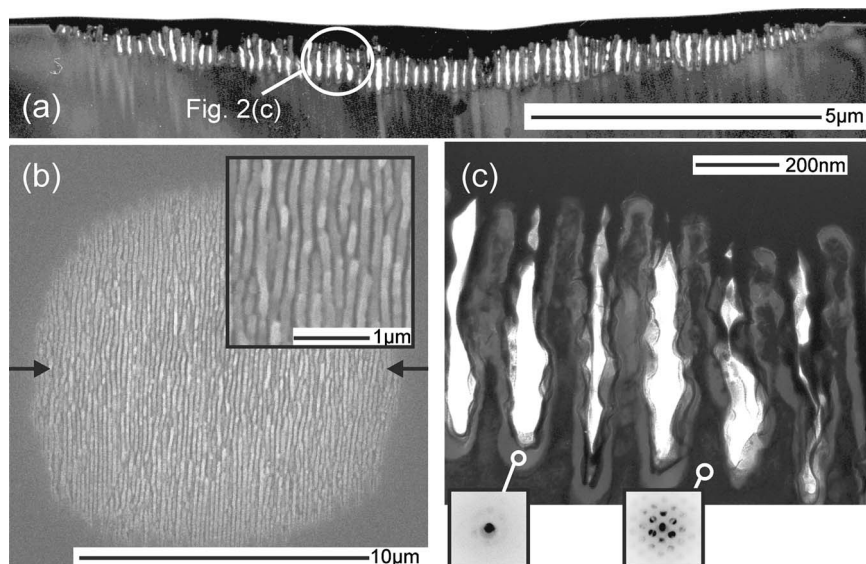
FIG. 2. HSFL observations from sites irradiated with 1000 laser pulses at a pulse energy of ~190 nJ. (a) Cross-sectional TEM image of the irradiation site. (b) SEM image. Arrows in this image indicate the location where the FIB cross-section specimen was prepared. The inset shows a higher magnification. (c) High magnification cross-sectional TEM image showing HSFL found at this site as labeled in (a), with diffraction patterns showing the crystalline structure of the bulk and an amorphous cap layer over the irradiated material. The white regions indicate vacuum.

tive index of the target is reduced as a result of the significant removal of material.

In conclusion, further cross-sectional TEM observations of HSFL on selected materials would be of value to explore the generality of the GaP results. In addition, the possible connection between the mechanisms for HSFL formation on surfaces and the generation of nanogratings in bulk fused silica should be explored.

[1]T. Q. Jia, H. X. Chen, M. Huang, F. L. Zhao, J. R. Qiu, R. X. Li, Z. Z. Xu, X. K. He, J. Zhang, and H. Kuroda, Phys. Rev. B **72**, 125429 (2005).

[2]F. Costache, M. Henyk, and J. Reif, Appl. Surf. Sci. **186**, 352 (2002).

[3]F. Costache, M. Henyk, and J. Reif, Appl. Surf. Sci. **208-209**, 486 (2003).

[4]P. Rudolph and W. Kautek, Thin Solid Films **453-454**, 537 (2004).

[5]Q. Wu, Y. Ma, R. Fang, Y. Liao, Q. Yu, X. Chen, and K. Wang, Appl. Phys. Lett. **82**, 1703 (2003).

[6]R. Wagner, J. Gottmann, A. Horn, and E. W. Kreutz, Appl. Surf. Sci. **252**, 8576 (2006).

[7]T. Tomita, K. Kinoshita, S. Matsuo, and S. Hashimoto, Appl. Phys. Lett. **90**, 153115 (2007).

[8]J. Bonse, H. Sturm, D. Schmidt, and W. Kautek, Appl. Phys. A: Mater. Sci. Process. **71**, 657 (2000).

[9]N. Yasumaru, K. Miyazaki, and J. Kiuchi, Appl. Phys. A: Mater. Sci. Process. **81**, 933 (2005).

[10]N. Yasumaru, K. Miyazaki, and J. Kiuchi, Appl. Phys. A: Mater. Sci. Process. **76**, 983 (2003).

[11]M. Couillard, A. Borowiec, H. K. Haugen, J. S. Preston, E. M. Griswold, and G. A. Botton, J. Appl. Phys. **101**, 033519 (2007).

[12]A. Borowiec and H. K. Haugen, Appl. Phys. Lett. **82**, 4462 (2003).

[13]T. H. R. Crawford and H. K. Haugen, Appl. Surf. Sci. **253**, 4970 (2007).

[14]E. M. Hsu, T. H. R. Crawford, H. F. Tiedje, and H. K. Haugen, Appl. Phys. Lett. **91**, 111102 (2007).

[15]J. Bonse, M. Munz, and H. Sturm, J. Appl. Phys. **97**, 013538 (2005).

[16]X. J. Wu, T. Q. Jia, F. L. Zhao, M. Huang, N. S. Xu, H. Kuroda, and Z. Z. Xu, Appl. Phys. A: Mater. Sci. Process. **86**, 491 (2007).

[17]J. Reif, M. Ratzke, O. Varlamova, and F. Costache, Mater. Sci. Eng., B **134**, 114 (2006).

[18]X. C. Wang, G. C. Lim, F. L. Ng, W. Liu, and S. J. Chua, Appl. Surf. Sci. **252**, 1492 (2005).

[19]A. Weck, T. H. R. Crawford, D. S. Wilkinson, H. K. Haugen, and J. S. Preston, Appl. Phys. A: Mater. Sci. Process. **89**, 1001 (2007).

[20]M. Birnbaum, J. Appl. Phys. **36**, 3688 (1965).

[21]J. E. Sipe, J. F. Young, J. S. Preston, and H. M. van Driel, Phys. Rev. B **27**, 1141 (1983).

[22]Y. Dong and P. Molian, Appl. Phys. Lett. **84**, 10 (2004).

[23]Y. Shimotsuma, P. G. Kazansky, J. Qiu, and K. Hirao, Phys. Rev. Lett. **91**, 247405 (2003).

[24]C. Hnatovsky, R. S. Taylor, E. Simova, V. R. Bhardwaj, D. M. Rayner, and P. B. Corkum, Opt. Lett. **30**, 1867 (2005).

[25]C. Hnatovsky, R. S. Taylor, E. Simova, P. P. Rajeev, D. M. Rayner, V. R. Bhardwaj, and P. B. Corkum, Appl. Phys. A: Mater. Sci. Process. **84**, 47 (2006).

[26]V. R. Bhardwaj, E. Simova, P. P. Rajeev, C. Hnatovsky, R. S. Taylor, D. M. Rayner, and P. B. Corkum, Phys. Rev. Lett. **96**, 057404 (2006).

[27]R. M. Langford and A. K. Petford-Long, J. Vac. Sci. Technol. A **19**, 2186 (2001).

[28]T. H. R. Crawford, J. Yamanaka, G. A. Botton, and H. K. Haugen, J. Appl. Phys. **103**, 053104 (2008).

[29]J. Bonse, J. M. Wrobel, J. Krüger, and W. Kautek, Appl. Phys. A: Mater. Sci. Process. **72**, 89 (2001).

[30]S. Akturk, M. Kimmel, P. O'Shea, and R. Trebino, Opt. Express **11**, 491 (2003).

[31]Z. Sacks, G. Mourou, and R. Danielius, Opt. Lett. **26**, 462 (2001).

[32]E. Coyne, J. P. Magee, P. Mannion, G. M. O'Connor, and T. J. Glynn, Appl. Phys. A: Mater. Sci. Process. **81**, 371 (2005).

8.2   Microscopic investigation of single-crystal diamond following ultrafast laser irradiation

The work presented in this section focused on ultrafast laser surface and bulk irradiations of synthetic single-crystal diamond. Due to the properties of diamond, cutting and shaping of diamond is often carried out with lasers. Also, the wide bandgap of diamond facilitates formation of high spatial frequency LIPSS, as discussed in Section 2.1.5, as well as the article included below. The key findings of this work include initial observations of suppression of ablation with single-shot irradiation at high fluences, surface ripples with crystalline cores and an amorphous cap layer under stationary and translational irradiation, crack formation under bulk irradiation, and the formation of substantially sub-wavelength periodic structures at the exiting side-surface under translational bulk irradiation. Suggested follow up work includes characterization of irradiation with suppressed ancillary pulses, irradiation with frequency-converted pulses, and widening the range of laser irradiation parameters to characterize the formation of nanostuctures. Follow-up efforts have been carried out by M.Sc. student Jasper Brawley-Hayes.

A detailed introduction, experimental procedures, analysis, results and discussions are included in the article to follow (reprinted with permission from: **E. M. Hsu**, N. A. Mailman, G. A. Botton and H. K. Haugen, "Microscopic investigation of single-crystal diamond following ultrafast laser irradiation", Appl. Phys. A **103**, 185 (2011). Copyright 2011, Springer-Verlag). This was a collaborative project primarily with M.Sc. student Nicholas Mailman. I was involved in the sample selection, laser

irradiation, technical discussions throughout the analysis process, results interpretation, as well as carrying out the preparation of the manuscript.

Microscopic investigation of single-crystal diamond following ultrafast laser irradiation

E.M. Hsu · N.A. Mailman · G.A. Botton · H.K. Haugen

Abstract We present a structural investigation of single-crystal diamond following ultrafast laser irradiation of the surface and the bulk material. Optical microscopy, atomic force microscopy, scanning electron microscopy, and focused-ion beam and transmission electron microscopy techniques were utilized to selectively examine the final state of the samples. Laser induced periodic surface structures (LIPSS) with high- and low-spatial frequencies were obtained with multiple-pulse surface irradiation under both stationary and translated target conditions. High magnification transmission electron microscopy analysis of cross sections of the LIPSS revealed modified layers of a few tens of nanometers in thickness capping the crystalline diamond matrix. Sub-surface irradiation of diamond at high laser fluences led to damaged regions and cracks in the bulk material. When translational bulk irradiation of the diamond was performed, substantially sub-wavelength periodic structures were observed at the unpolished side facet of the diamond plate where the laser focus was translated out of the bulk. Spatial periods were 140 nm and the structures largely consisted of single-crystal diamond with a 10 nm modified layer. Finally, preliminary studies of single-shot laser ablation craters at high laser fluences exhibited suppression of material removal for peak values above 45 J/cm^2.

E.M. Hsu (✉)
Department of Engineering Physics, McMaster University,
Hamilton, L8S 4L7, Ontario, Canada
e-mail: hsue2@mcmaster.ca
Fax: +1-905-5278409

N.A. Mailman
(Formerly with the) Department of Physics and Astronomy,
McMaster University, Hamilton, L8S 4M1, Ontario, Canada
e-mail: mailmana@mcmaster.ca

G.A. Botton
Department of Materials Science and Engineering, McMaster
University, Hamilton, L8S 4M1, Ontario, Canada
e-mail: gbotton@mcmaster.ca

H.K. Haugen
Department of Engineering Physics and Department of Physics
and Astronomy, McMaster University, Hamilton, L8S 4L7,
Ontario, Canada
e-mail: haugenh@mcmaster.ca

1 Introduction

The electronic, physical, thermal, optical and chemical properties of diamond lends itself to many applications in different areas. However, due to the hardness of the material, shaping of diamond for specific applications is difficult (see e.g. [1, 2]). Often times Nd:YAG lasers are used to shape and clean industrial diamond, while higher precision work has been demonstrated with ns-pulsed excimer lasers [1, 2], and even more so with ultrashort laser pulses [2–4]. Ultrashort laser pulses are generally found to enable the processing of materials with minimal collateral damage, allowing higher precision machining of materials (see e.g. [5]). Due to the high intensity of ultrashort laser pulses, both the surface and the bulk of large bandgap materials can be modified since the high laser focal intensity facilitates higher order nonlinear absorption. In [2–4], the potential of surface laser machining of single-crystal diamond was explored, showing several advantages of employing femtosecond laser pulses over other laser systems.

A common phenomena observed in laser irradiated samples is the formation of periodic surface structures. Laser induced periodic surface structures (LIPSS) with spatial periods close to the irradiation wavelength had been observed

since the very early work on laser irradiation of materials [6–9]. However, substantially sub-wavelength periodic structures have also been observed on sample surfaces irradiated with ultrashort laser pulses (see, e.g., [10–16]), and have been referred to as high-spatial frequency LIPSS, or HSFL. Conversely, the classic LIPSS with low-spatial frequency have been referred to as LSFL (low-spatial frequency LIPSS). The formation mechanism of these HSFL is still under discussion in the current literature. There are several proposed explanations for the formation of HSFL, including self-assembly (see e.g. [10, 11]), nonlinear interactions (e.g. [12, 13]), adaptations (e.g. [14, 15]) of existing LSFL theories [7–9], as well as insights gained by taking surface plasmons into account [16].

In this work we present morphological and cross-sectional crystallographic studies of type IIa synthetic single-crystal diamond plates that have undergone surface and bulk irradiation with ultrashort laser pulses in order to help gain insight into the ablation, modification and LIPSS formation mechanisms in diamond. Four selected regimes of ultrafast laser modification of diamond are reported in the work. First, experiments on LIPSS formation under irradiation of the polished diamond surfaces at normal incidence are presented (Sect. 3.1). Subsequently experiments aimed at observation of the modification of bulk diamond under ultrafast irradiation with high laser fluences are discussed (Sect. 3.2). In connection with the bulk irradiation of translated target samples, nanostructures are revealed on the rough sides of the samples. These novel side-surface features are qualitatively different from those observed under our current irradiation conditions of smooth diamond surfaces at normal incidence (Sect. 3.3). Finally, high-fluence single-shot laser irradiation of smooth diamond surfaces at normal incidence is reported (Sect. 3.4).

2 Experimental setup

The output of a commercial titanium:sapphire chirped-pulse amplification system (CPA) was used to perform surface and bulk irradiation of diamond samples. The CPA delivers laser pulses with nominally ∼170 fs pulse duration, a central wavelength of 800 nm with a full-width at half-maximum bandwidth of 10 nm, at a repetition rate of 1 kHz. Pulse durations were extracted using a non-collinear second-order autocorrelation setup. Occasional tests are also done with a GRENOUILLE [17] and a tilted-pulse front autocorrelator [18] to ensure laser pulse quality in terms of pulse front tilt. The typical levels of ancillary pulses such as pre- and post-pulses inherent of regenerative amplifiers as well as weak satellite pulses that may arise from optical elements are discussed in an earlier work [19]. The maximum laser power used in the experiment was adjusted using a combination of a half-wave plate and thin-film polarizers. Further

control of the attenuation was achieved using neutral density filters mounted in computer-controlled motorized housings, allowing incremental steps of 0.1 in the optical density. Irradiation of the samples were carried out in rough vacuum, with a typical pressure of ∼0.05 mbar.

The diamond samples employed were $3 \times 3 \times 0.5$ mm type IIa synthetic single-crystal diamond plates with {001} faces, purchased from elementsix™. Single-side polished samples (product reference number 145-500-0045) were used for surface irradiation work, while double-side polished samples (product reference number 145-500-0100) were used for bulk-irradiation experiments to help facilitate transmission optical microscopy studies. As indicated by the type IIa classification, the samples are expected to contain <5 ppm of major impurities of nitrogen, and a value of 0.1–0.2 ppm was quoted by the supplier. Other defects such as multi-vacancy clusters and hydrogen related defects can also be expected in the material. The commercial specifications for these samples indicate the polished surfaces have an average roughness of 10 nm, while the side surfaces have an average roughness of <250 nm.

For surface irradiation, a $5 \times$ microscope objective was used. The highest initial pulse energy was adjusted to 40 μJ per pulse, and each successive target area was irradiated with decreasing energies corresponding to an incremental optical density steps of 0.1 as provided by the neutral density filters, to the highest attenuation at an optical density of 2.4. The number of laser pulses per irradiation site N employed in stationary irradiation ranged from $N = 1$ to 1000. Translational irradiations were carried out with the sample moving at a rate of 500 μm/s.

Bulk irradiation was performed with a $50 \times$ microscope objective (numerical aperture of 0.42) to obtain a tighter focal spot. The focal plane was first located on the sample surface, then subsequently translated 100 μm towards the sample, placing the nominal focal plane of the objective at low light intensity at an estimated depth of ∼240 μm below the sample surface. The sample was translated with the laser pulses focused into the bulk such that the beam is scanned over and out of the rough side surface of the samples (Fig. 1). The side facet was then used for preliminary cross-sectional studies. Two sets of lines were irradiated in the bulk of the samples. One set of embedded lines was irradiated with a sample translation rate of 500 μm/s, with an initial pulse energy of ∼10.2 μJ per pulse. To increase the cumulative fluence for a given irradiated area, a second sample was translated at a rate of 1 μm/s, with an initial pulse energy of 40 μJ.

Using the D^2 technique [20], the associated $1/e^2$ intensity radii for the beam waists at the focus of the $5 \times$ and the $50 \times$ objectives were determined to be ∼4.7 μm and ∼2.9 μm, respectively. To avoid underestimating the laser

spot sizes on diamond using the D^2 technique, an effect observed in other large bandgap materials [21], the spot sizes were extracted from features irradiated on silicon samples immediately prior to the irradiation of diamond samples.

Characterization of the laser processed samples was carried out using several microscopy techniques. Initial surveys of the damaged regions were performed using optical microscopy (OM) with Nomarski mode as well as scanning electron microscopy (SEM). Once an area of interest is selected, a focused-ion beam (FIB) was used to prepare cross-sectional specimens for transmission electron microscopy (TEM) studies. Details of FIB preparation of TEM specimens can be found in, e.g., [22]. During the FIB sample preparation, a layer of platinum was first deposited using electrons to avoid damaging the sample surface, followed by a layer of platinum, then carbon deposition with a Ga beam. An atomic force microscope (AFM) was also used on some sites of interest to obtain profiles of the irradiated regions.
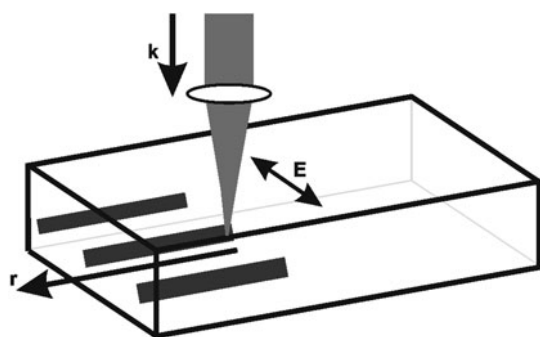
Fig. 1 Geometry of bulk irradiation. The laser pulses were focused into the bulk, and the sample was translated such that the laser focus was scanned across the sample and out of the rough side surface. Vectors **k**, **E** and **r** denote the directions of the laser beam propagation, electric field orientation and the direction of the translating laser focus, respectively

3 Results and discussion

3.1 Observation of surface ripples

Applying the D^2 technique on single-shot irradiated sites with OM analysis, the single-shot modification threshold for the diamond was found to be ~1.9 J/cm^2, comparable to 1.6 J/cm^2 reported in [4]. Following multiple-pulse stationary irradiation, laser induced periodic surface structures (LIPSS) were observed in irradiated sites over a range of fluences used and for different number of irradiating pulses, N. Translational irradiation also generated LIPSS in the irradiated regions.

In stationary irradiation at higher pulse energies, LIPSS can be observed for N as low as 2. At lower pulse energies, a higher number of shots were required for observable LIPSS. Low-spatial frequency LIPSS, or LSFL, with a period of 600–650 nm were present on all sites where LIPSS were observable. At $N = 10$ and a pulse energy of ~5.8 μJ (16.5 J/cm^2), only LSFL were observed (Fig. 2a). However, as N increases towards 50, high-spatial frequency LIPSS, or HSFL, with a spatial period of ~210 nm, become observable in regions where the local fluence is low. As an example, at $N = 50$ and a pulse energy of 0.4 μJ (~1.1 J/cm^2), HSFL is readily observed at the irradiation site (Fig. 2b). To further investigate the structures of the observed HSFL, cross-sectional TEM investigations were carried out on a FIB-prepared specimen from the crater irradiated with 50 pulses with a per-pulse energy of 0.4 μJ (~1.1 J/cm^2) (Fig. 2b–d). From high magnification TEM images, it was evident that there is a modified layer of ~25 nm capping the irradiated site, whereas the inner regions of the LIPSS consist of crystalline diamond matrix (Fig. 2c). Similar crystallography of HSFL had been observed in [23] on GaP.

Periodic surface structures were also observed in regions of the target under translational surface irradiation. For pulse energies greater than 1.9 μJ (~5.4 J/cm^2), LSFL with spatial periods of 550–660 nm were the dominant observable

Fig. 2 (**a**) SEM image of a site irradiated with $N = 10$ and a pulse energy of 5.8 μJ (~16.5 J/cm^2). (**b**) SEM image of a site irradiated with $N = 50$ and a pulse energy of 0.4 μJ (~1.1 J/cm^2). (**c**) Detailed TEM cross-sectional view of the *dashed rectangular area* in (**d**). (**d**) Cross-sectional TEM image of a specimen extracted from the *dashed rectangular region* shown in (**b**)
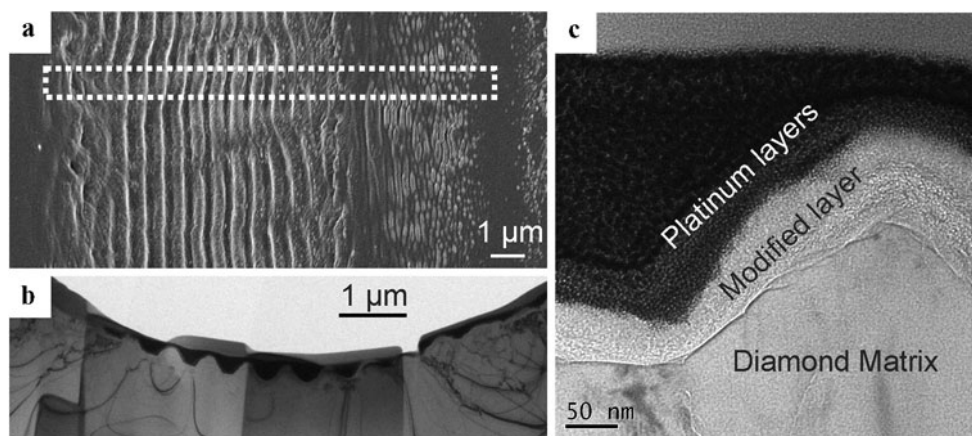
Fig. 3 Microscopy images of regions irradiated with 13.8 μJ (39.4 J/cm^2) pulses under irradiation of a translated target. (**a**) SEM top view. (**b**) Cross-sectional TEM image of a sample extracted from the *rectangular region* of (**a**). (**c**) High magnification TEM image showing a modified layer capping crystalline diamond matrix in the irradi-

ated region. The *black platinum top layers* were deposited during the sample preparation process with FIB. A layer of platinum was first deposited using electrons to avoid damaging the sample surface, followed by a layer of platinum and then carbon deposition using Ga-ion beam
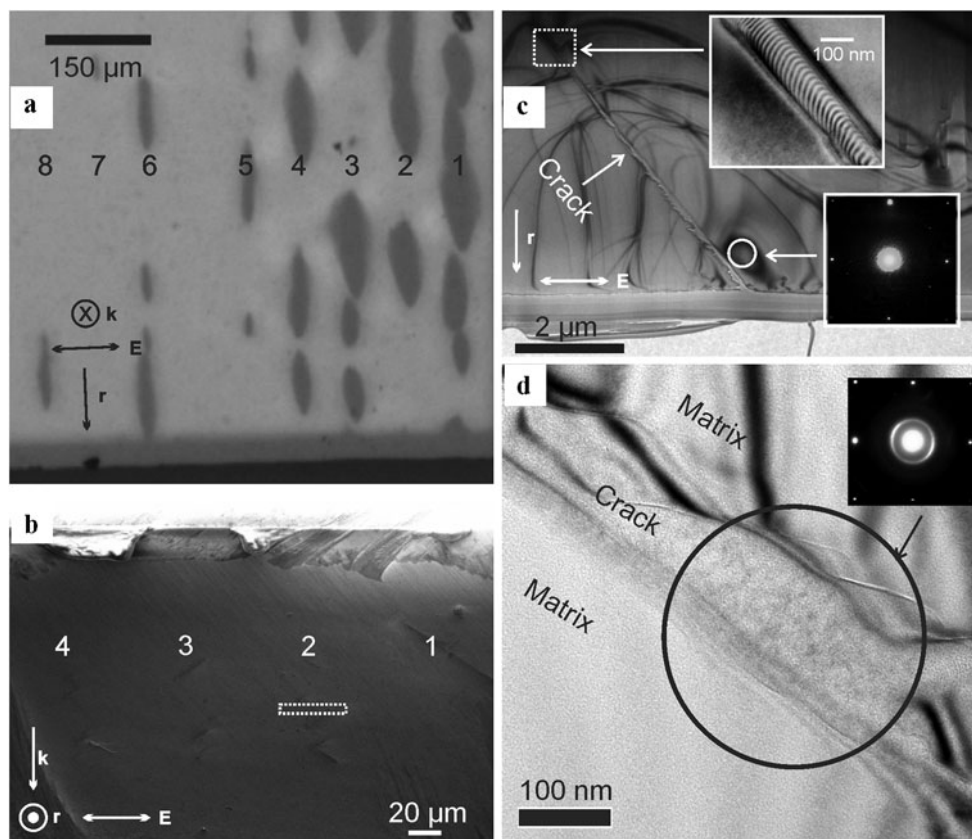
Fig. 4 Observations of laser irradiated regions in bulk diamond. Vectors **k**, **E** and **r** denote the directions of the laser beam propagation, electric field orientation and the direction of the translating laser focus, respectively. Region *1* was irradiated with 10.2 μJ pulses, *2*: 9.5 μJ, *3*: 8.0 μJ, *4*: 6.1 μJ, *5*: 4.9 μJ, *6*: 4.1 μJ, *7*: 3.8 μJ and *8*: 3.1 μJ. (**a**) Optical microscopy through the incident surface of the diamond, showing intermittent modified regions. (**b**) SEM image of the slightly polished side surface where the laser focus translated out of, showing cracks

in laser irradiated regions. (**c**) Cross-sectional TEM image of a FIB-prepared sample extracted from the region indicated by the *dashed rectangle* in region *2* in (**b**). Under higher magnification (*top inset*) periodic structures were observed at the termination of the crack. SAEDP *inset* shows single-crystal material near the crack. (**d**) High magnification of the crack, showing diamond matrix near the crack and SAEDP inset showing nanocrystalline material with very small grain size

feature. Below 1.9 µJ, a gradual transition of LSFL to HSFL was observed with decreasing energy. At low pulse energies HSFL with spatial periods of 230–240 nm become prominent. From a TEM cross-section analysis from a line irradiated with 13.8 µJ ($\sim$39.4 J/cm^2) pulses, a $\sim$50 nm of modified cap layer over the periodic structures was observed, while the inner regions consist of crystalline diamond matrix (Fig. 3). The TEM observations are qualitatively similar to results from stationary target irradiation.

Overall, for both stationary and translational irradiation schemes, the observed LIPSS were oriented perpendicular to the laser polarization. In stationary irradiation it was observed that lower numbers of pulses and higher fluences favours the formation of LSFL, while HSFL tend to form with higher numbers of pulses and lower local fluences. HSFL are also more prominent in translational irradiation when the local pulse fluence is low. The tendency for higher numbers of shots and lower fluences to favor the formation of HSFL is consistent with previous observation of LIPSS behavior in other material systems (e.g. [24]). The tendency for LSFL spatial periods to be somewhat less than the irradiation wavelength in air is commonly observed when ultrashort laser pulses are employed (see e.g. [16]), and the HSFL spatial periods relative to the irradiation wavelength in air and the material refractive index are on the order of those found in other material systems (see e.g. [10–16]). The LIPSS periods in translational irradiations are comparable to but slightly longer than those observed in the stationary irradiation. Electron energy loss spectroscopy (EELS) from the TEM samples showed that the modified cap layer consists of amorphous carbon in sp^2 hybridization.

3.2 Irradiation of bulk diamond

To investigate the effect of ultrashort-pulse laser irradiation of bulk diamond, the focal plane of the laser was positioned in the bulk by first locating the focus on the sample surface and subsequently translating the microscope objective 100 µm towards the sample surface. Irradiation was performed by translating the laser focus in the bulk and out of the unpolished side surface of the sample.

A set of embedded lines were irradiated with a sample translated at a rate 500 µm/s, with pulse energies ranging from 20 nJ to 10 µJ. Damage in the bulk was observable between pulse energies of $\sim$3.1–$\sim$10.2 µJ. Under OM, the modified regions in the bulk appeared to be intermittent rather than continuous along the direction of laser focus translation (Fig. 4a). The side facet of the crystal through which the laser beam exited was slightly polished to further expose the cross section of the bulk irradiated regions. SEM imaging of the side facet showed modified regions being observed at 110–200 µm below the surface, as well as cracks in these regions (Fig. 4b). A TEM study conducted on a FIB-prepared cross-sectional specimen from regions irradiated
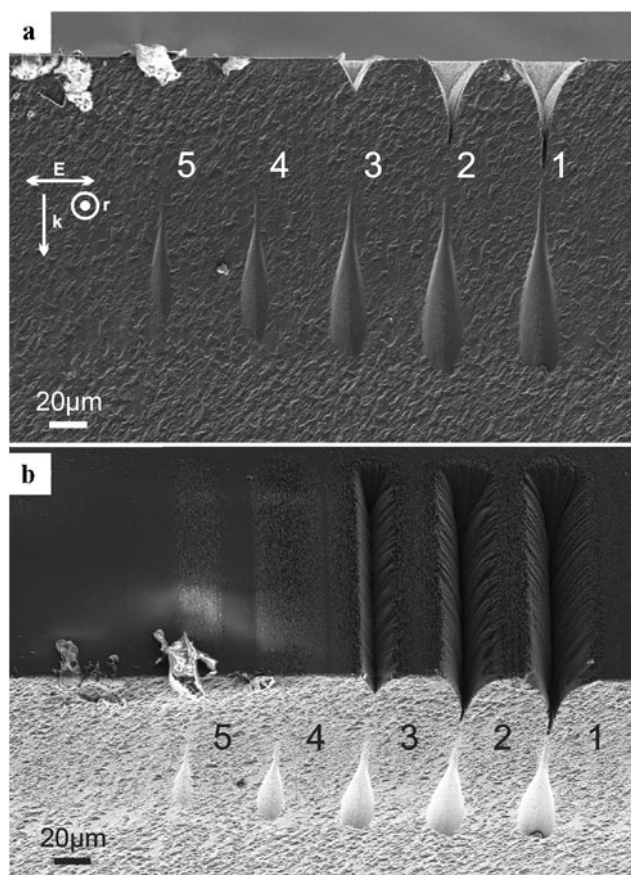
Fig. 5 SEM observations of the bulk diamond line-irradiated regions. The sample was translated at a rate of 1 µm/s. Vectors **k**, **E** and **r** denote the directions of the laser beam propagation, electric field orientation and the direction of the translating laser focus, respectively. Region *1* was irradiated with a per-pulse energy of 14.2 µJ, *2*: 12.9 µJ, *3*: 10.6 µJ, *4*: 7.7 µJ, *5*: 6.0 µJ. (**a**) Side view of the rough side surface where the laser focus translated out of the bulk, showing tear-drop shaped modified regions as well as evident material removal at the top surface where the laser was incident. (**b**) Bird's eye view of the same region

with 9.5 µJ pulses revealed a crack that is 200 nm in width, and indicates that the angle of these cracks corresponds to the {111} cleavage planes for diamond (Fig. 4c). Fine alternating structures were observed towards the termination of the observed crack (Fig. 4c inset), which may be due to contrast from a tilted twin or stacking fault. A selected area electron diffraction pattern (SAEDP) indicated the area near the crack is single-crystal (Fig. 4c inset), while the regions inside the crack contains nanocrystalline material with very small grain size (Fig. 4d and inset).

3.3 Nanostructures formed by irradiation of high angles of incidence

To increase the cumulative fluence for a given irradiated region in the bulk, a sample was irradiated with a set of embedded lines with the sample translating at a speed of 1 µm/s.

Fig. 6 Observations of periodic structures at the rough side surface through which the focused laser beam exited in experiments of bulk diamond irradiation using a translated laser beam. This particular site was irradiated with 7.7 µJ pulses. Vectors **k**, **E** and **r** denote the directions of the laser beam propagation, electric field orientation and the direction of the translating laser focus, respectively. (**a**)–(**e**) SEM images of different regions at various magnifications of the site as indicated by the respective labels. (**f**) TEM image of a cross-sectional specimen prepared perpendicularly to the orientation of the periodic structures, as indicated by the rectangle in (**c**)
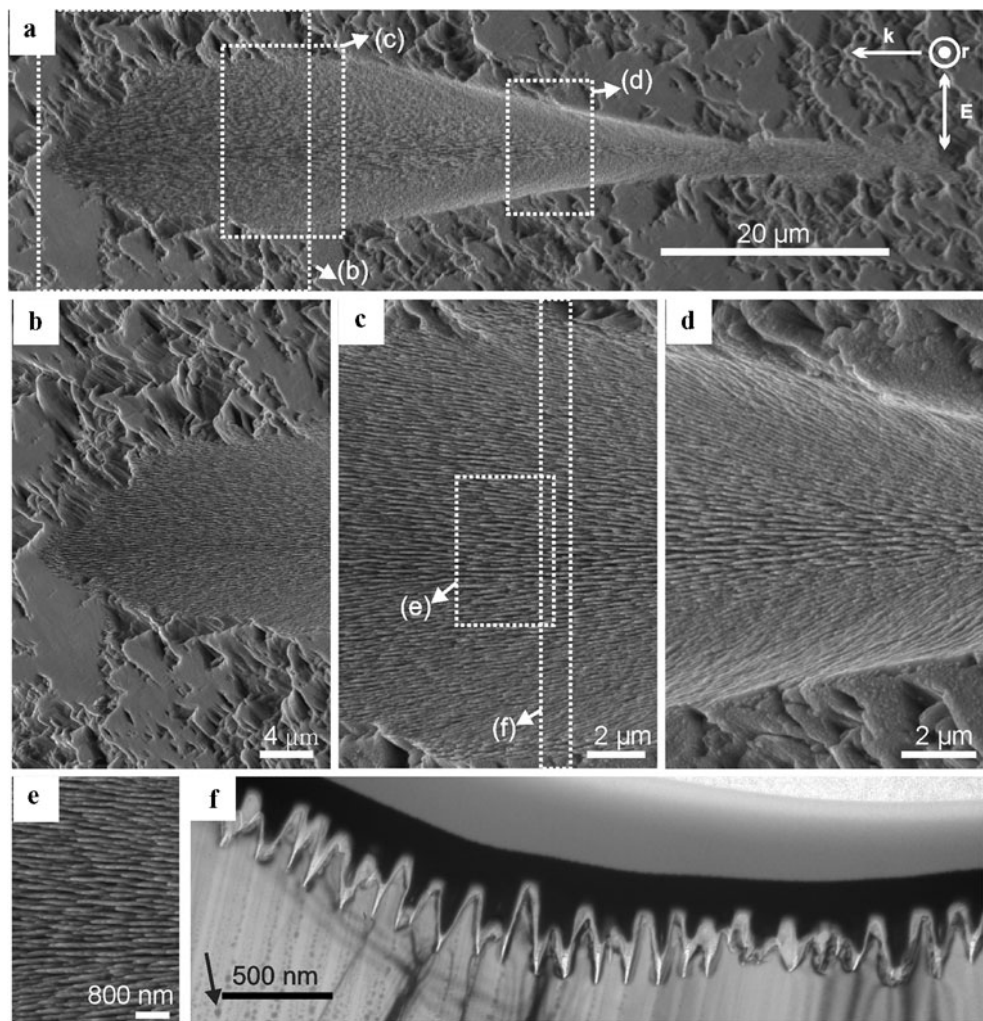
Pulse energies employed in this set of lines ranged from 20 nJ to ~40 µJ. No additional polishing of the side surface was performed following the irradiation of the sample. Bulk modifications, including material removal at higher pulse energies and generation of fine nanostructures at lower pulse energies, were observed at a depth of 150–200 µm. At pulse energies of 10.6 µJ and higher, material removal at the incident surface was observed. Under the focusing conditions for bulk irradiation, no bulk, incident- and side-surface modifications were evident for irradiation performed with pulse energies below 6.0 µJ. At 6.0 and 7.7 µJ, fine structures were observable at the top surface where the laser was incident, but material removal was not significant. SEM investigations of the side surface of the diamond plate through which the focused laser beam exited showed fine periodic structures in laser irradiated regions (Fig. 5). To facilitate a cross-sectional study of these periodic structures, a TEM specimen was prepared from the modified bulk region irradiated with 7.7 µJ pulses where the formation of these features appear to be the most pronounced (Fig. 6). The spatial periods of

these structures were found to be 140 nm, comparable to the average spacing observed in [25] under high repetition rate irradiation at normal incidence on synthetic single-crystal diamond. They were observed to mostly consist of unmodified single-crystal diamond matrix, capped with a very thin (~10 nm) layer of modified material. The dark spherical structures in the cross-sectional TEM image were artifacts from Ga ions introduced during the final stages of the FIB milling process, as confirmed using energy dispersive spectroscopy mapping. An example of such structure is indicated by the arrow in Fig. 6f.

Under the employed laser irradiation and microscopy conditions, no periodic structures were observed in the bulk of the diamond samples such as ones reported in other dielectric materials following post-laser irradiation microscopy, with (see e.g. [26, 27]) and without (see e.g. [28]) subsequent wet-etching procedures. It is possible that such structures may be present and were not observable with the microscopy techniques employed, or the favorable laser parameters for the generation of such structures in bulk diamond were not met.

3.4 High-fluence single-shot surface ablation

Initial OM and SEM observations showed rough annular features at the periphery of smoother central portions of the craters for irradiation sites using pulses with energies of 21.5 μJ (~62.5 J/cm^2) and above. Below this pulse energy the distinction between these two regions was not clearly evident. An AFM was used to obtain the profiles of selected craters exhibiting this two-region feature, showing that a higher material removal rate was achieved in the annular
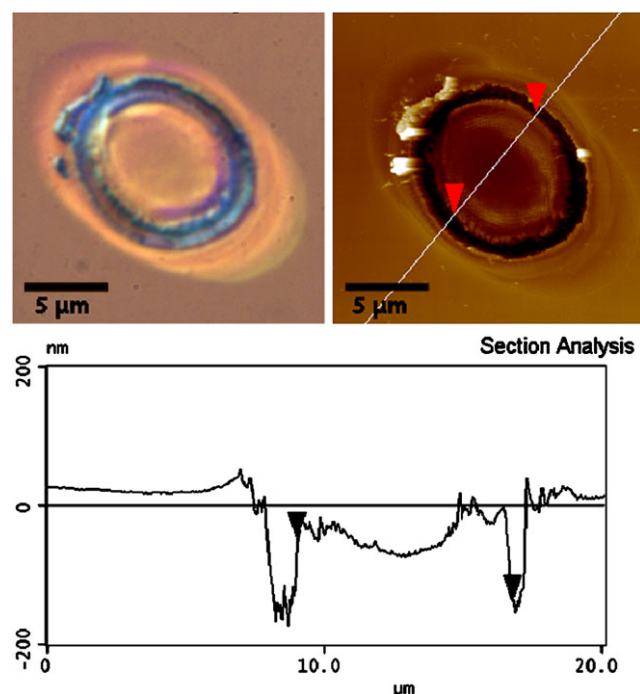
Fig. 7 OM (*top left*) and AFM (*top right*) images of a site irradiated with high 36.1 μJ (~105 J/cm^2) pulses, showing suppressions of material removal at the central portions of the craters, as better demonstrated in the AFM section analysis (*bottom*)
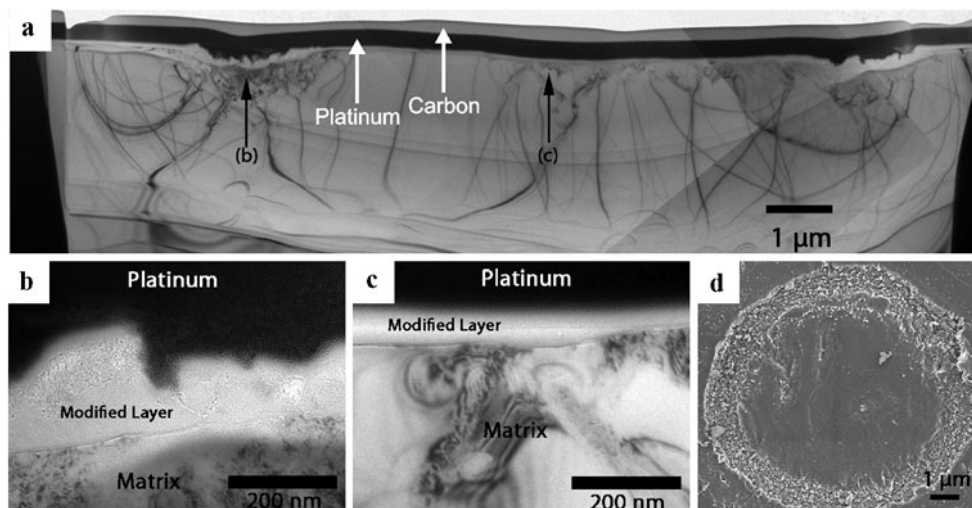
regions, while the material removal rate in the central regions are suppressed by comparison (Fig. 7). By applying the D^2 technique to track the evolution of the central suppressed region at sites irradiated with different pulse energies, a threshold fluence of ~45 J/cm^2 was found for the formation of the central feature. Although at this fluence the ≲1% post-pulse is significantly below that of the single-shot ablation threshold, consideration should be given to the state of the material in the ~7 ns time frame following energy deposition in the material from the main pulse. To enhance the extinction ratio between the ancillary pulses to the main pulse, follow-up studies can employ frequency conversion schemes to improve discrimination against pre- and post-pulses, as well as eliminating the use of neutral density filters in the attenuation scheme to prevent the generation of picosecond satellite pulses due to multiple reflection effects.

A TEM cross-sectional specimen was prepared using FIB from a single-shot crater irradiated with a pulse energy of 36.2 μJ (~104 J/cm^2), as shown in Fig. 8. The white and black top layers in Fig. 8 are protective carbon and platinum layers, respectively, that are deposited during the FIB-preparation process. In the rough annular region a modified layer is observed to be as thick as ~200 nm and exhibited a rough upper surface while showing a smooth interface with the underlying diamond matrix, as shown in Fig. 8b. Meanwhile, in the smooth central region of the crater the modified layer is ~50 nm thick and appeared smooth on both the upper surface and at the interface with the underlying diamond matrix (Fig. 8c). Due to the small thickness of the modified layer, a selected area or convergent beam electron diffraction pattern solely from this layer could not be obtained. However, a selected area diffraction pattern of the modified layer and parts of the protective platinum layer showed faint diffuse rings, indicating that this layer may be composed of nanocrystalline diamond and possibly amorphous carbon.

Fig. 8 Bright field image showing a section of a 36.2 μJ (~104 J/cm^2) single-pulse crater. *Arrows* (**b**) and (**c**) indicate the areas where higher magnification images are taken. (**d**) Overall SEM image of the irradiated area

Observations of central features in ablation craters in other materials have been reported in the literature. For example, protruding central features were observed in craters ablated in InP [29], as well as in GaAs [30]. In both [29] and [30], the formation of the central protruding features was attributed to the generation of a dense plasma on the sample surface. This argument is supported in the present work by the observation of the threshold behavior for the suppression in the central region, and the difference in the morphology and thickness of the modified cap layer in the different regions as discussed above. As an extension of these preliminary studies, additional tests for potential technical contributions to the suppression of ablation in the central region should be conducted.

4 Summary and future directions

In this work we presented structural and crystallographic investigations of single-crystal diamond plates following surface and bulk irradiation with ultrashort laser pulses. Both LSFL and HSFL were observed in multiple-shot stationary and translational irradiation of the samples, with LSFL being the dominant feature at higher fluences and lower numbers of shots, while low fluence, high N conditions favor the formation of HSFL. Bulk irradiation at high fluences was found to lead to creation of cracks in the irradiated region. Under bulk irradiation at a slow translation speed, substantially sub-wavelength periodic structures were observed at the side surface of the sample through which the focused laser beam exited. TEM studies revealed that the irradiated regions are generally capped by a layer of modified material. The thickness of the modified layer varied depending on the irradiation conditions. On another hand, the inner portions of the periodic structures, for both types of LIPSS, consist of unmodified single-crystal diamond matrix. Suppression of single-shot ablation was observed at very high fluences, with the effect exhibiting a threshold-like behavior. Future work can include high-fluence single-shot experiments under conditions of well-suppressed pre- and post-pulses and satellite pulses. Other wavelength regions could be explored as well. In terms of the sharp nanostructures, studies of their formation for a broad range of experimental parameters would be viable.

References

1. V.G. Ralchenko, S.M. Pimenov, *Processing, Handbook of Industrial Diamonds and Diamond Films* (Marcel Dekker, New York, 1998)
2. D. Ramanathan, P.A. Molian, J. Manuf. Sci. Eng. **124**, 389 (2002)
3. S. Preuss, M. Stuke, Appl. Phys. Lett. **67**, 338 (1995)
4. G. Dumitru, V. Romano, H.P. Weber, M. Sentis, W. Marine, Appl. Phys. A **74**, 729 (2002)
5. D. von der Linde, K. Sokolowski-Tinten, J. Bialkowski, Appl. Surf. Sci. **109/110**, 1 (1997)
6. M. Birnbaum, J. Appl. Phys. **36**, 3688 (1965)
7. H.M. van Driel, J.E. Sipe, J.F. Young, Phys. Rev. Lett. **49**, 1982 (1955)
8. J.E. Sipe, J.F. Young, J.S. Preston, H.M. van Driel, Phys. Rev. B **27**, 1141 (1983)
9. A.E. Siegman, P.M. Fauchet, IEEE J. Quantum Electron. **QE-22**, 1384 (1986)
10. F. Costache, M. Henyk, J. Reif, Appl. Surf. Sci. **186**, 352 (2002)
11. P. Rudolph, W. Kautek, Thin Solid Films **453–454**, 537 (2004)
12. J. Bonse, M. Munz, H. Sturm, J. Appl. Phys. **97**, 013538 (2005)
13. T.Q. Jia, H.X. Chen, M. Huang, F.L. Zhao, J.R. Qiu, R.X. Li, Z.Z. Xu, X.K. He, J. Zhang, H. Kuroda, Phys. Rev. B **72**, 125429 (2005)
14. Q. Wu, Y. Ma, R. Fang, Y. Liao, Q. Yu, X. Chen, K. Wang, Appl. Phys. Lett. **82**, 1703 (2003)
15. R. Wagner, J. Gottmann, A. Horn, E.W. Kreutz, Appl. Surf. Sci. **252**, 8576 (2006)
16. M. Huang, F. Zhao, Y. Cheng, N. Xu, Z. Xu, ACS Nano **3**, 4062 (2009)
17. S. Akturk, M. Kimmel, P. O'Shea, R. Trebino, Opt. Express **11**, 491 (2003)
18. Z. Sacks, G. Mourou, R. Danielius, Opt. Lett. **26**, 462 (2001)
19. T.H.R. Crawford, J. Yamanaka, G.A. Botton, H.K. Haugen, J. Appl. Phys. **103**, 053104 (2008)
20. J. Bonse, J.M. Wrobel, J. Krüger, W. Kautek, Appl. Phys. A **72**, 89 (2001)
21. D. Puerto, W. Gawelda, J. Siegel, J. Solis, J. Bonse, Appl. Phys. Lett. **92**, 219901 (2008)
22. R.M. Langford, A.K. Petford-Long, J. Vac. Sci. Technol. A **19**, 2186 (2001)
23. E.M. Hsu, T.H.R. Crawford, C. Maunders, G.A. Botton, H.K. Haugen, Appl. Phys. Lett. **92**, 221112 (2008)
24. E.M. Hsu, T.H.R. Crawford, H.F. Tiedje, H.K. Haugen, Appl. Phys. Lett. **91**, 111102 (2007)
25. M. Shinoda, R.R. Gattass, E. Mazur, Journal of Applied Physics **105**, 053102 (2009)
26. C. Hnatovsky, R.S. Taylor, E. Simova, P.P. Rajeev, D.M. Rayner, V.R. Bhardwaj, P.B. Corkum, Appl. Phys. A **84**, 47 (2006)
27. V.R. Bhardwaj, E. Simova, P.P. Rajeev, C. Hnatovsky, R.S. Taylor, D.M. Rayner, P.B. Corkum, Phys. Rev. Lett. **96**, 057404 (2006)
28. M. Budiman, E.M. Hsu, H.K. Haugen, G.A. Botton, Appl. Phys. A **98**, 849 (2010)
29. J. Bonse, G. Bachelier, J. Siegel, J. Solis, H. Sturm, J. Appl. Phys. **103**, 054910 (2008)
30. N. Stojanovic, D. von der Linde, K. Sokolowski-Tinten, U. Zastrau, F. Perner, E. Förster, R. Sobierajski, R. Nietubyc, M. Jurek, D. Klinger, J. Pelka, J. Krzywinski, L. Juha, J. Cihelka, A. Velyhan, S. Koptyaev, V. Hajkova, J. Chalupsky, J. Kuba, T. Tschentscher, S. Toleikis, S. Düsterer, H. Redlin, Appl. Phys. Lett. **89**, 241909 (2006)

8.3 Cross-sectional study of femtosecond laser bulk modification of crystalline α-quartz

This section presents a project focused on ultrafast laser irradiation of bulk crystalline quartz using ultrafast laser pulses. Due to its high intensity, ultrashort laser pulses are able to generate material modifications in a volume confined to the focal region, which has great potential for processing embedded features in transparent materials such as quartz. The key findings of this work showed the formation of alternating amorphous-crystalline quartz with sharp boundaries of density transitions in the irradiated bulk regions, leading to the formation of cracks. Future work can include further crystallographic studies to characterize the material response with a widened range of laser irradiation parameters.

Further introductory details, as well as descriptions of the experimental setup, results, and discussions are presented in the article below (reprinted with permission from: M. Budiman, **E. M. Hsu**, H. K. Haugen and G. A. Botton, "Cross-sectional study of femtosecond laser bulk modification of crystalline α-quartz" Appl. Phys. A **98**, 849 (2010). Copyright 2010, Springer-Verlag). This was a collaborative project primarily with M.A.Sc. student Mariana Budiman. I was involved in laser irradiation of samples, technical discussions throughout the analysis process, results interpretation, and contributed substantially to the manuscript preparation.

Cross-sectional study of femtosecond laser bulk modification of crystalline *α*-quartz

M. Budiman · E.M. Hsu · H.K. Haugen · G.A. Botton

Abstract Bulk irradiation of crystalline *α*-quartz was performed with ∼170-fs laser pulses with a wavelength of 800 nm focused below the sample surface. Investigations were carried out using transmission electron microscopy on a cross-sectional specimen prepared using focused ion beam techniques. We observed alternating amorphous–crystalline structures with sharp transitions and associated density changes, surrounded by a highly strained crystalline structure. The alternating sub-surface structures are parallel to the laser's electric field polarization and exhibit a spacing which is close to the laser wavelength in air. Cracking was also observed in the near proximity of these structures.

M. Budiman · G.A. Botton (✉)
Department of Materials Science and Engineering, McMaster University, Hamilton, Ontario L8S 4M1, Canada
e-mail: gbotton@mcmaster.ca
Fax: +1-905-5212773

M. Budiman
e-mail: budimam@mcmaster.ca
Fax: +1-905-5289295

E.M. Hsu
Department of Engineering Physics, McMaster University, Hamilton, Ontario L8S 4M1, Canada
e-mail: hsue2@mcmaster.ca
Fax: +1-905-5278409

H.K. Haugen
Department of Engineering Physics and Department of Physics and Astronomy, McMaster University, Hamilton, Ontario L8S 4M1, Canada
e-mail: haugenh@mcmaster.ca

1 Introduction

Ultra-short-pulse laser micromachining is a promising technique that offers precise and reproducible means of surface patterning and structuring, processing, energy deposition in minimized volume and heat-affected zone (HAZ), as well as contamination-free modification that is required for medical and biological applications. The precise processing and the minimum HAZ are made possible by the pulse duration that is shorter than the typical electron–phonon coupling time [1–3]. Cleaner features with minimal collateral damage can, in principle, be obtained. Nevertheless, there have been a number of reports on observed modifications of materials resulting in the formation of nanocrystalline, resolidified layers or even amorphous regions, suggesting melting of the material [4–9].

Certain applications such as waveguides [10, 11], microfluidic channels [12], and three-dimensional optical storage [13] can require modified regions embedded inside transparent materials. There have been a number of works on bulk irradiation of several crystalline and amorphous materials where localized refractive index, structural, as well as phase changes have been reported (see e.g. [10, 11, 13–24]). In some of these studies, chemical etching following laser irradiation revealed further structures in the irradiated volume [19–24]. Amongst transparent materials of potential technological interest, amorphous and crystalline quartz have wide applications in the fields of optoelectronics and photonics technologies because of its wide transparency ranging from the ultraviolet to the infrared region of the electromagnetic radiation. Given the technological importance and limited studies of laser irradiation of the bulk, we therefore report a detailed structural investigation with scanning electron microscopy (SEM) of quartz following laser irradiation, as well as cross-sectional transmission electron microscopy

(TEM) studies on a specimen prepared using focused ion beam (FIB) milling.

2 Experimental technique

A commercial Ti:sapphire chirped-pulse amplifier laser system was used to provide laser pulses with a central wavelength of 800 nm, a full width at half maximum bandwidth of ∼10 nm, a repetition rate of 1 kHz, and a pulse duration of ∼170 fs. The pulse duration was determined using a non-collinear second-order autocorrelator. A 50× microscope objective with a numerical aperture of 0.42 was used to irradiate a >1-mm-thick crystalline α-quartz sample with the C-direction parallel to the laser beam propagation. The focal plane of the objective was located in the bulk of the material by first finding the laser focus on the sample surface and subsequently translating the objective 200 μm towards the sample. During laser irradiation, the sample was translated at a rate of 500 μm/s, in the x direction as labeled in Fig. 1. The experiment was performed in a low vacuum of ∼0.05 mbar. Pulse energies employed in this experiment ranged from 0.2 to 5 μJ. The maximum pulse energy was first adjusted using a combination of a half-wave plate and thin-film polarizers, and further computerized control was achieved using a set of neutral density filters with steps of 0.1 in optical densities [25]. The typical level of weak pre- and post-pulses associated with the regenerative amplifier, and weak satellite pulses attributable to optical elements, has been discussed in an earlier publication [26]. In the sample irradiation with the 50× microscope objective, a 4.4-mm (e^{-2} diameter) beam was input onto a 3.3-mm entrance aperture on the objective. For the irradiation conditions described in this paper (1 kHz, 500 μm/s), it was determined that marking of the surface could just be observed for a pulse energy of 386 nJ as observed in a Zeiss AxioPlan 2 differential interference contrast optical microscope.

Following bulk irradiation of the sample, a cross section in the yz plane was prepared by polishing the sample with 30–0.5 μm diamond lapping films using a Techprep™ ALLIED (Multi-Prep) polisher. Initial investigations were carried out using a SEM to view the yz plane, followed by FIB milling with gallium ions (Zeiss NVision-40 Dualbeam) to expose the xy plane in the region marked by the dashed arrows in Fig. 2a. In order to prevent strong electron beam charging during the investigations, a 5-nm-thick carbon layer was deposited on the sample using a Gatan precision etching coating system (PECS, model-682). Following ion milling, imaging of the exposed areas was then carried out with the SEM using the in-lens detector of the SEM column of the dual-beam system so as to enhance the contrast due to the defects.

In order to further investigate the xy plane with TEM, a cross-sectional specimen was prepared with the FIB using the lift-out method, a technique detailed in [27]. The specimen was a ∼100-nm lamella, which was subsequently coated with a 2-nm-thick carbon film deposited with the PECS in order to prevent charging and sample damage in the TEM. The investigations were performed with a Philips CM-12 120-keV TEM for imaging and diffraction analysis

Fig. 1 Schematic diagram of the femtosecond laser irradiation inside transparent materials. Cross-sectional investigation is conducted along xy and yz planes. The scanning direction of the laser irradiation is along the x axis, the electric field polarization is along the y axis, and the C direction of the sample is along the z axis
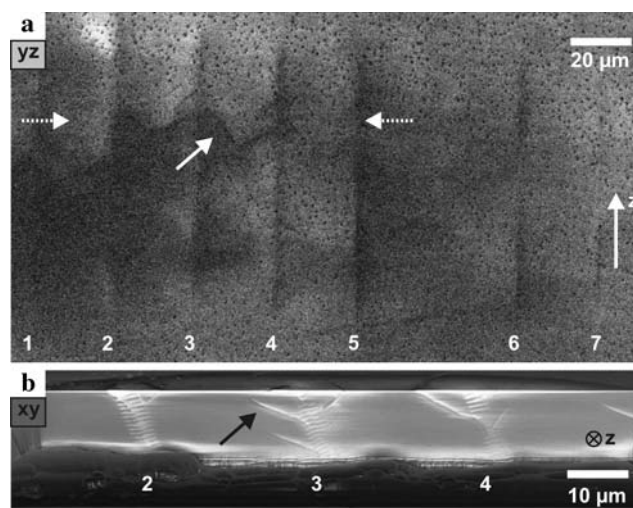
Fig. 2 SEM images show (**a**) the yz plane cross section of bulk-irradiated regions with decreasing laser pulse energies *from left to right*, (**b**) alternating fringes were observed in the SEM in the xy plane cross section, following gallium-ion milling of the laser-irradiated area indicated by the *dashed arrows* in (**a**). Areas 2, 3, and 4 indicate regions irradiated with pulse energies of 4.6 μJ, 3.7 μJ, and 2.8 μJ, respectively. *Solid arrows* in both (**a**) and (**b**) indicate examples of cracks observed. The tracks of alternating structures in the xy plane in (**b**) are not running parallel to the yz plane, since the scanning direction was not exactly perpendicular to the edge of the specimen

as well as a VG HB-601 UX scanning transmission electron microscope (STEM) operated at 100 keV for electron energy loss spectroscopy (EELS).

3 Results and discussion

Figure 2a shows initial SEM observations in the yz plane exhibiting signs of damage in regions irradiated with pulse energies from 1.6 to 5 µJ, extending from a depth of ∼220 µm to 310 µm and having a width of ∼5 µm. However, with the differential interference contrast optical microscope we were able to observe damage from regions irradiated with a pulse energy as low as 386 nJ.

Cracks are observed in the damaged regions of Fig. 2a, at about 45° from the C axis of the specimen, with an example indicated by the solid arrow. Cross-sectional SEM observations in the xy plane following ion milling in a selected region showed alternating crystalline–amorphous structures, as shown in Fig. 2b. These alternating structures are oriented parallel to the laser's electric field polarization, and have spacings of 725 nm, 785 nm, and 806 nm for lines irradiated with 4.6 µJ, 3.7 µJ, and 2.8 µJ, respectively. Cracks are also observed in the xy plane, with an example indicated by the arrow in Fig. 2b.

Figures 3a and d show bright-field TEM images of the periodic structure resulting from irradiation with a pulse energy of 3.7 µJ. A maximum contrast is obtained when the quartz is on the perfect zone axis orientation as in the central region of Fig. 3d. Electron diffraction patterns taken from the periodic structures (Fig. 3b) and the proximity (Fig. 3c)

Fig. 3 (**a**) The general overview of FIB-TEM sample of the periodic sub-surface features resulting from irradiation with pulse energy of 3.7 µJ. *The arrow* indicates an example of the cracks observed. (**b**) The diffraction pattern of amorphous fringes. (**c**) The diffraction pattern of the crystalline area. (**d**) Higher magnification of the fringes

show that the bright fringes observed in the SEM images (i.e. Fig. 2b) are amorphous material, surrounded by a crystalline matrix containing cracks (Figs. 2 and 3). The diffraction patterns also show that there is no detectable change in the quartz crystal structure outside the fringe regions. These conclusions are supported by the observation of bend contours arising from bending of the thin foil in the regions surrounding the amorphous fringes. Due to the relaxation in the foil and the presence of cracks, it is not possible to extract information about residual strain in the matrix in the proximity of the fringes.

Further investigations of the lamella with EELS in the scanning transmission electron microscope revealed no spectral changes in the energy range of 0 to 200 eV. This indicates that only structural modification of quartz (i.e. from crystalline to amorphous silica) took place, and compositional modification, such as an overabundance of Si, is not present. The structural changes were observed to be very localized to the fringes, with sharp transitions between the crystalline and amorphous regions. These structural changes are accompanied by significant local density changes (quartz has density of 2.65 g/cm^3 and fused silica 2.2 g/cm^3 [28]), and are likely to contribute to significant internal stresses in the sample and subsequently causing the observed cracks.

Observations of the cracks in the yz and the xy planes, as shown in Figs. 2 and 3 suggest that the cracks preferentially propagate in a plane approximately at 45° angle from the horizontal axis, possibly the r- and z-plane cleaving in quartz resulting from highly localized or confined pressure, as reported in [29]. The presence of the cracks in quartz was also observed in an additional surface irradiation experiment, in which case the cross-sectional SEM and TEM investigations revealed cracks on quartz with similar orientation, and an amorphous layer capping the unmodified quartz.

Comparisons can be made between the present work and the study of Gorelik et al. [15] on femtosecond laser induced bulk modifications of quartz. In the work [15], under low-energy single-shot irradiation conditions, laser-affected regions exhibiting amorphous structures having a sharp interface with a crystalline matrix with high residual strain were observed. On the other hand, under low-energy multi-shot as well as high-energy single- and multi-shot irradiations, a more complex outcome involving amorphous and damaged crystalline regions was observed. In addition, energy-dispersive X-ray line scans on low energy irradiated regions revealed no change in the Si and O ratio. In the present work, the observations of a sharp amorphous–crystalline interface, high residual strain in the crystalline matrix, and the lack of compositional change are consistent with the findings in [15]. It should be noted that in the comparison between [15] and the present study, the resulting amorphous regions were studied under different irradiation and observation geometries.
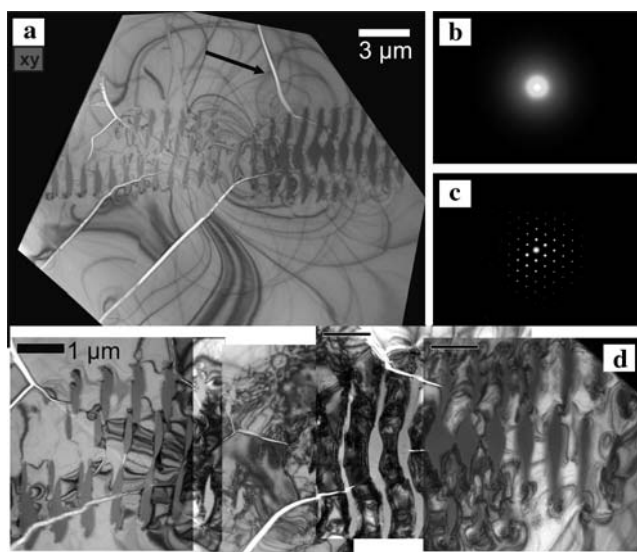
The observed periodic structures in this work, with a spacing near the irradiation wavelength and oriented parallel to the electric field, can be compared with structures observed in other studies of materials following ultra-short-pulse laser irradiations. In bulk irradiation experiments of fused silica, periodic structures perpendicular to the laser's electric field were observed following laser irradiation with 40–500 fs pulses and wet etching [19, 20]. However, the spacing of the periodic structures of ~242 nm in these works is significantly below the irradiation wavelength, comparable to $\lambda/2n$, where n is the refractive index of fused silica at the fundamental wavelength. It should also be noted that the irradiation conditions in these works differ considerably from ones employed in our experiment. More specifically, despite the use of a higher numerical aperture microscope objective, the works [19] and [20] would have resulted in a much higher effective number of pulses for a given region than in our work due to the use of a higher laser repetition rate of 100 kHz and a slower sample translation rate of 30 µm/s. In a recent study of bulk irradiation of sapphire [30], sub-wavelength ripples parallel to the electric field polarization, termed 'second kind' ripples, have been reported.

Comparisons can also be made with periodic structures observed following surface irradiations. In a study of periodic structures found on GaP surfaces following surface irradiation, it had been observed that irradiation with a low number of pulses tends to generate periodic structures with spatial periods somewhat close to the irradiation wavelength, while a high number of pulses favors the generation of periodic structures with spatial periods that are substantially sub-wavelength [31]. However, it should be noted that the spacing of periodic surface structures may not solely depend on the irradiation conditions, but also on material characteristics [32]. In reports of surface irradiation, periodic structures with near- and substantially sub-wavelength spacing have both been observed in different materials systems (see e.g. [1, 4, 6, 7, 31, 33–39]). Despite most reported periodic surface structures being perpendicular to the laser's electric field polarization, there have also been observations of surface structures oriented parallel to the laser's electric field on diamond film [38] and ZnSe [39].

Our high-resolution characterization did not reveal voids that have been attributed to microexplosions, as reported in other studies with tightly focused femtosecond laser pulses in the bulk of transparent materials [13, 16–18, 22, 24, 40]. In [18], it was reported that as the pulse energy increases the observed morphology evolved from surface relief to voids and cracking. However, it should be noted that conclusions drawn from comparisons between the present work and [18] should take into account the differences between the experimental parameters.

4 Summary and conclusions

Following femtosecond laser irradiation of bulk crystalline quartz, an alternating amorphous–crystalline structure with the spacing on the order of the laser wavelength in air has been observed with cross-sectional investigations. The absence of compositional changes has been confirmed using EELS. The sharp transitions of the density from crystalline to amorphous along the alternating structure contribute to the presence of the observed internal cracks. This preliminary work should be extended by incorporating a broader range of irradiation conditions, including laser spot size and irradiation fluence, scan speed, and polarization orientation. Wet etching may also be performed following laser irradiation and mechanical polishing of the sample to reveal features that may not have been observable with microscopy techniques employed in this work.

References

1. J.C. Miller, R.F. Haglund (eds.), *Laser Ablation and Desorption* (Academic Press, San Diego, 1998)
2. D. von der Linde, K. Sokolowski-Tinten, J. Bialkowski, Appl. Surf. Sci. **109–110**, 1 (1997)
3. Y.L. Yao, H. Chen, W. Zhang, Int. J. Adv. Manuf. Technol. **26**, 598 (2005)
4. A. Borowiec, M. Couillard, G.A. Botton, H.K. Haugen, Appl. Phys. A **79**, 1887 (2004)
5. J. Jia, M. Li, C.V. Thompson, Appl. Phys. Lett. **84**, 3205 (2004)
6. M. Couillard, A. Borowiec, H.K. Haugen, J.S. Preston, E.M. Griswold, G.A. Botton, J. Appl. Phys. **101**, 033519 (2007)
7. E.M. Hsu, T.H.R. Crawford, C. Maunders, G.A. Botton, H.K. Haugen, Appl. Phys. Lett. **92**, 221112 (2008)
8. J. Bonse, J.M. Wrobel, K.-W. Brzezinka, N. Esser, W. Kautek, Appl. Surf. Sci. **202**, 272 (2002)
9. J. Bonse, S.M. Wiggins, J. Solis, Appl. Surf. Sci. **248**, 151 (2005)
10. D. Liu, Y. Li, R. An, Y. Dou, H. Yang, Q. Gong, Appl. Phys. A **84**, 257 (2006)
11. V. Diez-Blanco, J. Siegel, J. Solis, Appl. Phys. A **88**, 239 (2007)
12. Y. Cheng, K. Sugioka, K. Midorikawa, Opt. Lett. **29**, 2007 (2004)
13. E.N. Glezer, M. Milosavljevic, L. Huang, R.J. Finlay, T.-H. Her, J.P. Callan, E. Mazur, Opt. Lett. **21**, 2023 (1996)
14. S. Nolte, M. Will, B.N. Chichkov, A. Tünnermann, Proc. SPIE **4637**, 188 (2002)
15. T. Gorelik, M. Will, S. Nolte, A. Tuennermann, U. Glatzel, Appl. Phys. A **76**, 309 (2003)
16. Y. Wang, S. Dong, Y. Yang, Y. Liang, H. Zou, Proc. SPIE **6149**, 61493F (2006)
17. E.N. Glezer, E. Mazur, Appl. Phys. Lett. **71**, 882 (1997)
18. C.B. Schaffer, A.O. Jamison, E. Mazur, Appl. Phys. Lett. **84**, 1441 (2004)
19. C. Hnatovsky, R.S. Taylor, E. Simova, P.P. Rajeev, D.M. Rayner, V.R. Bhardwaj, P.B. Corkum, Appl. Phys. A **84**, 47 (2006)
20. V.R. Bhardwaj, E. Simova, P.P. Rajeev, C. Hnatovsky, R.S. Taylor, D.M. Rayner, P.B. Corkum, Phys. Rev. Lett. **96**, 057404 (2006)

21. D. Wortmann, J. Gottmann, N. Brandt, H. Horn-Solle, Opt. Express **16**, 1517 (2008)
22. M. Mazilu, S. Juodkazis, T. Ebisui, S. Matsuo, H. Misawa, Appl. Phys. A **86**, 197 (2007)
23. S. Matsuo, Y. Tabuchi, T. Okada, S. Juodkazis, H. Misawa, Appl. Phys. A **84**, 99 (2006)
24. S. Juodkazis, K. Nishimura, S. Tanaka, H. Misawa, E.G. Gamaly, B. Luther-Davies, L. Hallo, P. Nicolai, V.T. Tikhonchuk, Phys. Rev. Lett. **96**, 166101 (2006)
25. T.H.R. Crawford, J. Yamanaka, G.A. Botton, H.K. Haugen, J. Appl. Phys. **103**, 053104 (2008)
26. T.H.R. Crawford, J. Yamanaka, E.M. Hsu, G.A. Botton, H.K. Haugen, Appl. Phys. A **91**, 473 (2008)
27. R.M. Langford, A.K. Petford-Long, J. Vac. Sci. Technol. A **19**, 2186 (2001)
28. E.D. Palik, *Handbook of Optical Constants of Solids II* (Academic Press, San Diego, 1991)
29. J.D. Dana, E.S. Dana, C. Palache, H.M. Berman, C. Frondel, *The System of Mineralogy of James Dwight Dana and Edward Salisbury Dana*, 7th edn. (Wiley/Chapman and Hall, New York/London, 1944)
30. M. Hörstmann-Jungemann, J. Gottmann, D. Wortmann, J. Laser Micro/Nanoeng. **4**, 135 (2009)
31. E.M. Hsu, T.H.R. Crawford, H.F. Tiedje, H.K. Haugen, Appl. Phys. Lett. **91**, 111102 (2007)
32. R. Wagner, J. Gottmann, A. Horn, E.W. Kreutz, Appl. Surf. Sci. **252**, 8576 (2006)
33. J. Bonse, S. Baudach, J. Krüger, W. Kautek, M. Lenzner, Appl. Phys. A **74**, 19 (2002)
34. N. Yasumaru, K. Miyazaki, J. Kiuchi, Appl. Phys. A **81**, 933 (2005)
35. G. Dumitru, V. Romano, H.P. Weber, M. Sentis, W. Marine, Appl. Phys. A **74**, 729 (2002)
36. A. Borowiec, H.K. Haugen, Appl. Phys. Lett. **82**, 4462 (2003)
37. T.H.R. Crawford, H.K. Haugen, Appl. Surf. Sci. **253**, 4970 (2007)
38. Q. Wu, Y. Ma, R. Fang, Y. Liao, Q. Yu, X. Chen, K. Wang, Appl. Phys. Lett. **82**, 1703 (2003)
39. T.Q. Jia, H.X. Chen, M. Huang, F.L. Zhao, J.R. Qiu, R.X. Li, Z.Z. Xu, X.K. He, J. Zhang, H. Kuroda, Phys. Rev. B **72**, 125429 (2005)
40. D.-L. Wang, C.-D. Li, L. Luo, H. Yang, Q.-H. Gong, Chin. Phys. Lett. **18**, 65 (2001)

8.4   Femtosecond laser irradiation of metal and thermal oxide layers on silicon: studies utilising cross-sectional transmission electron microscopy

This section of the thesis presents a project focused on ultrafast laser irradiation of metal-silicon dioxide-bulk silicon multilayered structures. Such structures are used in device applications, and characterization of ultrafast laser processing of this type of structure can open up potential usage of laser processing in device fabrication. The key findings of this work indicated that removal of the top-most metal layer without sub-surface damage to the oxide and silicon layers is possible. However there is a fluence range where the oxide layer appeared relatively undamaged under SEM investigations, but cross-sectional TEM studies showed extensive dislocations in the underlying silicon crystal matrix. Future work can include irradiation of similar multiple-layered structures with different materials and thicknesses to shed further insights into the laser-material interaction dynamics.

Further details of the background, experimental setup, results and discussions are presented in the article included below (reprinted with permission from T. H. R. Crawford, J. Yamanaka, **E. M. Hsu**, G. A. Botton, H. K. Haugen, "Femtosecond laser irradiation of metal and thermal oxide layers on silicon: studies utilising cross-sectional transmission electron microscopy", Appl. Phys. A **91**, 473 (2008). Copyright 2008, Springer-Verlag). This was a collaborative project with then Ph.D. student Dr. Travis Crawford, and Dr. Junji Yamanaka. I conducted the laser irradiation with 400 nm pulses, as well as carrying out the subsequent analysis.

T.H.R. CRAWFORD[1]
J. YAMANAKA[2]
E.M. HSU[1]
G.A. BOTTON[3,4,5,✉]
H.K. HAUGEN[1,4,5,6,✉]

Femtosecond laser irradiation of metal and thermal oxide layers on silicon: studies utilising cross-sectional transmission electron microscopy

[1] Department of Engineering Physics, McMaster University, Hamilton, Ontario, Canada, L8S 4L7

[2] Center for Crystal Science and Technology, University of Yamanashi, 7 Miyamae-cho,
Kofu 400-8511, Japan

[3] Department of Materials Science and Engineering, McMaster University, Hamilton, Ontario, Canada,
L8S 4L7

[4] Brockhouse Institute for Materials Research, McMaster University, Hamilton, Ontario, Canada, L8S 4L7

[5] Center for Emerging Device Technologies, McMaster University, Hamilton, Ontario, Canada, L8S 4L7

[6] Department of Physics and Astronomy, McMaster University, Hamilton, Ontario, Canada, L8S 4L7

ABSTRACT We present the results of 800 and 400 nm wavelength, femtosecond laser pulse irradiation of a sample consisting of a metal film on thermally-grown oxide on silicon. On selected sites, cross-sectional transmission electron microscopy was performed to provide information on sub-surface changes not observable with surface scanning electron microscopy. A range of pulse energies in single-pulse irradiation exists for which the metal film was removed but the oxide was not appreciably thinned. For a sufficiently high pulse energy within this range, substantial defects were observed in the underlying silicon. Five infrared pulses of a relatively high fluence created significant defects, as well as producing polycrystalline material on top of the original oxide and metal. We discuss various factors which may play a role in the formation of the observed features.

1 Introduction

Femtosecond laser micromachining of materials has become an active area of research, since the short pulse duration can provide potential benefits over longer pulses [1]. Transmission electron microscopy (TEM) has previously been used to investigate the crystallographic changes present in femtosecond laser irradiated semiconductors, both on plan-view samples [2, 3], and cross-sectional samples [4–10]. Analysis of the final crystallographic state of laser-irradiated structures can provide insight into the fundamental physical processes of ultrashort laser–matter interactions. Silicon covered with oxide and metallic layers is used extensively in the electronics industry, and provides a more complex configuration than a simple bulk substrate. Given the emergence of femtosecond laser machining applications in this industry, it is important to understand the effects of such pulses on these

layers. Laser pulses could potentially be used to selectively remove the metallization, but the resulting substructure and the possibility of damage below the surface should be understood. Such damage may not be apparent from surface imaging techniques such as scanning electron microscopy (SEM).

2 Experimental

Linearly polarized pulses with a duration and center wavelength of $\sim 150\,\mathrm{fs}$ and $\lambda = 800\,\mathrm{nm}$ respectively were produced by a commercial regeneratively amplified Ti:sapphire-based laser system operating at a 1 kHz repetition rate. A half-wave plate and thin film polarizer were used to reduce the pulse energy. Samples were irradiated either with $\lambda = 800\,\mathrm{nm}$ light or with 400 nm light generated by placing a 500 μm-thick AR-coated BBO crystal after the polarizer. In the 400 nm case the residual transmitted 800 nm light was removed by a series of highly reflective dielectric mirrors at $\lambda = 400\,\mathrm{nm}$. For some irradiation sites, one or two $\sim 1\,\mathrm{mm}$-thick metallic neutral density filters were then used to further attenuate the pulse energy. A mechanical chopper synchronized with the laser reduced the pulse repetition rate to 50 Hz, slow enough for the selection of single pulses using a synchronized mechanical shutter. Pulses were focused onto the sample at approximately normal incidence using a 5× microscope objective. The sample was placed on an aluminum cylinder inside a small vacuum chamber equipped with a 1 mm-thick fused silica window. The chamber was mounted on a computer-controlled xy translation stage, and evacuated to a rough vacuum of less than $\sim 0.1\,\mathrm{mbar}$. Observation of the sample during machining was accomplished with a confocal CCD camera and light source. Before the commencement of machining, a calibrated silicon photodiode power meter (quoted accuracy ±5%) was used to measure the average power after the objective and window. A CCD-based beam profiler confirmed that to a reasonable approximation, the unfocused beam profile was Gaussian.

The on-sample spot size $\omega_\circ$ (spatial radius at $1/e^2$ of peak intensity) was measured using a D^2 method as described in

✉ Fax: +1-905-528-9295, E-mail: gbotton@mcmaster.ca
✉ Fax: +1-905-527-8409, E-mail: haugenh@mcmaster.ca

a previous work [11]. This allowed the calculation of the peak pulse fluence $(2E)/(\pi\omega_\circ^2)$ from the pulse energy E. A set of metallic neutral density filters was used to provide attenuation in the D^2 method in steps of 0.1 OD (transmission $= 10^{-OD}$). Uncertainties in the pulse energy and spot size lead to an uncertainty in the fluence of approximately $\pm 30\%$. Fluences are those incident at the sample surface, as we did not consider reflection at that surface.

Silicon of (100) surface orientation and phosphorous-doping (quoted resistivity of 12 Ω cm) was used in this study. The wafer thickness was approximately 300 μm, with a polished front surface and a rough back surface. The wafer was cleaned using a standard cleaning procedure involving boiling H_2SO_4/H_2O_2, boiling H_2O_2/HCl, and an HF solution. Following cleaning, an oxide layer was thermally grown on the wafer by placing it inside a thermal oxidation furnace at approximately 1100 °C. Oxygen was bubbled through ~ 95 °C water before entering the furnace at one end. An oxide thickness on the order of 250 nm was estimated via comparisons to a thin-film colour chart. An ultrahigh vacuum electron beam evaporator with a quartz crystal thickness monitor was used to deposit ~ 25 nm of titanium, ~ 50 nm of platinum, and ~ 240 nm of gold on the oxide. The titanium and platinum layers improve adhesion of the gold and reduce possible migration of the gold into the substrate. On the rough back surface, ~ 25 nm of titanium and ~ 200 nm of gold were deposited.

After irradiation, the sites were imaged using the secondary electron imaging mode of SEM. Energy-dispersive X-ray spectroscopy (EDXS) was used in the scanning electron microscope to help identify the elemental composition of various locations on the sample surface. Cross-sectional slices of the bulk material were prepared using the focused ion beam (FIB) milling technique. This allows the preparation of an electron-transparent specimen, suitable for TEM imaging. Coatings of palladium and tungsten were deposited to protect the surface before gallium ion beam milling in the FIB machine. Bright-field TEM imaging, with an electron acceleration voltage of 120 kV, was used to image the FIB specimens.

3   Results and discussion

3.1   *Single pulse irradiation*

Figure 1 shows plan-view SEM images of the multiple-layer sample, with each site irradiated by a single pulse. A rather sharp boundary exists between the darker central area of the sites and the brighter material covering the rest of the sample. The SEM images suggest that the titanium/platinum/gold layer was removed in the central (darker) area of the sites, as the lower atomic number elements (silicon and oxygen) produce a lower secondary electron signal in the microscope. EDXS spectra taken at the centers of sites in Fig. 1 possessed prominent silicon and oxygen peaks with no significant peaks at energies corresponding to the three metals, indicating that the metal layer was removed there.

Below a peak pulse fluence between ~ 2.6 and ~ 3.2 J/cm^2 for 800 nm wavelength irradiation, the gold layer was not completely removed in the center of the site. A thin protruding
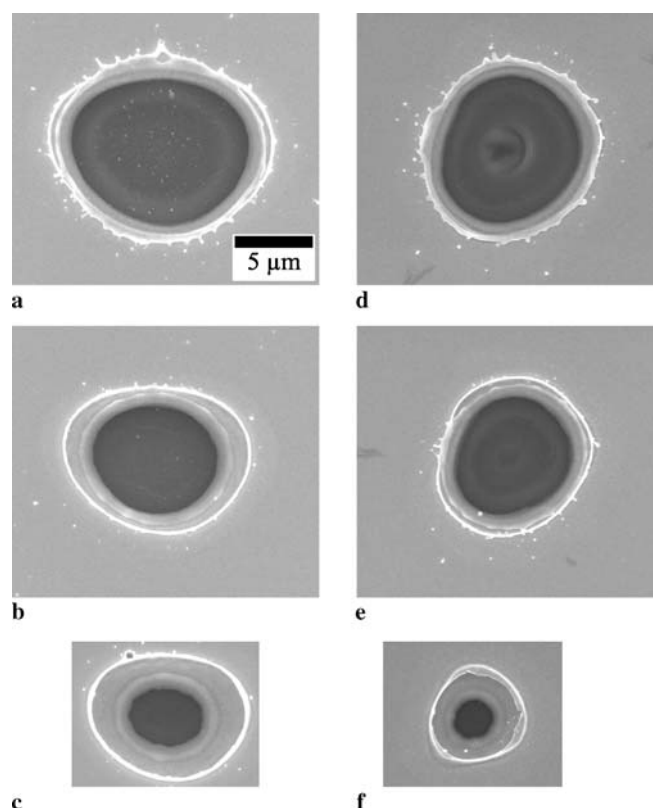
FIGURE 1   SEM plan-view images of the multiple-layer sample irradiated by a single pulse. The sites in images (**a**–**c**) are from 800 nm wavelength irradiation, while (**d**–**f**) are from 400 nm irradiation. The images all have the same scale. The incident energies and fluences at the material surface are: (**a**) ~ 5.01 μJ (~ 10.5 J/cm^2); (**b**) ~ 2.76 μJ (~ 5.75 J/cm^2); (**c**) ~ 1.73 μJ (~ 3.60 J/cm^2), (**d**) ~ 3.42 μJ (~ 10.1 J/cm^2); (**e**) ~ 1.86 μJ (~ 5.49 J/cm^2); (**f**) ~ 0.358 μJ (~ 1.06 J/cm^2)

shell-like feature, appearing as a bright outer ring in Fig. 1, can be observed at a radius larger than that at which the oxide is visible. This shell was seen under SEM for the 800 nm case for fluences above ~ 1.1–1.5 J/cm^2.

For single-pulse 400 nm wavelength irradiation, Fig. 1d and f show the approximate fluence extrema at which the oxide was exposed but the underlying silicon was still covered. Slightly above this fluence range silicon was partially exposed, and below fluences of ~ 0.9–1.1 J/cm^2 the gold was still present at the center. The shell-like feature was seen under SEM for fluences above ~ 0.41–0.47 J/cm^2 for the 400 nm wavelength case.

The results of irradiation with 400 and 800 nm wavelength pulses are not expected to be the same. For example, the reflectance of gold differs significantly between the two wavelengths [12]. In a study on copper [13], the surface reflectance has been shown to affect the ablation threshold for 800 nm irradiation. From SEM observations, incident fluence thresholds for the gold removal and shell formation were lower for 400 nm irradiation than for 800 nm irradiation. The spot size was somewhat smaller for the shorter wavelength, so although the spot size itself may influence structure formation, the use of peak fluences rather than pulse energies allows a more fair comparison.

Figure 2 shows the bright-field TEM cross-section of the ~ 10.5 J/cm^2, $\lambda = 800$ nm site (shown in Fig. 1a). Bend con-

FIGURE 2   Bright-field TEM images of a cross-section of the multiple-layer sample irradiated by a single $\lambda = 800$ nm, $\sim 5.01\,\mu$J ($\sim 10.5\,$J/cm^2) pulse. Image (**b**) shows a higher magnification of the area indicated by the *rectangle* in (**a**)

FIGURE 3   Bright-field TEM images of a cross-section of the multiple-layer sample irradiated by a single $\lambda = 400$ nm, $\sim 3.42\,\mu$J ($\sim 10.1\,$J/cm^2) pulse. Image (**b**) shows a higher magnification of the deformed oxide in (**a**)

tours, a TEM artifact due to slight bending of the FIB sample, are visible throughout the crystalline silicon. The oxide layer, approximately 230 nm thick, is present along the entire cross section with little variation in thickness. However, despite the relative lack of apparent change in the oxide, the silicon below the oxide at the irradiation site possesses significant crystalline damage. In a selected area electron diffraction pattern taken from the damaged silicon region there were no $\langle 111 \rangle$ streaks which would be a feature of stacking faults and twin boundaries. Thus, the straight lines in the bright-field TEM image (Fig. 2) are predominantly dislocations. The dislocations after laser irradiation lie on the {111} plane, as is typical for silicon in general. Due to the thickness of the FIB samples and the high atomic numbers of the metals, in bright-field 120 kV TEM images it was difficult to discriminate between the protective Pd and W metals for FIB preparation and the original Ti, Pt, and Au layers.

In contrast to the $\sim 10.5\,$J/cm^2 case shown in Figs. 1a and 2, TEM imaging of the $\lambda = 800$ nm sites produced by single $\sim 5.75\,$J/cm^2 and $\sim 3.60\,$J/cm^2 pulses (Fig. 1b and c) did not show any crystallographic damage in the silicon. For all three cases, the gold layer was removed and the oxide layer was not visibly thinned by the laser pulse irradiation. The use of cross-sectional TEM provides a significant advantage over surface SEM imaging, as the presence or absence of defects in the silicon substrate was not apparent from surface SEM imaging.

The cross-sectional TEM image in Fig. 3 shows the highest-energy $\lambda = 400$ nm single-pulse site ($\sim 10.1\,$J/cm^2).

As suggested by the corresponding SEM image (Fig. 1d), the oxide layer has been deformed but is still continuous except for a small crack. Crystallographic defects extend up to $\sim 4\,\mu$m below the surface, roughly double the depth as for the $\lambda = 800$ nm case with similar incident pulse fluence (see Fig. 2). Bend contours are visible throughout the crystalline silicon. Cross-sectional TEM imaging of the $\lambda = 400$ nm site irradiated by a single $\sim 5.49\,$J/cm^2 pulse (SEM image shown in Fig. 1e) revealed significant crystallographic defects up to $\sim 2\,\mu$m below the oxide. However, the oxide was not visibly thinned or deformed in this case. The presence of defects at this fluence is in contrast with irradiation with a single 800 nm wavelength pulse of similar incident fluence (see Fig. 1b), for which no defects were observed. For the lowest-fluence single-pulse 400 nm irradiation site ($\sim 1.06\,$J/cm^2, see Fig. 1f), no changes in the oxide or crystallographic changes in the silicon were seen in cross-sectional TEM. This case is shown in Fig. 4.

The cross-sectional TEM observation of greater damage effects for $\lambda = 400$ nm compared with 800 nm radiation (for similar incident fluences) is expected based on the higher absorption of incident light at the shorter wavelength. Although
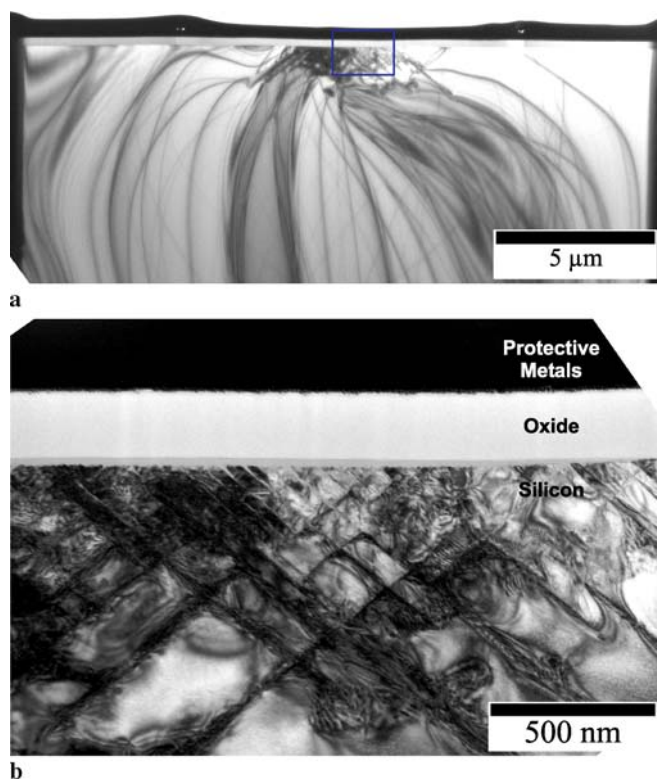

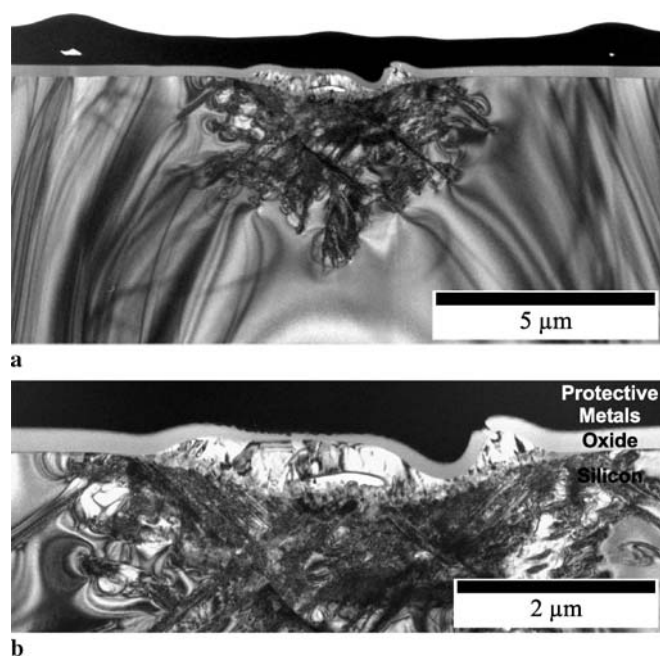**FIGURE 4**   Bright-field TEM image of a cross-section of the multiple-layer sample irradiated by a single $\lambda = 400$ nm, $\sim 0.358\,\mu$J ($\sim 1.06\,$J/cm^2) pulse. Single pulse $\lambda = 800$ nm irradiation at $\sim 5.75\,$J/cm^2 and $\sim 3.60\,$J/cm^2 yielded qualitatively similar TEM images, with no damage visible in the crystalline silicon

we have only examined three different fluences for each wavelength in single-pulse irradiation, there appears to be a fluence threshold below which crystallographic damage in the silicon does not occur. This threshold is higher for the longer wavelength, and is consistent with the gold-removal and shell-formation thresholds mentioned earlier being higher for the $\lambda = 800$ nm case.

A small void (appearing as a white spot in TEM images) is usually present in the FIB samples on either side of the irradiation site within the metal layer, and is visible in Figs. 2a, 3a, and 4. The voids are seen just inside the protruding shell-like feature seen in SEM images (see Fig. 1), between the original gold and the protective metal layer deposited for FIB milling. The shell-like feature, which extends a few hundred nanometers above the original gold layer, likely caused shadowing in the process of depositing the protective FIB metals.

3.2 *Multiple pulse irradiation*

Figure 5 shows a SEM image and Fig. 6 shows cross-sectional bright-field TEM images of the site irradiated by five $\lambda = 800$ nm pulses. Each pulse had a fluence of ~ 10.5 J/cm^2, the same as for the highest-fluence single-pulse 800 nm site. Bend contours are visible in the crystalline silicon area of the TEM images, along with significant crystallographic damage near the irradiated surface. The oxide is cut quite sharply, while near the cut, the metal layer protrudes above the original metal surface somewhat. The metal and oxide serve as a useful marker to delineate between the original substrate and material which was perturbed by the laser pulses. On the right side of the site, a significant amount of material has been deposited on top of the metal layer. Less material is visible on the left side (see Fig. 6b), which could be due to the rather uneven distribution of protruding material observed in the SEM image (Fig. 5). A continuous region of silicon exists from the central region to the area on top of the metal layer, suggesting that it either flowed or was redeposited from the substrate to the top surface. Other reports have noted

the existence of amorphous material and the protrusion of material above the original substrate surface, indicating that a liquid phase exists for part of the material modification process (see, eg. [4, 5]). Electron diffraction patterns obtained

FIGURE 6   Bright-field TEM images of a cross-section of the multiple-layer sample irradiated by five $\lambda = 800$ nm pulses (~ 5.01 μJ per pulse, ~ 10.5 J/cm^2 per pulse). The *thick uneven black layer* at the top of the images is the protective metal layer deposited in FIB preparation. Images (**a**) and (**c**) show higher magnifications of the *areas* indicated in (**b**)
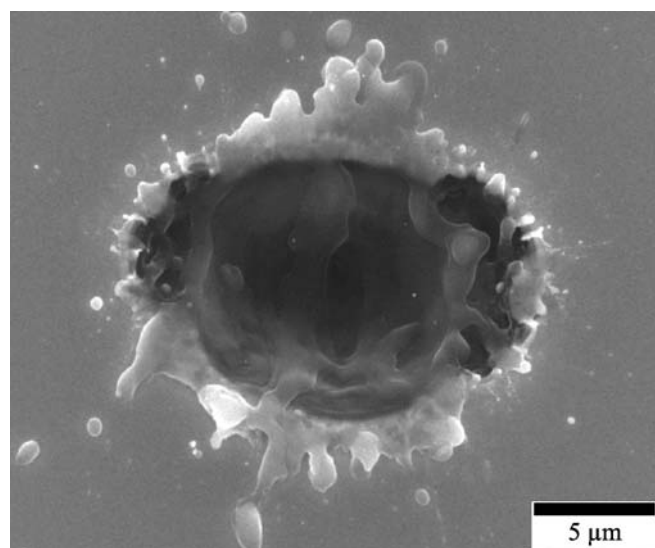

FIGURE 5   SEM image of the multiple-layer sample irradiated by five $\lambda = 800$ nm pulses (~ 5.01 μJ per pulse, ~ 10.5 J/cm^2 per pulse)
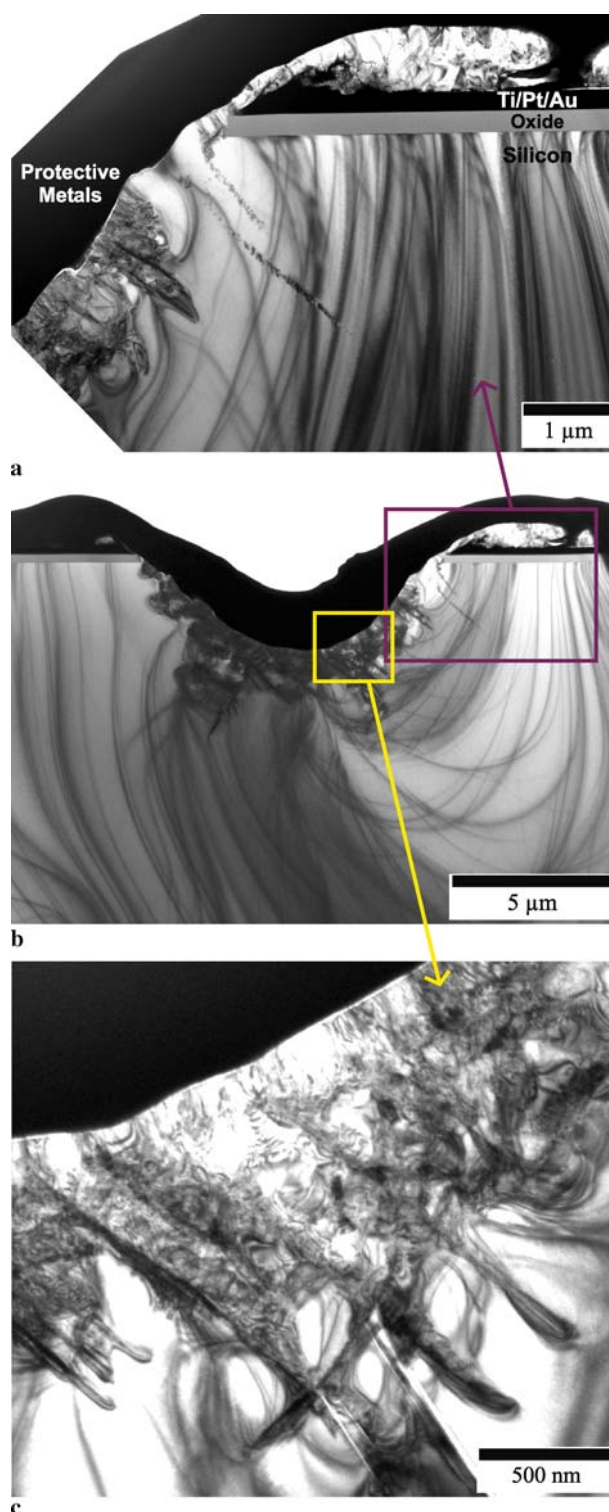
from the deposited layer above the metal in Fig. 6a and b indicate that it is polycrystalline. Two approximately-linear features in the silicon, extending roughly normal to the exposed silicon surface and intersecting the bend contours, are visible in Fig. 6a and b. These are periodic dislocation loops. Within the crystalline silicon substrate, dislocations extend up to $\sim 3\,\mu$m. In our previous work on uncoated silicon [10], four ultrashort laser pulses with a similar fluence ($\sim 11\,\mathrm{J/cm^2}$) and same wavelength also produced dislocations. Once the films are removed over much of the irradiation area, the target behaves primarily as a bulk silicon sample.

At an irradiation wavelength of 400 nm and incident pulse fluence of $\sim 0.59\,\mathrm{J/cm^2}$ (energy $\sim 0.20\,\mu$J), a single pulse did not completely remove the gold layer although the shell-like structure was still formed. Two pulses, each of the same fluence ($\sim 0.59\,\mathrm{J/cm^2}$), exposed oxide. Three such pulses exposed the underlying silicon substrate. Cross-sectional TEM of the two-pulse site showed an approximately uniform oxide thickness. Additionally, there were no crystallographic defects seen in the silicon beneath the irradiation location. The lack of defects is perhaps not surprising, as the fluence was very low compared to the cases where defects formed. For sufficiently high pulse fluences, the second and subsequent pulses begin removal of the oxide followed by the silicon substrate, as was suggested by selected EDXS examinations.

3.3   *General discussion*

Ultrashort laser irradiation has been shown experimentally to produce transient pressures of many gigapascals. For example, with aluminum films on fused silica, a pressure of 95 ± 15 GPa was deduced for a $\lambda = 800$ nm femtosecond pulse intensity of 77 TW/cm^2 [14]. This intensity is comparable to that from the $\sim 10.1\,\mathrm{J/cm^2}$ and $\sim 10.5\,\mathrm{J/cm^2}$ cases used in the present work. Other experiments and computer modeling have also shown high pressures in short pulse laser-material interaction (see, eg. [15–17]). Pressure waves, propagating through the silicon (and perhaps partially reflecting at interfaces as suggested in [15]) might be expected to induce dislocations.

We have recently reported cross-sectional TEM examinations of silicon not possessing metal or thermally grown oxide layers, after irradiation by single and low numbers of $\lambda = 800$ nm femtosecond pulses [10]. For a single pulse fluence of $\sim 11\,\mathrm{J/cm^2}$, crystalline defects did not form in those studies. The single pulse fluence used in the present work is similar ($\sim 10.5\,\mathrm{J/cm^2}$), yet the presence of the metal and oxide layers resulted in significant defects. It is conceivable that differing degrees of thermal expansion among the materials, in addition to the enhanced pressure wave due to strong absorption in the metal, led to stresses sufficient to cause defects.

McDonald et al. [18] irradiated various thicknesses of thermal oxide films on silicon with femtosecond laser pulses. A bubble or blister was observed resulting from the delamination and expansion of the film from the substrate. Although our oxide thickness was within the range used in [18] and we used a similar wavelength, a much greater single pulse fluence was employed in our work. The fact that our oxide film remained intact implies that the metal film played a major role

in the single-pulse irradiation process. In [18], the pulses were expected to pass through the oxide without depositing much energy into it, and thus deposit the laser energy into the underlying silicon. In our case however, the pulse fluences are near or significantly above the damage threshold of bulk silicon dioxide (see, eg. [19]).

Fractures and lattice defects caused by mechanical stress have been reported in cross-sectional scanning-TEM examinations of silicon irradiated by hundreds of femtosecond pulses at a wavelength of 775 nm and with fluences similar to those in our work [4]. On a sample consisting of crystalline silicon on SiO_2 on a silicon substrate, an amorphous layer has been observed by cross-sectional TEM after irradiation by five ultrashort pulses [5]. For our five-pulse case, crystalline damage, rather than an amorphous layer, was observed. We note however that our fluence was much higher than the $\sim 0.07\,\mathrm{J/cm^2}$ used in [5]. The 258 nm irradiation wavelength in [5] (and thus the linear absorption depth in the silicon [12]) was much shorter. Additionally, in our case the oxide and substantial underlying silicon were removed while in [5] the oxide was not exposed. The underlying oxide in [5] could have influenced the heat flow and pressure wave propagation, thus affecting crystallographic changes.

3.4   *Further considerations*

For ns-duration excimer laser irradiation, Giust and Sigmon [20] deposited polycrystalline silicon on silicon oxide of various thicknesses. A thinner oxide provided less thermal resistance between the polycrystalline silicon and the substrate under the oxide, affecting the cooling of the polysilicon. Examination of the crystallographic structure under various oxide thicknesses after femtosecond laser irradiation would be valuable. A thicker oxide layer could reduce the heat reaching the oxide-silicon interface, and could also somewhat dissipate the generated pressure waves before they reach the silicon substrate.

Additional studies with other thicknesses or compositions of the overlying metal film could indicate the role of the absorbing material above the oxide. In gold, the linear optical penetration depth is ~ 12.5 nm [12] (at 800 nm wavelength), but the effective penetration depth of the laser energy is much larger [17, 21], on the scale of the current metal film thickness. The damage threshold fluence depends on the thickness of the film when the film is thinner than a certain critical value. This value is strongly dependent on the strength of electron–phonon coupling [22]. Noble metals, such as gold, have a much slower electron-phonon relaxation compared to transition metals, and thus the molten phase in noble metals exists longer [23]. Compared to nickel, for example, gold has a larger effective penetration depth of excited electrons [17], and a larger critical film thickness [22]. Differences in the properties of selected metal overlayers could play a significant role in the extent to which the underlying substrate becomes damaged under femtosecond laser irradiation of such layered samples.

Finally, we note that through the regenerative amplification process a series of pre-pulses and post-pulses, approximately 7 ns apart, are emitted from the amplifier cavity. This

minor technical issue has been discussed previously [10], but should be considered in the analysis of laser-irradiated material. Due to the nonlinear nature of second harmonic generation, such pulses will be greatly attenuated in the case of 400 nm wavelength irradiation. Additionally, a weak satellite pulse is produced by each neutral density filter, although delayed only a short time (~ 10 ps) from the main pulse. Further studies would be needed to conclusively show that such technical issues do not contribute to the level of crystalline damage observed.

4   Conclusions

We have presented cross-sectional examinations of metal-on-oxide-on-silicon irradiated by ultrashort laser pulses. Although the metallization can be removed by the laser pulses, care should be taken to consider the potential damage, not apparent from simple surface observations, of the underlying substrate covered by the insulating layer. For a sufficiently high pulse energy, crystallographic changes were observed in the silicon under the oxide despite the oxide layer not being appreciably reduced in thickness. After five pulses, defects were also formed, with substantial redistribution of material being evident. A variety of experiments, using different metals and different oxide and metal thicknesses could elucidate the role of various phenomena in the defect formation. In addition, experiments based on varying the laser pulse length, or employing a pair of pulses with adjustable time delay, could be a valuable direction for future studies.

REFERENCES

1 D. Bäuerle, *Laser Processing and Chemistry*, 3rd edn. (Springer, Berlin, 2000)
2 A. Borowiec, M. MacKenzie, G.C. Weatherly, H.K. Haugen, Appl. Phys. A **76**, 201 (2003)
3 A. Borowiec, M. MacKenzie, G.C. Weatherly, H.K. Haugen, Appl. Phys. A **77**, 411 (2003)
4 E. Coyne, J.P. Magee, P. Mannion, G.M. O'Connor, T.J. Glynn, Appl. Phys. A **81**, 371 (2005)
5 J. Jia, M. Li, C.V. Thompson, Appl. Phys. Lett. **84**, 3205 (2004)
6 A. Borowiec, M. Couillard, G.A. Botton, H.K. Haugen, Appl. Phys. A **79**, 1887 (2004)
7 T. Höche, D. Ruthe, T. Petsch, Appl. Phys. A **79**, 961 (2004)
8 Y. Izawa, Y. Izawa, Y. Setsuhara, M. Hashida, M. Fujita, R. Sasaki, H. Nagai, M. Yoshida, Appl. Phys. Lett. **90**, 044 107 (2007)
9 M. Couillard, A. Borowiec, H.K. Haugen, J.S. Preston, E.M. Griswold, G.A. Botton, J. Appl. Phys. **101**, 033 519 (2007)
10 T.H.R. Crawford, J. Yamanaka, G.A. Botton, H.K. Haugen, J. Appl. Phys. **103**, 053 104 (2008)
11 A. Borowiec, H.K. Haugen, Appl. Phys. A **79**, 521 (2004)
12 E.D. Palik (Ed.), *Handbook of Optical Constants of Solids* (Academic, Boston, 1985)
13 S.E. Kirkwood, A.C. van Popta, Y.Y. Tsui, R. Fedosejevs, Appl. Phys. A **81**, 729 (2005)
14 R. Evans, A.D. Badger, F. Falliès, M. Mahdieh, T.A. Hall, P. Audebert, J.-P. Geindre, J.-C. Gauthier, A. Mysyrowicz, G. Grillon, A. Antonetti, Phys. Rev. Lett. **77**, 3359 (1996)
15 K. Sokolowski-Tinten, C. Blome, C. Dietrich, A. Tarasevitch, M. Horn von Hoegen, D. von der Linde, A. Cavalleri, J. Squier, M. Kammler, Phys. Rev. Lett. **87**, 225 701 (2001)
16 C. Schäfer, H.M. Urbassek, L.V. Zhigilei, Phys. Rev. B **66**, 115 404 (2002)
17 E. Leveugle, D.S. Ivanov, L.V. Zhigilei, Appl. Phys. A **79**, 1643 (2004)
18 J.P. McDonald, V.R. Mistry, K.E. Ray, S.M. Yalisove, J.A. Nees, N.R. Moody, Appl. Phys. Lett. **88**, 153 121 (2006)
19 T.Q. Jia, Z.Z. Xu, X.X. Li, R.X. Li, B. Shuai, F.L. Zhao, Appl. Phys. Lett. **82**, 4382 (2003)
20 G.K. Giust, T.W. Sigmon, Appl. Phys. Lett. **70**, 3552 (1997)
21 J. Koch, F. Korte, T. Bauer, C. Fallnich, A. Ostendorf, B.N. Chichkov, Appl. Phys. A **81**, 325 (2005)
22 J. Güdde, J. Hohlfeld, J.G. Müller, E. Matthias, Appl. Surf. Sci. **127–129**, 40 (1998)
23 F. Korte, J. Koch, B.N. Chichkov, Appl. Phys. A **79**, 879 (2004)

8.5 Porcine cortical bone ablation by ultrashort pulsed laser irradiation

Lastly a project focusing on ultrafast laser ablation of porcine cortical bone is presented here. The goal of this project is to adapt laser drilling to improve precision and accuracy of bone drilling in medical procedures, while using ultrafast laser pulses to minimize collateral damage. Porcine cortical bone was chosen as the target since it is a close approximation to human bone structures. The key thrust of this work focused on the ablation threshold under single-shot irradiation as well as the characterization of incubation behavior under multiple-shot irradiation. Follow-up work can include modifications to the laser irradiation setup to use a long focal length lens in an attempt to eliminate surface flatness issues of the bone samples contributing to the statistics in the data points.

More detailed introduction, experimental procedures, as well as results and discussions from initial characterizations are resented in the manuscript included below (reprinted with permission from SPIE: B. Emigh, R. An, **E. M. Hsu**, T. H. R. Crawford, H. K. Haugen, G. R. Wohl, J. E. Hayward and Q. Fang,"Porcine cortical bone ablation by ultrashort pulsed laser irradiation", J. Biomed. Opt. **17**, 028001 (2012)). This project was a collaboration effort with M.Sc. student Brent Emigh and post doctoral fellow Dr. Ran An, under the initiative of Dr. Qiyin Fang. I was involved in the early stages of the experimental design, carried out the early laser irradiation work, modified the micromachining control program for customized routines, was involved in the prototyping of the sample containers, as well as participated in the discussions during the analysis process.

Porcine cortical bone ablation by ultrashort pulsed laser irradiation

Brent Emigh,[a] **Ran An,**[b] **Eugene M. Hsu,**[b] **Travis H. R. Crawford,**[b] **Harold K. Haugen,**[c] **Gregory R. Wohl,**[d]
Joseph E. Hayward,[a] **and Qiyin Fang**[e]
[a]McMaster University, Department of Medical Physics and Applied Radiation Sciences, 1280 Main Street West, Hamilton, Ontario, Canada L8S 4K1
[b]McMaster University, Department of Engineering Physics, 1280 Main Street West, Hamilton, Ontario, Canada L8S 4K1
[c]McMaster University, Department of Engineering Physics, and Department of Physics and Astronomy, 1280 Main Street West, Hamilton, Ontario, Canada L8S 4K1
[d]McMaster University, Department of Mechanical Engineering, and School of Biomedical Engineering, 1280 Main Street West, Hamilton, Ontario, Canada L8S 4K1
[e]McMaster University, Department of Engineering Physics, and School of Biomedical Engineering, 1280 Main Street West, Hamilton, Ontario, Canada L8S 4K1

Abstract. Ultrashort pulsed lasers in bone ablation show promise for many orthopedic applications. To minimize collateral tissue damage and control the ablation process, the ablation threshold fluence must be well characterized. Using an amplified femtosecond laser (170 fs, 800 nm, 1 kHz), the ablation threshold on unaltered porcine cortical bone was measured using the D^2 method at multiple incident pulse numbers ranging from 25 to 1000 pulses per spot. The lowered threshold at greater pulse numbers indicated an incubation effect. Using a power law model, the incubation coefficient of unaltered porcine cortical bone was found to be 0.89 ± 0.03. Through extrapolation, the single-pulse ablation threshold was found to be 3.29 ± 0.14 J/cm^2. © *2012 Society of Photo-Optical Instrumentation Engineers (SPIE).* [DOI: 10.1117/1.JBO.17.2.028001]

1 Introduction

It has been demonstrated that lasers may be used to cut or drill bone tissue for orthopedic surgical applications.[1–3] Compared to the mechanical drill or saw, laser ablation has a number of potential advantages, including minimal mechanical vibration, the ability to focus to small spot size, no direct target contact, and the ability to integrate with real-time optical sensing. These advantages allow for an intricate cut geometry as well as precise control with real-time feedback. Recent work with ultrashort pulsed lasers (pulse durations <10 ps) has produced highly efficient ablation (i.e., small laser energy input per ablated volume of tissue) in bone while resulting in only minimal collateral damage.[4–7] At sufficiently high irradiances, the ablation process is a direct solid-plasma transition,[8] which explains the aforementioned benefits of ultrashort laser pulses. The high instantaneous peak power induces nonlinear absorption and subsequent tissue removal while the low average power deposited during ultrashort laser ablation results in minimal thermal buildup. Due to the avoidance of cumulative thermal effects with ultrashort pulsed lasers for bone ablation, the chemical properties of hydroxyapatite, the main component of bone mineral, are preserved at the ablation site.[9]

The ablation threshold is the minimum laser fluence required to initiate substantial material removal from a surface. Using polished porcine cortical bone, Girard et al. found the ablation threshold to be 0.69 J/cm^2 when irradiated with 1000 pulses at

775 nm, a repetition rate of 1 kHz, and a pulse duration of 200 fs, but did not investigate the threshold with different pulse numbers.[6] It has been reported that material surfaces, such as metals[10,11] and semiconductors,[12] become damaged at fluences below the single-pulse ablation threshold when irradiated with multiple pulses. This phenomenon is referred to as the incubation effect. Described using a power law model,[13] the incubation coefficient, ξ, characterizes the degree of this effect and is an intrinsic property of the material. Using laser pulses at 775 nm, a repetition rate of 3 kHz, and a pulse duration of 150 fs, Lim et al. conducted single-pulse ablation and linear scanned ablation tests to measure the single-pulse ablation threshold and incubation coefficient in polished bovine cortical bone.[14] From their results, the authors calculated the ablation threshold at 1000 pulses per spot to be 1.22 ± 0.29 J/cm^2. The difference in the reported ablation threshold values may be attributed to differences in the samples (e.g., porcine versus bovine, moisture, etc.) and the experimental design (e.g., single-pulse versus multiple-pulse ablation).

In both studies, the surfaces of the cortical bone samples were polished to achieve a uniformly flat and smooth ablation surface. Laser ablation strongly depends on the material composition and properties of the sample. In the context of investigating ablation thresholds, a polished bone surface may differ considerably from the natural cortical bone surface. For example, sanding the bone surface can increase specular reflection, while surface corrugations can change the local field intensity and affect the threshold fluence.[15] Therefore, it is also important to investigate the ablation threshold using unaltered bone samples.

Address all correspondence to: Qiyin Fang, McMaster University, Department of Engineering Physics, and School of Biomedical Engineering, 1280 Main Street West, Hamilton, Ontario, Canada L8S 4K1. Tel: 9055259140; E-mail: qiyin.fang@mcmaster.ca.

Laser machining of bone during surgical procedures requires a large number of laser pulses. Therefore, characterizing the incubation effect from multiple pulses would have important implications in determining the optimum ablation parameters. In this study, we used a varying number of pulses to obtain the single-pulse ablation threshold. The incubation effect in unpolished porcine cortical bone was quantified through the measurement of the incubation coefficient.

2 Methods

2.1 Ablation Experimental Setup

The ablation experiments were performed using a customized ultrafast laser machining system whose schematic is shown in Fig. 1, which was similar to the setup used in our previous work.[16] Briefly, a Ti:Sapphire mode-locked oscillator (Tsunami, Spectra Physics) seeded a chirped-pulse amplifier (Spitfire, Spectra Physics) to generate laser pulses at ~325 μJ and 170 fs [full width half maximum (FWHM)], which was measured using a second-order noncollinear autocorrelator. For all experiments in this report, a 1 kHz repetition rate and 800 nm wavelength output were used and the peak wavelength was verified by a fiber-coupled spectrometer (PC2000, Ocean Optics). The collimated beam was reduced in diameter through the use of a telescope and had a final $1/e^2$ diameter of 4.42 mm. The beam had a near Gaussian intensity profile that was measured using a laser beam profiler (BeamStar, Ophir Optronics). The pulse energy was controlled using a set of neutral density filters. A small portion of the laser beam was reflected onto a calibrated photodiode (DET210, ThorLabs) that monitored the laser energy after passing through the filters. The laser exposure time (i.e., number of pulses delivered to the sample) was adjusted by a computer-controlled mechanical shutter (VS25S2S1, Uniblitz). Beyond the shutter, the beam was steered into a plano-convex lens (f = 12.5 cm, BK7), which focused the collimated beam down to a $1/e^2$ spot size diameter of 30.2 μm.

The spot size was confirmed by measurement in preliminary experiments using the same focusing scheme to avoid potential

errors caused by the rough bone surface. Using a piece of silicon as the target, the laser focusing plane was found by iteratively reducing the laser power and moving the lens along the optical axis. The lens position was found where ablation of silicon occurred, while a small change of the lens position caused ablation to no longer occur. As shown in Fig. 1, the target was imaged to the CCD through both the laser focusing lens and another lens in front of the CCD. After the laser focusing plane was located, the focusing lens in front of the CCD was adjusted to give this position a sharp image on the camera display. These steps assured the laser focusing and the CCD imaging planes were the same and images of the target were collimated between the two lenses before focusing on the CCD. Before each ablation experiment, the focusing lens was adjusted on its translational stage until the image of the bone surface on the camera display appeared to be in sharp focus, which meant the laser also focused on the bone surface. Using a 125-mm focusing lens, there is a 200-μm range in which the sharpness of the bone surface appears to remain at a maximum. Assuming Gaussian beam propagation, a translational uncertainty of 200 μm in locating the laser focus on the sample in the viewing camera and a $1/e^2$ spot size diameter of 30.2 μm would result in a beam waist uncertainty of 0.74 μm and subsequent uncertainty in the fluence calculation.[16]

The bone sample was irradiated within a chamber mounted on a computer-controlled X-Y translational stage (UTM100PP.1, Newport). The focusing lens was mounted on a Z translation stage (MFN25PP, Newport) independent of the X-Y stage. A confocal monochrome CCD camera and white LED illuminator were used to monitor the sample alignment and the ablation process during the course of the experiments. The laser beam focal plane and CCD imaging focal plane were aligned before commencing each experiment.

2.2 Bone Samples

The experimental protocol was approved by the McMaster Animal Research Ethics Board. Bone specimens were harvested from the scapulae of skeletally immature pigs obtained from a local butcher. After harvesting, soft tissue and periosteum were cleaned off the specimens, which were then cut to include both the outer cortical layer (thicknesses 1 to 3 mm) as well as cancellous bone (~5 mm). In all ablation experiments, the laser beam was directed onto the surface of the cortical layer through a quartz cover glass slide inside a sealed glass chamber. The surface of the bone was left unaltered to mimic real-life conditions. All ablation experiments were performed within 24 h of harvesting. Following ablation, specimens were fixed in 10% formalin and stored in saline until further processing.

2.3 Ablation Procedure

Surface craters were ablated in bone with 25, 50, 75, 100, 300, 500, and 1000 incident pulses. Crater ablation was repeated over a range of 30 fluence levels from 0.1 to 13.0 J/cm². This procedure was repeated three times on bone specimens from the scapulae of three different pigs. The craters were viewed using reflected-light microscopy (Axioplan 2, Zeiss), and crater diameters were measured using image analysis software (Northern Eclipse, Empix Imaging). The crater diameter was defined as the maximum diameter of the region of removed tissue. The D^2 technique,[17] where the diameter of the ablated crater is correlated to the known laser energy used for that specific crater,
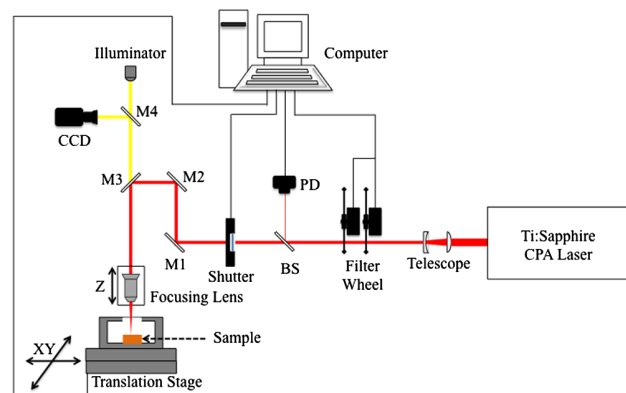
Fig. 1 Schematics of the laser ablation setup. After exiting the chirped-pulse amplifier (CPA), the beam energy was adjusted with a set of two computer-controlled filter wheels. A beam splitter (BS) picked off a portion of the beam and directed it onto a calibrated photodiode (PD). The signal from the PD was sent to a box-car integrator (not shown), whose output was read out by the computer. The shutter was computer controlled. The CCD camera monitored the ablation process to ensure laser—sample alignment. M1 and M2 are high reflection mirrors. M3 is a dichroic mirror, and M4 is a beam splitter.
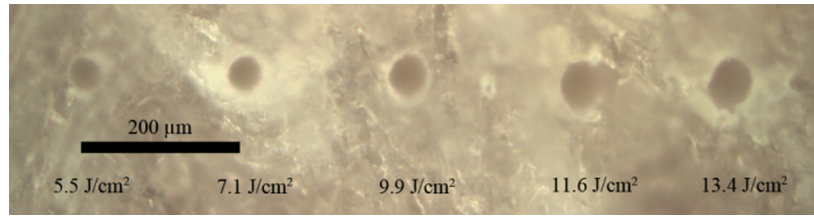
Fig. 2 Ablation craters cut into the surface of porcine cortical bone with 1000 pulses per spot at five different fluence levels. Imaged using a reflected-light optical microscope and a 20× objective.

was used to determine the threshold fluence for each incident pulse number. The relationship between the crater diameter and the peak laser fluence is given by:

$$D^2 = 2\omega_0^2 \ln\left(\frac{\phi}{\phi_{\text{th}}}\right), \tag{1}$$

where D is the diameter of removed tissue, ω_0 is the $1/e^2$ radius of the focused beam incident spot, ϕ is the fluence used for each crater, and ϕ_{th} is the threshold fluence for the sample. From the semilog plot of D^2 versus fluence, the ablation threshold can be determined from the x-intercept. The $1/e^2$ focal spot size can also be obtained from this plot and verified for consistency with previous investigations.

The incubation model of Jee et al.[13] relates the fluence threshold for N pulses, $\phi_{\text{th}}(N)$, with the single-pulse ablation threshold, $\phi_{\text{th}}(1)$, and is given by:

$$\phi_{\text{th}}(N) = \phi_{\text{th}}(1) \times N^{\xi-1}, \tag{2}$$

where ξ is defined as the incubation coefficient. A rearrangement yields a logarithmic relationship between the accumulated fluence, $N \times \phi_{\text{th}}(N)$, and N, with the proportionality constant equal to ξ. A log–log plot of the accumulated fluence versus the incident pulse number will have a slope equal to the incubation coefficient and a y-intercept equal to the single-pulse ablation threshold.

3 Results

3.1 Ablation Threshold

An example of ablation craters in cortical bone after irradiation with 1000 pulses per spot is shown in Fig. 2. Using an optical microscope under 20× microscope viewing, orthogonal measurements of the diameter were carried out and the geometric average diameter was determined. Note that a small rim of discolored tissue surrounding each crater was observed and not taken into account when measuring the crater diameter (maximum diameter of removed tissue).

Squared diameter (D^2) versus log of the fluence plots were created for all incident pulse numbers. Exemplar plots (Fig. 3) are shown for 75 and 1000 incident pulses. The results from all three scapulae are plotted on the same figure as trials 1, 2, and 3. Scatter between trials was attributed to changes in bone surface topography and uncertainty in beam focus alignment. At fluences greater than 2 J/cm², the trend between squared diameter and fluence appeared to be logarithmic; however, craters ablated with fluence below 2 J/cm² appeared to follow a different trend.

Each individual trial was fit using a linear least-squares algorithm (not shown), and the weighted average slope and

y-intercept were calculated from the three trials and used to construct the trend lines shown in Fig. 3. From these lines, the energy fluence ablation thresholds were obtained for each incident pulse number and are shown in Table 1. Experimental
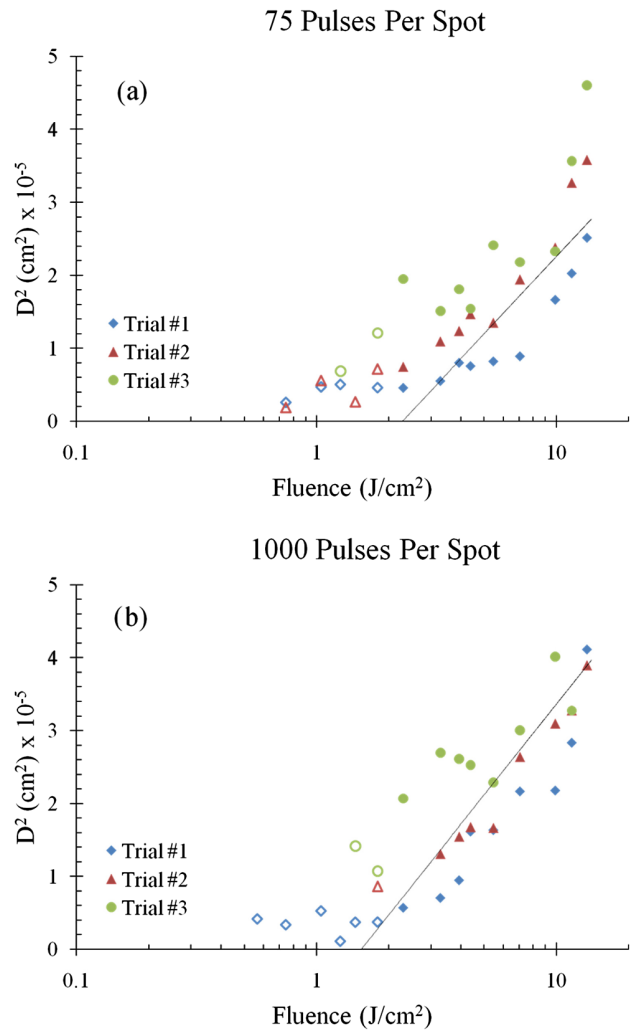
Fig. 3 Squared diameter (D^2) of ablated craters versus fluence in porcine cortical bone ablated by multiple pulses per spot: (a) 75 pulses per spot and (b) 1000 pulses per spot. Samples were irradiated with $\lambda = 800$ nm, $\tau = 170$ fs pulses at a repetition rate of 1 kHz. Three trials were performed on the scapular bones of individual pigs. Solid data points were assumed to be the result of a faster material-removal ablation regime and used in creating the lines of best fit. Hollow points indicate the results of an ablation regime with little material removal and were not included in the fit. The slope and intercept of the plotted trend line were obtained from the weighted average slope and intercept of the three individual trial least-squares lines.

Table 1 Ablation threshold fluence at different incident pulse numbers as measured using the D^2 method.[a]

Incident pulse number (N)	Ablation threshold fluence (J/cm^2)
25	2.37 ± 0.78
50	2.36 ± 0.87
75	2.28 ± 0.76
100	1.72 ± 0.93
300	1.66 ± 0.87
500	1.69 ± 0.65
1000	1.75 ± 0.55

[a]Uncertainties were obtained from the standard errors in the fits from each individual trial.

values of ω_0 were obtained from the slopes of the least-square lines and yielded spot size diameters ($2\omega_0$) of 28.3 ± 2.1 μm and 30.3 ± 0.7 μm for 75 and 1000 pulses per spot, respectively. These experimental values agreed well with the spot diameter of 30.2 μm measured using silicon as the target.

3.2 Incubation Effects

The results for the accumulated fluence, $N \times \phi_{th}(N)$, versus incident pulse number, N, are shown in Fig. 4. The data were fit with a power function, and the R^2 value was 0.988. From the equation of the best-fit line, the incubation coefficient, ξ, in Eq. (2) was found to be 0.89 ± 0.03. From extrapolation, the single-pulse ablation threshold, $\phi_{th}(1)$, was found to be 3.29 ± 0.14 J/cm^2. The incubation coefficient of porcine bone found in our experiments is in the same range as that found for bovine bone.[14] However, the single-pulse ablation threshold with a femtosecond laser source is higher than that found by Lim et al. (2.70 ± 0.16 J/cm^2)[14] using a comparable wavelength and pulse duration.
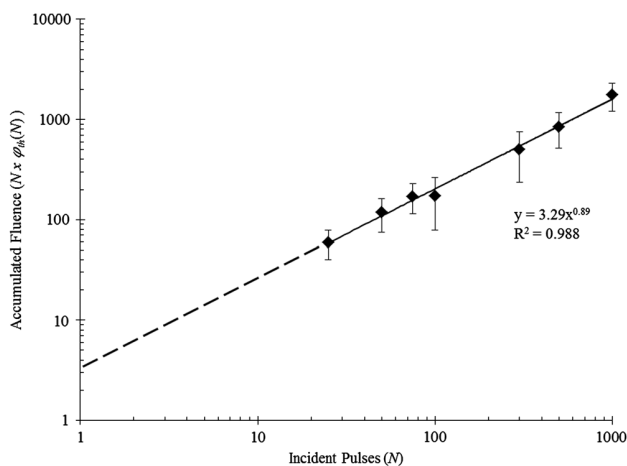

Fig. 4 Incubation power law for porcine cortical bone irradiated with $\lambda = 800$ nm $\tau = 170$ fs pulses. The data were fit with a power function with $R^2 = 0.988$. The incubation coefficient, ξ, was 0.89 ± 0.03, and the single-pulse ablation threshold fluence was 3.29 ± 0.14 J/cm^2.

4 Discussion

The possible use of ultrashort ($<$10 ps) lasers in cutting and drilling hard biological tissue has been explored since the 1990s in studies mostly involving dental tissue.[4,19,20] More recently, studies have investigated the ablation ability and characteristics of ultrashort lasers in cortical bone[6,14] for the purpose of replacing the mechanical drill and saw used in orthopedic surgery. In these studies, ultrashort pulsed lasers have been shown to result in relatively high rates of tissue removal with minimal thermal damage or mechanical injury—ideal for use in calcified bone since its shear and compressive characteristics make it susceptible to fracture. The ablation threshold has been previously found in porcine cortical bone;[6] however, it was only investigated at an incident pulse number of 1000. A previous study by Kim et al. using dental tissue showed a decreasing damage threshold with an increasing number of incident pulses.[15] In order to take advantage of the ablation benefits of ultrashort pulsed lasers, the incubation effects in bone must be understood.

In their work on micropillars in bone, Lim et al. characterized the incubation effect in bovine cortical bone.[14] The single-pulse ablation threshold was obtained experimentally, and the 1000-pulse ablation threshold was calculated. However, the calculated 1000-pulse threshold is different from the previous findings of Girard et al. in porcine cortical bone.[6]

Porcine cortical and cancellous bone have been previously shown to best match human bones in their degree of mineralization, composition,[21] and lamellar structure.[22] Unlike previous investigations with bone, the samples in this study were not altered before ablation, which is close to practical surgical conditions. In addition, the use of the scanning electron microscope (SEM) was avoided in this study due to the permanent tissue alterations that would have resulted from the required SEM biological sample preparation.

Figure 2 shows a sample image of ablated craters under 20× microscope viewing. The crater diameter was measured to be the span of the darkened region. The craters appear to have rims of discolored tissue surrounding them. Due to their lightened color, the rims were presumed not to be charred tissue but instead the result of ablation debris or the result of a pressure-driven flow of molten bone tissue from the center to the edge of the crater followed by resolidification at the rim.[23] Some craters were noticeably asymmetrical, which could be the result of surface roughness, heterogeneities in the bone specimens, or the nonideal alignment of optics.

Based on the Gaussian intensity profile approximation, the D^2 method describes a relationship between the diameter of an ablated crater, the material-dependent ablation threshold fluence, the Gaussian beam radius, and the peak fluence of the beam.[17] Figure 3 shows the squared diameter of ablated craters versus the peak laser fluence for incident pulse numbers of 75 and 1000. The slope of the data allows the determination of the effective beam spot size, and an extrapolation of D^2 to intersect with the x axis provides a value for the ablation threshold fluence, $\phi_{th}(N)$. Since the three trials do not have the same uncertainty, a simple least-squares line fitting all data points would not suffice. Instead, the least-square line was found for each trial (not shown in Fig. 3), and the weighted average slope and intercept were calculated. The resulting fit line was constructed from this average slope and intercept.

As seen in Fig. 3 there appear to be different trends for D^2 through the range of fluence. Above $\sim$2 J/cm^2, the crater area

appears to increase logarithmically with fluence. At lower fluences, however, the crater area is less deterministic as a function of laser fluence, while a change in ablation mechanism has been reported to occur at a certain fluence in other materials.[24] The depths of the craters at fluences <2 J/cm^2 were comparable in size to the bone surface irregularities (ridges, pits) and likely do not constitute meaningful tissue removal. Large-scale bone removal or drilling will require greater ablation rates; therefore, this study focused on the characterization of the thresholds of this higher-fluence ablation regime. As a result, our least-square lines were fit using only the data points above 2 J/cm^2, denoted as solid points in Fig. 3. The irregularities in crater diameter seen in Fig. 3 were likely due to the irregular surface of the sample or the uncertainty in the laser focusing scheme.

The ablation thresholds for different pulse numbers, N, are shown in Table 1. The uncertainties were calculated from the standard deviation in the fit of each individual trial following the weighted-average method for independent measurements. As expected, the ablation threshold decreases as the pulse number increases, from 2.37 ± 0.78 J/cm^2 with 25 incident pulses to 1.75 ± 0.55 J/cm^2 at 1000 pulses. After reaching 100 pulses per spot, the accumulation effect appears to saturate. This agrees well with results on ablation of transparent materials from Rosenfeld et al., who found the most dramatic changes in threshold occurred at lower pulse numbers and the reduction in threshold was less pronounced at higher pulse numbers.[25] The measured ablation threshold at 1000 pulses differs significantly from that found by Girard et al. with the same number of pulses (0.69 J/cm^2).[6] One of the likely causes of this discrepancy may be differences in the definition of *ablation*. In the Girard study, ablation was deemed to occur when visual inspection of polished bone SEM images showed laser-induced damage.[6] In this study, ablation was defined as a definitive removal of tissue and formation of a crater. This measured threshold at 1000 pulses was somewhat greater than the strong ablation threshold found by Lim et al. (1.22 ± 0.29 J/cm^2),[14] but there was good agreement at 100 pulses per spot (1.56 ± 0.09 J/cm^2). Discrepancies in ablation thresholds found by both Girard et al.[6] and Lim et al.[14] and those presented in this study are also likely the result of using unaltered bone samples in the current study versus polished bone samples in the other studies.

The reduction in ablation threshold with incident pulse number is referred to as the incubation effect and follows a power law equation[13] that was originally developed for metals under nanosecond pulse irradiations, but which has been adopted for semiconductors[12] and insulators[25] with the use of femtosecond laser pulses. In metals, cumulative effects have been attributed to the accumulation of plastic deformations resulting from thermal stresses caused by incident pulses with fluences below the ablation threshold.[26] As a result of these deformations, the metal is then successfully ablated by pulses with laser fluences less than the single-pulse ablation threshold. In the case of semiconductors and insulators, laser-induced alterations such as defects or modifications in chemical properties are believed to be the main reason for incubation effects.[12,25]

A rearrangement of Eq. (2) yields a double logarithmic relationship between the accumulated fluence, $N \times \phi_{\text{th}}(N)$, and the pulse number, N. The material-dependent incubation coefficient, ξ, is then determined from the log–log plot. The incubation coefficient characterizes the degree of incubation—the change in the ablation threshold with pulse number. A value

of $\xi = 1$ indicates that there is no incubation effect in the material and the ablation threshold will not change with pulse number. As seen in Fig. 4, the porcine cortical bone ablation data fits well with this incubation model. The incubation coefficient was found to be 0.89 ± 0.03, which agrees very well with the results for the bovine cortical bone incubation coefficient (0.89 ± 0.02).[14] When the incubation data was extrapolated back to $N = 1$ pulses, the single-pulse ablation threshold was found. For porcine cortical bone, it was found to be 3.29 ± 0.14 J/cm^2. This threshold is marginally higher than the previously found bovine cortical bone single-pulse strong ablation threshold of 2.70 ± 0.16 J/cm.[2,14] This increase in fluence could be attributed to the rough surface of the bone samples used in this investigation and the difference between bovine and porcine bones. While similar incubation effects occur in porcine and bovine cortical bone, we feel that the greater similarity between the bones of humans and pigs on the microscopic level and the use of unaltered bone allows for the application of the data presented in this study to human subjects.

5 Conclusions

Ultrashort pulsed lasers appear to be ideal for use in orthopedic surgery due to their high ablation efficiency and low collateral damage. Establishing the laser fluence ablation threshold of bone is crucial for understanding the ablation mechanism and for designing clinical ablation protocols. Using the D^2 method, the ablation threshold was determined in unaltered porcine cortical bone at multiple incident pulse numbers ranging from 25 to 1000 pulses per spot. The lowered threshold at greater pulse numbers indicated an incubation effect. Using a power model, the incubation coefficient was found to be 0.89 ± 0.03, which agreed well with previous results found using bovine tissue. The single-pulse ablation threshold was found to be 3.29 ± 0.14 J/cm^2, which was higher than the previous findings in bovine bones. The difference in ablation threshold may be attributed to different microstructure and surface topography due to different sample preparation. Unpolished bone specimens were used in our study and are believed to be a better approximation to *in vivo* bone ablation scenarios.

References

1. C. Gonzalez et al., "Comparison of the erbium-yttrium aluminum garnet and carbon dioxide lasers for in vitro bone and cartilage ablation," *Laryngoscope* **100**(1), 14–17 (1990).
2. A. Charlton et al., "Erbium-YAG and holmium-YAG laser ablation of bone," *Laser Med. Sci.* **5**(4), 365–373 (1990).
3. H. Devlin et al., "Healing of bone defects prepared using the erbium-YAG laser," *Laser Med. Sci.* **9**(4), 239–242 (1994).
4. J. Neev et al., "Ultrashort pulse lasers for hard tissue ablation," *IEEE J. Sel. Top. Quant.* **2**(4), 790–800 (1996).

5. W. B. Armstrong et al., "Ultrashort pulse laser ossicular ablation and stapedotomy in cadaveric bone," *Laser Surg. Med.* **30**(3), 216–220 (2002).

6. B. Girard et al., "Effects of femtosecond laser irradiation on osseous tissues," *Laser Surg. Med.* **39**(3), 273–285 (2007).

7. R. G. McCaughey et al., "Femtosecond laser ablation of the stapes," *J. Biomed. Opt.* **14**(2), 024040 (2009).

8. M. Niemz, *Laser-Tissue Interactions: Fundamentals and Applications*, Springer-Verlag, GmbH & Co., Berlin, Heidelberg (1996).

9. K. Ozono and M. Obara, "Tailored ablation processing of advanced biomedical hydroxyapatite by femtosecond laser pulses," *Appl. Phys. A: Mater.* **77**(2), 303–306 (2003).

10. J. Byskov-Neilsen and J.-M. Savolainen, "Ultra-short pulse laser ablation of metals: threshold fluence, incubation coefficient and ablation rates," *Appl. Phys. A: Mater.* **101**(1), 97–101 (2010).

11. P. T. Mannion et al., "The effect of damage accumulation behavior on ablation thresholds and damage morphology in ultrashort laser micro-machining of common metals in air," *Appl. Surf. Sci.* **233**(1–4), 275–287 (2004).

12. J. Bonse et al., "Ultrashort-pulse laser ablation of indium phosphide in air," *Appl. Phys. A: Mater.* **72**(1), 89–94 (2001).

13. Y. Jee, M. F. Becker, and R. M. Walser, "Laser-induced damage on single-crystal metal surfaces," *J. Opt. Soc. Am. B* **5**(3), 648–659 (1988).

14. Y. C. Lim et al., "Micropillar fabrication on bovine cortical bone by direct-write femtosecond laser ablation," *J. Biomed. Opt.* **14**(6), 064021 (2009).

15. B. M. Kim et al., "Effects of high repetition rate and beam size on hard tissue damage due to subpicosecond laser pulses," *Appl. Phys. Lett.* **76**(26), 4001–4003 (2000).

16. A. Borowiec and H. K. Haugen, "Femtosecond laser micromachining of grooves in indium phosphide," *Appl. Phys. A: Mater.* **79**(3), 521–529 (2004).

17. J. M. Liu, "Simple technique for measurements of pulsed Gaussian-beam spot sizes," *Opt. Lett.* **7**(5), 196–198 (1982).

18. D. Ashkenasi et al., "Laser processing of sapphire with picosecond and sub-picosecond pulses," *Appl. Surf. Sci.* **120**(1–2), 65–80 (1997).

19. J. Kruger, W. Kautek, and H. Newesely, "Femtosecond-pulse laser ablation of dental hydroxyapatite and single-crystalline fluoroapatite," *Appl. Phys. A: Mater.* **69**(7), S403–S407 (1999).

20. L. B. Da Silva et al., "Comparison of soft and hard tissue ablation with sub-ps and ns pulse lasers," *Proc. SPIE* **2681**, 196–200 (1996).

21. J. Aerssens et al., "Interspecies differences in bone composition, density, and quality: potential implications for in vivo bone research," *Endocrinology* **139**(2), 663–670 (1998).

22. L. Mosekilde, J. Kragstrup, and A. Richards, "Compressive strength, ash weight, and volume of vertebral trabecular bone in experimental fluorosis in pigs," *Calcif. Tissue Int.* **40**(6), 318–322 (1987).

23. A. Ben-Yakar and R. L. Byer, "Femtosecond laser ablation properties of borosilicate glass," *J. Appl. Phys.* **96**(9), 5316–5323 (2004).

24. S. Nolte et al., "Ablation of metals by ultrashort laser pulses," *J. Opt. Soc. Am. B* **14**(10), 2716–2722 (1997).

25. A. Rosenfeld, M. Lorenz, and D. Ashkenasi, "Ultrashort-laser-pulse damage threshold of transparent materials and the role of incubation," *Appl. Phys. A: Mater.* **69**(7), S373–S376 (1999).

26. C. S. Lee, N. Koumvakalis, and M. Bass, "Spot-size dependence of laser-induced damage to diamond-turned Cu mirrors," *Appl. Phys. Lett.* **41**(7), 625–627 (1982).

Chapter 9

Summary

The results presented in this thesis showed that there are several areas where ultrafast laser processing show potential to be used in conjunction with conventional device fabrication techniques for improved device applications. Findings of experiments in this thesis also provided insights into ultrafast laser ablation and LIPSS formation mechanisms. Several areas were explored in parallel, and the key findings are presented below.

Using positron annihilation spectroscopy, initial results showed a change in the near-surface region divacancy density under pseudo-uniform large-area irradiation of silicon at different pulse energy levels relative to a reference energy at which visible modification (discoloration) just occurs. The results from this work and suggested future work will provide insights into elucidating the origin of observed incubation effects under pulsed laser irradiation. When the samples were heated during the laser irradiation process, the single-shot ablation threshold exhibits a general decreasing trend, with a tendency to plateau for temperatures below 100°C and above 400°C. With increasing temperature, the incubation effect is suppressed above 100°C, and

the suppression effect saturates above 300°C up to 600°C. The results of this work can be put into context of the existing knowledge of defects in silicon to help elucidate the origin of incubation effect under pulsed laser irradiation, and further characterization can potentially enable defect engineering based applications.

A side finding of laser irradiation carried out on samples with elevated temperatures is the surface morphological dependence on the sample temperature. It was observed that there is a gradual diminishing tendency to generate LIPSS and fragmented structures at elevated temperatures, where smoother features can be obtained. The results might be valuable for applications where the surface morphology and roughness following ultrafast laser processing had been the limiting factor, and combined with hydrodynamic simulations can shed insight into the formation of ultrafast laser induced LIPSS.

Altering the laser repetition rate from 0.5 Hz to 50 Hz did not show a difference in the incubation behavior for irradiation carried out at room temperature and at $\lesssim$300°C, suggesting there is no significant change in the lifetime component of the contributing factor to the observed incubation effect. Expanding the laser irradiation parameters and temperature range of this experiment can provide insights into the incubation effect as well.

Repeated surface irradiation under translational irradiation geometry with sub-threshold energies showed the initial formation of subtle material modifications (discoloration). With repeated irradiation these features expanded in area and with enough cumulated fluence the formation of ripples began and subsequently dominated. The findings of this work can shed insight into both ultrafast laser ablation and LIPSS formation mechanisms.

Irradiation of ion-implanted silicon showed a dependence of the single-shot ablation threshold on the ion implantation conditions, such as implantation energy and dose. The results may be an interplay between several factors, including mechanical, optical and chemical modifications due to the ion implantation. This area requires follow-up effort before fine control for applications can be realized, and can also shed insight into the ultrafast laser interactions with materials.

Large-area surface texturing of silicon provided a single-surface absorption of $\sim$ 45% at 1550 nm. However, improvement in the absorption was not obtained with the introduction of sulfur into the near-surface region through ion implantation, in contrast to irradiation with an SF_6 ambient atmosphere as reported in the literature. An initial attempt at device fabrication did not yield a photoresponsivity at 1550 nm. Extensive material characterization should be carried out to examine the optical absorption and electronic properties of the implanted textured surface to gain better insights.

Single-shot laser ablation of SiO_2 showed a dependence of the single-shot threshold fluence on the oxide thickness, potentially due to optical effects from interference or mechanical effect from the mechanical strength from the oxide layer. Translational irradiation yielded ripples oriented parallel (dielectric-like behavior) and perpendicular (metal-like, and often observed in semiconductors) to the incident laser electric field. Initial observations indicated that these ripples can be formed in the buried interface, without the removal of the oxide from bulk silicon. On-going and future characterizations can provide insights into the formation mechanisms of ablation and LIPSS formation mechanisms, and can potentially contribute to applications of ultrafast laser processing of similar structures.

Several key findings of ultrafast laser irradiation of various other material systems, including gallium phosphide, synthetic diamond, quartz, metal-silicon dioxide-silicon structures, and porcine bone, are supplementary to various findings in the silicon work.

Overall the works presented in this thesis contribute to the potential use of ultrafast laser processing of silicon for different aspects of device applications, while the results also provide insights into the fundamental processes of ultrafast laser ablation and the generation of surface ripples. The supplementary work along with the main thrust on the silicon theme along with proposed future work can help contribute to further understanding of ultrafast laser ablation mechanisms.

Appendix A

Nanowire formation under ultrafast laser ablation of silicon at 600°C

A complementary finding from the experiments described in Section 3.2 is presented here for laser irradiation carried out with the sample surface at 600°C with no barrier material between the silicon sample the copper heating stage. Under such irradiation conditions, the formation of nanowires oriented in orthogonal directions was observed at the silicon surface. Qualitatively similar structures, although not as pronounced, are somewhat noticeable at 500°C as well. These wires do not occur just at the laser target sites. At target sites irradiated with single and low numbers of laser pulses, dense islands of qualitatively similar short structures can also be observed.

Figure A.1 shows examples of OM observations of these wires on the sample surface and dense islands that are qualitatively similar at laser target sites.
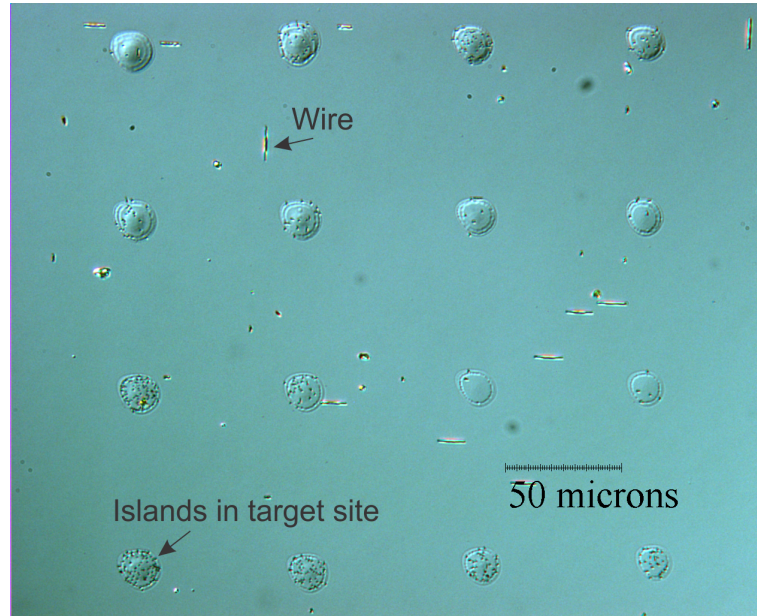
Figure A.1: Examples of nanowires on sample surface and island-like structures in laser target sites.

SEM images of a nanowire outside of the laser target sites and dense island structures are shown in Figure A.2.

An energy dispersive x-ray spectrum (EDX) showed copper and aluminum signals from the wires (Figure A.3). The results are compared to the EDX spectrum from the bare substrate where only a silicon signal is observed. EDX spectra from the island formation at laser irradiated sites yielded similar results.

The observed nanowires are oriented in orthogonal directions, suggesting a preferential orientation likely related to the crystallographic orientation. Without further sophisticated characterization techniques, possible causes are proposed.

A possible formation mechanism of the nanowires can arise from having an environment analogous to vapor-liquid-solid (VLS) nanowire growth mechanisms initiated with metal seeds [186, 187]. VLS nanowire growth shows a preferential growth

Figure A.2: SEM images of a nanowire outside of the laser target sites (left) as well as dense island formations in the laser target site (right) irradiated with a single 1.39 μJ pulse.
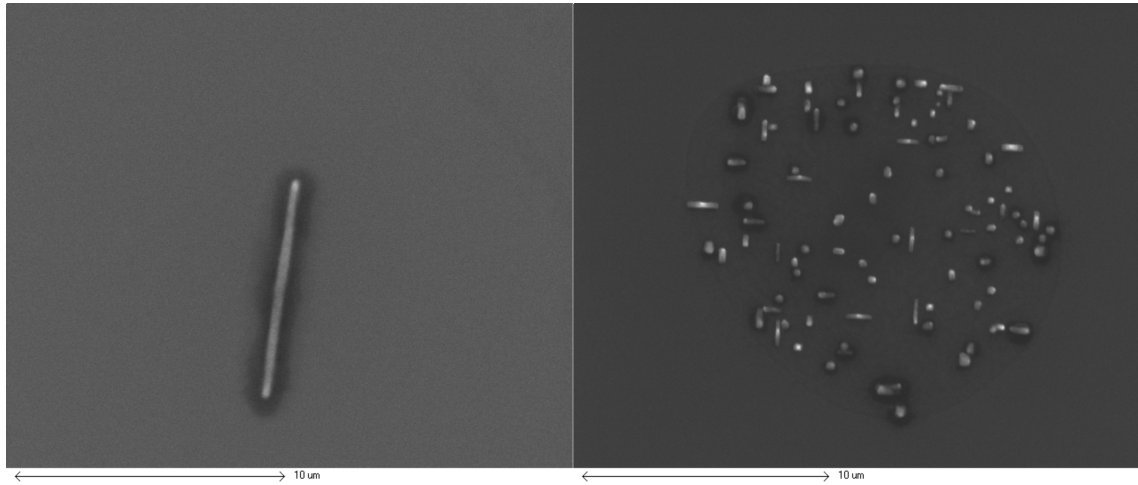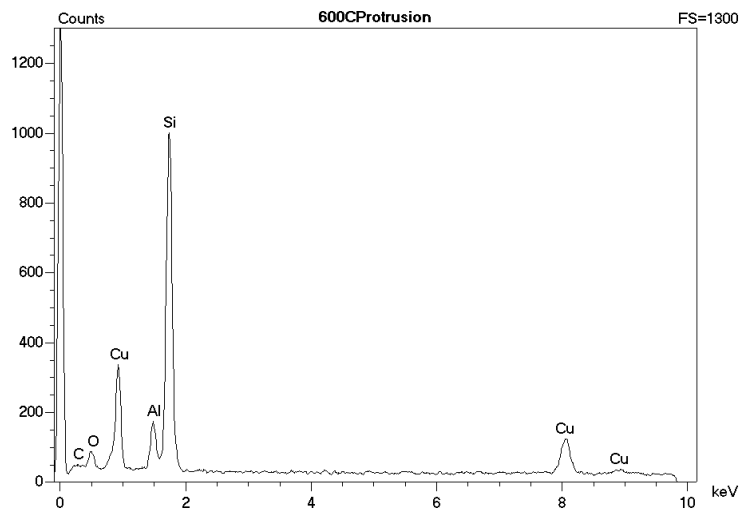

Figure A.3: EDX spectrum from the nanowire region, showing copper and aluminum signals that were not observed in signals from the bare substrate region.

direction relative to the substrate crystal orientation. In this case if copper particles landed on the silicon surface, the environment created by material ablation may generate favorable conditions for nanowire growth with an analogous mechanism. Silicon nanowire growth using pulsed laser ablation has been reported in the literature. However the wires do not show a preferred orientation in several of the reports (e.g., [188–190]). This VLS growth mechanism will yield final wire structures with metal droplets capping the ends of the wire, and can be verified using high resolution SEM or TEM.

Another possible mechanism is the analogous process to aluminum spiking in silicon [191]. The binary phase diagram of an Al-Si system shows that even though aluminum does not have a solid solubility into silicon, diffusion can occur in the reverse direction [192]. Silicon diffusion into an aluminum contact leaves behind voids that are subsequently filled in with aluminum, leaving a spike-like aluminum structure into the silicon substrate (e.g., [123, 193]). Analogous behavior may be occurring in the copper-silicon interface in the high temperature experiment [194, 195]. This scenario may be tested by carrying out a selective etch to preferentially etch away one of copper or silicon to examine if the observed wires and islands are the tips of copper spikes.

Overall, follow-up characterizations are required to determine the formation mechanisms of the nanowires and dense island structures. Further understanding may lead to novel techniques of preparing copper-silicon (or metal-silicon) nanostructures.

Bibliography

[1] D. Ashkenasi, M. Lorenz, R. Stoian, and A. Rosenfeld, *Applied Surface Science* **150**, 101 (1999).

[2] X. Liu, D. Du, and G. Mourou, *IEEE Journal of Quantum Electronics* **33**, 1706 (1997).

[3] B. Rethfeld, K. Sokolowski-Tinten, D. von der Linde, and S. I. Anisimov, *Applied Physics A: Materials Science & Processing* **79**, 767 (2004).

[4] N. H. Rizvi, *RIKEN Review* **50**, 107 (2003).

[5] D. Bäuerle, *Laser Processing and Chemistry*, Springer-Verlag Berlin Heidelberg, third edition, 2000.

[6] D. Perez and L. J. Lewis, *Physical Review Letters* **89**, 255504 (2002).

[7] D. Perez and L. J. Lewis, *Physical Review B: Condensed Matter and Materials Physics* **67**, 184102 (2003).

[8] P. Lorazo, L. J. Lewis, and M. Meunier, *Physical Review Letters* **91**, 225502 (2003).

[9] P. Lorazo, L. J. Lewis, and M. Meunier, *Physical Review B: Condensed Matter and Materials Physics* **73**, 134108 (2006).

[10] L. J. Lewis and D. Perez, *Applied Surface Science* **255**, 5101 (2009).

[11] A. Cavalleri, K. Sokolowski-Tinten, J. Bialkowski, M. Schreiner, and D. von der Linde, *Journal of Applied Physics* **85**, 3301 (1999).

[12] D. von der Linde and K. Sokolowski-Tinten, *Applied Surface Science* **154-155**, 1 (2000).

[13] E. Leveugle, D. S. Ivanov, and L. V. Zhigilei, *Applied Physics A: Materials Science & Processing* **79**, 1643 (2004).

[14] J. Reif, F. Costache, S. Eckert, and M. Henyk, *Applied Physics A: Materials Science & Processing* **79**, 1229 (2004).

[15] K. Sokolowski-Tinten, J. Bialkowski, A. Cavalleri, D. von der Linde, A. Oparin, J. Meyer-ter Vehn, and S. I. Anisimov, *Physical Review Letters* **81**, 224 (1998).

[16] H. Dachraoui, W. Husinsky, and G. Betz, *Applied Physics A: Materials Science & Processing* **83**, 333 (2006).

[17] I. V. Hertel, R. Stoian, D. Ashkenasi, A. Rosenfeld, and E. E. B. Campbell, *RIKEN Review* **32**, 23 (2001).

[18] Y. Jee, M. F. Becker, and R. M. Walser, *Journal of the Optical Society of America B* **5**, 648 (1988).

[19] J. Byskov-Nielsen, J.-M. Savolainen, M. S. Christensen, and P. Balling, *Applied Physics A: Materials Science & Processing* **101**, 97 (2010).

[20] P. T. Mannion, J. Magee, E. Coyne, G. M. O'connor, and T. J. Glynn, *Applied Surface Science* **233**, 275 (2004).

[21] F. Costache, S. Eckert, and J. Reif, *Applied Physics A: Materials Science & Processing* **92**, 897 (2008).

[22] A. Rosenfeld, M. Lorenz, R. Stoian, and D. Ashkenasi, *Applied Physics A: Materials Science & Processing* **69**, 373 (1999).

[23] J. Bonse, S. Baudach, J. Krüger, and W. Kautek, *Proceedings of SPIE* **4065**, 161 (2000).

[24] J. Bonse, S. Baudach, J. Krüger, W. Kautek, and M. Lenzner, *Applied Physics A: Materials Science & Processing* **74**, 19 (2002).

[25] J. Bonse, J. M. Wrobel, J. Krüger, and W. Kautek, *Applied Physics A: Materials Science & Processing* **72**, 89 (2001).

[26] J. Bonse, P. Rudolph, J. Krüger, S. Baudach, and W. Kautek, *Applied Surface Science* **154-155**, 659 (2000).

[27] J. Bonse, S. M. Wiggins, J. Solis, H. Sturm, L. Urech, A. Wokaun, and T. Lippert, *Journal of Physics: Conference Series* **59**, 105 (2007).

[28] D. Gómez and I. Goenaga, *Applied Surface Science* **253**, 2230 (2006).

[29] S. E. Kirkwood, A. C. van Popta, Y. Y. Tsui, and R. Fedosejevs, *Applied Physics A: Materials Science & Processing* **81**, 729 (2004).

[30] S. E. Kirkwood, M. T. Taschuk, Y. Y. Tsui, and R. Fedosejevs, *Journal of Physics: Conference Series* **59**, 591 (2007).

[31] S. Baudach, J. Bonse, J. Krüger, and W. Kautek, *Applied Surface Science* **154**, 555 (2000).

[32] S. Baudach, J. Bonse, and W. Kautek, *Applied Physics A: Materials Science & Processing* **69**, 395 (1999).

[33] D. Ashkenasi, R. Stoian, and A. Rosenfeld, *Applied Surface Science* **154-155**, 40 (2000).

[34] S. Beke, K. Sugioka, K. Midorikawa, A. Péter, L. Nánai, and J. Bonse, *Journal of Physics D: Applied Physics* **43**, 025401 (2010).

[35] M. Birnbaum, *Journal of Applied Physics* **36**, 3688 (1965).

[36] A. E. Siegman and P. M. Fauchet, *IEEE Journal of Quantum Electronics* **QE-22**, 1384 (1986).

[37] P. M. Fauchet and A. E. Siegman, *Applied Physics A: Materials Science & Processing* **32**, 135 (1983).

[38] H. M. van Driel, J. E. Sipe, and J. F. Young, *Physical Review Letters* **49**, 1955 (1982).

[39] J. F. Young, J. E. Sipe, J. S. Preston, and H. M. van Driel, *Applied Physics Letters* **41**, 261 (1982).

[40] J. E. SIPE, J. F. YOUNG, J. S. PRESTON, and H. M. VAN DRIEL, *Physical Review B: Condensed Matter and Materials Physics* **27**, 1141 (1983).

[41] J. F. YOUNG, J. S. PRESTON, H. M. VAN DRIEL, and J. E. SIPE, *Physical Review B: Condensed Matter and Materials Physics* **27**, 1155 (1983).

[42] J. F. YOUNG, J. E. SIPE, and H. M. VAN DRIEL, *Physical Review B: Condensed Matter and Materials Physics* **30**, 2001 (1984).

[43] T. H. R. CRAWFORD and H. K. HAUGEN, *Applied Surface Science* **253**, 4970 (2007).

[44] M. COUILLARD, A. BOROWIEC, H. K. HAUGEN, J. S. PRESTON, E. M. GRISWOLD, and G. A. BOTTON, *Journal of Applied Physics* **101**, (2007).

[45] A. BOROWIEC and H. K. HAUGEN, *Applied Physics Letters* **82**, 4462 (2003).

[46] E. M. HSU, T. H. R. CRAWFORD, H. F. TIEDJE, and H. K. HAUGEN, *Applied Physics Letters* **91**, 111102 (2007).

[47] E. M. HSU, T. H. R. CRAWFORD, C. MAUNDERS, G. A. BOTTON, and H. K. HAUGEN, *Applied Physics Letters* **92**, 221112 (2008).

[48] E. M. HSU, N. A. MAILMAN, G. A. BOTTON, and H. K. HAUGEN, *Applied Physics A: Materials Science & Processing* **103**, 185 (2011).

[49] J. BONSE, A. ROSENFELD, and J. KRÜGER, *Journal of Applied Physics* **106**, 104910 (2009).

[50] M. HUANG, F. ZHAO, Y. CHENG, N. XU, and Z. XU, *ACS Nano* **3**, 4062 (2009).

[51] J. Reif, F. Costache, O. Varlamova, G. Jia, and M. Ratzke, *physica status solidi (c)* **6**, 681 (2009).

[52] J. Bonse, M. Munz, and H. Sturm, *Journal of Applied Physics* **97**, 13538 (2005).

[53] J. Bonse and J. Krüger, *Journal of Applied Physics* **108**, 034903 (2010).

[54] R. Wagner, J. Gottmann, A. Horn, and E. W. Kreutz, *Applied Surface Science* **252**, 8576 (2006).

[55] T. Q. Jia, H. X. Chen, M. Huang, F. L. Zhao, J. R. Qiu, R. X. Li, Z. Z. Xu, X. K. He, J. Zhang, and H. Kuroda, *Physical Review B: Condensed Matter and Materials Physics* **72**, 125429 (2005).

[56] R. Le Harzic, H. Schuck, D. Sauer, T. Anhut, I. Riemann, and K. Knig, *Optics Express* **13**, 6651 (2005).

[57] R. Le Harzic, D. Dörr, D. Sauer, M. Neumeier, M. Epple, H. Zimmermann, and F. Stracke, *Optics Letters* **36**, 229 (2011).

[58] F. Costache, M. Henyk, and J. Reif, *Applied Surface Science* **186**, 352 (2002).

[59] F. Costache, M. Henyk, and J. Reif, *Applied Surface Science* **208-209**, 486 (2003).

[60] F. Costache, S. Kouteva-Arguirova, and J. Reif, *Applied Physics A: Materials Science & Processing* **79**, 1429 (2004).

[61] J. REIF, F. COSTACHE, M. HENYK, and S. PANDELOV, *Applied Surface Science* **197-198**, 891 (2002).

[62] X. WANG, T. JIA, X. LI, C. LI, D. FENG, H. SUN, S. XU, and Z. XU, *Chinese Optics Letters* **3**, 615 (2005).

[63] N. YASUMARU, K. MIYAZAKI, and J. KIUCHI, *Applied Physics A: Materials Science & Processing* **81**, 933 (2005).

[64] J. BONSE, H. STURM, D. SCHMIDT, and W. KAUTEK, *Applied Physics A: Materials Science & Processing* **71**, 657 (2000).

[65] A. M. OZKAN, A. P. MALSE, T. A. RAILKAR, W. D. BROWN, M. D. SHIRK, and P. A. MOLIAN, *Applied Physics Letters* **75**, 3716 (1999).

[66] Q. WU, Y. MA, R. FANG, Y. LIAO, Q. YU, X. CHEN, and K. WANG, *Applied Physics Letters* **82**, 1703 (2003).

[67] C. HNATOVSKY, R. S. TAYLOR, P. P. RAJEEV, E. SIMOVA, V. R. BHARD-WAJ, D. M. RAYNER, and P. B. CORKUM, *Applied Physics Letters* **87**, 014104 (2005).

[68] V. R. BHARDWAJ, E. SIMOVA, P. P. RAJEEV, C. HNATOVSKY, R. S. TAY-LOR, D. M. RAYNER, and P. B. CORKUM, *Physical Review Letters* **96**, 057404 (2006).

[69] D. WORTMANN, J. GOTTMANN, N. BRANDT, and H. HORN-SOLLE, *Optics Express* **16**, 1517 (2008).

[70] M. Hoerstmann-Jungemann, J. Gottmann, and D. Wortmann, *Journal of Laser Micro/Nanoengineering* **4**, 135 (2009).

[71] M. Budiman, E. M. Hsu, H. K. Haugen, and G. A. Botton, *Applied Physics A: Materials Science & Processing* **98**, 849 (2010).

[72] T. H. Her, R. J. Finlay, C. Wu, S. Deliwala, and E. Mazur, *Applied Physics Letters* **73**, 1673 (1998).

[73] T. H. Her, R. J. Finlay, C. Wu, and E. Mazur, *Applied Physics A: Materials Science & Processing* **70**, 383 (2000).

[74] D. Riedel, J. L. Hernandez-Pozos, R. E. Palmer, and K. W. Kolasinski, *Applied Physics A: Materials Science & Processing* **78**, 381 (2004).

[75] V. Zorba, I. Alexandrou, I. Zergioti, A. Manousaki, C. Ducati, A. Neumeister, C. Fotakis, and G. A. J. Amaratunga, *Thin Solid Films* **453-454**, 492 (2004).

[76] Z. Jingtao, Y. Gang, Z. Ming, C. Deying, and Z. Li, *Applied Surface Science* **245**, 102 (2005).

[77] X. Chen, J. Zhu, G. Ying, and L. Zhao, *Materials Letters* **60**, 63 (2006).

[78] Z. Li, Z. Jingtao, L. Wen, W. Yu, F. Guojin, and W. Zhanshan, *Materials Letters* **60**, 2187 (2006).

[79] J.-T. Zhu, Y.-F. Shen, W. Li, X. Chen, G. Ying, D.-Y. Chen, and L. Zhao, *Applied Surface Science* **252**, 2752 (2006).

[80] M. C. Gupta, B. K. Nayak, and K. W. Kolasinski, *Applied Surface Science* **253**, 6580 (2007).

[81] T. H. R. Crawford, G. A. Botton, and H. K. Haugen, *Applied Surface Science* **256**, 1749 (2010).

[82] M. A. Bassam, P. Parvin, B. Sajad, A. Moghimi, and H. Coster, *Applied Surface Science* **254**, 2621 (2008).

[83] J. D. Fowlkes, A. J. Pedraza, and D. H. Lowndes, *Applied Physics Letters* **77**, 1629 (2000).

[84] D. H. Lowndes, J. D. Fowlkes, and A. J. Pedraza, *Applied Surface Science* **154-155**, 647 (2000).

[85] A. J. Pedraza, J. D. Fowlkes, S. Jesse, C. Mao, and D. H. Lowndes, *Applied Surface Science* **168**, 251 (2000).

[86] C. Wu, C. H. Crouch, L. Zhao, J. E. Carey, R. Younkin, J. A. Levinson, E. Mazur, R. M. Farrell, P. Gothoskar, and A. Karger, *Applied Physics Letters* **78**, 1850 (2001).

[87] C. Wu, C. H. Crouch, L. Zhao, and E. Mazur, *Applied Physics Letters* **81**, 1999 (2002).

[88] M. Y. Shen, C. H. Crouch, J. E. Carey, R. Younkin, E. Mazur, M. Sheehy, and C. M. Friend, *Applied Physics Letters* **82**, 1715 (2003).

[89] C. H. Crouch, J. E. Carey, J. M. Warrender, M. J. Aziz, E. Mazur, and F. Y. Génin, *Applied Physics Letters* **84**, 1850 (2004).

[90] C. H. Crouch, J. E. Carey, M. Shen, E. Mazur, and F. Y. Génin, *Applied Physics A: Materials Science & Processing* **79**, 1635 (2004).

[91] J. E. Carey, C. H. Crouch, M. Shen, and E. Mazur, *Optics Letters* **30**, 1773 (2005).

[92] M. A. Sheehy, L. Winston, J. E. Carey, C. M. Friend, and E. Mazur, *Chemistry of Materials* **17**, 3582 (2005).

[93] Z. Huang, J. E. Carey, L. Mingguo, G. Xiangyi, E. Mazur, and J. C. Campbell, *Applied Physics Letters* **89**, 33506 (2006).

[94] L. Ji-Ming and X. Jian-Ting, *Laser Physics* **18**, 1539 (2008).

[95] S. Lee, D. Yang, and S. Nikumb, *Applied Surface Science* **254**, 2996 (2008).

[96] B. R. Tull, M. A. Sheehy, C. M. Friend, and E. Mazur, *Materials Science & Engineering B: Solid-State Materials for Advanced Technology* **137**, 289 (2007).

[97] Y. Liu, S. Liu, Y. Wang, G. Feng, J. Zhu, and L. Zhao, *Laser Physics* **18**, 1148 (2008).

[98] R. Younkin, J. E. Carey, E. Mazur, J. A. Levinson, and C. M. Friend, *Journal of Applied Physics* **93**, 2626 (2003).

[99] T. Sarnet, M. Halbwax, R. Torres, P. Delaporte, M. Sentis, S. Martinuzzi, V. Vervisch, F. Torregrosa, H. Etienne, L. Roux, and S. Bastide, *Proceedings of SPIE* **6881**, 688119 (2008).

[100] V. Zorba, N. Boukos, I. Zergioti, and C. Fotakis, *Applied Optics* **47**, 1846 (2008).

[101] A. V. Kabashin, P. Delaporte, A. Pereira, D. Grojo, R. Torres, T. Sarnet, and M. Sentis, *Nanoscale Research Letters* **5**, 454 (2010).

[102] P. G. Maloney, P. Smith, V. King, C. Billman, M. Winkler, and E. Mazur, *Applied Optics* **49**, 1085 (2010).

[103] M. J. Smith, M. Winkler, M.-J. Sher, Y.-T. Lin, E. Mazur, and S. Gradeĉak, *Applied Physics A: Materials Science & Processing* **105**, 795 (2011).

[104] J. Thogersen, A. Borowiec, H. K. Haugen, F. E. McNeill, and I. M. Stronach, *Applied Physics A: Materials Science & Processing* **73**, 361 (2001).

[105] R. Trebino, S. Akturk, X. Gu, P. Gabolde, and Z. Wang, *Laser Focus World* **41**, 65 (2005).

[106] Z. Sacks, G. Mourou, and R. Danielius, *Optics Letters* **26**, 462 (2001).

[107] M. Raghuramaiah, A. K. Sharma, P. A. Naik, and P. D. Gupta, *Optics Communications* **223**, 163 (2003).

[108] R. M. Langford and A. K. Petford-Long, *Journal of Vacuum Science & Technology A: Vacuum, Surfaces, and Films* **19**, 2186 (2001).

[109] J. M. Liu, *Optics Letters* **7**, 196 (1982).

[110] J. Bonse, K.-W. Brzezinka, and A. J. Meixner, *Applied Surface Science* **221**, 215 (2004).

[111] T. H. R. CRAWFORD, J. YAMANAKA, G. A. BOTTON, and H. K. HAUGEN, *Journal of Applied Physics* **103**, 053104 (2008).

[112] T. H. R. CRAWFORD, A. BOROWIEC, and H. K. HAUGEN, *Applied Physics A: Materials Science & Processing* **80**, 1717 (2005).

[113] J. EICHSTÄDT, G. RÖMER, and A. VELD, *Physics Procedia* **12**, 7 (2011).

[114] P. G. COLEMAN, A. P. KNIGHTS, and R. M. GWILLIAM, *Journal of Applied Physics* **86**, 5988 (1999).

[115] G. D. WATKINS, *Physical Review B: Condensed Matter and Materials Physics* **13**, 2511 (1976).

[116] R. HULL, *Properties of crystalline silicon*, Institution of Electrical Engineers, 1999.

[117] J. C. CORELLI, R. C. YOUNG, and C. S. CHEN, *IEEE Transaction on Nuclear Science* **17**, 128 (1970).

[118] D. C. SCHMIDT, B. G. SVENSSON, S. GODEY, E. NTSOENZOK, J. F. BARBOT, and C. BLANCHARD, *Nuclear Instruments & Methods in Physics Research, Section B: Beam Interactions with Materials and Atoms* **147**, 106 (1999).

[119] R. POIRIER, V. AVALOS, S. DANNEFAER, F. SCHIETTEKATTE, and S. ROORDA, *Nuclear Instruments & Methods in Physics Research, Section B: Beam Interactions with Materials and Atoms* **206**, 85 (2003).

[120] C. V. Anto, S. Abhaya, P. Magudapathy, G. Amarendra, and K. G. M. Nair, *Journal of Physics D: Applied Physics* **43**, 325401 (2010).

[121] S. M. Sze, *Semiconductor devices - physics and technology*, Wiley, 1985.

[122] L. Csepregi, E. F. Kennedy, J. W. Mayer, and T. W. Sigmon, *Journal of Applied Physics* **49**, 3906 (1978).

[123] J. W. Mayer and S. S. Lau, *Electronic materials science: for integrated circuits in Si and GaAs*, Macmillan Publishing Company, Ithaca, New York, 1990.

[124] G. K. Hubler, C. N. Waddell, W. G. Spitzer, J. E. Fredrickson, S. Prussin, and R. G. Wilson, *Journal of Applied Physics* **59**, 3294 (1979).

[125] P. D. Townsend, *Reports on Progress in Physics* **50**, 501 (1987).

[126] C. C. Katsidis, *Journal of the Optical Society of America B: Optical Physics* **25**, 854 (2008).

[127] E. D. Pilak, *Handbook of Optical Constants of Solids*, Academic Press, San Diego, California, 1985.

[128] M. Argument, S. Kirkwood, K. Chau, A. van Popta, Y. Tsui, and R. Fedosejevs, *Technical Digest of SPIE Opto-Canada* **2002**, 196 (2002).

[129] J. S. Yahng, J. R. Nam, and S. C. Jeoung, *Optics and Lasers in Engineering* **47**, 815 (2009).

[130] J. S. Yahng and S. C. Jeoung, *Optics and Lasers in Engineering* **49**, 1040 (2011).

[131] A. Braun, K. Zimmer, and F. Bigl, *Applied Surface Science* **154-155**, 73 (2000).

[132] J. R. Platenak, R. M. Walser, and M. F. Becker, *Laser induced optical damage in optical materials, NIST Special Publication from Boulder Damage Symposium* **752**, 216 (1986).

[133] T. Gupta, *Copper interconnect technology*, Springer Verlag, 2009.

[134] H. O. Jeschke, M. E. Garcia, M. Lenzner, J. Bonse, J. Krüger, and W. Kautek, *Applied Surface Science* **197-198**, 839 (2002).

[135] A. Borowiec, D. M. Bruce, D. T. Cassidy, and H. K. Haugen, *Applied Physics Letters* **83**, 225 (2003).

[136] J. Bonse, J. M. Wrobel, K.-W. Brzezinka, N. Esser, and W. Kautek, *Applied Surface Science* **202**, 272 (2002).

[137] S. E. Kirkwood, *Characterization of metal and semiconductor nanomilling at near threshold intensities using femtosecond laser pulses*, PhD thesis, 2007.

[138] D. J. Hwang, C. P. Grigoropoulos, and T. Y. Choi, *Journal of Applied Physics* **99**, 083101 (2006).

[139] A. Borowiec, M. Mackenzie, G. C. Weatherly, and H. K. Haugen, *Applied Physics A: Materials Science & Processing* **76**, 201 (2003).

[140] K. Sokolowski-Tinten, J. Bialkowski, and D. von der Linde, *Physical Review B: Condensed Matter and Materials Physics* **51**, 14186 (1995).

[141] K. Sokolowski-Tinten and D. von der Linde, *Physical Review B: Condensed Matter and Materials Physics* **61**, 2643 (2000).

[142] S. I. Kudryashov and V. I. Emel'yanov, *JETP Letters* **73**, 666 (2001).

[143] J. Bonse, G. Bachelier, J. Siegel, and J. Solis, *Physical Review B: Condensed Matter and Materials Physics* **74**, 134106 (2006).

[144] K. Rajkanan, R. Singh, and J. Shewchun, *Solid State Electronics* **22**, 793 (1979).

[145] H. A. Weakliem and D. Redfield, *Journal of Applied Physics* **50**, 1491 (1979).

[146] G. E. Jellison, *Applied Physics Letters* **41**, 594 (1982).

[147] G. E. Jellison, *Applied Physics Letters* **41**, 180 (1982).

[148] C. K. Min, J. Y. Park, D. G. Cahill, and S. Granick, *Journal of Applied Physics* **106**, 013102 (2009).

[149] J. Corelli, G. Oehler, J. Becker, and K. Eisentraut, *Journal of Applied Physics* **36**, 1787 (1965).

[150] P. G. Coleman, C. P. Burrows, and A. P. Knights, *Applied Physics Letters* **80**, 947 (2002).

[151] J. Ziegler, M. Ziegler, and J. Biersack, *Nuclear Instruments & Methods in Physics Research, Section B: Beam Interactions with Materials and Atoms* **268**, 1818 (2010).

[152] W. Kautek and J. Krüger, *Materials Science Forum* **173-174**, 17 (1995).

[153] Y. Izawa, Y. Izawa, Y. Setsuhara, M. Hashida, M. Fujita, R. Sasaki, H. Nagai, and M. Yoshida, *Applied Physics Letters* **90**, 044107 (2007).

[154] A. Borowiec and H. K. Haugen, *Applied Physics A: Materials Science & Processing* **79**, 521 (2004).

[155] J. Bonse, S. M. Wiggins, and J. Solis, *Journal of Applied Physics* **96**, 2352 (2004).

[156] G. Yu, J. Watanabe, K. Izumi, K. Nakashima, T. Jimbo, and M. Umeno, *Japanese Journal of Applied Physics* **40**, L183 (2001).

[157] P. J. Burnett and T. F. Page, *Journal of Materials Science* **19**, 845 (1984).

[158] J. Bonse, A. Rosenfeld, C. Grebing, G. Steinmeyer, N. Mailman, G. A. Botton, and H. K. Haugen, *Journal of Applied Physics* **106**, 074907 (2009).

[159] M. Guillermin, F. Garrelie, N. Sanner, E. Audouard, and H. Soder, *Applied Surface Science* **253**, 8075 (2007).

[160] J. Bonse, S. Wiggins, J. Solis, and T. Lippert, *Applied Surface Science* **247**, 440 (2005).

[161] E. Coyne, J. P. Magee, P. Mannion, G. M. O'Connor, and T. J. Glynn, *Applied Physics A: Materials Science & Processing* **81**, 371 (2005).

[162] J. Jia, M. Li, and C. V. Thompson, *Applied Physics Letters* **84**, 3205 (2004).

[163] D. C. Deshpande, A. P. Malshe, E. A. Stach, V. Radmilovic, D. Alexander, D. Doerr, and D. Hirt, *Journal of Applied Physics* **97**, 74316 (2005).

[164] Y. Izawa, Y. Setuhara, M. Hashida, and M. Fujita, *Japanese Journal of Applied Physics, Part 1 (Regular Papers, Short Notes & Review Papers)* **45**, 5791 (2006).

[165] T. H. R. Crawford, J. Yamanaka, E. M. Hsu, G. A. Botton, and H. K. Haugen, *Applied Physics A: Materials Science & Processing* **91**, 473 (2008).

[166] J. Z. P. Skolski, G. R. B. E. Römer, J. V. Obona, V. Ocelik, A. J. Huis in 't Veld, and J. T. M. De Hosson, *Proceedings of LPM2012* , 1 (2012).

[167] J. Z. P. Skolski, G. R. B. E. Römer, J. V. Obona, V. Ocelik, A. J. Huis in 't Veld, and J. T. M. De Hosson, *Physical Review B* **85**, 075320 (2012).

[168] J. E. Carey and J. Sickler, *Laser Focus World* (August 2009).

[169] A. Y. Vorobyev and C. Guo, *Optics Express* **19**, A1031 (2011).

[170] A. Vorobyev and C. Guo, *Applied Surface Science* **257**, 7291 (2011).

[171] D. G. Goebel, *Applied Optics* **6**, 125 (1967).

[172] J. Palmer, *Handbook of optics* **2**, 25.11 (1995).

[173] L. Hanssen, *Applied Optics* **40**, 3196 (2001).

[174] LABSPHERE, General purpose integrating spheres (Technical Guide).

[175] J. E. CAREY III, *Femtosecond-laser microstructuring of silicon for novel op-toelectronic devices*, PhD thesis, 2004.

[176] D. LIU, Y. LI, M. LIU, H. YANG, and Q. GONG, *Applied Physics B: Lasers and Optics* **91**, 597 (2008).

[177] T. G. KIM, J. M. WARRENDER, and M. J. AZIZ, *Applied Physics Letters* **88**, 241902 (2006).

[178] S. GUHA, M. D. PACE, D. N. DUNN, and I. L. SINGER, *Applied Physics Letters* **70**, 1207 (1997).

[179] G. LEDOUX, J. GONG, F. HUISKEN, O. GUILLOIS, and C. REYNAUD, *Applied Physics Letters* **80**, 4834 (2002).

[180] S. HERMANN, N. P. HARDER, R. BRENDEL, D. HERZOG, and H. HAFERKAMP, *Applied Physics A: Materials Science & Processing* **99**, 151 (2010).

[181] J. P. MCDONALD, V. R. MISTRY, K. E. RAY, S. M. YALISOVE, J. A. NEES, and N. R. MOODY, *Applied Physics Letters* **88**, 153121 (2006).

[182] T. RUBLACK, S. HARTNAUER, P. KAPPE, C. SWIATKOWSKI, and G. SEIFERT, *Applied Physics A: Materials Science & Processing* **103**, 43 (2011).

[183] T. RUBLACK and G. SEIFERT, *Optical Materials Express* **1**, 543 (2011).

[184] J. P. MCDONALD, J. A. NEES, and S. M. YALISOVE, *Journal of Applied Physics* **102**, 063109 (2007).

[185] J. P. McDonald, V. R. Mistry, K. E. Ray, and S. M. Yalisove, *Applied Physics Letters* **88**, 183113 (2006).

[186] R. R. LaPierre, 2011, Private communication.

[187] S. C. Ghosh, P. Kruse, and R. R. LaPierre, *Nanotechnology* **20**, 115602 (2009).

[188] J. Zhang, K. Sugioka, and K. Midorikawa, *Applied Physics A: Materials Science & Processing* **67**, 499 (1998).

[189] N. Fukata, T. Oshima, T. Tsurui, S. Ito, and K. Murakami, *Science and Technology of Advanced Materials* **6**, 628 (2005).

[190] N. Fukata, M. Mitome, Y. Bando, M. Seoka, S. Matsushita, K. Murakami, J. Chen, and T. Sekiguchi, *Applied Physics Letters* **93**, 203106 (2008).

[191] R. N. Kleinman, 2011, Private communication.

[192] J. L. Murray and A. J. McAlister, *Journal of Phase Equilibria* **5**, 74 (1984).

[193] S. Wolf, *Silicon Processing for the VLSI Era vol. 2: Process Integration, Multi-Level-Interconnect Technology for VLSI and ULSI*, Lattice Press, Sunset Beach, Sunset Beach, California, 1990.

[194] H. Okamoto, *Journal of Phase Equilibria* **23**, 281 (2002).

[195] A. A. Istratov and E. R. Weber, *Journal of the Electrochemical Society* **149**, G21 (2002).